Université Paris Diderot (Paris 7)
Laboratoire de Physique Nucléaire et de Hautes Énergies
École Doctorale: Particules, Noyaux et Cosmos (ED 517)

Thèse
pour obtenir le grade de
Docteur ès Sciences

Observation d'une nouvelle particule dans la recherche du boson de Higgs se désintégrant en deux photons dans l'expérience ATLAS au LHC

par
Heberth Torres Dávila

Commission d'examen:

Giovanni Calderini	directeur de thèse
Louis Fayard	président du jury
Gautier Hamel de Monchenault	
Stephane Monteil	
Aleandro Nisati	rapporteur
Yves Sirois	rapporteur

Soutenue le 25 Mars 2013

University Paris Diderot (Paris 7)
"Laboratoire de Physique Nucléaire et de Hautes Énergies"
Doctoral school: "Particules, Noyaux et Cosmos" (ED 517)

Thesis
to obtain the degree of
"Docteur ès Sciences"
(Doctor of Philosophy)

Observation of a NEW PARTICLE in the search for the Higgs boson in the TWO PHOTON decay channel in the ATLAS experiment at the LHC

by
Heberth Torres Dávila

Examination Committee:

Giovanni Calderini	supervisor
Louis Fayard	president of the jury
Gautier Hamel de Monchenault	
Stephane Monteil	
Aleandro Nisati	referee
Yves Sirois	referee

Presented on March 25th, 2013

A mis padres,
a mis hermanos
y a Joany

Acknowledgements

I am grateful to the ATLAS group at LPNHE for hosting me during my PhD studies.
It has been a great pleasure for me to work with Giovanni Calderini, Sandro De Cecco, Frederic Derue, Bertrand Laforge, Sandrine Laplace, Giovanni Marchiori, Irena Nikolic-Audit, José Ocariz and Lydia Roos. I owe them my deepest gratitude for their valuable advices and friendship.
I would like to thank very specially my supervisor Giovanni C. and also Bertrand and José for their guidance and teaching.
I thank Frederic and Giovanni M. for the introduction to and help with the technical tools used in ATLAS.
I thank Philippe Schwemling, who was the leader of this ATLAS group and the director of the doctoral school during my studies.

I would like to thank as well the doctoral and postdoctoral fellows Olivier Davignon, Yuji Enari, Marine Kuna, Kun Liu, Camila Rangel Smith, Nguyet Trinh, Liwen Yao and Li Yuan for their company and for the corridor discussions.

In addition, I would like to thank Reynald Pain and the LPNHE for their hospitality, and Eli Ben-Haim for his advices.

I would like to thank the ATLAS collaboration for allowing me to participate in this great experiment and in the exciting discovery of the new boson.
I thank many people I had the opportunity to work with in the Standard Model Direct Photon group and the Higgs Subgroup 1. I acknowledge particularly the support of Leonardo Carminati, Louis Fayard, Marumi Kado, Kerstin Tackmann and Junichi Tanaka.

I thank Louis Fayard, Gautier Hamel de Monchenault, Stephane Monteil, Aleandro Nisati and Yves Sirois for the evaluation of this thesis.

I equally acknowledge the *Fundación Gran Mariscal de Ayacucho* (Fundayacucho) and the Embassy of France in Venezuela for the financial support.

I acknowledge the HELEN project (High Energy Physics Latinamerican-European Network) for a training internship, which was the bridge between my undergraduate studies and my doctoral studies in particle physics.
I thank Luis Núñez and again José Ocariz for their support in this project.

Contents

Introduction **13**

1 The Standard Model Higgs boson **15**
1.1 The Prediction of the SM Higgs boson 15
1.1.1 Gauge symmetries 15
1.1.2 Spontaneous symmetry-breaking 16
1.1.3 The Higgs mechanism 18
1.1.4 The SM Higgs boson 19
1.2 Constraints on the Higgs boson mass 20
1.2.1 Theoretical constraints 20
1.2.2 Experimental exclusion before the LHC 21
1.2.3 Indirect experimental constraints 21
1.3 The Higgs boson search at the LHC 23
1.3.1 Higgs boson production at the LHC 23
1.3.2 Higgs boson search channels 24
1.3.3 The $H \to \gamma\gamma$ channel 25

2 The ATLAS experiment at the LHC **29**
2.1 The Large Hadron Collider 29
2.1.1 Introduction 29
2.1.2 Objectives 30
2.1.3 General layout 30
2.1.4 The LHC main ring 32
2.1.5 Performance 34
2.1.6 Operational history 35
2.2 The ATLAS experiment 36
2.2.1 Detector overview 36
2.2.2 The ATLAS collaboration 39
2.2.3 Detector requirements 40
2.2.4 Coordinate system and nomenclature 41
2.3 Magnet system 42
2.3.1 Central solenoid 42
2.3.2 Barrel and end-cap toroids 43
2.4 Inner detector 43
2.4.1 Precision silicon sensors 45
2.4.2 Transition radiation tracker 45
2.5 Calorimeters 46

2.5.1 The electromagnetic calorimeter . . . 46
2.5.2 Hadronic calorimeter . . . 52
2.5.3 Forward calorimeters . . . 52
2.6 Muon spectrometer . . . 52
2.7 Trigger system . . . 54
2.8 Computing framework . . . 54
2.8.1 Computing facilities . . . 54
2.8.2 Software . . . 55
2.8.3 Data processing and formats . . . 55
2.9 Simulation . . . 56

3 Identification and reconstruction of photons in ATLAS 57
3.1 Reconstruction of photon candidates . . . 57
3.2 Identification of electrons, converted and unconverted photons . . . 59
3.3 Photon energy measurement . . . 61
3.4 Photon identification . . . 66
3.5 Isolation criteria . . . 70

4 Statistical analysis procedure 75
4.1 General aspects . . . 75
4.2 Testing the signal-plus-background hypothesis . . . 76
4.3 Asymptotic approximation for setting exclusion limits . . . 78
4.4 Testing the background-only hypothesis . . . 81
4.5 Systematic uncertainties . . . 84

5 The $H \to \gamma\gamma$ analysis 85
5.1 Introduction . . . 85
5.2 Samples . . . 86
5.2.1 Data samples . . . 86
5.2.2 Monte Carlo samples . . . 86
5.2.3 Diphoton event selection . . . 88
5.2.4 Selection of the primary vertex . . . 94
5.2.5 Diphoton invariant mass . . . 96
5.3 Expected signal . . . 98
5.3.1 Signal mass distribution . . . 98
5.3.2 Uncertainty on the signal peak position . . . 99
5.3.3 Signal efficiency and yields . . . 99
5.4 Background composition . . . 101
5.4.1 Decomposition methods . . . 101
5.4.2 Drell Yan Background . . . 103
5.4.3 Background composition results . . . 103
5.5 Event categorization . . . 104
5.5.1 Categorization according to the photon conversion status and η direction . . . 105
5.5.2 Categorization based on the $p_{\mathrm{Tt}}^{\gamma\gamma}$ discriminant variable . . . 106
5.5.3 2-jet category . . . 107
5.5.4 Categorization summary . . . 110

5.5.5 Systematic uncertainties on the distribution of signal events among the categories . . . 115
5.6 Data modeling . . . 116
5.6.1 Signal parametrization . . . 116
5.6.2 Signal systematic uncertainties . . . 118
5.6.3 Background parameterization and uncertainties . . . 119
5.7 Results . . . 122
5.7.1 Exclusion limits . . . 122
5.7.2 Excess quantification . . . 124
5.7.3 Excess characterization . . . 127

6 Overview of recent results of the Higgs boson search 131
6.1 Observation of a new particle . . . 132
6.2 Properties of the new boson . . . 134

Conclusions 139

A Studies of non-collision background for photon production measurements 141
A.1 Introduction . . . 141
A.2 Background estimation method . . . 143
A.3 Event selections . . . 144
A.4 Results . . . 145
A.4.1 Photons at low p_{T} . . . 146
A.4.2 Photons at high p_{T} . . . 149
A.4.3 Diphotons . . . 151
A.5 Conclusions . . . 154

Bibliography 155

Introduction

Along with the discovery of a large variety of sub-atomic particles during the twentieth century, a set of models were developed trying to explain the elementary composition of matter and the fundamental interactions. In the second half of the century, a quantum field theory that described the experimental observations was successfully built, the so-called *Standard Model* (SM) [1–3].

An important piece of the Standard Model is the mechanism of spontaneous electroweak symmetry breaking proposed by Higgs, Brout, Englert, Guralnik, Hagen and Kibble [4–6]. It is introduced in the Standard Model to make it compatible with the massive vector bosons $W^{\pm}$ and Z^0, mediators of the weak interactions, as well as with the masses of the fermions. In addition, this mechanism predicts the existence of a new particle, the longly searched Higgs boson.

Experiments at the LEP and Tevatron colliders searched the Higgs boson during years, without finding evidences of it, but setting exclusion at different ranges for its mass [7, 8].

One of the main objectives for the construction of the Large Hadron Collider (LHC) at CERN was to give a final answer to the question of the existence of the SM Higgs boson. The LHC is currently the newest and most powerful instrument for particle physics research. It is designed to collide protons with an unprecedented center-of-mass energy of $\sqrt{s} = 14$ TeV and a luminosity of 10^{34} cm^{-2}s^{-1}. It has already been operated during three years at 7 and 8 TeV, reaching a luminosity of 7.73×10^{33} cm^{-2}s^{-1}. Several detectors have been built to probe the collisions at the LHC, among which the general purpose detectors ATLAS and CMS are the ones that allow the Higgs boson search.

In the frame of my doctoral studies, I have worked in the ATLAS experiment, participating in the measurement of the photon production, and principally in the search for the Standard Model Higgs boson in the diphoton decay channel. This channel has been the most promising one for the Higgs boson search and its study at low mass.

In 2009, the sensitivity of the $H \to \gamma\gamma$ analysis to observe or exclude the Higgs boson with collisions at $\sqrt{s} = 10$ TeV was evaluated, based on Monte Carlo simulations. I have contributed to this analysis in particular in the estimation of a component of the background, the so-called reducible background. The result of this analysis was later extrapolated to $\sqrt{s} = 7$ TeV, and this work is reported in [9].

With the first LHC collision data, collected in 2010 at $\sqrt{s} = 7$ TeV, some measurements of the prompt photon and diphoton production cross-section were performed [10–12]. I have participated in these analyses estimating the possible contributions to the background from non-collision events. These non-collision events include those induced by the proton beams through interactions different from the

proton-proton collisions, and cosmic-ray showers that reach the ATLAS detector. Additionally, I have studied an alternative method for the measurement of the photon sample purity, based on photon isolation criteria using tracking information.

The first results of the $H \to \gamma\gamma$ analysis considering collision data were reported at beginning of 2011 in [13, 14], based on the data collected in 2010; after that, five documents were published based on data collected in 2011 [15–19], and two documents [20, 21] have been published in 2012 reporting results from the combination of data collected in 2011 and 2012, at $\sqrt{s} = 7$ TeV and $\sqrt{s} = 8$ TeV respectively.

In the ATLAS collaboration, the $H \to \gamma\gamma$ analysis is performed by a group of about one hundred people. I have been part of this group, participating at different levels of the working chain, that includes: data-preparation, optimizations of the event selection, statistical analysis, and the edition of ATLAS internal and public notes.

This document begins with an introduction to the Standard Model Higgs boson in Chapter 1. Then the LHC and the ATLAS experiment are presented in Chapter 2. The reconstruction, calibration and identification of prompt photons with the ATLAS detector are described in Chapter 3. The statistical procedure followed for the Higgs boson search is explained in Chapter 4. Chapter 5 presents the $H \to \gamma\gamma$ analysis performed between spring and summer of 2012, and the corresponding results, based on data collected in 2011 and the first half of 2012. A summary of other results on the search for the SM Higgs boson considering different channels and experiments are reported in Chapter 6, and then the conclusions are given. Additionally, the Appendix A presents the non-collision background studies performed in the frame of the photon production measurements.

Chapter 1

The Standard Model Higgs boson

The factors that brought to the prediction of existence of the Higgs boson in the Standard Model (SM) are briefly presented in this chapter; details can be found in [22–24]. It also presents the scenario of the Higgs boson search before the era of the Large Hadron Collider (LHC), the Higgs production mechanism at the LHC, and the decay modes that are used for its search.

1.1 The Prediction of the SM Higgs boson

1.1.1 Gauge symmetries

In the Standard Model, the description of the interactions between elementary particles is derived using symmetry principles. A symmetry is understood as an operation that can be performed on a system leaving it invariant. From Noether's theorem, every symmetry of nature is associated with the conservation of a physics quantity.

The Standard Model is constructed using the so-called *local gauge symmetry*, in which the symmetry of the interactions is associated with the conservation of some quantities (charge, color, etc.) locally, i.e. at the point where the interaction occur. A *local gauge transformation* is one whose parameters depend on the space-time point where it is applied, like:

$$\psi \rightarrow e^{i\theta(x)}\psi; \tag{1.1}$$

where θ is a function of the time and space coordinates.

Consider the Dirac Lagrangian, which describes a spinor field, associated with an electron like particle with spin $\frac{1}{2}$ and mass m,

$$\mathcal{L} = i\bar{\psi}\gamma^{\mu}\partial_{\mu}\psi - m\bar{\psi}\psi. \tag{1.2}$$

If the transformation of Equation 1.1 is applied to this Lagrangian, one can see that it is not invariant under this transformation.

In order to make this Lagrangian locally gauge invariant, one is obliged to add some extra terms. One ends up introducing a vector field A^{μ}, that transforms as follows

$$A_{\mu} \rightarrow A_{\mu} + \frac{1}{q}\partial_{\mu}\theta(x); \tag{1.3}$$

where q is a free parameter that corresponds to the charge of the particle associated

with the spinor field.

The Lagrangian for a vector field A^μ, associated with a spin 1 particle, is

$$\mathcal{L} = -\frac{1}{4}F^{\mu\nu}F_{\mu\nu} + \frac{1}{2}m_A^2 A^\nu A_\nu \tag{1.4}$$

The first term is the kinetic term of the field, where $F^{\mu\nu} = \partial^\mu A^\nu - \partial^\nu A^\mu$. It is invariant under the transformation in Equation 1.3, but the second term is not. Thus, the vector field has to be necessarily *massless* ($m_A = 0$), to keep the local gauge invariance.

After the introduction of the vector field, the resulting new Lagrangian is

$$\mathcal{L} = \left[i\bar{\psi}\gamma^\mu\partial_\mu\psi - m\bar{\psi}\psi\right] - \frac{1}{4}F^{\mu\nu}F_{\mu\nu} - \left(q\bar{\psi}\gamma^\mu\psi\right)A_\mu. \tag{1.5}$$

The vector field A_μ represents the photon field, and the Lagrangian in fact describes the interactions between Dirac fields and the photon Maxwell fields (quantum electrodynamics).

The symmetry considered above is called $U(1)$ *gauge invariance*. Similarly, a model that describes the strong interactions is obtained with local gauge transformations of a group $SU(3)$, and the whole Standard Model is constructed with a symmetry group denoted as $SU(3)_C \otimes SU(2)_L \otimes U(1)_Y$. The rules that govern the interactions are extracted by interpreting the Lagrangians after making them satisfying these symmetries.

1.1.2 Spontaneous symmetry-breaking

While the procedure explained above works to describe the strong and electromagnetic interactions, its implementation is not straightforward for the weak interaction. The gauge field introduced in Equation 1.5 must be massless, otherwise the desired local gauge invariance is broken. But, the $W^\pm$ and Z^0 vector bosons that mediate the weak interactions are massive; their mass explains the relative weakness of the weak force with respect to the electromagnetic force, and the short range of weak interactions.

The way to introduce the massive vector bosons in the Standard Model keeping the local gauge invariance is to use the mechanism proposed by Higgs, Brout, Englert, Guralnik, Hagen and Kibble [4–6], commonly known as Higgs mechanism, in which a phenomenon called spontaneous symmetry-breaking is used. Here, an example is given to show how this mechanism works.

Consider a complex field that combines two real fields

$$\phi = \frac{1}{\sqrt{2}}\left(\phi_1 + i\phi_2\right), \tag{1.6}$$

with Lagrangian

$$\mathcal{L} = \frac{1}{2}(\partial_\mu\phi)^*(\partial^\mu\phi) - V(\phi), \tag{1.7}$$

with

$$V(\phi) = -\mu^2(\phi^*\phi) + \lambda(\phi^*\phi)^2. \tag{1.8}$$

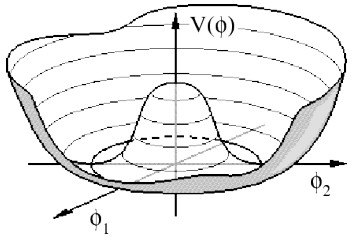

Figure 1.1: Potential of the Lagrangian in Equation 1.11 (in square brackets) as a function of the potential components ϕ_1 and ϕ_2.

Require this Lagrangian to be invariant under local gauge symmetry transformations of the group $U(1)$,

$$\phi \rightarrow e^{i\theta(x)}\phi. \tag{1.9}$$

As above, some terms need to be added, introducing gauge fields. In fact, there is a procedure to find the required terms, which consists on replacing the derivative of the Lagrangian by a covariant derivative, which for this example is

$$\mathcal{D}_\mu \equiv \partial_\mu + iqA_\mu. \tag{1.10}$$

Thus, the result is

$$\mathcal{L} = \frac{1}{2}\mathcal{D}_\mu\phi^* \, \mathcal{D}^\mu\phi - \left[-\mu^2(\phi^*\phi) + \lambda(\phi^*\phi)^2\right] - \frac{1}{4}F^{\mu\nu}F_{\mu\nu}. \tag{1.11}$$

In order to interpret this Lagrangian, a particular treatment is required because of the form of the potential (in square brackets). The ground state of this potential is infinitely degenerated, as illustrated in Figure 1.1. There are infinite states in the circle of minimum potential,

$$\phi_1{}^2 + \phi_2{}^2 = v^2, \quad \text{with } v^2 \equiv \frac{\mu^2}{\lambda}. \tag{1.12}$$

v is called *vacuum expectation value*. One has to choose one ground state as reference, and develop the Lagrangian re-writing the field ϕ in terms of fields that fluctuate around the chosen ground state. For simplicity one can choose the minimum $\phi_1 = v$ and $\phi_2 = 0$, and define the fields η and ξ as

$$\eta = \phi_1 - v, \quad \xi = \phi_2. \tag{1.13}$$

The fact of choosing one ground state among the infinite possibilities and reformulating the Lagrangian based on it is what is called *spontaneous symmetry-breaking*, because the symmetry is left with an arbitrary selection to perform the calculation.

The result of developing Equation 1.11 in terms of η and ξ is

$$\begin{aligned}\mathcal{L} = &\left[\frac{1}{2}(\partial_\mu\eta)(\partial^\mu\eta) - v^2\lambda\eta^2\right] + \left[\frac{1}{2}(\partial_\mu\xi)(\partial^\mu\xi)\right] \\ &+ \left[-\frac{1}{4}F^{\mu\nu}F_{\mu\nu} + \frac{1}{2}q^2v^2A^\nu A_\nu\right] \\ &- 2ivq(\partial_\mu\xi)A^\mu \\ &+ \text{ cubic and quartic terms.}\end{aligned} \tag{1.14}$$

The first term in square brackets corresponds to a scalar field that is associated with a particle of spin 0 and mass

$$m_\eta = \sqrt{2v^2\lambda}. \tag{1.15}$$

The second term corresponds to a massless scalar field; this type of fields are called *Nambu-Goldstone bosons*, and are known to appear when there is spontaneous symmetry breaking. And the third term is a massive gauge vector field, just as required in the electroweak model; the mass of this gauge vector field is

$$m_A = qv \tag{1.16}$$

1.1.3 The Higgs mechanism

In the previous section, the required massive vector field has been introduced; nevertheless, the Goldstone boson also introduced is not compatible with the experimental observations, and in addition the term in the third line suggest that the current interpretation of the Lagrangian is not correct. This issue is solved in the so-called Higgs mechanism [4–6] by choosing a particular gauge.

Re-define η and ξ in such a way that the field ϕ can be written as

$$\phi = \frac{1}{\sqrt{2}}(v+\eta)e^{i\xi/v}, \tag{1.17}$$

and consider a vector field that transforms as

$$A_\mu \to A_\mu + \frac{1}{qv}\partial_\mu\xi, \tag{1.18}$$

The result of re-developing the Lagrangian of Equation 1.11 in terms of these re-defined η and ξ is the following

$$\begin{aligned}\mathcal{L} = &\left[\frac{1}{2}(\partial_\mu)(\partial^\mu) - v^2\lambda\eta^2\right] + \left[-\frac{1}{16}F^{\mu\nu}F_{\mu\nu} + \frac{1}{2}q^2v^2A^\nu A_\nu\right] \\ &+ \text{ cubic and quartic terms.}\end{aligned} \tag{1.19}$$

The Goldstone boson has disappeared; more precisely, it has been "eaten" by a new A_μ polarization. And the particle associated with η is what is called a *Higgs particle*.

1.1.4 The SM Higgs boson

In the Standard Model, the Higgs mechanism is used to introduce the mass terms of the $W^{\pm}$ and Z^0 vector bosons. In this case, a $SU(2)$ doublet of complex scalar fields is introduced

$$\phi = \begin{pmatrix} \phi^+ \\ \phi^0 \end{pmatrix} = \frac{1}{\sqrt{2}} \begin{pmatrix} \phi_1 + i\phi_2 \\ \phi_3 + i\phi_4 \end{pmatrix}, \tag{1.20}$$

with Lagrangian

$$\mathcal{L} = (\partial_\mu \phi)^\dagger (\partial^\mu \phi) - \left[-\mu^2 (\phi^\dagger \phi) + \lambda (\phi^\dagger \phi)^2 \right]. \tag{1.21}$$

This time, the Lagrangian is required to be invariant under local gauge transformations of the group $SU(2)_L \otimes U(1)_Y$, which introduces four gauge vector fields W^a_μ, $a = 1, 2, 3$, and B_μ, for the $SU(2)$ and $U(1)$ symmetry groups respectively. These gauge fields are introduced by replacing the derivative of the Lagrangian by the following covariant derivative

$$\mathcal{D}_\mu \equiv \partial_\mu + \frac{i}{2} g \sigma^a W^a_\mu + \frac{i}{2} g' Y B_\mu; \tag{1.22}$$

where g and g' are coupling strength constants, σ^a are the Pauli matrices, and Y is a hyper-charge associated to the $U(1)$ group.

In order to interpret the Lagrangian, the potential ground state considered is

$$\phi_1 = \phi_2 = \phi_4 = 0, \quad \phi_3 = v, \tag{1.23}$$

and the scalar doublet field is parametrized around this ground state with four real fields θ_a (with $a = 1, 2, 3$) and h,

$$\phi = \frac{1}{\sqrt{2}} \begin{pmatrix} 0 \\ v + h \end{pmatrix} e^{i\sigma^a \theta_a / v}. \tag{1.24}$$

After developing the Lagrangian, the three fields θ_a disappear, and h is the only one that remains. The particle associated with h is the predicted Standard Model Higgs boson. Its mass is given by the relationship

$$m_{\mathrm{H}} = \sqrt{2v^2 \lambda}. \tag{1.25}$$

λ and μ are free parameters, and so the Higgs boson mass is also free in the theory.

The physical vector boson fields are linear combinations of the fields W^a_μ and B_μ. The charged weak boson fields are combinations of $W^{1,2}$,

$$W^{\pm} = \frac{1}{\sqrt{2}} \left(W^1 \mp i W^2 \right). \tag{1.26}$$

The mass for these bosons is found to be

$$m_W = \frac{1}{2} g v. \tag{1.27}$$

Similarly, the photon and the neutral weak boson fields are combinations of W^3

and B,

$$A = \frac{g'W^3 + gB}{\sqrt{g^2 + g'^2}}, \quad \text{and} \quad Z = \frac{gW^3 - g'B}{\sqrt{g^2 + g'^2}}, \tag{1.28}$$

and their masses are found to be

$$m_A = 0, \quad \text{and} \quad m_Z = \frac{1}{2}v\sqrt{g^2 + g'^2}. \tag{1.29}$$

In addition, a relation between the $W^{\pm}$ and the Z^0 masses can be also derived

$$\frac{m_W}{m_Z} = \cos\theta_W \quad \text{with} \quad \tan\theta_W = \frac{g'}{g}. \tag{1.30}$$

θ_W is called Weinberg angle or weak mixing angle.

The masses of the fermions would violate the gauge symmetry, but they are also allowed thanks to the scalar doublet. The coupling between the fermions and the Higgs boson are related to the fermion masses.

1.2 Constraints on the Higgs boson mass

1.2.1 Theoretical constraints

There are some theoretical constraints on the mass of the Standard Model Higgs boson m_{H}, correlated with the energy scale Λ beyond which the SM is not anymore valid and from which new phenomena should emerge. Namely, the requirements bringing these constraints are: unitarity of the amplitude for electroweak scattering processes, renormalization and triviality of the electroweak theory, and vacuum stability.

- The unitarity requirement constraints the Higgs boson mass to be below ~ 700 GeV; otherwise unitarity is violated, unless there is physics beyond the SM at energies in the TeV range that restores it. This is because the participation of the Higgs boson in some vector boson scattering processes regularizes their cross-sections at high energies, avoiding unitarity violation, but the Higgs boson coupling with the vector bosons depends on its mass.

- The renormalization and triviality of the electroweak theory sets an upper limit to the Higgs boson mass that vary with the energy scale Λ, as shown in Figure 1.2 by the red band. From the theory renormalization, the Higgs boson quartic self-coupling depends on the energy scale of the interaction; at high energy, the quartic self-coupling of the Higgs boson grows and eventually becomes infinite. The energy scale point where the coupling becomes infinite, called Landau pole, depends on the Higgs boson mass. Then, from another point of view, for a given energy domain of validity of the Standard Model there is a limit for the Higgs boson mass.

- From the theory renormalization a lower limit for m_{H} also results, that also depends on the Λ; it is known as the vacuum stability bound and is shown by

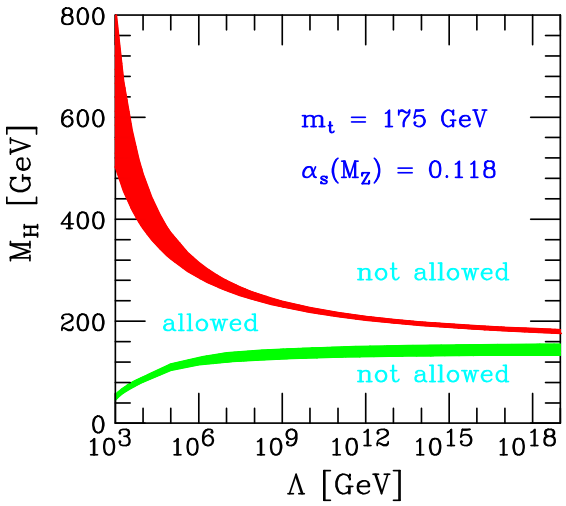

Figure 1.2: Theoretical constraints over the Higgs boson mass as a function of the energy scale limit Λ for the validity of the Standard Model [24]. The upper (red) band corresponds to the triviality bound and its uncertainties, and the lower (green) band corresponds to the vacuum stability bound and its uncertainties.

the green band in Figure 1.2.

More details about these theoretical constraints can be found in [24].

1.2.2 Experimental exclusion before the LHC

The experiments at the Large Electron-Positron collider (LEP) have excluded the existence of a Standard Model Higgs boson with mass below 114.4 GeV, with 95% of confidence level. This exclusion has been obtained from data collected in e^+e^- collisions at different center-of-mass energies between 91 and 209 GeV. In these collisions the SM Higgs boson was expected to be produced through the so-called Higgs-strahlung process $e^+e^- \rightarrow Z^* \rightarrow HZ$, where the Higgs boson is radiated by a Z vector boson. The plot on the left side of Figure 1.3 shows the final results on the Higgs boson search at LEP [7]. In this plot, the exclusion limits are expressed as limits on the Higgs boson to Z vector boson coupling.

On top of the LEP results, the Tevatron experiments also set exclusion limits on the SM Higgs boson mass; the right side plot of Figure 1.3 shows the results published by Tevatron in the summer of 2011 [8]. From these results, the SM Higgs boson was excluded in the mass range 156 - 177 GeV, and also in a small range at low mass till ~108 GeV, confirming the LEP results. These limits were set based on data collected on proton-antiproton collisions at a center-of-mass energy of $\sqrt{s} = 1.96$ TeV.

1.2.3 Indirect experimental constraints

In addition to the direct mass range exclusions, information about the possible value of the Higgs boson mass have been obtained through a global fit to electroweak precision measurements, and testing the coherence of the Standard Model. This is done exploiting predicted dependency of electroweak processes on the Higgs boson mass.

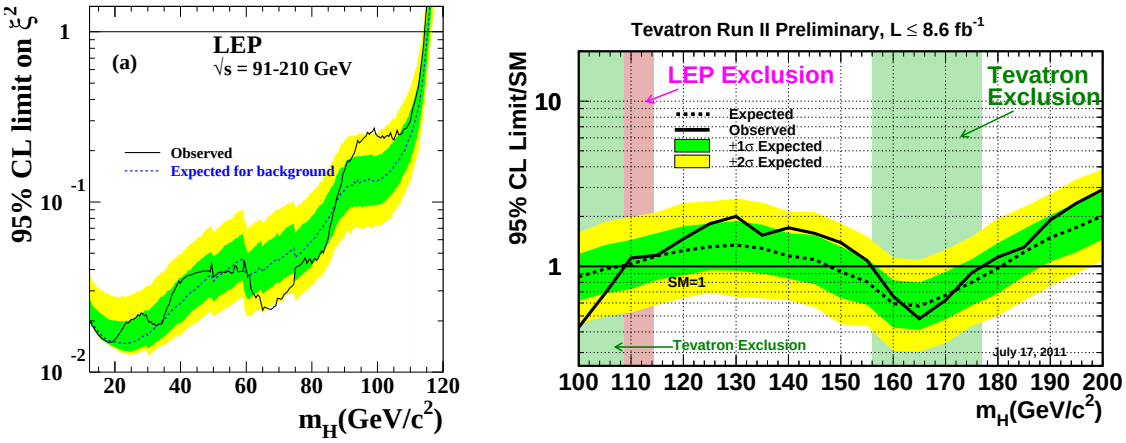

Figure 1.3: 95% confidence level upper limits on a SM-like Higgs boson produciton cross-section, normalized to the SM predicted cross-section, as a function of the boson mass hypothesis m_{H}, obtained by the LEP experiments [7] on the left side and Tevatron experiments [8] for the summer of 2011 on right side.

This fit has been performed by several groups: among others the LEP Electroweak Working Group [25] and the Gfitter group [26]; Figure 1.4 shows as an example the result obtained by Gfitter for the summer of 2011.

The plot shows the resulting $\Delta\chi^2$ test statistic values as a function of the Higgs boson mass hypothesis m_{H}. Independently of the Higgs boson direct search, if the Standard Model is the right theory, this result indicated that the Higgs boson mass is below $\sim$ 130 GeV with 68% of confidence level, and below $\sim$ 170 GeV with 95% of confidence level. Further details can be found in [27].

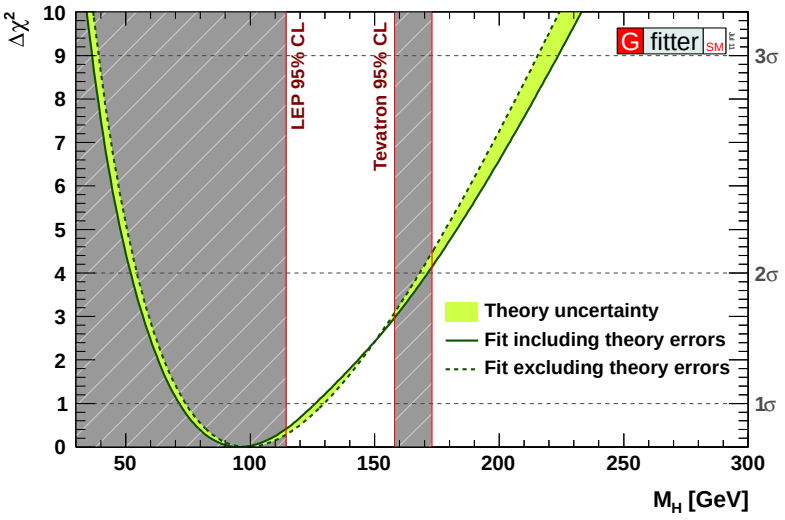

Figure 1.4: $\Delta\chi^2$ as a function of the Higgs boson mass hypothesis M_{H} for the electroweak fit performed by Gfitter for the summer of 2011 [26]. The solid line gives the results obtained when theoretical errors are included, and the dashed line when they are ignored. The grey regions correspond to the exclusions set by LEP and Tevatron with 95% of confidence level.

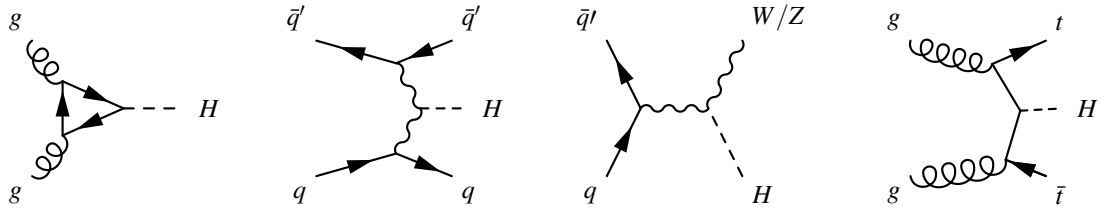

(a) $gg \to H$ (b) VBF (c) VH (d) $t\bar{t}H$

Figure 1.5: Feynman diagrams for the different Higgs boson production processes at the LHC proton-proton collisions: a) gluon fusion, b) vector boson fusion (VBF), c) associated production with a vector boson (VH), d) associated production with a top quark pair [29, 30].

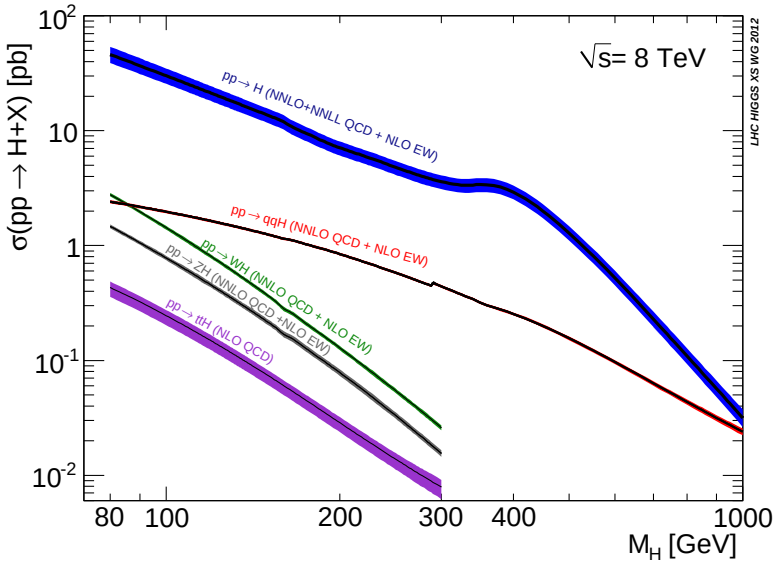

Figure 1.6: Standard Model Higgs boson production cross-section as a function of the Higgs boson mass hypothesis, for the LHC proton-proton collisions at a center-of-mass energy $\sqrt{s} = 8$ TeV [28].

1.3 The Higgs boson search at the LHC

1.3.1 Higgs boson production at the LHC

In the proton-proton collisions at the LHC, the Higgs boson is expected to be produced through four different main processes: gluon fusion, vector boson fusion (VBF), associated production with a vector boson and associated production with a top-antitop quark pair. Figure 1.5 shows Feynman diagram examples for these four processes, and Figure 1.6 shows the Standard Model expected cross-sections for each process as a function of the Higgs boson mass hypothesis, for proton-proton collisions at a center-of-mass energy of $\sqrt{s} = 8$ TeV [28–30].

The gluon fusion (Figure 1.5-a) is the main Higgs boson production mode at the LHC. The gluon fusion is produced through a loop of quarks, mainly top quarks. Its cross-section is computed up to next-to-next-to-leading order (NNLO) in QCD [31–36], improved with QCD soft-gluon re-summation calculations up to next-to-next-to-leading logarithmic order (NNLL) [37, 38] and next-to-leading order (NLO) EW

corrections [39, 40]. The computed values are compiled in [41–43]. The theoretical uncertainty on the gluon fusion cross-section is about 10%.

The vector boson fusion VBF (Figure 1.5-b) is the second-leading mode in the Higgs boson production at the LHC, contributing to about 10% of the production for a Higgs boson mass of 150 GeV. In this process the Higgs boson is produced by the interaction of two vector bosons radiated by incoming quarks. The VBF has an experimental signature that consists in the presence of two jets (the experimental signature of quarks) in the forward regions of the detector, close to the proton beam axis (details about the experiment geometry are discussed in Chapter 2). This signature allows reducing backgrounds in the Higgs boson search and disentangling VBF events from other production modes. The cross-section for the vector boson fusion is calculated at NLO in QCD, with electroweak (EW) corrections [44–46] and approximate NNLO QCD corrections [47]. The uncertainty on this cross-section is about 3%.

In the associated production with a vector boson (Figure 1.5-c), the Higgs boson is radiated by a vector boson, the so-called Higgs-strahlung mechanism. The presence of the vector boson in the final state represents an important distinguishing signature for this process. (This process was the main Higgs boson production mode at LEP, and the second leading one at Tevatron, where its signature was exploited by the search channels with the highest sensitivity.) The cross-sections for this process is calculated at NLO [48] and at NNLO [49], and NLO EW radiative corrections [50] are applied. The uncertainty on this cross-section is about 4%.

The associated production with top quarks (Figure 1.5-d) has a low cross-section, two orders of magnitude below the one for the gluon fusion; nevertheless its signature can be exploited in the event selections, for instance for a low mass Higgs boson, when it decays to a b-quark pair (see next section). For the $t\bar{t}H$ associated production, the cross-section calculations are done at NLO in QCD [51–54].

1.3.2 Higgs boson search channels

The Higgs boson decay branching ratios are shown on the left side of Figure 1.7, and the cross-section times branching ratio for the Higgs boson search channels at the LHC are presented on the right side; both sets of values are shown as a function of the Higgs boson mass hypothesis (M_{H}).

At the very low mass, the Higgs boson decays mainly to a $b\bar{b}$ pair; nevertheless, at the LHC, due to the high cross-sections for the QCD processes with the same signature, the background for an inclusive $b\bar{b}$ channel is too high to allow a sensitive search. Additionally, the experimental $b\bar{b}$ invariant mass resolution is low, which makes the observation of a signal even more difficult in this decay channel. This Higgs boson decay is only considered when the signature of the VH and $t\bar{t}H$ associated production processes are exploited. For similar reasons the $H \to gg$, $H \to \tau\tau$ and $H \to c\bar{c}$, decays does not provide good sensitivity for a Higgs boson observation. However, the $H \to \tau\tau$ decay is considered exploiting the VBF production mode signature.

In this low mass range (below $m_{\mathrm{H}} \sim 125$ GeV), the rare $H \to \gamma\gamma$ decay is the one providing the highest sensitivity. The $\gamma\gamma$ invariant mass resolution is good, and therefore this channel provides a clear signal and allows precise measurements of a

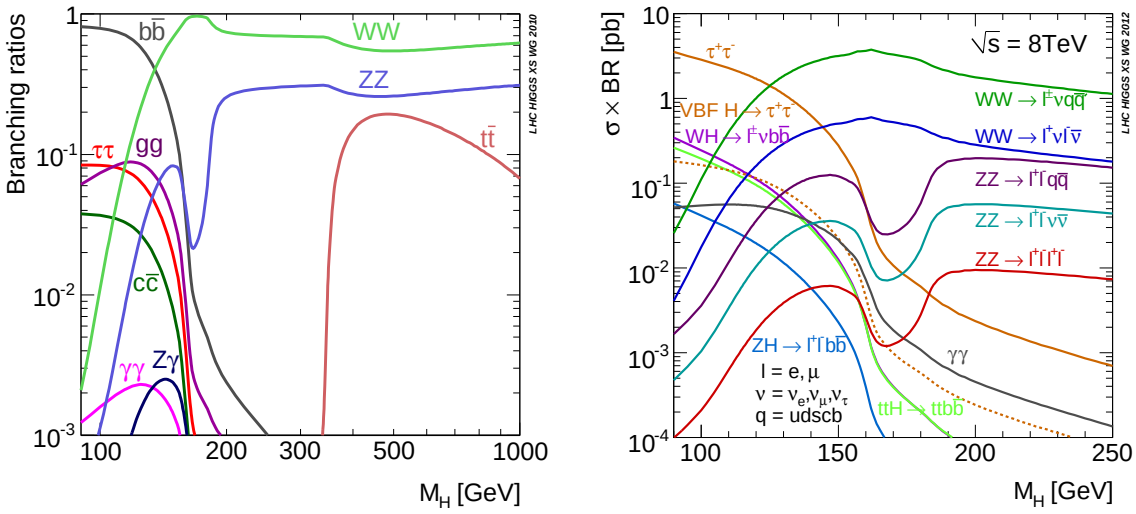

Figure 1.7: Left: Standard Model Higgs boson decay branching ratios as a function of the Higgs boson mass hypothesis. Right: Cross-section times branching ratios for the SM Higgs boson at $\sqrt{s} = 8$ TeV as a function of the mass hypothesis, for the decay channels used for the Higgs search at the LHC [28–30].

signal mass.

Above $m_{\mathrm{H}} \sim 125$ GeV, the $H \to WW^{(*)} \to l\nu l\nu$ channel becomes the one with highest sensitivity, until $m_{\mathrm{H}} \sim 200$ GeV. Due to the presence of neutrinos in the final state (which are invisible for the detectors), the full invariant mass can not be reconstructed, but only the transverse invariant mass, which corresponds to the particles' kinematics in the plane perpendicular to the beam axis. But, the high cross-section and the experimental signature for this channel give a favorable signal-to-background ratio.

For $m_{\mathrm{H}} \gtrsim 200$ GeV, the $H \to ZZ$ channels are dominant in sensitivity.

The $H \to ZZ^{(*)} \to 4l$ with $l = e, \mu$ is a particularly good channel. It has good invariant mass resolution, it provides high sensitivity to a Higgs boson signal in basically all the mass range (120 - 600 GeV), and the background rate for this channel is quite low; for this reason it is sometimes referred to as the *golden channel*.

Around twice the top quark mass, $m_{\mathrm{H}} \sim 350$ GeV, the branching ratio for the $H \to t\bar{t}$ decay increases rapidly. Nevertheless, the high QCD background prevents the Higgs boson search in this channel.

Details on the Higgs boson production at the LHC and the decay processes can be found in [29, 30].

1.3.3 The $H \to \gamma\gamma$ channel

As mentioned above, the $H \to \gamma\gamma$ channel is the most sensitive to observe the Higgs boson at the very low mass, below 125 GeV. At the LHC, the search in this channel is performed from 110 GeV, around the exclusion limit set by LEP and Tevatron, up to 150 GeV.

The Higgs boson decays to two photons through loops of W bosons and fermions, mainly top quarks, as shown in Figure 1.8. The branching ratio for this decay in the mentioned mass range is about 0.2%. The calculation of this branching ratio include NLO corrections in QCD and EW [55, 56], and it has an uncertainty of 5%. The

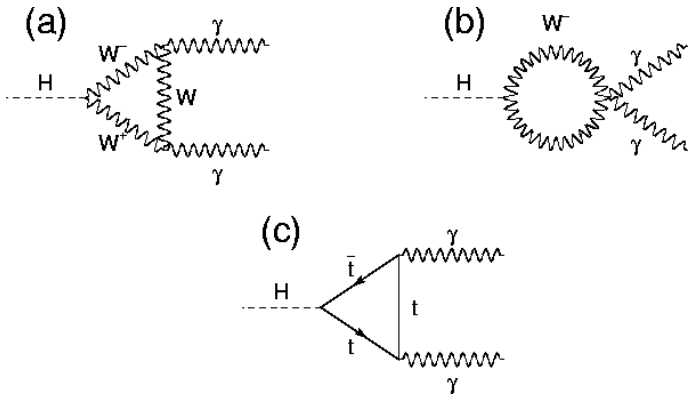

Figure 1.8: Feynman diagrams for the Standard Model Higgs boson decay to two photons in the lowest order.

Table 1.1: Cross-section and diphoton branching ratio for a Higgs boson with mass $m_{\mathrm{H}} = 125$ GeV [29, 30]. The total cross-section and the one for the two mayor production modes are quoted for center-of-mass energies of 7 and 8 TeV.

m_{H}	$\sqrt{s}$	σ_{tot} $(pp \to H)$	σ_{ggF} $(gg \to H)$	σ_{VBF} $(q\bar{q}' \to H + q\bar{q}')$	$\mathcal{BR}$ $(H \to \gamma\gamma)$	$\sigma \times \mathcal{BR}$ $(pp \to H \to \gamma\gamma)$
125 GeV	7 TeV	17.5 pb	15.3 pb	1.2 pb	$2.3 \cdot 10^{-3}$	40.3 fb
	8 TeV	22.3 pb	19.5 pb	1.6 pb		51.3 fb

cross-section times branching ratio for this channel is around 50 fb at $\sqrt{s} = 8$ TeV. Precise values of the cross-section and the $H \to \gamma\gamma$ branching ratio for a Higgs boson of mass $m_{\mathrm{H}} = 125$ GeV are quoted in Table 1.1, for center-of-mass energies of 7 and 8 TeV.

This channel is affected by a large amount of background. The main background source is the QCD diphoton production, called *irreducible background*. Figure 1.9 shows Feynman diagrams for the three main processes contributing to the photon pair production at the LHC: a) the Born process $q\bar{q} \to \gamma\gamma$, b) the bremsstrahlung process $qg \to q\gamma\gamma$, and c) the box process $gg \to \gamma\gamma$. The total cross-section for the diphoton production [57] is about three orders of magnitude higher than the one for the signal process $pp \to H \to \gamma\gamma$.

The second most important source of background is the associated production of a photon with one quark or gluon, experimentally one jet. The experimental signal of a quark or a gluon in the detector can eventually be wrongly taken as a photon signal (details are discussed in Chapter 3). Feynman diagrams for the main photon-jet production processes are shown in Figure 1.10. At the LHC, the total cross-section for these processes [10, 58] is about six orders of magnitude above the $pp \to H \to \gamma\gamma$ cross-section. Therefore, a good photon-jet discriminating power is necessary in the experiments, for keeping this background low.

Additional sources of background are the QCD production of multi-jets and the Drell-Yan processes; the Drell-Yan processes are those that yield two electrons in the final state. They contribute to the background when both objects, both jets or both electrons, are mis-identified as photons. Thanks to the photon identification capabilities of ATLAS, the background corresponding to these processes represents only a few percent of the diphoton candidate samples.

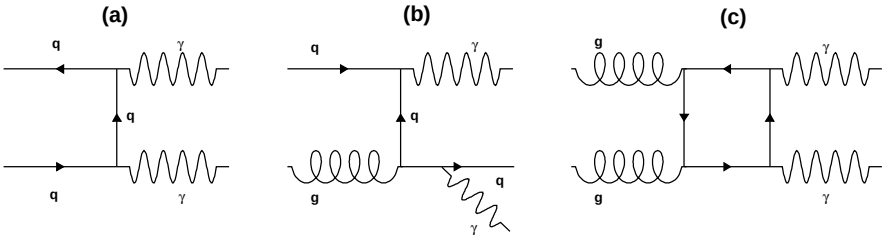

Figure 1.9: Feynman diagrams for the three main processes contributing to the photon pair production at the LHC: a) the Born process $q\bar{q} \to \gamma\gamma$, b) the bremsstrahlung process $qg \to q\gamma\gamma$, and c) the box process $gg \to \gamma\gamma$.

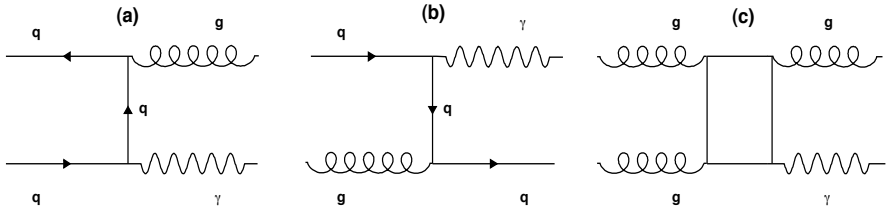

Figure 1.10: Feynman diagrams for the three main processes contributing to the production of a photon associated with quark of gluon at the LHC.

Chapter 2

The ATLAS experiment at the LHC

ATLAS is one of the detectors installed at the Large Hadron Collider (LHC) at the European Laboratory for Particle Physics (CERN) [59]. The LHC is currently the most powerful instrument for particle physics research. It collides particles at unexplored high energies, at very high rate, allowing the study of a large variety of interesting physics processes. ATLAS has been designed to probe as much as possible this new physics domain.

This chapter starts with a brief presentation of the LHC and continues with a summarized description of the ATLAS detector and its components. Some emphasis is given to one ATLAS component, the electromagnetic calorimeter, since it is a key component for the reconstruction of photons. A complete description of the LHC can be found in [60], and the ATLAS detector is described on details in [61, 62].

2.1 The Large Hadron Collider

2.1.1 Introduction

Among the large particle colliders used for particle physics research, there are hadron-hadron, lepton-lepton and combined hadron-lepton colliders. Hadron-hadron colliders are in general the most appropriate to explore new energy domains; lepton-lepton colliders are more convenient than the others to perform precision measurements; whereas hadron-lepton colliders are particularly useful to study the internal structure of the hadrons.

Hadron-hadron colliders allow exploring simultaneously a wide range of energies in the particles' search. Though they operate with a fixed beam energy, they actually provide interactions in a wide energy range. The reason is that in hadron collisions at high energies the interactions actually occur between the hadron constituents, quarks and gluons, rather than between the hadrons as a whole. The interacting quarks and gluons carry a fraction of the hadron energy, that vary between zero and one.

To reach the high unexplored energies, using hadrons is a better option than using leptons/electrons. Since hadrons are heavier than electrons, they lose less energy than electrons through synchrotron radiation in circular accelerators.

The Large Hadron Collider (LHC) is a proton-proton circular accelerator and collider constructed at CERN, at the Franco-Swiss frontier, near Geneva. It has a circumference of 27 km and is installed underground, about 100 m below the surface. It is placed in a tunnel that was previously occupied by the LEP collider. The LHC has been designed to perform collisions at an unprecedented energy and luminosity[1], specifically a proton-proton center-of-mass energy of $\sqrt{s} = 14$ TeV and a luminosity of $L = 10^{34}$ cm^{-2}s^{-1} (the collisions at the previous most powerful hadron collider, the Tevatron, were performed at $\sqrt{s} = 1.96$ TeV and $L = 4 \times 10^{32}$ cm^{-2}s^{-1} [63]). The LHC can also collide heavy ions, specifically lead nuclei, with an energy of 2.8 TeV per nucleon and a luminosity of 10^{27} cm^{-2}s^{-1}.

2.1.2 Objectives

The LHC allows to perform a large variety of particle physics studies. Here, they are synthesized in three general objectives:

- The main objective is the search of new particles, starting with the Standard Model Higgs boson (on which this thesis is reporting about), the particles predicted by supersymmetric theories and others predicted by more exotic models. The beam energy at the LHC will allow exploring up to a few TeV's in the mass scale.

- Studying with high precision the Standard Model (SM) physics processes. The LHC is a large source of b-quarks, top quarks, vector bosons, among other particles and physics processes. It will allow for instance to improve the measurements of the top quark and the W boson masses, and of their production cross-sections. The large amount of B hadrons produced allows studying CP violation and determining with higher precision the CKM matrix parameters. Deviations of these precision measurements from the Standard Model predictions would be indirect evidences of new physics.

- Studying the strong interaction in a quark-gluon plasma. The heavy ion collisions at the LHC produce a state of matter with extremely high energy density and temperature. At this state, quarks and gluons are expected to be no longer confined inside hadrons. This state is the so called quark-gluon plasma.

2.1.3 General layout

A set of linear and circular accelerators are used to accelerate protons and heavy ions before their injection into the LHC. Most of these accelerators already existed at CERN before the design of the LHC, and they were upgraded to satisfy the LHC necessities. Figure 2.1 shows a schematic view of the CERN accelerator complex. For protons, the acceleration chain is as follows: protons reach 50 MeV of energy in a linear accelerator (LINAC), then 1.4 GeV in the Synchrotron Booster, 25 GeV in the Proton Synchrotron (PS) and 450 GeV in the Super Proton Synchrotron

[1] In particle physics, *luminosity*, or *instantaneous luminosity*, is an important quantity to characterize the performance of particle colliders because the particle interaction rate depends on this quantity (more details about luminosity are discussed in Section 2.1.5).

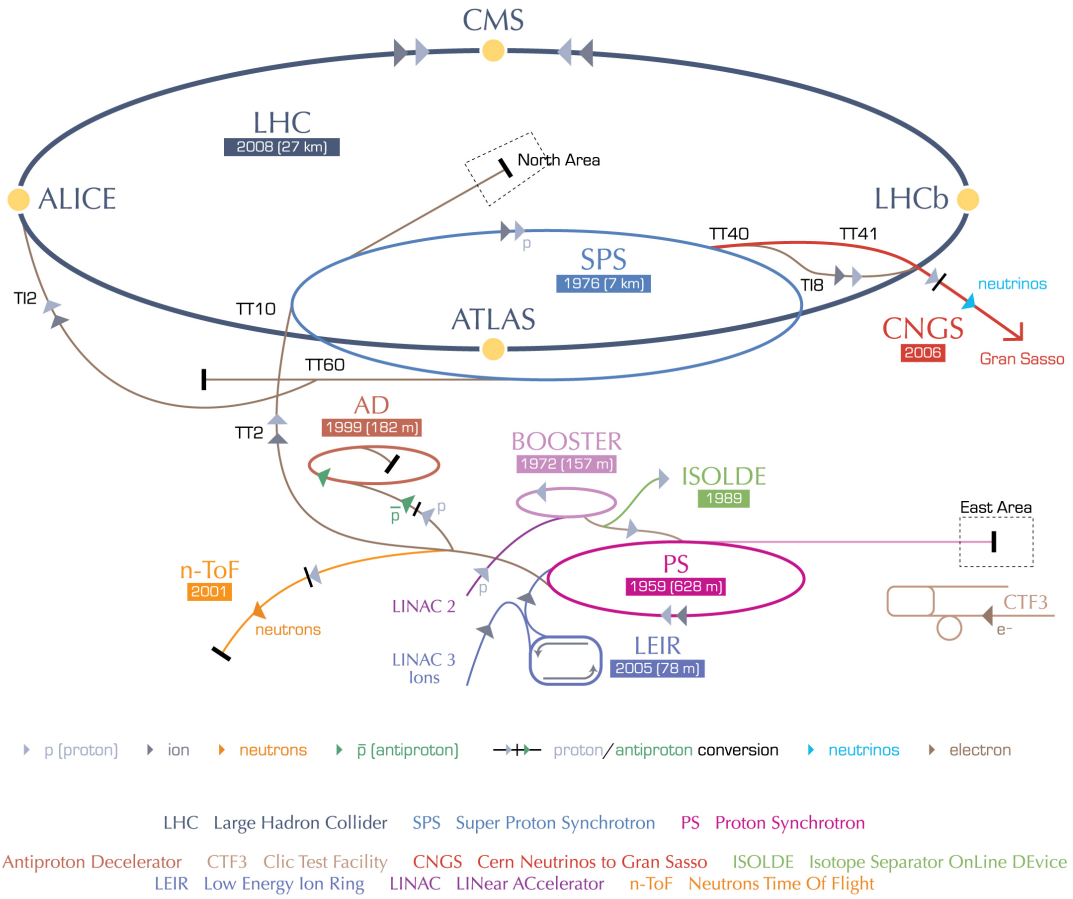

Figure 2.1: The CERN accelerator complex [64]. The LHC is the last ring (dark grey line) in a chain of particle accelerators. The smaller machines are used in a chain to help boost the particles to their final energies. The yellow spots correspond to the main detectors installed at the LHC. For some of the machines, the construction finishing year and the length are indicated.

(SPS). Then, they are injected into the LHC in both directions, clockwise and anti-clockwise. Once there, protons are accelerated up to the nominal energy and they collide at four different points. At these interaction points, detectors have been constructed to probe the showers of particles produced in such collisions.

There are six detectors installed at the LHC: ATLAS, CMS, ALICE, LHCb, TOTEM and LHCf. ATLAS and CMS are designed to cover the widest possible range of physics in the proton-proton and heavy ion collisions, while LHCb and ALICE are designed to study specific phenomena.

- LHCb [65] is dedicated to probe the decay of B hadrons for precision measurements of CP violation and rare decays.

- ALICE [66] is dedicated to the heavy ion collisions to study the strong interaction.

The detectors used by the TOTEM and LHCf experiments are positioned near the CMS and ATLAS detectors, respectively. They are designed to focus on particles which are scattered very forward, i.e. in directions very close to the beams.

- TOTEM [67] measures the total cross-section of proton-proton collisions. This information will complement the physics analysis done at the other experiments at the LHC.

- LHCf [68] is dedicated to the measurement of neutral particles emitted in the very forward region. Its measurements will help to interpret and calibrate cosmic-ray experiments.

2.1.4 The LHC main ring

In a circular particle accelerator, particles circulate in a vacuum pipe and they are driven using electromagnetic devices. Some of them are: dipole magnets utilized to keep the particles in their nearly circular orbits; quadrupole magnets to focus the beam; and electromagnetic resonator cavities to accelerate the particles and then keep them at a constant energy, by compensating for energy losses.

At the LHC, the beam pipe is kept at ultrahigh vacuum, specifically at 10^{-13} atm. This is necessary to avoid collisions with gas molecules.

Among the electromagnetic devices, at the LHC, the ones with most challenging requirement are the dipole magnets. They need to provide a magnetic field of 8.33 T to keep protons at 7 TeV in the LHC circular orbit. This is achieved using niobium-titanium (NbTi) superconducting coils, which are cooled down to a temperature below 2 K using superfluid helium; working at this temperature is necessary to reach the required magnetic field. Other accelerators, Tevatron, HERA and RHIC, use the same superconductor alloy, but cooled by supercritical helium to temperatures slightly above 4.2 K. Those machines operate with magnetic fields, below and around 5 T, lower than the one required by the LHC.

The LHC is a proton-proton collider unlike the previous hadron colliders Tevatron and SPS, where collisions were done between protons and anti-protrons. Using antiprotons would have limited the luminosity at the LHC, for they are more complicated to produce at high rates and to store for large periods of time than protons.

The proton-proton collisions imply of course two counter-rotating proton beams, and therefore the necessity of two rings with opposite magnetic fields. But the reduced space in the early created LEP/LHC tunnel didn't allow having two separated rings. Therefore, in order to fit the two rings inside the tunnel, the LHC use a magnet design called "twin bore".

The twin bore magnet consists of two sets of coils and beam channels within the same mechanical structure and cryostat. Figure 2.2 shows a cross-section of the LHC dipole magnet. In addition to satisfying the space constraint, this design has also the advantage of reducing the cost.

The LHC is not a perfect circle, it has eight arcs and eight straight sections. The straight sections are approximately 528 m long and house the interaction points and the accelerator utilities; Figure 2.3 shows how these elements are distributed at the eight straight sections. There are four points where the beams cross from one magnet bore to the other providing the particles' interactions. The ATLAS and CMS detectors are located at interaction points that provide high luminosity; they are at the straight sections 1 and 5, respectively. The ALICE and LHCb detectors are located at medium luminosity interaction points in the sections 2 and 8. These two straight sections also house the injection systems for the beams. The remaining four

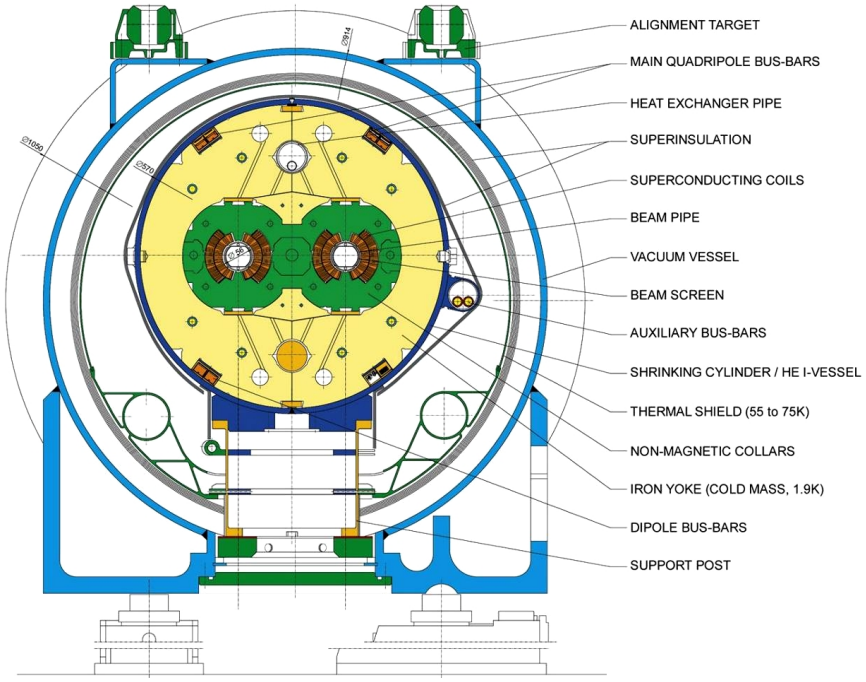

Figure 2.2: Cross-section of LHC superconducting dipole magnet [60].

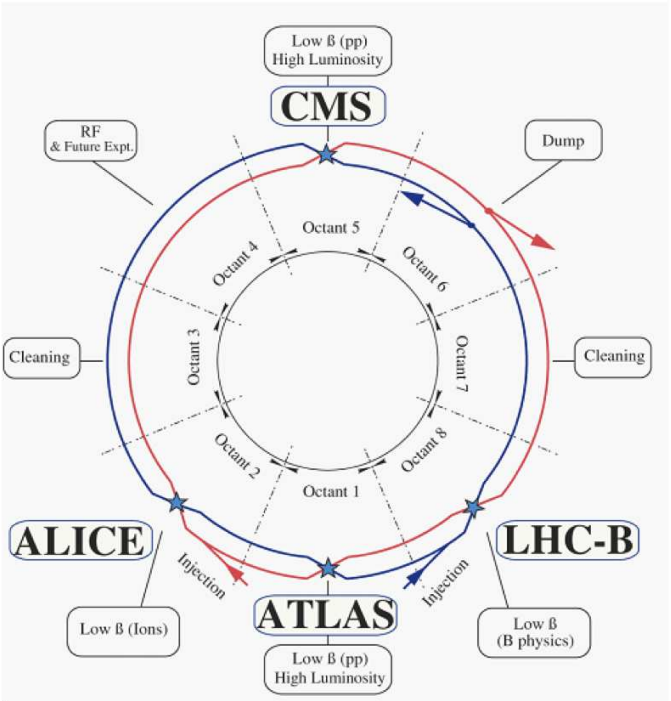

Figure 2.3: Schematic view of the LHC layout [60].

straight sections do not have beam crossings; the sections 3 and 7 contain collimation systems, the section 4 contains the accelerating cavities, and the section 6 house the beam dumping system.

2.1.5 Performance

The goal of the LHC is producing as many events as possible corresponding to the physics processes of interest, with the highest possible signal-to-background ratio; of course, these criteria drive the observation sensitivity in the search of new particles, and the precision of the measurements. The rate of events for a given physics process R_p is equal to the machine luminosity L times the process cross-section σ_p.

$$R_p = L\sigma_p \tag{2.1}$$

Integrating this expression over a given time period of collision yields the following expression for the number of events N_p that occur:

$$N_p = \sigma_p \int L dt \tag{2.2}$$

The cross-sections for the processes of interest at the LHC increase with the center-of-mass energy in the collisions, as shown in Figure 2.4. This figure shows for instance the cross-section evolution with $\sqrt{s}$ for a Standard Model Higgs boson hypothesis with mass 150 GeV. This cross-section increases by a factor of one hundred from the Tevatron operating energy of $\sqrt{s} = 2$ TeV to the LHC design energy of $\sqrt{s} = 14$ TeV; for the currently operating energy of the LHC, $\sqrt{s} = 8$ TeV, the increment factor is about thirty.

The machine luminosity depends on the particle beam characteristics. At the LHC, protons circulate assembled in bunches with around 10^{11} protons per bunch. The machine is nominally designed to accommodate one bunch every 25 ns in the beam, and a total of 2808 bunches per beam. The beams will circulate at almost the speed of light, which makes a beam revolution frequency of about 10 kHz for the LHC circumference. For a beam with particles distributed in a Gaussian way in each direction, the luminosity can be written as follow:

$$L = \frac{N_{\mathrm{b}}^2 n_{\mathrm{b}} f_{\mathrm{rev}} \gamma_{\mathrm{r}}}{4\pi \epsilon_{\mathrm{n}} \beta^*} F \tag{2.3}$$

where N_{b} is the number of particles per bunch, n_{b} the number of bunches per beam, f_{rev} the revolution frequency, γ_{r} the relativistic gamma factor, ϵ_{n} the normalized transverse beam emittance, β^* the beta function at the collision point, and F a geometric luminosity reduction factor due to the crossing angle at the interaction point. The emittance is a measure of the spread of the particles' position and momentum, and the beta function is a measure of the beam focalization at the interaction point.

Nominal design values for some of these beam parameters are quoted in the last column of Table 2.1. For these values, the corresponding instantaneous luminosity is about 10^{34} cm^{-2}s^{-1}.

The luminosity at the LHC is not constant during collisions, but it decays due

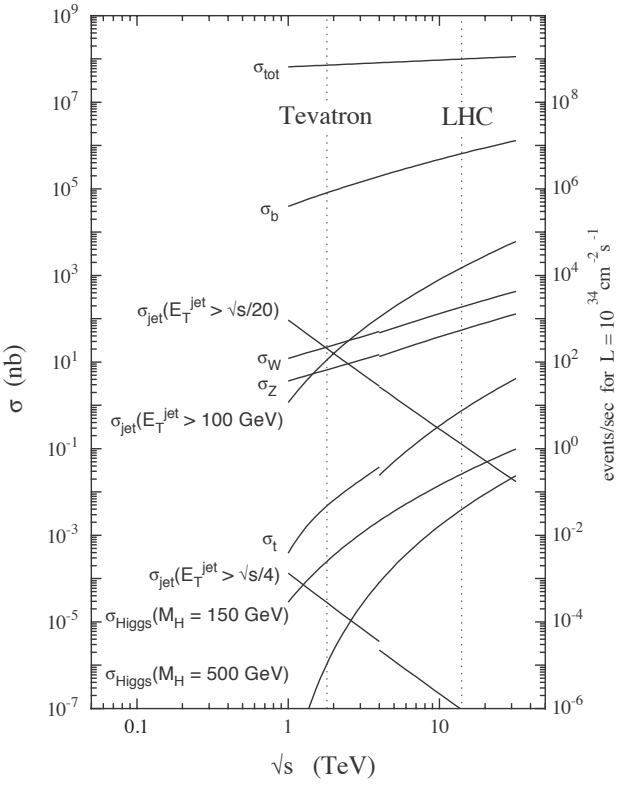

Figure 2.4: Cross-section and rates (for a luminosity of 10^{34} cm^{-2}s^{-1}) for various physics processes in proton-(anti)proton collisions, as a function of the centre-of-mass energy $\sqrt{s}$ [69].

to the degradation of the intensity and the emittance of the beams. There are several factors contributing to this beam quality degradation, but the main cause is simply the reduction of the number of protons per bunch because of the collisions. Considering all the affecting factors, the luminosity lifetime is estimated to be about 15 hours (this is the time required to reach $1/e$ of the initial luminosity).

In the machine operating cycle, there is an amount of time required to pre-accelerate the protons up to 450 GeV and fill the LHC, to further accelerate them to the collision energy, and after a collision period and the beams are dumped to ramp down the magnets to the 450 GeV working configuration. This turnaround time is theoretically at least 70 minutes, but in practice it is estimated to be on average 7 hours.

Then, given the luminosity lifetime and the average turnaround time, the optimal amount of time for the collision period in each operating cycle is 12 hours. Finally, assuming that the machine can operate for 200 days per year, the total integrated luminosity per year is expected to be around 80 fb^{-1}.

2.1.6 Operational history

The LHC started to collide protons at the end of 2009. These firsts collisions were performed at a center-of-mass energy of $\sqrt{s} = 900$ GeV, and later at $\sqrt{s} = 2.36$ TeV, above the Tevatron operating energy.

After a winter shutdown, the LHC restarted operating in march 2010, this time

Table 2.1: Parameters of the LHC proton-proton collisions for the data-taking periods: 2010, 2011 and 2012 [70,71], and the design values [60]. The quoted parameters are: the center-of-mass energy $\sqrt{s}$, the number of protons per bunch N_{b}, the number of bunches per beam n_{b}, the bunch-to-bunch time spacing Δt, the normalized transverse beam emittance ϵ_{n}, the instantaneous peak luminosity L and integrated luminosity per year. Each value quoted corresponds to the one of best performance achieved during the year.

Parameter	2010	2011	2012	Nominal
$\sqrt{s}$ [TeV]	7	7	8	14
N_{b}				1.15×10^{11}
n_{b}	368	1380	1380	2808
Δt [ns]	150	50	50	25
ϵ_{n} [μm rad]				3.75
β^* [m]	3.5	1.0	0.60	0.55
L [cm^{-2}s^{-1}]	2.07×10^{32}	3.65×10^{33}	7.73×10^{33}	10^{34}
Int. lumi. per year [fb^{-1}]	0.0481	5.61	21.7	80

with collision at 7 TeV, during about eight months. It started with a low luminosity of about 10^{27} cm^{-2}s^{-1} that was gradually increased, achieving 2.07×10^{32} cm^{-2}s^{-1} at the end of the year. After this period of proton-proton collision, the LHC performed heavy ion collisions for a few weeks.

During 2011, the LHC continued colliding protons at 7 TeV and increasing the luminosity up to 3.65×10^{33} cm^{-2}s^{-1}, with a few weeks of heavy ion collisions at the end of the year. During that year the LHC provided a total integrated luminosity of about 6 fb^{-1} to each of the high luminosity experiments, ATLAS and CMS.

In 2012, the proton-proton center-of-mass energy has been increased to 8 TeV, and ATLAS has recorded a total of 21.7 fb^{-1} of data.

There were a few weeks of proton-heavy ion collisions at beginning of 2013, and now there is a long shutdown of about two years. During this period the machine is being prepared to achieve the design goal energy of $\sqrt{s} = 14$ TeV, and the detectors will be upgraded.

Figure 2.5 shows how the instantaneous peak luminosity has increased as a function of the time during the last three year. In Table 2.1, the beam parameters for each operating year are compared with each other and with the design values. Each value quoted in this table corresponds to the one of best performance achieved during the year. Additionally, Figure 2.6 shows the cumulative integrated luminosity delivered to ATLAS per day, for each year.

2.2 The ATLAS experiment

2.2.1 Detector overview

ATLAS as well as CMS is a general-purpose detector. It has been designed to probe both the proton-proton and heavy ion collisions at the LHC, and to study the different physics processes that could occur in these collisions.

These detectors measure a shower of relatively stable particles traveling in all directions, particles able to travel at least some meters before decaying. This shower of particles is the product of the different physics processes that occur, and it carries information about these processes. It is composed of electrons, muons, neutrinos,

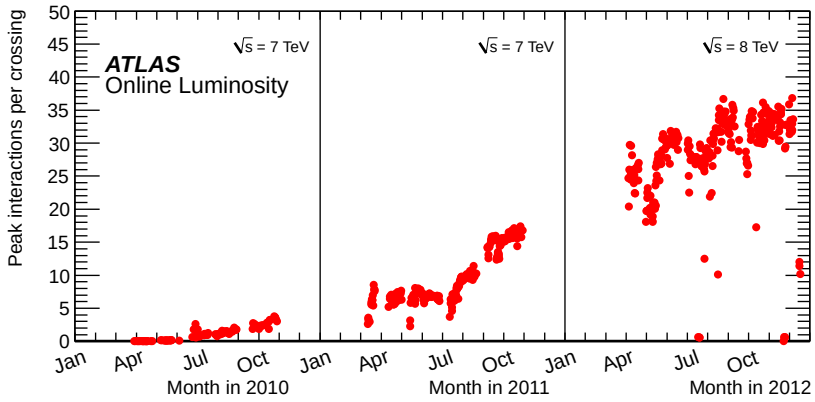

Figure 2.5: Peak instantaneous luminosity delivered by the LHC to ATLAS per day versus time, during the proton-proton runs of 2010, 2011 and 2012 [71].

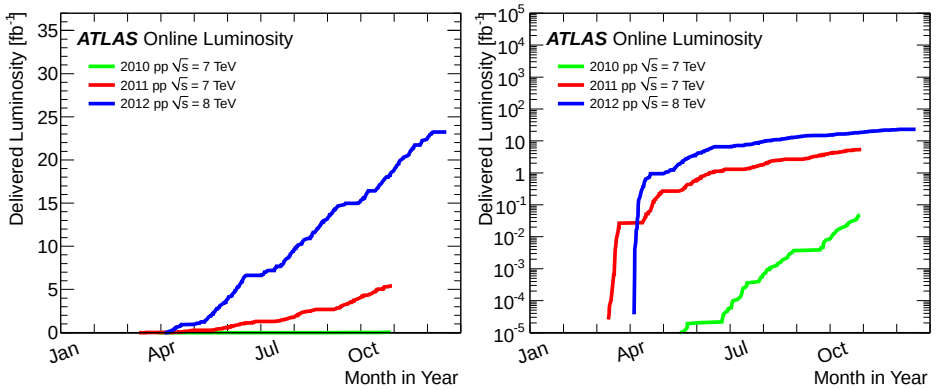

Figure 2.6: Cumulative integrated luminosity delivered to ATLAS versus time, during stable beams and for proton-proton collisions, in linear (left side) and logarithmic scale (right side) [71]. This is shown for the 2010 (green), 2011 (red) and 2012 (blue) runs.

photons, neutral and charged hadrons, and perhaps still unknown particles. They are either direct product of the hard processes (called *prompt* particles), or they are the product of secondary processes. The prompt particles usually travel isolated from other particles, and there are also groups of particles assembled together in objects called *jets*. The jets are the product of quark or gluon hadronization and subsequent decays of unstable hadronic particles, or the hadronic decay of tau-leptons; the jet direction and energy are associated with the direction and energy of its originating particle. The task of the detector is to measure the direction of flight and the momentum (or kinetic energy) of these different particles and jets, and to allow identifying them.

Like most of the detectors in this kind of experiments, ATLAS has a cylindrical shape, as shown in Figure 2.7. It has been designed and arranged in such a way that the proton beams pass through the cylindrical axis, and the collisions take place at its center. ATLAS is 44 m long and has a diameter of 25 m; it weights 7000 tons. It is the largest in volume among the LHC detectors.

In order to accomplish its objectives, ATLAS as most of this type of detectors is composed of four concentric, also cylindrical, layers or sub-detectors. From the inside to the outside, there are: an inner tracker or inner detector, an electromagnetic

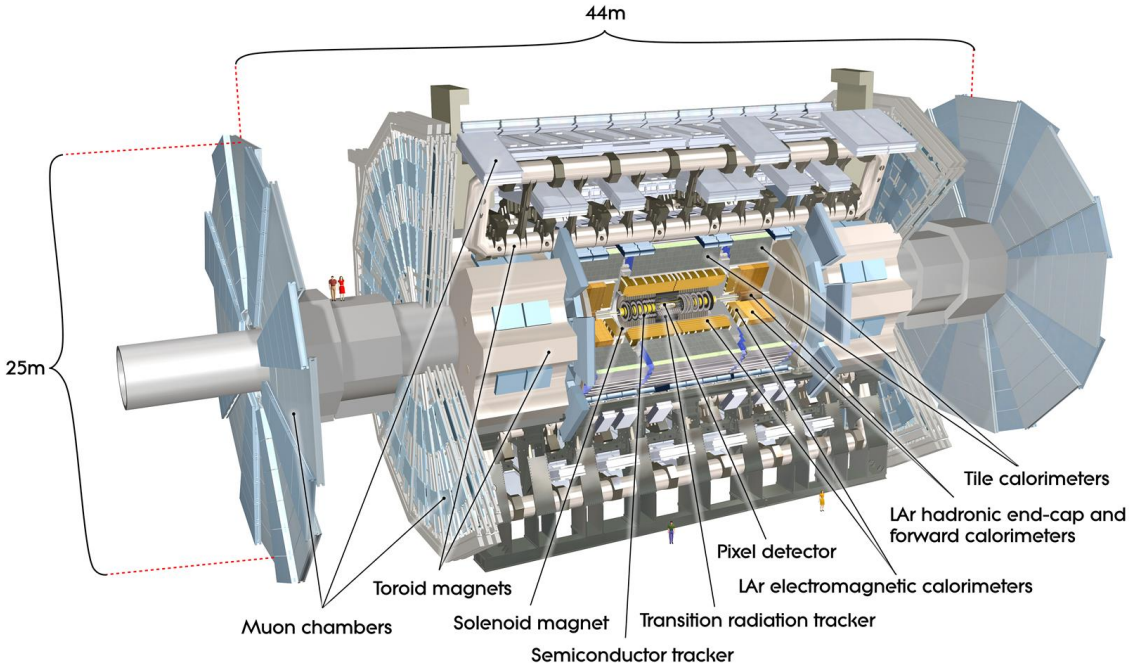

Figure 2.7: Schematic view of the ATLAS detector with its different constituent parts [62].

calorimeter, a hadronic calorimeter, and an outer tracker or muon spectrometer. These different sub-detectors are highlighted in the ATLAS sketch shown in Figure 2.7, and Figure 2.8 shows how the different particles interact with them.

The inner tracker allows reconstructing the trajectory of charged particles while they are bent by a magnetic field. The curvature of the particles in the magnetic field allows deducing their charge sign and computing their momentum. By extrapolating the measured trajectories, the vertexes formed by the particles can be reconstructed. The neutral particles are invisible to the tracker.

The calorimeters allow measuring the energy of the particles by stoping them, absorbing all their energy. Photons and electrons deposit their energy in the electromagnetic calorimeter by generating an electromagnetic shower of secondary particles, while hadrons pass throughout the electromagnetic calorimeter without loosing much energy, and deposit most of their energy in the hadronic calorimeter. Only muons and neutrinos traverse the hadronic calorimeter without being stopped.

Muons leave their track through all the different sub-detectors, but without loosing much energy. They are the only particles sensed by the outer tracker, and that is why this last sub-detector is called muon spectrometer. Muons are also bent by a magnetic field while they traverse the muon detector, which allows performing an additional measurement of their momentum, after the inner tracker measurement. The magnetic field in the barrel of the muon detector is generated by an enormous toroidal-shape magnet; the ATLAS name is in fact due to this enormous toroid that surround the detector, **A** **T**oroidal **L**HC **A**pparatu**S**.

Neutrinos very rarely interact with matter and so they are not sensed by the detector. Nevertheless, their presence in an event can be inferred through the mea-

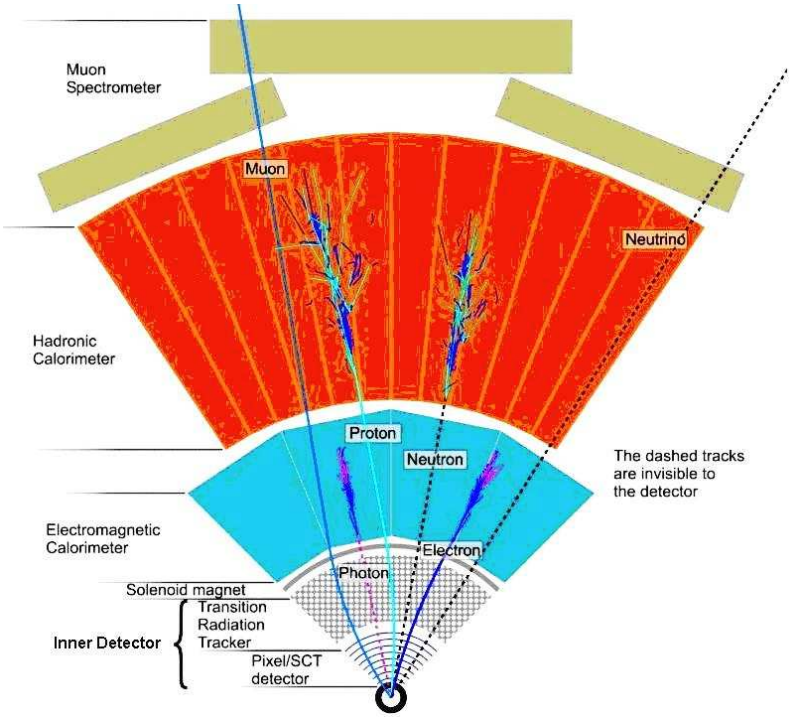

Figure 2.8: Sketch representative of different kind of particles passing through the ATLAS sub-detectors [72].

surement of the vectorial total momentum in the plane transverse to the beam. For momentum conservation, this total momentum component is expected to be approximately zero, otherwise it indicates the presence of one or more neutrinos not detected, or the presence of others weakly interacting particles not known yet.

As explained above, jets are a bunch of particles arriving all together in a given region of the detector. In general, jets contain mainly hadrons. In the detector, a jet is characterized by a wide cluster of energy deposited in both calorimeters (wide cluster in comparison with what a single particle does), and a bunch of tracks in the inner detector depending on its content of charged particles.

Combining all the information provided by the different sub-detectors allows an identification of the different particles, and a reconstruction of the events.

There is an additional important component of this type of detectors not mentioned yet, it is the trigger. Each event that is detected represents a large amount of information to record, and the collision rate in these experiments is extremely high. Usually, with the computational technologies available at the time of each experiment, there is neither the disk-space to store all the information, nor the way to record it with the speed it would demand. Additionally, the fraction of events interesting to study is usually very small among all the collisions. So, the task of the trigger is to perform an extremely quick preselection of the events, at the same time that the collisions occur, before recording them.

2.2.2 The ATLAS collaboration

The ATLAS detector has been constructed and is now operated by an international collaboration, with the participation of over three thousands physicists, engineers,

technicians and students, from 174 institutes and 38 countries.

2.2.3 Detector requirements

The detectors in this kind of experiments typically have to fulfill stringent constraints:

- Fast detection technologies; components able to measure particles quickly and without significant dead-time. As mentioned above, the LHC in nominal operation mode will provide proton bunch-crossings for ATLAS every 25 ns.
- Detectors and electronics resistant to high radiation doses; in particular the inner tracker sensors and the components in the forward region, which receive the highest radiation.
- Detectors with high granularity able to distinguish several particles traveling very close to each other.

In addition, since the LHC provides unprecedented high energy collisions and high luminosity, these requirements becomes more stringent for the LHC detectors than for previous experiments. For instance, at the high luminosity provided by the LHC, not one but several interactions occur per proton bunch crossing, the so-called event *pileup*. On average, 23 interactions per bunch crossing are expected in nominal conditions at the LHC (at the Tevatron experiments, there were on average about 6 pileup interactions). This entails a large number of particles arriving to the detector at the same time, and therefore the necessity of high granularity components. The number of particles is even larger in the heavy ion collisions.

For the design of ATLAS, the performance requirements have been evaluated considering the physics processes that could occur at the LHC collisions, at the TeV scale. The considered processes include Standard Model (SM) physics, Higgs boson processes and physics beyond the SM at high energies, in particular the different production and decay modes of the Higgs boson. They provide a varied set of experimental signatures to detect, including all the different particles mentioned in Section 2.2.1. Possible new particles at high mass, masses of a few TeV, would decay to very energetic leptons, photons, etc.

Another point that has been considered is that the hadron collisions are highly dominated by the QCD production of jets. Therefore, ATLAS needs to provide very good separation between prompt particles and jets, especially photons and electrons which are more easily faked by jets. It is necessary to allow to disentangle the rare events of interest from this large QCD background.

Then, the requirements for the ATLAS detector can be summarized in the following items:

- High precision reconstruction of tracks and vertices. The reconstruction of secondary vertices is crucial for the identification of jets originated by b-quark (b-jets). The B-hadrons have relatively long lifetime, and so they are usually able to fly slightly away of the primary vertex before decaying. Also a precise reconstruction of the collision primary vertices permits to disentangle an interesting event from simultaneous pileup events.

- The particles' transverse energy needs to be measured with good precision over a large range, from some GeVs up to a few TeVs.
- The calorimeters have to provide information to discriminate electrons and photons from jets.
- The particles in the events are distributed in all directions, so the sub-detectors have to cover as much as possible the solid angle around the interaction point; in particular the calorimeters, which have to provide almost full coverage until the forward region close to the beam direction. This large coverage is very important to allow the good calculation of the missing transverse energy.
- The muon spectrometer is required to measure the muon p_{T} with good precision up to a few TeV's.
- A trigger able to keep a high efficiency for the events of interest while providing high background rejection.

2.2.4 Coordinate system and nomenclature

The left side sketch of Figure 2.9 shows the coordinate system used to describe the detector, and the motion of the particles resulting from the collisions. The origin of the system is set at the nominal interaction point, at the center of the detector. The z-axis is set in the direction of the beams, the positive x-axis is defined as pointing to the center of the LHC ring, and the positive y-axis is defined as pointing upwards. The azimuthal angle ϕ is measured around the beam axis, and the polar angle θ is measured with respect to the beam axis.

The variables labeled "transverse" are defined in the plane transverse to the beam direction, the x-y plane, unless it be stated otherwise; for example, the transverse momentum p_{T} or the transverse energy E_{T}. In the same way, the variables labeled "longitudinal" are referred to the z-axis direction.

There are some others variables frequently employed; they are:

- The rapidity y; for a particle with energy E and longitudinal momentum p_z, it is defined as

$$y = \frac{1}{2} \ln \left(\frac{E + p_{\mathrm{z}}}{E - p_{\mathrm{z}}} \right). \tag{2.4}$$

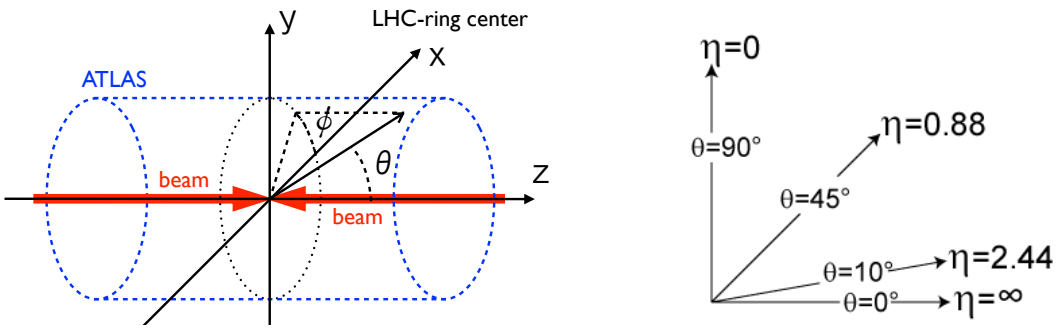

Figure 2.9: Left: Coordinate system used in ATLAS. Right: Correspondence between the pseudorapidity η and the polar angle θ for some specifics values.

The rapidity of a particle is a quantity that transforms in an additive way under boosts in the z direction, and thus the rapidity difference Δy between two particles is a Lorentz invariant. It means that at hadron colliders where the collision products are boosted along the beam axis, the Δy difference between two particles at the lab frame is the same as in the collision center of mass frame, which is convenient.

- The pseudorapidity η; it is defined as

$$\eta = -\ln\left[\tan\left(\frac{\theta}{2}\right)\right]. \tag{2.5}$$

It is an approximation of the rapidity of a particle when the particle's mass is negligible with respect to its momentum. In hadron colliders, the rapidity y or the pseudorapidity η are used as polar coordinates, and they are used more commonly than the angle θ. This is also convenient because the distribution of the particles emerging from the collisions as a function of y or η tends to be flat. The right side of Figure 2.9 shows the η values for some specifics values of the angle θ.

The relation between the momentum p and the transverse momentum p_{T} of a particle can be written as a function of the particle's pseudorapidity η as follows:

$$p = p_{\mathrm{T}} \cosh\eta \tag{2.6}$$

- The distance ΔR in the pseudorapidity-azimuthal-angle space (η-ϕ); it is defined as

$$\Delta R = \sqrt{\Delta\eta^2 + \Delta\phi^2}. \tag{2.7}$$

- The transverse d_0 and the longitudinal z_0 impact parameters; they are defined for a particle track as the transverse and the longitudinal distances to the nominal collision point at the point of closest approach.

2.3 Magnet system

The magnet system of ATLAS consists of a central solenoid and three toroidal magnets, the large barrel toroid and two end-cap toroids, as shown in Figure 2.10.

2.3.1 Central solenoid

The solenoid provides a 2 T magnetic field for the inner detector, which is located inside it. The magnetic field is parallel to the beam axis; therefore the charged particles are bent in the x-y plane, changing their ϕ direction of flight. The solenoid is 5.8 m long and has a diameter of about 2.5 m.

An important constrain for the design of the solenoid was to keep a low amount of material in front of the electromagnetic calorimeter. Hence, the solenoid consists of a single-layer coil of an Al-stabilized niobium-titanium (NbTi) superconductor, that allows producing the high magnetic field while keeping the solenoid thin. Additionally, it shares the cryogenic and vacuum system with the barrel of

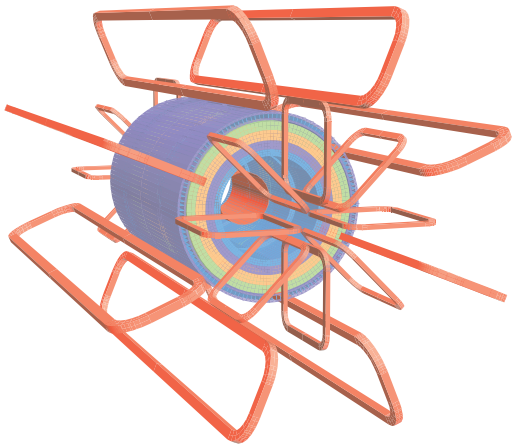

Figure 2.10: Toroidal magnets and the central solenoid in red, and the barrel of the hadronic calorimeter in various colors (blue, green and orange).

the electromagnetic calorimeter, in order to avoid having additional walls between the two components and therefore minimizing the amount of material. In this way, the solenoid constitutes only about 0.66 radiation lengths X_0 for particles at normal incidence.

2.3.2 Barrel and end-cap toroids

The barrel and end-cap toroids produce magnetic fields of about 0.5 T and 1 T, respectively, for the muon detector. These toroidal magnets consist each one of eight superconducting coils arranged to form cylinders, as shown in Figure 2.10. The large barrel toroid is 25.3 m long and has internal and external diameters of 9.4 m and 20.1 m respectively. While the end-cap toroids are 5 m long and have internal and external diameters of 1.65 m and 10.7 m. Ideally, the magnetic field lines make big circles around the beam axis, and so the muons are bent changing their η direction.

2.4 Inner detector

The inner detector (ID) is used to reconstruct the trajectory of charged particles; for this, it has a set of layers where the charged particles are sensed as they pass throughout them. The ID is shown Figure 2.11; (a) shows the whole tracking system, while (b) and (c) show detailed sketches of the barrel and end-cap sections. The whole system is 6.2 m long and it has a 2.1 m diameter. Beginning from the innermost part, there are layers of silicon pixels sensors, layers of silicon micro-strip sensors (SCT), and a transition radiation tracker (TRT).

As the magnetic field at the ID bents particles in the x-y plane, the precision of the transverse momentum estimation relies on the precision of the ϕ coordinate measurements at the various layers.

(a)

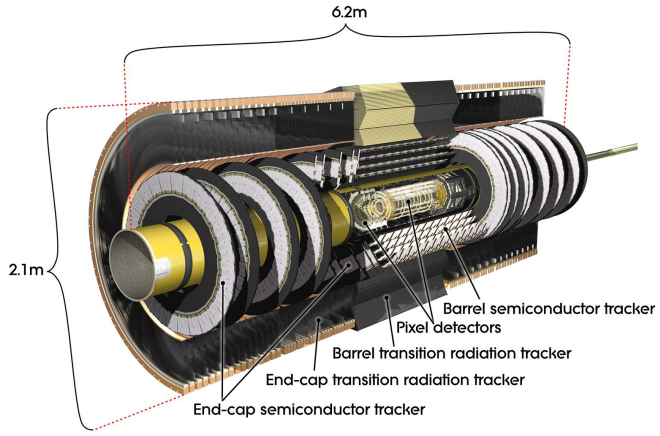

(b)

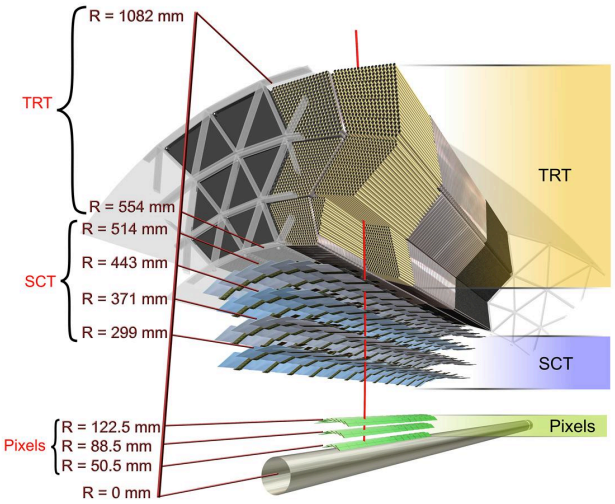

(c)

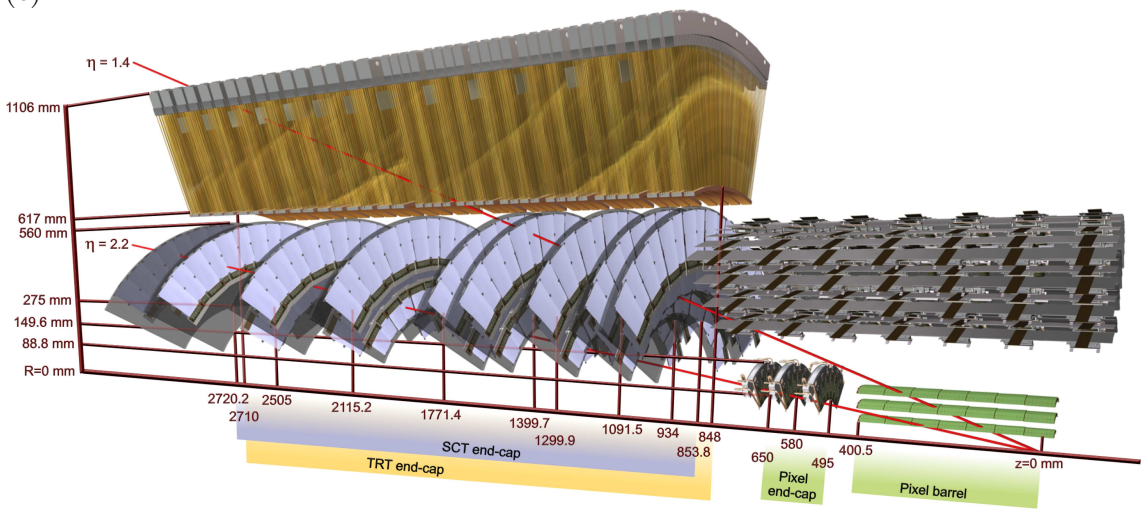

Figure 2.11: (a): Schematic view of the Inner Detector. (b): Structure of the inner detector in the barrel region. (c): Structure of the inner detector in the end-cap regions. [62]

2.4.1 Precision silicon sensors

At the inner detector barrel, the silicon sensors (pixels and micro-strips SCT) are arranged on concentric cylinders around the beam axis (see Figure 2.11-b), while in the end-caps, they are located on disks perpendicular to the beam axis (see Figure 2.11-c). Each particle crosses nominally three pixel layers and four micro-strip double layers. These silicon sensors cover the region $|\eta| < 2.5$.

These sensors consist of crystals of a silicon semiconductor material submitted to a potential difference. When particles pass through the semiconductor they create electron-hole pairs. Then, the electrons are collected by electrodes generating a current that is measured.

In a pixel sensor, the electrodes are arranged in a two-dimensional matrix, and thus these sensors provide two-dimensional information at the sensor plane. They give an intrinsic measurement accuracy of 10 μm in the azimuthal ϕ direction, and 115 μm in the longitudinal z direction at the barrel and transverse-radial R direction at the end-caps. The pixel layers have a total of about 80.4 million readout channels.

The micro-strip sensors themselves only provide information in one direction at the sensor plane (the electrodes are "strips"). Therefore, the sensor modules are arranged in pairs forming double sensor layers, with a small rotation of 40 mrad between them. In this way, they create a grid and provide the required two-dimensional information. The micro-strip double layers provide an intrinsic accuracy of 17 μm in ϕ, and 580 μm in z and R, and they have a total of about 6.3 million readout channels.

For a good performance in the high radiation environment at the LHC, these silicon sensors need to operate at temperatures between -10°C and -5°C. With this purpose, the sensor supporting structure has a refrigeration system with a coolant circulating at -25°C.

The first pixel layer is just at 5 cm from the beam axis. It is called B-layer. It allows determining whether a particle is originated at the collision point (primary vertex) or a few millimeters away as a decay product of another particle (at a secondary vertex).

An additional sensor layer is planned to be inserted in the future; it will be closer to the beam axis than the current B-layer. It will improve the vertices reconstruction precision, and therefore the capability to disentangle multiple vertices very close to each other, in high pileup conditions.

2.4.2 Transition radiation tracker

The transition radiation tracker (TRT) provides a large number of $R - \phi$ measurements per track, typically 36, which complement the silicon sensor measurements for the transverse momentum estimation. It doesn't provide information in the η direction. The inner radius of the TRT is about 60 cm, and the outer radius is about 1 m. It covers the region $|\eta| < 2.0$.

The TRT consists of several tens of thousands, 4 mm diameter, straw tubes. They are parallels to the beam axis in the barrel region and they are arranged radially in wheels in the end-caps (see Figure 2.11). These straws are filled with a gas that is ionized whenever charged particles pass through. Each straw has in the center a wire, and a potential difference is applied between the wire and the straw's

inner wall. Thus, the ions are drawn to the straw's wall, while the electrons are drawn to the central wire generating a current.

Additionally, the straws are made of materials with different refraction indices. Then, when the charged particles pass through, they radiate photons that also ionize the gas, which makes the signal stronger. Since electrons radiate more photons than charged hadrons like pions (because electrons are lighter than hadrons), the TRT has also electron identification capabilities.

Each straw tube provide an intrinsic accuracy of 130 μm. The whole TRT has a total of 351 000 readout channels.

By design, the tracking system is expected to provide a transverse momentum resolution $\sigma_{p_{\mathrm{T}}}/p_{\mathrm{T}} = 0.05\%\, p_{\mathrm{T}} \oplus 1\%$ (with p_{T} in GeV).

2.5 Calorimeters

The energy of the particles is measured with the calorimeters, by stopping them with dense materials and measuring the energy that they deposite. The incident particles interact with these materials generating secondary particles with lower energy, that further interact with the material and generate more of them, thus creating a shower. Photons and electrons interact electromagnetically with the electrons and nuclei in the matter, while hadrons have mainly strong interactions with the nuclei.

Consequently, the typical amounts of matter necessary for the development of an electromagnetic and a hadronic shower are different. For electromagnetic interactions at high energy, the characteristic amount of matter is the *radiation length* X_0, while for hadronic interactions the equivalent quantity is the *nuclear interaction length* λ_I; X_0 is typically one order of magnitude smaller than λ_I. Therefore, one can take advantage of those interaction differences to measure separately the energy of electrons or photons, and hadrons, in different calorimeter sections.

The ATLAS calorimeters are presented in Figure 2.12. A set of different electromagnetic and hadronic calorimeters cover all the region $|\eta| < 4.9$. This η coverage gives a large acceptance for jets and allows a good measurement of the missing transverse energy. The electromagnetic calorimeter has a fine granularity in both η and ϕ directions in the region $|\eta| < 2.5$, which is also the η region covered by the inner detector; it allows a good reconstruction of photons and electrons in this region.

2.5.1 The electromagnetic calorimeter

The electromagnetic (EM) calorimeter is of primary importance for the search of the Higgs boson in the diphoton decay channel. Photons are reconstructed in this sub-detector, where their energy and direction of flight is measured. In the mass range where $H \to \gamma\gamma$ is a key decay channel for the Higgs boson search, the intrinsic width of the Higgs boson mass peak is negligible; therefore, the width of the experimental signal peak in the diphoton invariant mass spectrum relies completely on the resolution of the reconstructed photon kinematic variables.

Before describing the ATLAS EM calorimeter, its geometry and performance, the characteristics of electromagnetic showers are briefly presented.

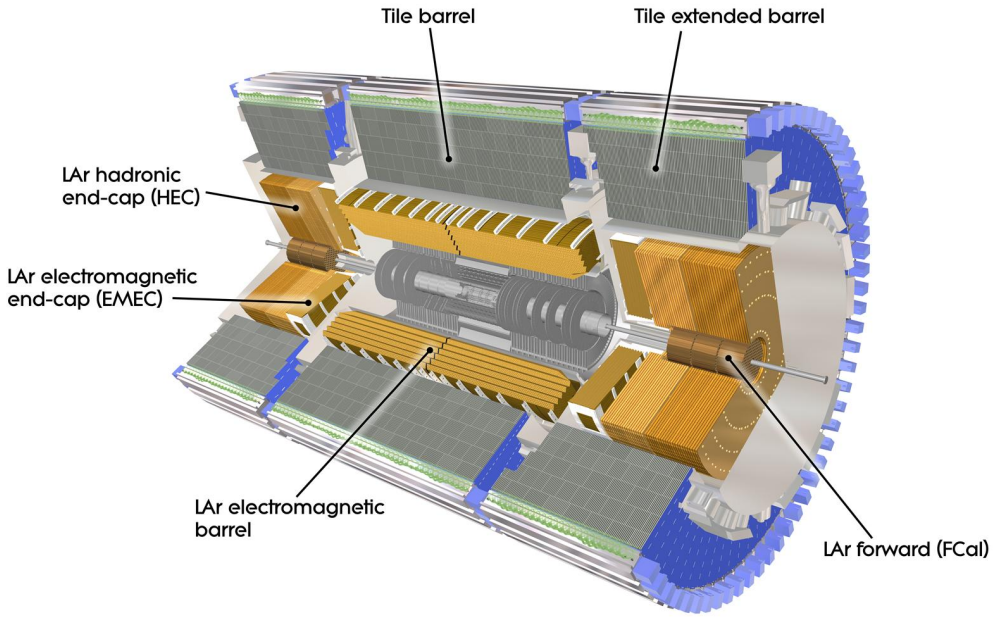

Figure 2.12: Schematic view of the ATLAS calorimeters [62].

Electromagnetic showers

Electrons and photons interact with matter through different processes depending on their energy. Figure 2.13 shows on the left side the fractional energy loss by electrons per radiation length X_0, in lead, as a function of the electron or positron energy, for the different interaction processes. On the right side, it shows also the cross-section for different photon interaction processes as a function of the photon energy, in lead.

At high energy, above a few tens of MeV, the electron and photon interactions with matter are dominated by two related processes, the electron bremsstrahlung radiation of photons and the production of electron-positron pairs by photons (on the right side plot of Figure 2.13, the labels κ_{nuc} and κ_e correspond to the cross-sections for pair production by photon interactions with nuclei and electrons respectively).

The radiation length X_0 is both: the mean distance over which a high-energy electron loses $1/e$ of its energy by bremsstrahlung radiation, and 7/9 of the mean free path for pair production by a high-energy photon [73,74]. It is usually measured in g cm^{-2}, and it changes from one material to another. The typical values for the ratio radiation length over density X_0/ρ are of a few centimeters or fractions of a centimeter; for lead which is used in the ATLAS calorimeter, this ratio is about 0.6 cm [73].

At low energy, electrons interact predominantly by ionizing atoms, ejecting electrons out of them; the energy at which the electron fractional loss of energy by bremsstrahlung and ionization are equivalent is known as *critical energy* E_{c}, and it is another important quantity in the characterization of EM showers. It is also a material dependent parameter; for lead, the critical energy is about 7 MeV.

The main photon interaction at the MeV energy scale is the Compton inelastic

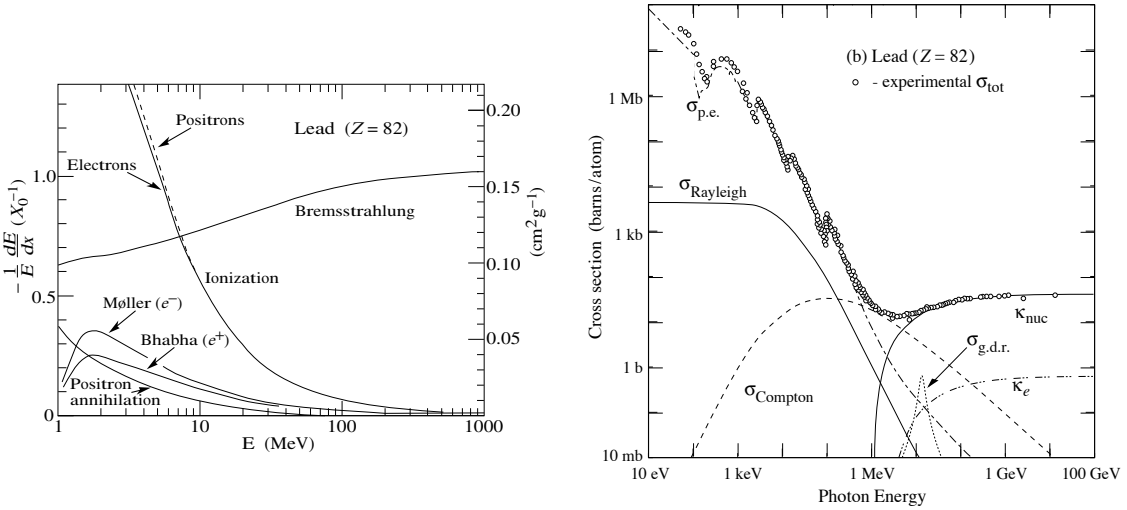

Figure 2.13: Left: Fractional energy loss by electrons per radiation length, in lead, as a function of the electron or positron energy, for the different interaction processes. Right: Cross-section for different photon interaction processes as a function of the photon energy, in lead [73] (the labels $\kappa_{\rm nuc}$ and κ_e correspond to the cross-sections for pair production by photon interactions with nuclei and electrons respectively).

scattering, and at lower energy than these ones, the main process is the photoelectric effect (p.e.), accompanied by the Rayleigh elastic scattering.

For high energy electrons and photons, the longitudinal development of the electromagnetic shower is driven by the high-energy part of the cascade, it scales as the radiation length in the material, and it drives the thickness of the electromagnetic calorimeters. The mean longitudinal profile of energy deposition is reasonably well described by a gamma distribution, with the maximum differential deposition of energy typically occurring at a $x_{\rm max}$ depth:

$$x_{\rm max} = X_0 \left[\ln \left(\frac{E}{E_{\rm c}} \right) + C_j \right], \qquad j = e, \gamma; \tag{2.8}$$

where E is the energy of the incident particles, and $C_e = -0.5$ for electron-induced cascades and $C_\gamma = +0.5$ for photon-induced cascades. For electrons and photons with energies between 10 and 100 GeV, in lead, $x_{\rm max}$ is between 7 and 10 radiation lengths.

The transverse development of electromagnetic showers in different materials scales with the *Molière radius* $R_{\rm M}$, given by [73, 75, 76]

$$R_{\rm M} = X_0 \frac{E_{\rm s}}{E_{\rm c}}, \tag{2.9}$$

where $E_{\rm s} \approx 21 MeV$. On the average, only 10% of the energy lies outside a cylinder with radius $R_{\rm M}$, and about 99% is contained inside of $3.5 R_{\rm M}$ [73]. In lead, the Molière radius is about 3 radiation lengths.

A lead-liquid argon accordion calorimeter

The ATLAS EM calorimeter uses lead layers with liquid argon (LAr) in-between, as shown in Figure 2.14. The interactions of an incident particles through the

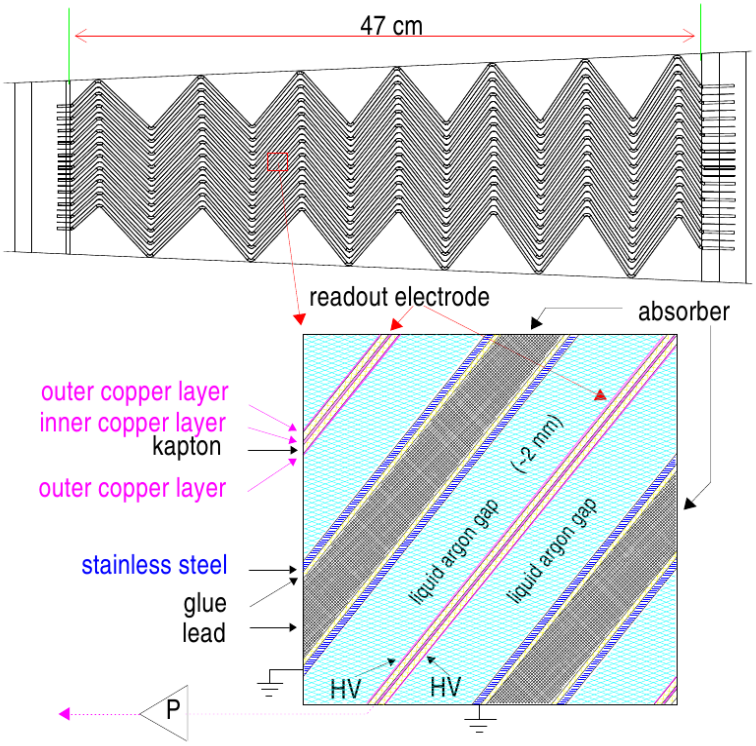

Figure 2.14: Sketch of a transverse section of the barrel electromagnetic calorimeter. It shows the accordion-shape lead liquid-argon layers.

lead generate the electromagnetic shower, and a fraction of the resulting low energy particles, mainly electrons and positrons, ionize the liquid argon. Then, the electrons produced in the ionization are collected in copper electrodes kept at a high voltage potential in the middle of the liquid argon gap, generating a current that is measured. The number of particles ionizing the argon is proportional to the energy of the incident particle, and so is the measured charge and maximum current.

This kind of calorimeter is called *sampling calorimeter*; the lead in this case is said to be the *absorber material*, while the LAr is the *active material*.

In this calorimeter, the structure of absorbers and electrodes has an accordion geometry, as shown in Figures 2.14 and 2.15. This is a characteristic feature of this calorimeter. This accordion geometry provides a full coverage in ϕ without any cracks.

Calorimeter geometry

The EM calorimeter consists of a barrel that covers the region $|\eta| < 1.475$, and two end-cap components covering the regions $1.375 < |\eta| < 3.2$. The barrel surrounds the superconducting solenoid; it is 6.4 m long, and its inner and outer radii are 1.4 m and 2 m respectively. Each end-cap wheel is 63 cm thick, and have inner and outer radii of 33.0 cm and 2.1 m respectively.

This calorimeter has a fine granularity in η and ϕ in the region $|\eta| < 2.5$, and a coarser granularity in the rest of the end-caps. The calorimeter is also divided in the longitudinal direction; there are three layers in the region $|\eta| < 2.5$, and two

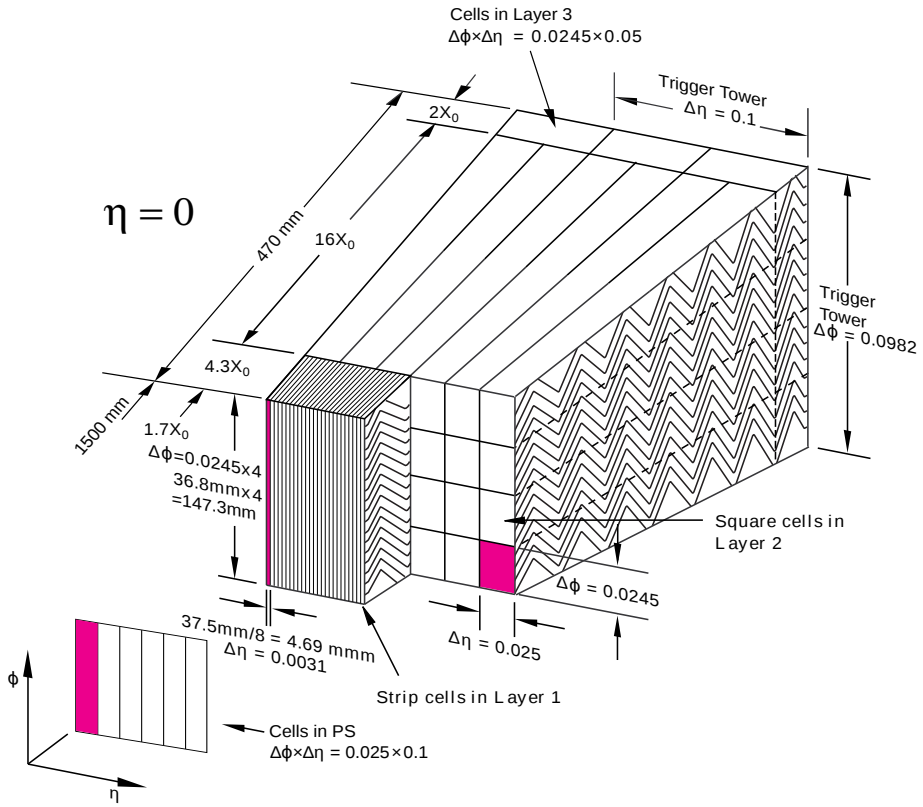

Figure 2.15: Sketch of a barrel module where the different layers are clearly visible. The granularity in η and ϕ of the cells of each of the three layers is also shown. [62].

Table 2.2: Granularity on η and ϕ in different η regions for each layer of the electromagnetic calorimeter [62].

	Barrel		**End-cap**	
EM calorimeter				
Number of layers and $\|\eta\|$ coverage				
Presampler	1	$\|\eta\| < 1.52$	1	$1.5 < \|\eta\| < 1.8$
Calorimeter	3	$\|\eta\| < 1.35$	2	$1.375 < \|\eta\| < 1.5$
	2	$1.35 < \|\eta\| < 1.475$	3	$1.5 < \|\eta\| < 2.5$
			2	$2.5 < \|\eta\| < 3.2$
Granularity $\Delta\eta \times \Delta\phi$ versus $\|\eta\|$				
Presampler	0.025×0.1	$\|\eta\| < 1.52$	0.025×0.1	$1.5 < \|\eta\| < 1.8$
Calorimeter 1st layer	$0.025/8 \times 0.1$	$\|\eta\| < 1.40$	0.050×0.1	$1.375 < \|\eta\| < 1.425$
	0.025×0.025	$1.40 < \|\eta\| < 1.475$	0.025×0.1	$1.425 < \|\eta\| < 1.5$
			$0.025/8 \times 0.1$	$1.5 < \|\eta\| < 1.8$
			$0.025/6 \times 0.1$	$1.8 < \|\eta\| < 2.0$
			$0.025/4 \times 0.1$	$2.0 < \|\eta\| < 2.4$
			0.025×0.1	$2.4 < \|\eta\| < 2.5$
			0.1×0.1	$2.5 < \|\eta\| < 3.2$
Calorimeter 2nd layer	0.025×0.025	$\|\eta\| < 1.40$	0.050×0.025	$1.375 < \|\eta\| < 1.425$
	0.075×0.025	$1.40 < \|\eta\| < 1.475$	0.025×0.025	$1.425 < \|\eta\| < 2.5$
			0.1×0.1	$2.5 < \|\eta\| < 3.2$
Calorimeter 3rd layer	0.050×0.025	$\|\eta\| < 1.35$	0.050×0.025	$1.5 < \|\eta\| < 2.5$

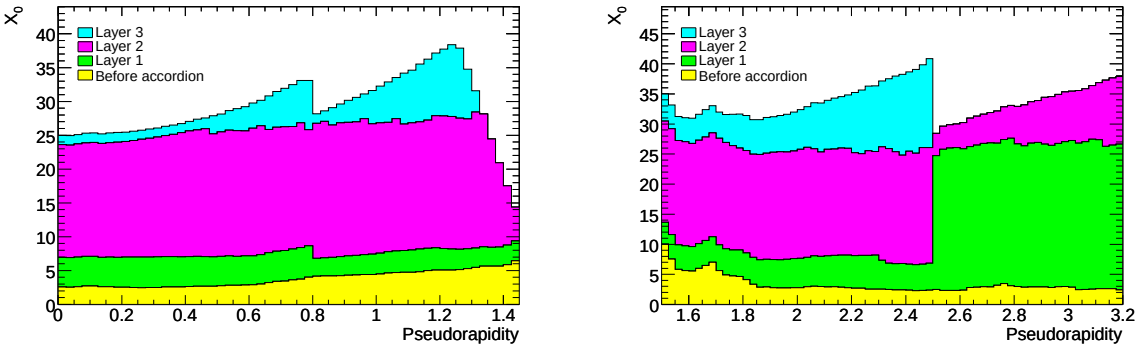

Figure 2.16: Cumulative amounts of material in front of the accordion calorimeter and in the different calorimeter layers [62], for the barrel (left) and end-cap (right) regions. It is shown in units of radiation length X_0, and as a function of $|\eta|$.

layers in the rest. In addition, there is a thin LAr layer with electrodes before the other layers; it is called pre-sampler and covers the region $|\eta| < 1.8$. The η coverage and granularity of each layer are quoted in Table 2.2. Figure 2.15 shows a sketch of the different layers in the barrel, with the granularity details.

Figure 2.16 shows the cumulative amounts of material in front of the accordion calorimeter and in the different calorimeter layers. It is shown in units of radiation length X_0, as a function of $|\eta|$. The thickest layer is the second one. The EM showers deposit most of the energy in this second layer and finish in the third layer.

The pre-sampler or layer 0 serve to estimate the energy lost by the particles when traversing the material in front of the calorimeter. If the electromagnetic shower starts before the calorimeter, there will be certain amount of energy deposited in the pre-sampler; measuring it allows applying a correction later.

The first layer has very thin granularity on η; it is also called strip-layer because the cells have a strip-shape. This thin granularity provide very useful information for discriminating prompt electrons or photons from jets (details about the photon-jet separation with information from this first layer are discussed in Chapter 3, Section 3.4). It allows also to compute precisely the η direction of the particles (as discussed in Chapter 5, Section 5.2.4).

Performance

The energy measurement resolution can be written as follows:

$$\frac{\sigma_E}{E} = \frac{a}{\sqrt{E}} \oplus b \oplus \frac{c}{E}, \tag{2.10}$$

where the energy E is in GeV.

The first term is a stochastic term. It corresponds to the statistical fluctuations on the number of low energy particles generated in the electromagnetic shower that ionize the liquid argon. The coefficient a is called *sampling term*; it is associated with the dead material in front of the calorimeter, and with the fraction of secondary particles that ionize the argon (there is another fraction that is absorbed by the lead layers). a is typically 10% for sampling calorimeters.

The second term b is called *constant term*. It is due to the non-uniformities of

the calorimeter. For the ATLAS EM calorimeter, the global constant term for the region $|\eta| < 2.5$ is nominally expected to be reduced to 0.7%. Currently, it has been estimated to be $(1.2 \pm 0.1(\text{stat.}) \, ^{+0.5}_{-0.6}(\text{syst.}))\%$ for the barrel and $(1.8 \pm 0.4(\text{stat.}) \pm 0.4(\text{syst.}))\%$ for the regions $1.52 < |\eta| < 2.47$ of the end-caps [77]. This is the dominant term on the energy resolution for photons in the $H \to \gamma\gamma$ analysis.

The last term is due to electronic noise summed over the readouts of the various calorimeter cells covered by the shower. This term is only significant for low energy particles.

2.5.2 Hadronic calorimeter

The hadronic calorimeter is used to measure the energy of hadrons, which traverse the EM calorimeter without loosing much energy. This calorimeter consists in a barrel section ($|\eta| < 1.7$) and two end-cap components ($1.5 < |\eta| < 3.2$). In this case, the barrel calorimeter uses scintillating plates as active material, whereas the end-caps are LAr calorimeters.

The barrel calorimeter uses steel sheets in order to generate the hadronic shower and scintillating fibers as active material. They are placed in planes perpendiculars to the beam, forming layers of steel and the scintillating material. When the particle shower pass through the scintillating tiles, they emit light in an amount proportional to the incident energy. Then fibers carry the light to devices where the light intensity is measured.

The LAr end-caps of the hadronic calorimeter function based on the same principle used by the EM calorimeter. But in this case, copper is used as absorber and the structure geometry is different.

2.5.3 Forward calorimeters

The forward calorimeters cover the region $3.1 < |\eta| < 4.9$. There are three modules in each end-cap. The first one uses copper as absorber and is optimized for electromagnetic measurements, while the other two use tungsten and measure mainly the hadronic energy. In these calorimeter, the electrode structure consists of concentric rods and tubes parallel to the beam axis, and they use also liquid argon as active material.

2.6 Muon spectrometer

The muon spectrometer measures the muon trajectories and momentum. The momentum is estimated from the muon trajectory curvature caused by the magnetic field provided by the toroidal magnets. A view of this sub-detector is shown in Figure 2.17. It covers the region $|\eta| < 2.7$.

The muon spectrometer is built with gaseous detectors of different models. All of them function based on the same principle, which is also the working mechanism of the TRT in the inner detector (described in Section 2.4.2). A gas is ionized when a charged particle pass by, and the ions and electrons drift towards electrodes, generating a current. In the barrel, these gaseous detectors are arranged on large concentric cylinders around the beam axis, while in the end-cap, they are located on

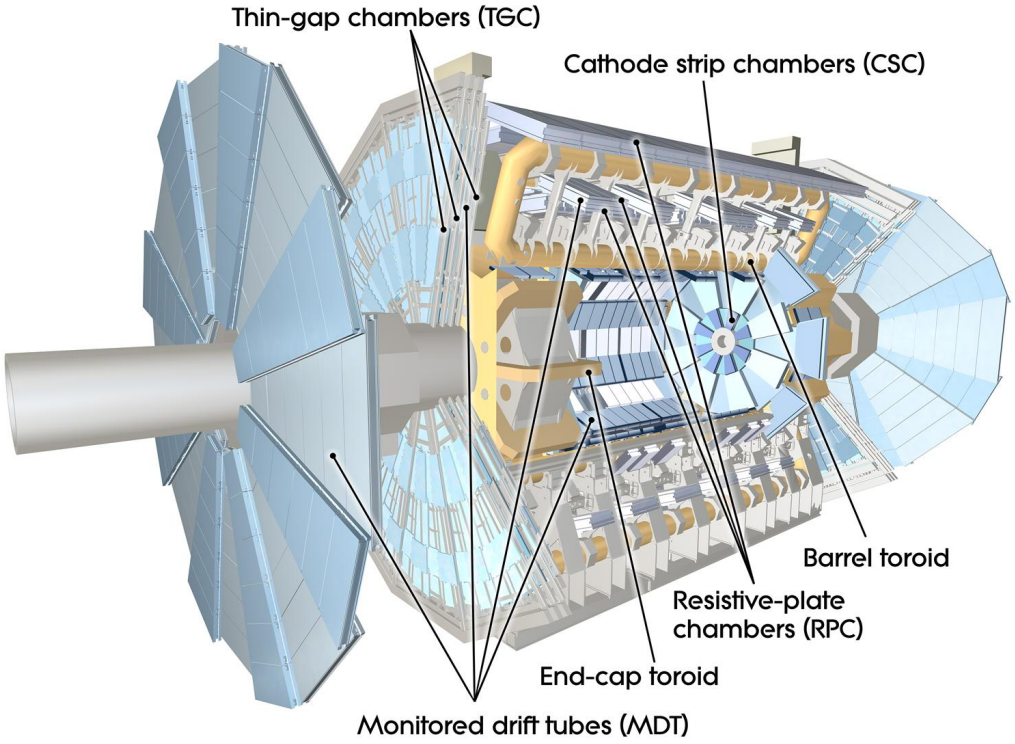

Figure 2.17: Schematic view of the ATLAS muon spectrometer [62].

large disks perpendicular to the beam axis. There are three main layers in the barrel and three in each end-cap; each of these layers is composed of various sub-layers of detectors.

The different detector models are used to attend different requirements. Some detectors provide precision measurements of the track coordinate in the principal muon bending direction (η), and some others provide quick information for the trigger system.

The detectors providing precision measurements on η are: Monitored Drift Tubes (MDT) in the barrel and the external part of the end-caps ($|\eta| < 2.0$), and Cathode Strip Chambers (CSC) in the forward region ($2.0 < |\eta| < 2.7$). The MDTs only provide information in the η direction, with a resolution of about 35 μm per chamber; while the CSCs measure both coordinates η and ϕ with resolutions of 40 μm and 5 mm, respectively.

The detectors providing quick information to the trigger are: Resistive Plate Chambers (RPC) in the barrel, and Thin Gap Chambers (TGC) in the end-caps. They deliver signals with a spread of 15–25 ns, which satisfy the time requirements. These detectors also complement the MDTs measurements by providing information in both directions, η and ϕ.

In this large spectrometer, the chamber alignment and the detailed knowledge of the magnetic field are important factors that affect the p_{T} resolution. The inter-chamber alignment has to achieve a precision of 30 μm. For this, the chambers are continuously aligned using a system of 12000 optical devices. The magnetic field needs to be known with a precision of a few per mil. It is achieved monitoring the

field continuously with a system of about 1800 Hall sensors.

The muon spectrometer is expected to provide a 10% transverse momentum resolution for muons of one TeV.

2.7 Trigger system

The trigger system is basically a filter that has the task of selecting the interesting events. It has to decrease the event rate from the nominal bunch crossing rate of 40 MHz to a rate of about 200 Hz, a rate at which data can be written to permanent storage. The trigger system consists of three different levels, called, level 1 (L1), level 2 (L2) and event filter (EF).

The first level uses a limited amount of the total detector information to take a decision in less than 2.5 μs. It reduces the event rate to about 75 kHz. The L1 trigger searches for objects with high transverse momentum, muons, electrons, photons and jets, as well as large missing and total transverse energy. In order to do that, L1 utilizes the trigger chambers in the muon spectrometer, and reduced-granularity information from all the calorimeters. For each event, the L1 trigger also defines one or more *Regions-of-Interest* (RoI's); these are the regions of the detector where the selection process has identified interesting features. This information is then used by the higher level triggers.

The second level uses all the information available within the RoI's, with full granularity and precision. This is approximately 2% of the total event information. The L2 reduces the trigger rate to approximately 3.5 kHz, with an event processing time of about 40 ms.

Finally, in the EF trigger, events are reconstructed completely, using algorithms similar to the ones used for the offline analysis. It is done in about four seconds, and it reduces the event rate to ~ 200 Hz, such as it is desired.

All the selection criteria used by the different trigger levels are organized in trigger menus. These trigger menus serve to classify events into physics channels and store them separately. For example, there is a trigger menu that requires at least two reconstructed photons with $E_{\mathrm{T}} > 20$ GeV and satisfying some photon quality minimal requirements. To perform the $H \to \gamma\gamma$ analysis reported here, it was enough to process events triggered by this menu or similar ones; it didn't required processing all the data recorded by ATLAS. The criteria used in these menus are optimized as the luminosity increases, to satisfy the limits on the output rate.

2.8 Computing framework

2.8.1 Computing facilities

The LHC produces an enormous amount of data, about 25 PB per year; the computing resources to store, distribute and analyze these data are provided to all the scientists around the world participating in the LHC experiments through the Worldwide LHC Computing Grid (WLCG) [78]. The WLCG links more than 170 computing centers in 36 countries.

At the WLCG, the computing facilities are organized in four tiers. The first processing of the data coming out from the experiments is done at CERN, on what is called the Tier-0. A copy of the raw data and the product of this first processing is stored at the Tier-0, and a backup copy is made on Tier-1 facilities. There are eleven Tier-1 centers distributed around the world. These centers are used to reprocess the data, and allow the access and analysis of the processed data. Derived datasets for specific analysis are copied to the Tier-2 facilities for further analysis. There are currently around 140 Tier-2 sites. Individual scientists access these facilities through local computing resources, which are referred to as Tier-3. The Tier-3's are either local clusters in a laboratory or even personal computers.

A CERN Analysis Facility provides an additional analysis capacity, with an important role in the calibration and algorithmic development work.

2.8.2 Software

In order to process and analyze the data coming from the detector, as well as for producing simulation samples and analyzing them, the ATLAS collaboration uses a software framework called Athena [79]. It is also used at the level 2 and event filter of the trigger. It is based on a software architecture called Gaudi [80] that was originally developed by the LHCb experiment, but nowadays it is a common project of both experiments. The Athena framework is primarily based on the C^{++} programming language, and Python language scripts are used to set the configuration options for the program execution.

2.8.3 Data processing and formats

The ATLAS detector produces about one petabyte of data per year; for an efficient distribution and analysis of these data, various storage formats have been defined, containing information at different processing levels.

The raw data delivered by the detector is stored in a format called *Raw Data Object* (RDO), which contains about 1.6 MB per collision event.

These datasets are processed to derive physical parameters and objects associated to the particles found in each event. This process is called *reconstruction*. Initially, the information from individual calorimeter cells is combined to build energy clusters, the hits on the different layers of the tracker are combined to reconstruct track segments and later the particle tracks, among others. Then, this information is further combined to obtained the more complex objects associated to the particles, objects like photons, electrons, muons, tau-leptons, jets, missing transverse energy, primary vertices, etc. The output of this process is store in two data formats, *Event Summary Data* (ESD) and *Analysis Object Data* (AOD). The ESD contains typically one megabyte per event, and it has sufficient information to allow a rapid tuning of the reconstruction algorithms and calibrations. The AOD represent about 100 kB per event and contains the information necessary for the physics analysis.

Finally from the AOD format, a *Derived Physics Data* (DPD) is created to reduce further the size of the analysis objects. These DPDs are defined by the different physics groups according to the individual necessities. On average DPDs contains 10 kB/event. DPDs can be read directly with ROOT [81], which is an analysis

package commonly used in Particle Physics.

A complete description of the ATLAS software and computing framework can be found in [82].

2.9 Simulation

Since the beginning in the ATLAS experiment, there has been the necessity of doing simulations in order to prepare physics analysis, as well as to evaluate both the detector and the analysis performances. The ATLAS simulation program can be divided into three separate modules, event generation, detector simulation, and digitization. Then, the simulated data is processed through the same reconstruction chain described in the previous section used for real data.

At the *event generation*, the physics processes that occur at the collisions are modeled. Generators model the initial and final-state radiation in these processes, the hadronization process and decays. The event generators most commonly used in ATLAS are PYTHIA [83, 84] and HERWIG [85]; they are based on the Monte Carlo technique.

The pileup is simulated by overlaying each event with a variable number of simulated inelastic proton-proton collisions, taking into account the structure of the beam bunch train at the LHC. The samples are usually prepared in advance, before the data-taking; they are prepared with a distribution of the mean number of interactions per bunch crossing some wider than what is expected for real data, and then event weights are used to match the real data distribution.

The ATLAS *detector simulation* is done using GEANT4 [86]; this is a toolkit that provides both a framework and the necessary functionalities for running detector simulations in Particle Physics. It includes optimized solutions for geometry description and navigation through the geometry, the propagation of particles through detectors, description of materials, as well as modeling of physics processes.

Then, the hits produced by G4ATLAS need to be translated into the output actually produced by the ATLAS detector. This is the *digitization*. In this step the propagation of charges or light into the active media as well as the response of the readout electronics are taken into account.

A complete description of the ATLAS simulation framework can be found in [87], and the tuning of the MC generators to describe the collision environment is presented in [88].

Chapter 3

Identification and reconstruction of photons in ATLAS

The search of the Higgs boson decaying in two photons requires the identification of photons and the reconstruction or measurement of their energy and direction of flight. This chapter explains how this is done in ATLAS.

As discussed in the previous chapter, Section 2.5.1, photons as well as electrons deposit most of their energy in the electromagnetic (EM) calorimeter, generating electromagnetic showers. The photon reconstruction is performed using mainly this sub-detector, and it has many aspects in common with the reconstruction of electrons, starting by the fact that photon and electron candidates have the same seeds in the EM calorimeter.

In the reconstruction of photons, two different signatures are distinguished, corresponding to *converted* and *unconverted* photons. A converted photon is the one that produces an electron-positron pair before arriving to the calorimeter, by interacting with the material that is in front of the calorimeter. The converted photons are distinguished thanks to the reconstruction of the electron/positron tracks and the associated vertices, in the inner detector.

The ATLAS detector allows a precise reconstruction of photons and electrons in the region $|\eta| < 2.5$. The electromagnetic calorimeter has been designed to have high granularity in this region, and the inner detector has been designed to provide tracking information in the same region.

The identification and reconstruction of photons have been developed based on Monte Carlo simulations, and validated and refined using test beams and collision data.

3.1 Reconstruction of photon candidates

The shower generated by an electron or photon in the electromagnetic calorimeter spans various cells; the electron and photon reconstruction starts with the clustering of neighboring cells in the EM calorimeter in which energy has been deposited. The algorithm used for this clustering procedure is described in details in [89]; it is called "sliding-window".

The η-ϕ space of the EM calorimeter is scanned, looking for local maximums of the sum of the transverse energy deposited in cells enclosed by a rectangular window

of fixed size. Cells from the three layers of the EM calorimeter and the pre-sampler are all considered. The size of the window is $\Delta\eta \times \Delta\phi = 0.075 \times 0.125$, which corresponds to 3×5 cells of the second layer of the EM calorimeter (in Chapter 2, Figure 2.15 and Table 2.2 give details about the EM calorimeter granularity). If a local maximum is found and the corresponding transverse energy is above a threshold of 2.5 GeV, a *pre-cluster* of cells is built. The η and ϕ positions of each pre-cluster are calculated as the energy-weighted barycenter of the cells in the core of the pre-cluster, in a window of $\Delta\eta \times \Delta\phi = 0.075 \times 0.075$ (3×3 cells of the calorimeter second layer).

Then, these pre-clusters are classified according to tracking information as corresponding to electrons, converted or unconverted photons. If one or more of the tracks reconstructed in the inner detector are found to match with a pre-cluster, the pre-cluster is classified either as electron candidate, as converted photon candidate or as both; otherwise, i.e. if no track is found to match the cluster, it is classified as unconverted photon candidate. Details about this classification are discussed in the next section.

After this classification is done, the electromagnetic *clusters* are built, with a transverse size that depends on the η region where the cluster is located and on the hypothetical corresponding particle. For electrons and converted photons in the calorimeter barrel, the cluster size used is $\Delta\eta \times \Delta\phi = 0.075 \times 0.175$ (3×7 cells of the EM calorimeter second layer); for unconverted photons in the barrel it is 0.075×0.125 (3×5 cells); and for any object in the end-caps it is 0.125×0.125 (5×5 cells). The cluster size has been optimized to be large enough to include most of the electromagnetic shower, but not too large to minimize the noise impact. Since the magnetic field in the inner detector bents the trajectories of the electron and positron resulting from a photon conversion, in opposite directions in the transverse plane, the electromagnetic showers from converted photons are wider in ϕ than the ones from unconverted photons. The electron showers are also wider in ϕ than the ones from unconverted photons because of the electrons' curved trajectories in the inner detector, throughout which electrons suffer bremsstrahlung radiation and interactions with the material. In the end-caps, the ϕ cluster size is the same for all the particle types because the effect of the magnetic field is small. The clusters in the end-caps are larger in terms of $\Delta\eta$ and number of cells than the ones in the barrel; this is because in the end-caps the cells are physically smaller than in the barrel.

For each cluster, the η and ϕ positions are calculated at each layer of the electromagnetic calorimeter independently, computing the energy-weighted barycenter of the cluster cells. Then, these position measurements are corrected for systematic biases, induced for instance by the size of the cells, or by the accordion geometry (details about these corrections can be found in [90]).

The measurement of the photon energy is discussed later, in Section 3.3.

The photon reconstruction efficiency has been evaluated using Monte Carlo simulation of $H \to \gamma\gamma$ events (with a Higgs boson mass hypothesis of $m_{\mathrm{H}} = 120$ GeV), considering photons with transverse momentum above 20 GeV [91]. Figure 3.1 shows the obtained efficiency as function of the photons pseudorapidity η (left side) and their transverse momentum p_{T} (right side), for converted and unconverted photons separately, as well as for all of them. Here, the efficiency is defined as the frac-

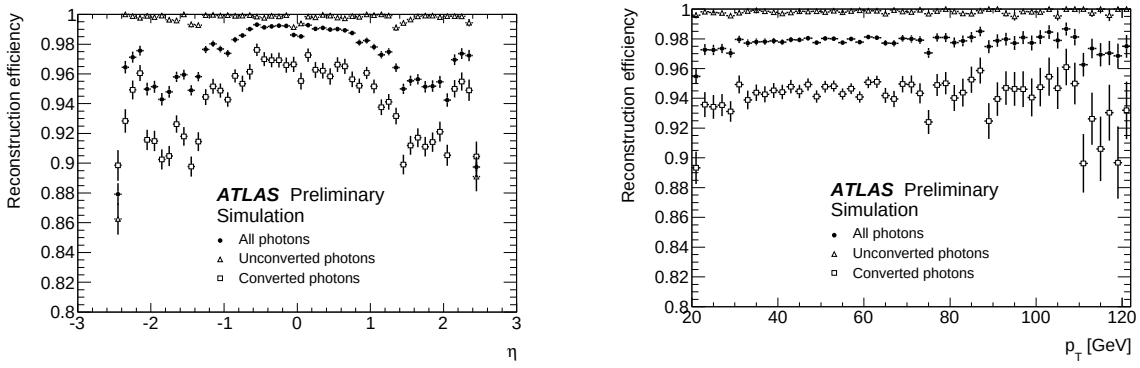

Figure 3.1: Photon reconstruction efficiencies as a function of photons true η and p_{T}, for unconverted and converted photons separately. This efficiency estimation has been done using Monte Carlo simulation of $H \to \gamma\gamma$ events ($m_{\mathrm{H}} = 120$ GeV), considering photons with transverse momentum above 20 GeV [91].

tion of the true photons with a given η position and p_{T} that are reconstructed as photons candidates by ATLAS. In the physics analysis, only photons in the regions $|\eta| < 1.37$ and $1.52 < |\eta| < 2.37$ are actually considered; photons in the transition regions between the barrel and end-caps of the calorimeter ($1.37 < |\eta| < 1.52$) are not considered because they are poorly reconstructed. Considering only photons in the allowed η regions, the reconstruction efficiency has been found to be $97.82 \pm 0.03\%$; for converted photons it is $94.33 \pm 0.09\%$, and for unconverted photons it is $99.83 \pm 0.01\%$. $2.11 \pm 0.03\%$ of the photons are wrongly reconstructed only as electron candidates, and only $0.06 \pm 0.01\%$ of the photons are not reconstructed at all.

3.2 Identification of electrons, converted and unconverted photons

The classification of electromagnetic clusters as corresponding to electrons, converted or unconverted photons is done based on tracking information.

After the reconstruction of tracks, oppositely charged tracks with transverse momentum $p_{\mathrm{T}} > 0.5$ GeV are associated to built photon conversion vertex candidates. For the reconstruction of each vertex, a fit is performed considering the parameters of the two tracks with the constraint that the two tracks form a vertex, and since photons are massless the angle between the two tracks is constrained to be zero.

Conversion candidates with a single track are also reconstructed. They correspond to conversions in which one of the electrons has transverse momentum $p_{\mathrm{T}} < 0.5$ GeV and is not detected, or to conversions in which the two electrons have high p_{T}, they travel very close to each other and they are reconstructed as a single track; the last case happens mostly when the conversion occurs in the transition radiation tracker (TRT). Only tracks without associated measurements in the first layer of the tracker are considered as single-track conversion candidates. For these conversion candidates, the vertex is taken as placed at the location of the first measurement in the tracker.

The matching between the tracks and the electromagnetic clusters is done by extrapolating the tracks from their last measurement to the calorimeter second layer.

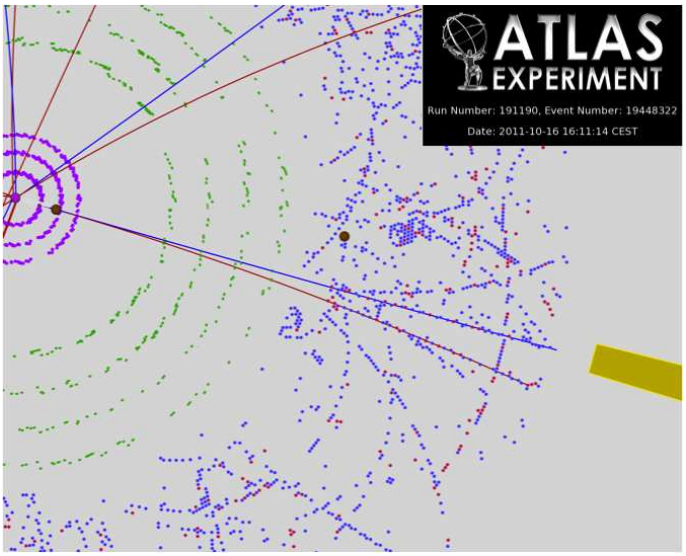

Figure 3.2: Close-up view in the transverse plane of a converted photon candidate. Only reconstructed tracks with $p_{\mathrm{T}} > 2$ GeV and $|\eta| < 1.4$ are shown, and only the hits in the pixel, SCT and TRT layers with $-1 < |\eta| < 0$ are shown. Starting from the primary vertex (shown as a large magenta dot on the left), the photon conversion vertex (brown dot) can be seen at a radius of 8.1 cm, followed by the pixel hits (magenta dots), SCT clusters (green segments) and TRT hits (blue dots and red dots). The electron track (blue line) has $p_{\mathrm{T}} = 56.1$ GeV and matches well with the electromagnetic cluster (shown in yellow at the outer radius). The positron track has $p_{\mathrm{T}} = 4.0$ GeV [18].

If the η and ϕ distances between the track and the cluster at this layer are below 0.05, they are said to match with each other; it is extended to 0.1 in ϕ on the side where the bremsstrahlung losses are expected.

In order to further distinguish between photons and electrons, especially between converted photons and electrons, a combination of additional criteria on the characteristics of the cluster-associated tracks are considered, like the following:

- the type of reconstructed tracks, i.e. if they were reconstructed only from TRT measurements or if they included also measurements from the silicon tracker; it is taken into account because TRT-only tracks have less momentum resolution and η information than the ones with information in the silicon layers;

- the transverse momentum of the tracks;

- the compatibility between the track momentum and the energy measured in the cluster;

- as mentioned before, the presence of associated measurements in the first layer of the tracker (the so-called B-layer) is considered; for this requirement, a map of the dead modules of the tracker is taken into account, in order to check if the required measurement should be expected or if the corresponding module is dead.

Figure 3.2 displays as example a two-track photon conversion candidate. Further details about the photon conversion reconstruction can be found in [61, 90, 91].

The high pileup conditions at the high luminosity LHC complicates the identification of converted and unconverted photons. The large amount of tracks reconstructed in the inner detector increases the probability of finding by chance a

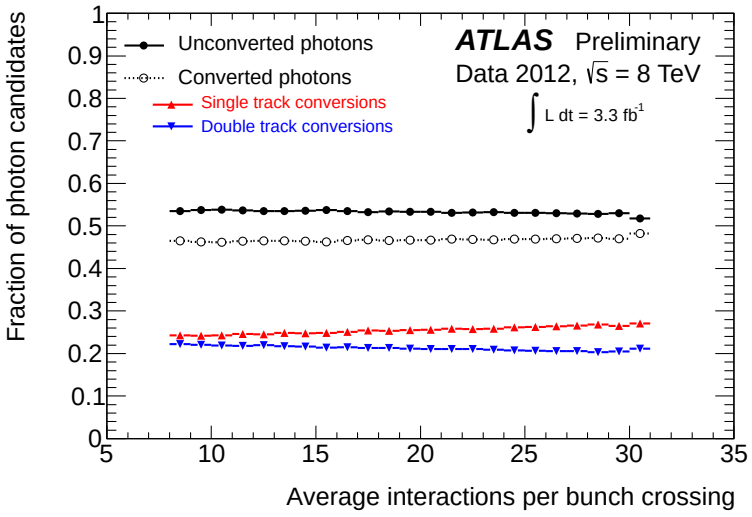

Figure 3.3: Fraction of reconstructed photons classified as unconverted and converted, with one and two associated tracks, as a function of the average number of interactions per bunch crossing [92]. This plot has been done with collision data collected in 2012 at $\sqrt{s} = 8$ TeV.

track matching the electromagnetic clusters. Recently, the criteria considered for the identification of converted photons have been re-optimized in order to make the photon conversion reconstruction more robust against the pileup. Figure 3.3 shows the stability of the fraction of reconstructed photons classified as unconverted and converted, with one and two associated tracks, as a function of the average number of interactions per bunch crossing, after this optimization. This plot has been done with collision data collected in 2012 at $\sqrt{s} = 8$ TeV.

The fraction of electrons that is misidentified as photons has been estimated to be around 8%. It has been estimated from collision data, selecting $Z \to ee$ events.

3.3 Photon energy measurement

Most of the energy carried by a photon or electron is deposited in the cells included in the corresponding cluster, but there is also a small fraction of energy lost by interactions with the material in front of the calorimeter, a fraction that is left out on the sides of the cluster boundary and another deposited behind the EM calorimeter. Additionally, as discussed in the previous chapter, Section 2.5.1, a fraction of the particles generated in the electromagnetic shower in the cells is absorbed by the lead layers and not by the liquid-argon, and thus a fraction of the energy is not directly measured. In order to take all this into account, the energy of the particle is reconstructed as follows [90].

$$E_{\text{reco}} = E_{\text{front}} + E_{\text{cal}} + E_{\text{back}}. \tag{3.1}$$

The energy deposited by the particle in the three layers of the accordion calorimeter E_{cal} is estimated as a function of the energy measured by the cells in each layer of the cluster $E_{1,2,3}$, considering a calibration factor f_{cal} (accounting for the calorimeter sampling fraction), and a correction factor f_{out} for the fraction of energy left out on

the sides of the cluster:

$$E_{\text{cal}} = f_{\text{cal}}(X, |\eta|) \left(\sum_{i=1}^{3} E_i \right) [1 + f_{\text{out}}(X, |\eta|)]. \tag{3.2}$$

The factors f_{cal} and f_{out} are estimated separately in bins of $|\eta|$ and of the longitudinal barycenter of the shower X, or shower depth, defined as:

$$X = \frac{E_{\text{ps}} X_{\text{ps}} + \sum_{i=1}^{3} E_i X_i}{E_{\text{ps}} + \sum_{i=1}^{3} E_i}; \tag{3.3}$$

where X_{ps}, $X_{1,2,3}$ are the longitudinal depths, expressed in radiation lengths (X_0), of the pre-sampler and the layers of the calorimeter respectively, computed from the centre of the detector. $X_{1,2,3}$ and X_{ps} are functions of $|\eta|$.

The energy deposited in front of the calorimeter E_{front} is parametrized as a function of the energy deposited in the pre-sampler E_{ps}:

$$E_{\text{front}} = a(E_{\text{cal}}, |\eta|) + b(E_{\text{cal}}, |\eta|) E_{\text{ps}} + c(E_{\text{cal}}, |\eta|) {E_{\text{ps}}}^2. \tag{3.4}$$

The parameters a, b and c are estimated separately in bins of $|\eta|$ and the computed E_{cal} value. In the region $1.8 < |\eta| < 3.2$, not covered by the pre-sampler, the energy deposited in front of the calorimeter is parametrized as a function of X.

Finally, the energy deposited behind the EM calorimeter E_{back} is estimated from the computed E_{cal} value, with a leakage correction factor f_{leak}:

$$E_{\text{back}} = E_{\text{cal}} f_{\text{leak}}(X, |\eta|). \tag{3.5}$$

The factor f_{leak} is estimated also separately in bins of $|\eta|$ and X.

The different calibration parameters are estimated separately for electrons, converted and unconverted photons, using Monte Carlo simulation of single particles with different fixed energies from 5 GeV to 1 TeV.

As done for the cluster position, some fine corrections are applied to this measured energy, to take into account systematic effects from the accordion structure of the calorimeter and the size of the cells (details can be found in [90]). These corrections change as a function of the η and ϕ position of the clusters, with a periodicity equal to the size of the cells in the η direction, and with a periodicity equal to the lead absorber spacing in the ϕ direction since the amount of passive material varies slightly.

Performance of the energy measurement

For the design constant term of the EM calorimeter of 0.7% (Chapter 2, Section 2.5.1), the expected relative resolution on the photon energy measurement σ/E is shown in Figure 3.4 as a function of η, for different photon energies, and separately for unconverted and converted photons on the left and right side respectively. This energy resolution is extracted from a Gaussian fit to the core of the distribution of the ratio $E_{\text{reco}}/E_{\text{true}}$, the reconstructed energy over the photon true energy. For the design constant term, for photons with transverse energy around 50 GeV like those

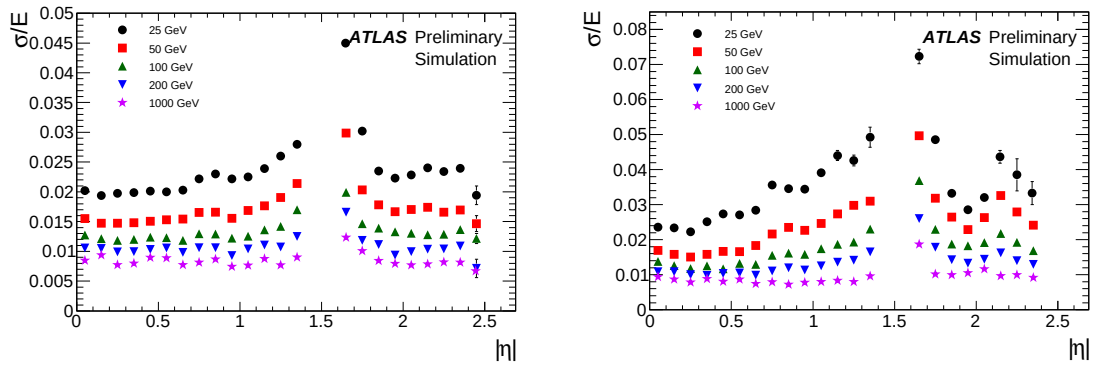

Figure 3.4: Fractional photon energy resolution as a function of the photon measured pseudorapidity, for different photon energies, and separately for unconverted and converted photons on the left and right side respectively. These plots reflect the performance of the photon energy measurement at beginning of 2010, evaluated with Monte Carlo simulation [93].

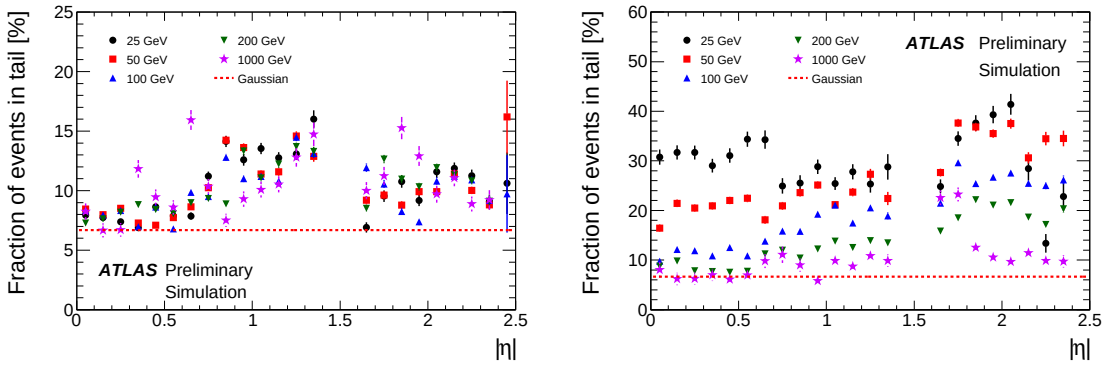

Figure 3.5: Fraction of photons for which the ratio $E_{\text{reco}}/E_{\text{true}}$ is below the fitted Gaussian mean minus 1.5σ, for different photon energies, and separately for unconverted and converted photons on the left and right side respectively. The dashed red line in these plots indicates the value expected for a Gaussian distribution. These plots reflect the performance of the photon energy measurement at beginning of 2010, evaluated with Monte Carlo simulation [93].

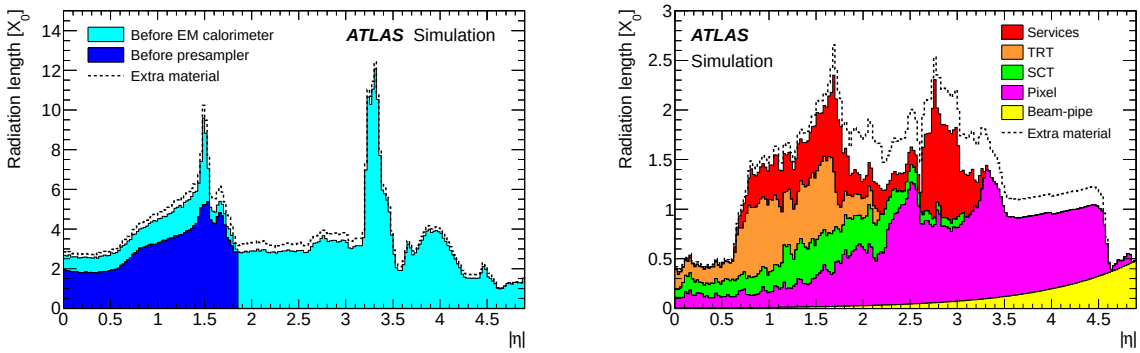

Figure 3.6: Amount of material, in units of radiation length X_0, traversed by a particle as a function of eta. The left side plot shows material in front of the pre-sampler and the electromagnetic calorimeter, and the right side plot shows the material up to the inner detector boundaries. The last plot shows the contributions of the different detector elements separately. The extra material used for systematic studies is also indicated, by the dashed lines [77].

expected from a Higgs boson decay, the relative resolution in the central part of the detector ($|\eta| < 0.6$) would be around 1.5%. For other η regions the resolution is expected to be less good, due to the higher amount of material in front of the calorimeter, in particular for converted photons. These figures can be compared with the plots in Figure 3.6, which show the estimated amount of material in front of the calorimeter as a function of η.

In addition, the plots in Figure 3.5 show the fraction of photons on the low energy tail of the distribution of $E_{\text{reco}}/E_{\text{true}}$; specifically, the fraction of photons for which the ratio $E_{\text{reco}}/E_{\text{true}}$ is below the fitted Gaussian mean by more than 1.5σ. It is shown separately on the left side for unconverted photons and on the right side for converted photons. The dashed red line in these plots indicates the value expected for a Gaussian distribution. The values obtained for converted photons are significantly larger than the value expected for the Gaussian, and also larger than the values obtained for unconverted photons. These mis-calibrated converted photons correspond to conversion electrons and positrons that deposit a significant fraction of energy out of the cluster. These plots reflect the performance of the photon energy measurement at beginning of 2010, evaluated with Monte Carlo simulation. Now additional corrections are applied to the energy measured for converted photons, which consider the radius at which the conversions occur, partially reducing this effect.

In-situ energy calibration

After computing the photon energy using the simulation-based calibration described above, additional corrections are applied to rectify for mis-simulated non-uniformities of the calorimeter. These corrections are derived from an inter-calibration of different η regions of the calorimeter, performed with real collision data. This is done using $Z \to ee$ events, constraining the observed di-electron invariant mass distribution to follow the well-known shape of the Z boson peak from the Monte Carlo. Details can be found in [77]. In this inter-calibration, residual mis-calibration factors α_i are defined for different i-th η bins, in such a way that

$$E_{\text{reco}} = E_{\text{true}}(1 + \alpha_i). \tag{3.6}$$

The values obtained for α_i from the collision data collected in 2010 are shown in Figure 3.7. They are within $\pm 2\%$ in the barrel region, and within $\pm 4\%$ in the regions $1.52 < |\eta| < 2.47$ of the end-caps.

Similarly, the α_i factors have been estimated for low transverse energy electrons from $J/\psi \to ee$ events. The values obtained are in good agreement with the ones computed from the $Z \to ee$ events. This allowed checking the linearity of the energy measurement.

The α_i factors have been additionally cross-checked comparing the electron energy measured in the electromagnetic calorimeter with the momentum measured in the inner detector, with $W \to e\nu$ events, and directly with photons from $Z \to ll\gamma$ events, with $l = e, \mu$. Figure 3.8 shows a comparison of the di-electron invariant mass distribution for $Z \to ee$ events on 4.6 fb^{-1} of data collected in 2011, after applying the inter-calibration corrections.

The constant term of the EM calorimeter has been also estimated from the

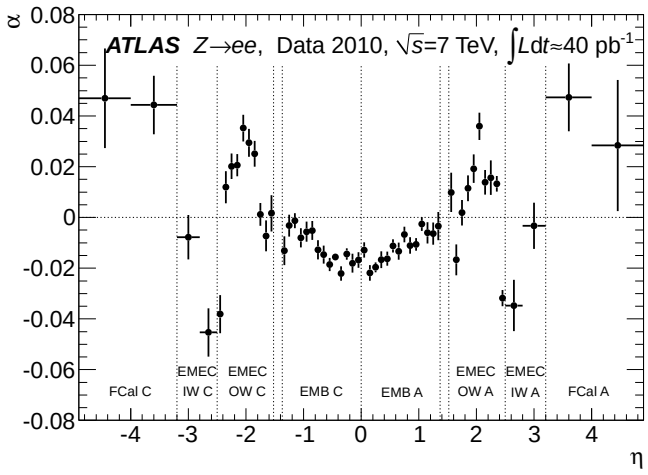

Figure 3.7: Energy-scale correction factors α for different η regions, derived using $Z \to ee$ events from real collision data, constraining the observed di-electron invariant mass distribution to follow the well-known shape of the Z boson peak from the Monte Carlo [77].

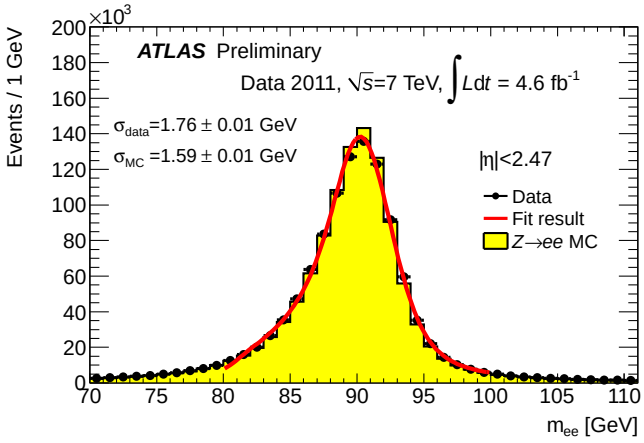

Figure 3.8: Comparison of the di-electron invariant mass distribution for $Z \to ee$ events from data collected in 2011, after applying the inter-calibration corrections [92].

Table 3.1: Photons-jet discriminant variables used for the identification of photons [91]. Two sets of cut thresholds have been defined for the selection of photons with these variables; they are called *loose* and *tight* . The variables considered for each of the two selections are indicated.

Category	Description	Name	Loose	Tight
Acceptance	$\|\eta\| < 2.37$, $1.37 < \|\eta\| < 1.52$ excluded	–		✓
Hadronic leakage	Ratio of E_T in the first sampling of the hadronic calorimeter to E_T of the EM cluster (used over the range $\|\eta\| < 0.8$ and $\|\eta\| > 1.37$)	R_{had_1}	✓	✓
	Ratio of E_T in all the hadronic calorimeter to E_T of the EM cluster (used over the range $0.8 < \|\eta\| < 1.37$)	R_{had}	✓	✓
EM Middle layer	Ratio in η of cell energies in 3×7 versus 7×7 cells	R_η	✓	✓
	Lateral width of the shower	w_2	✓	✓
	Ratio in ϕ of cell energies in 3×3 and 3×7 cells	R_ϕ		✓
EM Strip layer	Shower width for three strips around maximum strip	$w_{s\,3}$		✓
	Total lateral shower width	$w_{s\,\text{tot}}$		✓
	Fraction of energy outside core of three central strips but within seven strips	F_{side}		✓
	Difference between the energy associated with the second maximum in the strip layer, and the energy reconstructed in the strip with the minimal value found between the first and second maxima	ΔE		✓
	Ratio of the energy difference associated with the largest and second largest energy deposits over the sum of these energies	E_{ratio}		✓

measured and predicted di-electron invariant mass distribution for $Z \to ee$ events, from the resolution of the peak [77]. The constant term is the dominant term on the energy resolution in the range relevant for the $H \to \gamma\gamma$ analysis. In order to estimate the constant term, the sampling and noise terms have been taken from the Monte Carlo simulation. The resulting values are the ones quoted in Chapter 2, Section 2.5.1. Then, the Monte Carlo simulations used for physics analysis have been arranged according to the results of this estimation.

3.4 Photon identification

The photons that need to be measured are those directly produced by the interaction of quarks and gluons, photons radiated by quarks before the hadronization process, and photons from the decay of a fundamental boson (like the Higgs boson); they are called *prompt photons*.

Any reconstructed photon candidate that does not correspond to a prompt photon is considered/called *fake photon*. The largest fraction of fake photons in ATLAS corresponds to jets, which deposit a significant fraction of their energy in the electromagnetic calorimeter. In particular, the jets that most look like a photon in the EM calorimeter are jets with a leading neutral hadron, mainly π^0, decaying to a collimated photon pair.

In order to reject fake photons, a set of discriminant variables is defined, based on the shape of the photon electromagnetic shower in the calorimeter. In total, ten variables are defined; they are explained briefly in Table 3.1, and details can be found in [90].

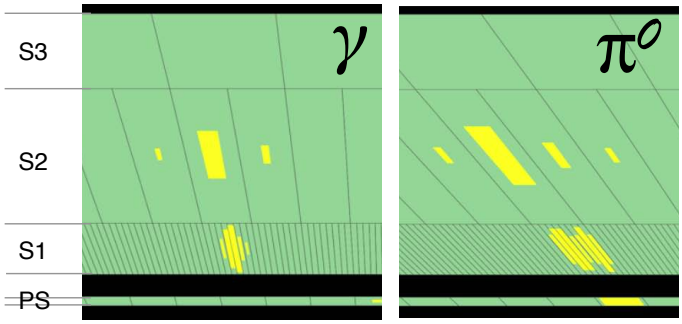

Figure 3.9: Photon candidates in the electromagnetic calorimeter. The yellow spots correspond to the energy deposited by the photons in the different cells. The pre-sampler (PS) and the three layers of the EM calorimeter are indicated. The photon candidate on the left side has the shower shape typically expected for a prompt photon, while the deposit on the right side corresponds very likely to two photons from a π^0 decay.

Jets typically deposit a large fraction of energy in the hadronic calorimeter. So, two variables (R_{had1} and R_{had}) are based on the amount of energy deposited in the hadronic calorimeter in the region behind the electromagnetic cluster. The two variables are used alternatively in different η regions.

The energy deposition by jets in the calorimeter is usually wider than the photon showers. This difference between jets and photons is exploited with three variables (R_η, w_2 and R_ϕ). They consider the lateral distribution of energy in the second (middle) layer of the EM calorimeter.

After filtering the photon candidates considering these variables, most of the fake photons correspond to the collimated photon pairs from neutral hadrons. The fine granularity of the first (strip) layer allows computing five discriminant variables (w_{s3}, $w_{\text{s tot}}$, F_{side}, ΔE and E_{ratio}), which provide an excellent separation between photons and fake photons. The strip layer allows to distinguish between two maxima of deposited energy very close to each other and a single one, as illustrated in Figure 3.9. This figure shows two photon candidates in the EM calorimeter; the one on the left side has the shower shape typically expected for a prompt photon, but the one on the right side corresponds very likely to a photon pair from a π^0 decay.

Figure 3.10 shows as example the normalized distributions of these discriminating variables obtained from Monte Carlo simulation, for unconverted photon candidates with $E_{\text{T}} > 20$ GeV in the region $0 < |\eta| < 0.6$ [91]. This is shown separately for prompt photons and for fake photons from jets.

Two sets of cut thresholds have been defined for the selection of photons with these discriminant variables; they are called *loose* and *tight* [91]. The optimization of the thresholds is performed separately in bins of η, to take into the account variation of the variable distributions due to the geometry of the detector. The optimization is done based on Monte Carlo simulation, using the TMVA toolkit [94].

The *loose* selection allows performing a sort of pre-selection. As indicated in Table 3.1, *loose* only includes cuts on the hadronic leakage variable and on two of the variables computed with the calorimeter's second layer information. The same thresholds are used for converted and unconverted photons, as well as for the identification of electrons in a similar *loose* set of cuts. The efficiency of this selection is above 95% and 90% for unconverted and converted photons respectively. *Loose* is used at the trigger level to select photon and electron candidates.

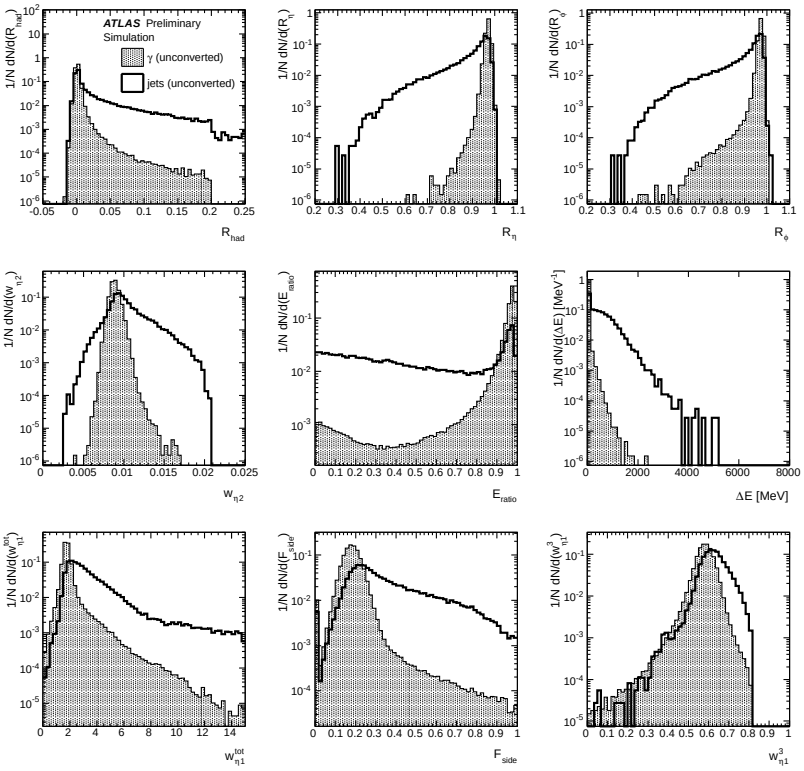

Figure 3.10: Normalized distributions of the calorimetric discriminating variables obtained from Monte Carlo simulation, for unconverted photon candidates with $E_{\mathrm{T}} > 20$ GeV in the region $0 < |\eta| < 0.6$. This is shows separately for prompt photons and for fake photons from jets [91].

Tight represents the nominal selection used for physics analysis and includes cuts in all the discriminant variables. The cut thresholds are optimized to provide a selection efficiency around 85% for prompt photons with $E_{\mathrm{T}} > 40$ GeV, and to maximize the fake photon rejection. The optimization is done separately for converted and unconverted photon candidates.

The *tight* selection also includes an acceptance restriction, requiring the photon candidates to be in the region $|\eta| < 2.37$, excluding the region $1.37 < |\eta| < 1.52$, which corresponds to the transition between the barrel and end-caps, where photons are poorly reconstructed.

As an alternative to the *tight* set of cuts, a neural-network [94] based selection has been also defined. It deals better with the correlations between the different variables and provides a better separation between photons and jets than the cut-based selection. Nevertheless, it also requires an accurate knowledge of the discriminant variable distributions for prompt and fake photons. Detailed studies of these distributions with Monte Carlo and collision data have allowed to use the neural-network based selection in the $H \to \gamma\gamma$ search with the collision data collected in 2011.

After requiring the photon candidates to satisfy the *tight* identification criteria, only one jet out of a few thousands is mis-identified as photon.

When comparing the distributions of the discriminant variables predicted by Monte Carlo (MC) simulations with the ones observed in real collision data, some small differences are observed. In order to take this into account when using the simulation for physics analysis, the discriminant variable values are slightly shifted

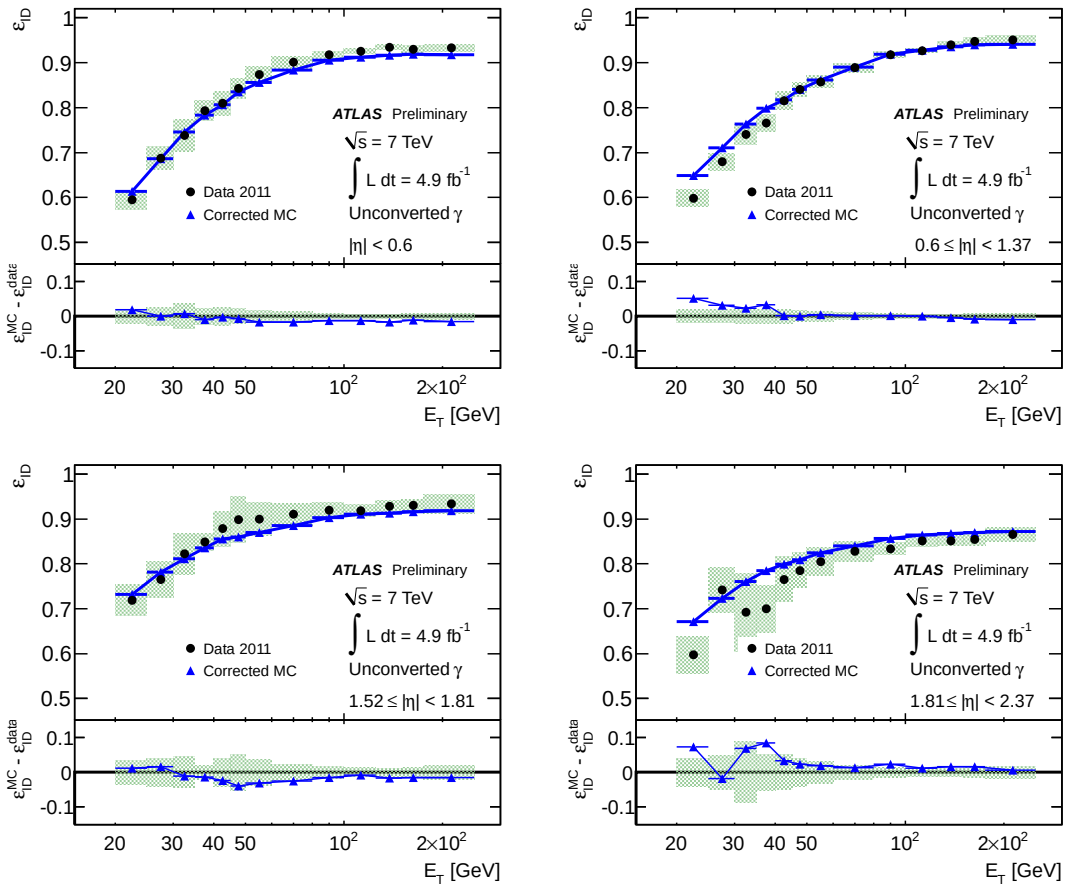

Figure 3.11: Photons identification efficiencies as a function of the photon transverse energy E_{T}, for different η regions, for the $\sqrt{s} = 7$ TeV collision collected in 2011 [95]. These plots show both the values obtained from corrected Monte Carlo simulation and the ones obtained with data-driven methods [95].

by a factor equal to the difference between the MC and data distribution means.

Additionally, the photon identification efficiency is monitored using real collision data with three independent methods (data-driven methods). One of the methods uses photons from $Z \to \ell\ell\gamma$ decays to directly measure the efficiency for low E_{T} photons; another method uses $Z \to ee$ events as reference sample, and exploits the similarities between the electromagnetic showers induced by electrons and photons to calculate the photon identification efficiency; the third method uses a sample of photon candidates and sidebands defined using isolation criteria (details can be found in [95]).

After the Monte Carlo simulations are corrected, only small differences of the order of 5% remains between the efficiencies obtained from MC and from the data. These small differences are taken as systematic uncertainties on the efficiency for the physics analysis presented in this thesis. Figure 3.11 shows for example the identification efficiencies obtained for unconverted photons as a function of the photon transverse energy E_{T}, for different η regions, for the data collected at $\sqrt{s} = 7$ TeV in 2011 [95].

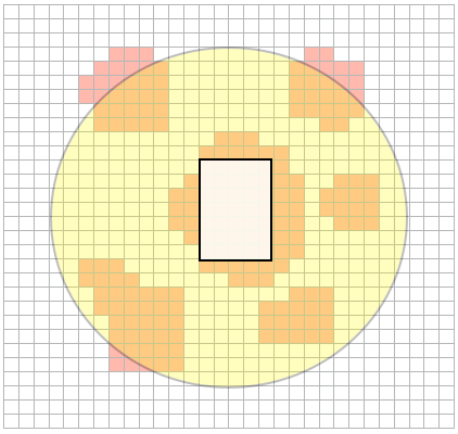

Figure 3.12: Illustration of the isolation transverse energy $E_{\mathrm{T}}^{\mathrm{isol}}$ computation [92]. It shows the η-ϕ space of the calorimeters around a photon candidate. The grid indicates the cells of the second layer of the electromagnetic calorimeter. Reconstructed topological-clusters are indicated in red, and the yellow region represents the area where the topological-clusters are considered. The transverse energy deposited in the electromagnetic cells indicated by the central white rectangle is subtracted in the computation, to exclude the energy deposited by the photon itself.

3.5 Isolation criteria

Around fake photons from jets, there is usually some activity in the detector (i.e. tracks, deposited energy), corresponding to the jet additional particles; while around prompt photons, on average, there is not much activity. Thus, in order to further reject fake photons from jets, the photon candidates are required to satisfy some isolation criteria. In ATLAS, two isolation criteria are defined: the *isolation transverse energy* $E_{\mathrm{T}}^{\mathrm{isol}}$ that considers the transverse energy deposited around photon candidates in the calorimeters; and the *tracking isolation* $p_{\mathrm{T}}^{\mathrm{isol}}$ that considers the transverse momentum of the tracks reconstructed around the photon candidates [91].

Calorimetric isolation

The isolation transverse energy $E_{\mathrm{T}}^{\mathrm{isol}}$ is built using cell clusters reconstructed in the electromagnetic and hadronic calorimeters; these clusters are reconstructed following an algorithm described in [89], and they are called *topological clusters*. The clustering algorithm groups together neighboring cells as long as the signal in the cells is significant compared to the noise.

For a photon candidate, $E_{\mathrm{T}}^{\mathrm{isol}}$ is computed by summing up the transverse energy of the topological clusters whose barycenters are located within a circle of radius of 0.4, in the η-ϕ space around the photon, as illustrated in Figure 3.12. In order to exclude the energy deposited by the photon itself, the transverse energy deposited in the electromagnetic cells within a rectangular window centered on the photon candidate is subtracted from the sum; the size of this rectangular window is $\Delta\eta \times \Delta\phi = 0.125 \times 0.175$ (5×7 cells of the EM calorimeter second layer).

Various η-ϕ radii are tested for the reconstruction of the $E_{\mathrm{T}}^{\mathrm{isol}}$ variable. On the one hand, the largest is the region considered, the largest fraction of the jet energy is collected, but on the other hand, also more noise is included. The $E_{\mathrm{T}}^{\mathrm{isol}}$ used in the analysis presented in this thesis have been reconstructed using a radius of 0.4, which has been found to be the optimal for this analysis.

Various corrections are applied to the isolation transverse energy to maximize its discrimination power. The photon energy that leaks out of the central rectangle of 5×7 cells is subtracted from $E_{\mathrm{T}}^{\mathrm{isol}}$. This energy leakage is estimated using Monte Carlo simulation, as a function of the transverse energy and η position of the photon candidate.

The *ambient transverse energy* contribution to the isolation transverse energy is estimated and subtracted from $E_{\mathrm{T}}^{\mathrm{isol}}$. This is the contribution from the underlying event and both in-time and out-of-time pileup. The *underlying event* represents all the activity resulting from a proton-proton interaction that is not associated with the hard interaction process. The *in-time* pileup contribution corresponds to the activity resulting from the additional multiple proton-proton interactions that occur simultaneously in the analyzed event bunch-crossing. The *out-of-time* pileup corresponds to the collisions occurred in previous bunch-crossings; the time required by the calorimeter cells to achieve their ground state is larger than the time separation between consecutive bunch-crossings, thus the remnants of the activity in the calorimeter from previous events affect $E_{\mathrm{T}}^{\mathrm{isol}}$.

Actually, part of the noise from pileup is reduced in the reconstruction of the topological clusters, which is performed with a noise-suppressing algorithm that also minimizes the electronic noise in the cell energy measurement [89].

The ambient transverse energy to be corrected is estimated event per event following the algorithm suggested in [96]. For each reconstructed jet, a transverse energy density is computed as the ratio between the jet transverse energy and its area. Considering the jets reconstructed in a given event, the median of the distribution of this density is taken as an ambient transverse energy density in the event, which is later multiplied by the area considered in the isolation computation to estimate the correction. Details about the implementation of this correction in ATLAS, as well as about the photon energy leakage correction, can be found in [10, 97].

In Figure 3.13, the black points show the $E_{\mathrm{T}}^{\mathrm{isol}}$ distribution of a sample of photon candidates that satisfy the identification criteria. The solid black line corresponds to the result of a multi-component template fit of the distribution, the template distribution corresponding to prompt photons is shown in red, and the template corresponding to fake photons from jets is shown in blue.

The computation of the isolation transverse energy using topological clusters has been recently implemented in ATLAS. Previously, instead of using these clusters, the individual cells of the calorimeter were directly considered. The previous variable had a remaining sensitivity to the out-of-time pileup, that has been removed in the new variable, thanks to the noise suppression procedure used for the reconstruction of the topological clusters. This is shown in Figure 3.14, which presents the mean of a Crystal Ball [98] function fitted to the isolation transverse energy distribution for electrons from $Z \to ee$ events, as a function of the bunch crossing identifiers; the plot on the left side corresponds to the previous isolation variable, and the one on the right side corresponds to the newly implemented isolation computation.

In the $H \to \gamma\gamma$ analysis, the photon candidates are required to have $E_{\mathrm{T}}^{\mathrm{isol}} < 4$ GeV; above 95% of the prompt photons that satisfy the identification criteria, described in the previous section, pass this isolation cut, which rejects more than half of the fake photons remaining.

The validity of the $E_{\mathrm{T}}^{\mathrm{isol}}$ distribution predicted by the Monte Carlo simulations

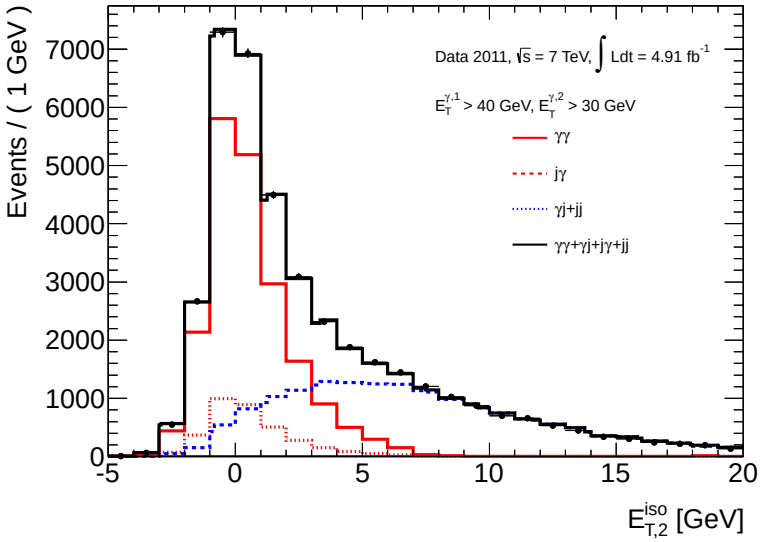

Figure 3.13: $E_{\mathrm{T}}^{\mathrm{isol}}$ distribution of a sample of photon candidates that satisfy the identification criteria. The solid black line corresponds to the result of a multi-component template fit of the distribution, the template distribution corresponding to prompt photons is shown in red, and the template corresponding to fake photons from jets is shown in blue.

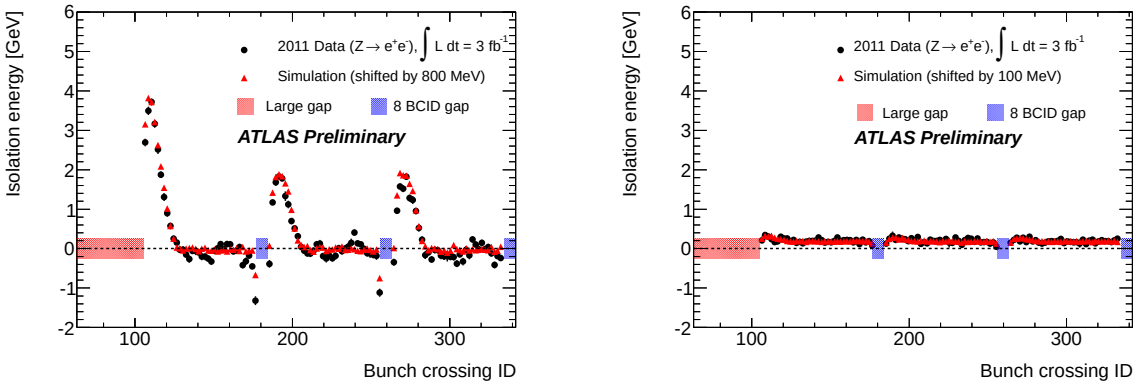

Figure 3.14: Calorimetric isolation versus pileup [92]. Specifically, it shows the mean of a Crystal Ball [98] function fitted to the isolation transverse energy distribution for electrons from $Z \to ee$ events, as a function of the bunch crossing identifiers; the plot on the left side corresponds to the previous isolation variable, and one on the right side corresponds to the newly implemented isolation computation, using topological clusters.

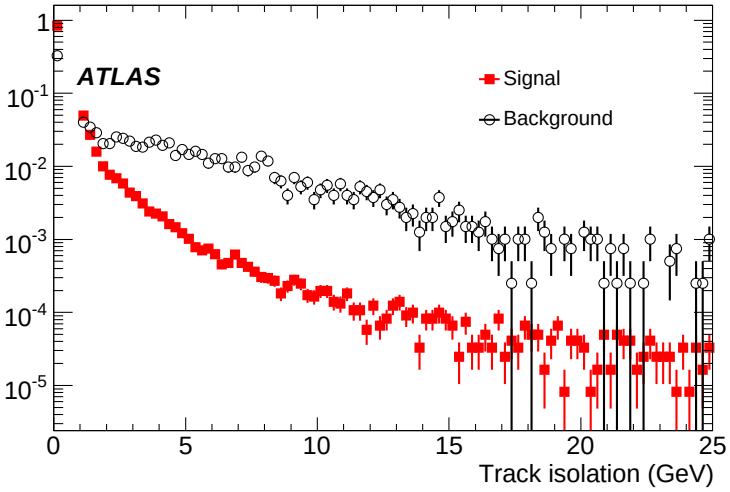

Figure 3.15: Normalized tracking isolation $p_{\mathrm{T}}^{\mathrm{isol}}$ distributions obtained from Monte Carlo simulation for prompt photons (red squares) and fake photons (circles), after requiring them to satisfy the identification criteria [90]

is monitored comparing the collision data and Monte Carlo distributions obtained for electrons from $Z \to ee$ events, and for photons in $Z \to ll\gamma$, with $l = e, \mu,$. The Monte Carlo distributions are slightly shifted with respect to the collision data distributions by about 100 MeV; this shift implies a difference on the isolation cut efficiency for prompt photons of about 0.2%, which has a negligible impact in the results of the $H \to \gamma\gamma$ analysis presented in this thesis.

Tracking isolation

The tracking isolation $p_{\mathrm{T}}^{\mathrm{isol}}$ is computed as the scalar sum of the transverse momentum $p_{\mathrm{T}}^{\mathrm{trk}}$ of the tracks reconstructed around the photon candidate, with the distance ΔR between each track and the photon candidate direction below a given radius (typically 0.3). The tracks to be considered are required to have transverse momentum $p_{\mathrm{T}}^{\mathrm{trk}} > 1$ GeV; this cut rejects a large amount of tracks from the underlying event and pileup, and thus minimizes their effects on the tracking isolation. In the case of converted photons, the tracks associated to the conversion are excluded. In addition, in order to avoid including conversion tracks corresponding to the photon candidate but that have not been associated to it, the tracks are required to have an associated hit in the first layer of the tracker, and to have a transverse impact parameter $d_0 < 1$ mm.

Figure 3.15 shows the normalized $p_{\mathrm{T}}^{\mathrm{isol}}$ distributions obtained from Monte Carlo simulation for prompt photons (red squares) and fake photons (empty circles), after requiring them to satisfy the identification criteria [90].

The tracking isolation has both advantages and disadvantages compared with the calorimetric isolation.

On the one hand, the tracking isolation only considers information of charged particles, while the calorimetric isolation includes information of both charged and neutral particles. Therefore, the jet rejection achieved using the tracking isolation is lower than the rejection achieved with the calorimetric isolation. For the same

reason, the association of the calorimetric isolation with the partonic isolation is more straightforward than for the tracking isolation; the *partonic isolation* is the one computed in Monte Carlo generators, considering quarks and gluons around a photon. In the measurements of the production cross-section of isolated prompt photons performed in ATLAS, only calorimetric isolation has been used to facilitate the comparison of the measurements with the theoretical predictions.

On the other hand, a tracking isolation might be more robust against pileup than the calorimetric isolation. First, the tracking isolation does not suffer the out-of-time pileup that affects the calorimeter. Second, a very robust tracking isolation may be computed if the primary vertex of the analyzed event is identified, by considering only tracks associated to it. This is straightforward in the case of electrons and muons, but this is not the case for photons. In this case, a sufficiently precise identification of the primary vertex is only achieved for photons with early conversions, with hits in the silicon tracker. (The identification of the primary vertex in diphoton events for the $H \to \gamma\gamma$ analysis is discussed in Chapter 5, Section 5.2.4).

In the analysis presented in this thesis, only the calorimetric isolation has been used, but in a later version of the analysis reported in [21], the tracking isolation has been also used as a complement to the calorimetric one.

Chapter 4

Statistical analysis procedure

In the search for the Standard Model (SM) Higgs boson, the compatibility between a dataset and two different hypotheses is tested, the background-only hypothesis and the background plus SM Higgs boson-signal hypothesis. This chapter describes the statistical procedure used to perform this comparison quantitatively. Slightly different approaches have been used in the various experiments where the Higgs boson search has been performed. This chapter describes the procedure that the ATLAS and CMS collaborations have agreed to use, which is presented in [99].

4.1 General aspects

The tests of the different hypotheses are performed based on data distributions that are sensitive to the underlying physics on which the hypotheses have been made. For example, in the search of the Higgs boson in the diphoton decay channel in ATLAS, the diphoton invariant mass distribution is used. In this case, while the background has a smoothly decreasing distribution, the Higgs boson signal distribution is a narrow peak.

For the hypothesis tests a likelihood function needs to be defined. In the case of the ATLAS $H \to \gamma\gamma$ analysis, an un-binned likelihood function is used. It is defined as follows:

$$\mathcal{L}(\text{data}|\mu,\theta) = k^{-1} \prod_i \left[\mu S f_s(x_i) + B f_b(x_i)\right] e^{-(\mu S+B)}; \tag{4.1}$$

where f_s and f_b are probability density functions for the expected signal and background respectively, and S and B are the corresponding number events expected. μ is referred as the *signal strength*; it is a scale factor on the number of signal events, which is defined with respect to the expected number of signal events expected for the SM Higgs boson. θ represents the set of so-called *nuisance parameters*. The nuisance parameters are all the function parameters that are not of central interest, but that are needed to model the pdf's; in this case μ is the parameter of central interest. The data for which the likelihood function is evaluated are either the actual experimental data or *pseudo-data* (also called *toy*). The pseudo-data are generated randomly, considering a hypothesized probability density function (pdf). k is the number of events in the dataset for which the likelihood function is evaluated.

The values of the parameters for which the likelihood function achieves a maximum are the values that best fit the data sample; they are denoted with the cor-

responding parameter symbol and a hat, for example $\hat{\mu}$ or $\hat{\theta}$. Technically, they correspond to the parameters that are left free in a fit, while the symbols without hat correspond to parameters fixed in the fit.

4.2 Testing the signal-plus-background hypothesis

In the search for the SM Higgs boson, usually, various signal-plus-background hypotheses with different signal strengths are tested. For each signal strength μ, one computes the confidence level at which signal strengths equal or larger than μ can be excluded. Then, the μ value for which a given confidence level is achieved is reported, commonly the one corresponding to 95% confidence level, denoted as $\mu^{95\%CL_s}$. In this way, a *95% confidence level upper limit* is set over the possible signal strengths.

Assuming the Higgs boson decay branching ratios to be as expected in the Standard Model, these limits can be taken as limits over the Higgs boson production cross-section.

At the LHC, the exclusion limits are computed using a method called CL_s [99, 100], which is a modified version of a classical frequentist method. In this method, the hypothesis tests are done using a function of the data called *test statistic*, defined in this case in terms of a likelihood function ratio, as follows:

$$\tilde{q}_\mu = \begin{cases} -2\ln\left[\frac{\mathcal{L}(\text{data}|\mu,\hat{\theta}_\mu)}{\mathcal{L}(\text{data}|0,\hat{\theta}_0)}\right] & \text{for } \hat{\mu} < 0, \\ -2\ln\left[\frac{\mathcal{L}(\text{data}|\mu,\hat{\theta}_\mu)}{\mathcal{L}(\text{data}|\hat{\mu},\hat{\theta})}\right] & \text{for } 0 \leqslant \hat{\mu} \leqslant \mu, \\ 0 & \text{for } \hat{\mu} > \mu; \end{cases} \tag{4.2}$$

where $\hat{\theta}_\mu$ refers to the values of θ that maximizes the likelihood function, given the data and a specific signal strength value μ, $\mu = 0$ in the case of $\hat{\theta}_0$. On the other hand, $\hat{\mu}$ and $\hat{\theta}$ correspond to the global maximum of the likelihood function.

Figure 4.1 shows example distributions of $\tilde{q}_{\mu=1}$; the blue line distribution corresponds to toys generated with a background-only pdf, and the red line distribution corresponds to toys generated with a signal-plus-background pdf with $\mu = 1$. As can be seen in this figure, the background-only datasets tend to have higher values of $\tilde{q}_\mu$ than the signal-plus-background datasets.

In the definition of $\tilde{q}_\mu$, on the one hand, the different definition for the cases with $\hat{\mu} < 0$ corresponds to the physics fact that the number of signal events can only be positive. On the other hand, the definition $\tilde{q}_\mu = 0$ for the cases with $\hat{\mu} > \mu$ produces a Dirac peak in the distribution of $\tilde{q}_\mu$, at $\tilde{q}_\mu = 0$; it is imposed because the objective is to set exclusion limits on signal strengths equal or larger than a given value, and not on a specific signal strength value. Without this, $\tilde{q}_\mu$ would be a variable discriminant of a specific μ value.

The signal confidence level $CL_s(\mu)$ for a given dataset and the μ value under test is computed as the ratio

$$CL_s(\mu) = \frac{p_\mu}{1 - p_b}. \tag{4.3}$$

Here, p_μ is the probability for signal-plus-background datasets to be more background-

like than the analyzed dataset,

$$p_\mu = P(\tilde{q}_\mu \geqslant \tilde{q}_\mu^{obs} | \text{ signal + background}); \tag{4.4}$$

where $\tilde{q}_\mu^{obs}$ is the "observed" value of $\tilde{q}_\mu$ (the value found for the analyzed dataset). Similarly, $(1 - p_b)$ is the probability for background-only datasets to be more background-like than the analyzed dataset,

$$1 - p_b = P(\tilde{q}_\mu \geqslant \tilde{q}_\mu^{obs} | \text{ background-only}). \tag{4.5}$$

Technically, the procedure to compute $CL_s(\mu)$ for a given μ value is:

1. Find $\tilde{q}_\mu^{obs}$.

2. Find the values of the nuisance parameters $\hat{\theta}_0^{obs}$ and $\hat{\theta}_\mu^{obs}$ that best fit the analyzed dataset when the signal strength is fixed to zero and μ, respectively.

3. Generate background-only toys with the nuisance parameters $\hat{\theta}_0^{obs}$, and signal-plus-background toys with signal strength μ and with the nuisance parameters $\hat{\theta}_\mu^{obs}$.

4. Compute for each toy the value $\tilde{q}_\mu$, as done for the real dataset, and build probability density functions $f(\tilde{q}_\mu|\mu, \hat{\theta}_\mu^{obs})$ and $f(\tilde{q}_\mu|0, \hat{\theta}_0^{obs})$ for the signal-plus-background and background-only hypothesis respectively.

5. Based on these pdf's, compute p_μ and $(1 - p_b)$, as follows

$$p_\mu = \int_{\tilde{q}_\mu^{obs}}^{\infty} f(\tilde{q}_\mu|\mu, \hat{\theta}_\mu^{obs}) d\tilde{q}_\mu, \tag{4.6}$$

$$1 - p_b = \int_{\tilde{q}_0^{obs}}^{\infty} f(\tilde{q}_\mu|0, \hat{\theta}_0^{obs}) d\tilde{q}_\mu, \tag{4.7}$$

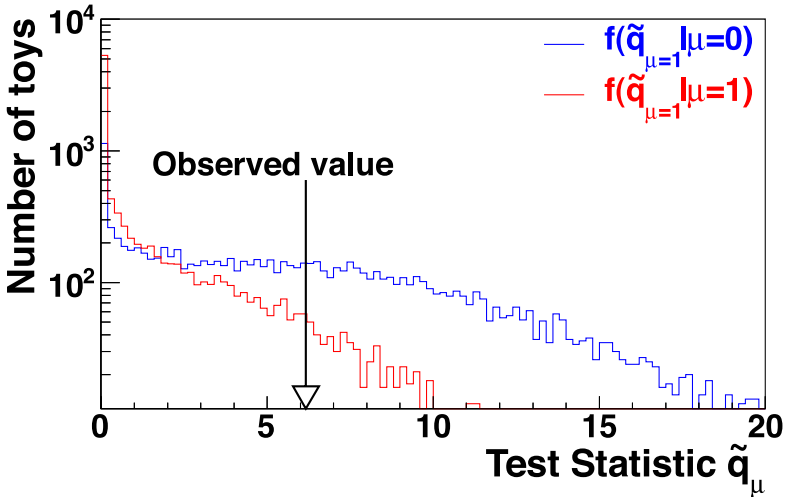

Figure 4.1: Example distributions of the $\tilde{q}_{\mu=1}$ test statistic for toy (pseudo-data) generated with a background-only pdf in blue and with a signal-plus-background pdf in red [99].

6. Finally, compute $CL_s(\mu)$ using Equation 4.3.

If the obtained value is $CL_s = \alpha$, one can state that signal strengths equal or larger than the tested value are excluded with $(1 - \alpha)$ confidence level.

Usually, this procedure is repeated for several μ values until finding $CL_s = 0.05$. The corresponding signal strength value is the one denoted as $\mu^{95\%CL_s}$. Then, it can be stated that signal strengths equal or larger than $\mu^{95\%CL_s}$ are excluded at 95% of confidence level.

The limits set using $\mathrm{CL_s}$ are more conservative than the ones obtained with other methods, for a protection against setting limits on very weak signal strengths for which there is not sensitivity; the limits in these cases can be driven by downward fluctuations of the background [99].

Expected limits

When exclusion limits are computed using a given dataset, usually, the median expected limits for the background-only hypothesis are also computed; they are used as reference values. In order to obtain these median expected limits, one has to generate background-only toys, and to find for each of them $\mu^{95\%CL_s}$ following the procedure described above. In this way a distribution of $\mu^{95\%CL_s}$ values is obtained for background-only datasets. From this distribution, one can extract the median μ value that would be excluded in 50% of equivalent experiments, and one can extract also the μ values excluded in 16%, 84%, 2.5% and 97.5% of the times. These last values correspond to the $\pm 1\sigma$ and $\pm 2\sigma$ bands for the expected limits.

Technically, it is not necessary to re-built the probability density functions $f(\tilde{q}_\mu|\mu, \hat{\theta}_\mu^{obs})$ and $f(\tilde{q}_\mu|0, \hat{\theta}_0^{obs})$ of a given signal strength for each of these toys; they can be built only once and used for the different background-only toys.

4.3 Asymptotic approximation for setting exclusion limits

The computation of exclusion limits as described above consumes significantly computing resources and time, in particular the extraction of the expected limits. In addition, during the optimization of an analysis, the expected limits are usually computed several times with alternative configurations, looking for the one that provides the best sensitivity. For this reason, an approximation, proposed in [101], is used for the computation of the limits. With this approximation, the generation and analysis of toy pseudo-experiments is not required, and thus the computing time and resources required is largely reduced.

For the analysis of a small number of events, the results from this approximation are not guaranteed to be accurate, but their validity improves as the number of events increases. For the analysis presented in this thesis, the asymptotic approximation has been used, after checking the validity of the results with toys.

Before presenting the approximation, the so-called *Asimov dataset* is explained. It is a special artificial dataset introduced in [101] that is used in the asymptotic

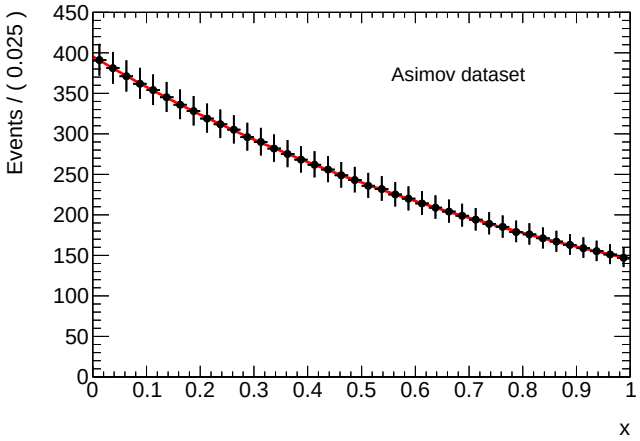

Figure 4.2: Asimov dataset. The black points correspond to an Asimov dataset with ten thousand values, built to follow the pdf shown by the red line.

approximation. Actually, the Asimov dataset is a powerful tool that has allowed a quick computation of several quantities in the $H \to \gamma\gamma$ analysis.

Asimov dataset

An Asimov dataset is one artificially built to follow perfectly a probability density function (pdf), without statistical fluctuations.

For an observable x, a range (x_0, x_f), and a pdf $f(x)$ normalized in this range, an Asimov dataset can be built in the following way. The first value x_1 in the dataset is set in such a way that the following condition is satisfied,

$$\int_{x_0}^{x_1} f(x)dx = \frac{1}{2N_{\text{evt}}}; \tag{4.8}$$

where N_{evt} is the total number of events in the dataset. Then, the following values x_i are determined using the condition

$$\int_{x_{i-1}}^{x_i} f(x)dx = \frac{1}{N_{\text{evt}}}. \tag{4.9}$$

Figure 4.2 shows as an example a histogram (black points) filled with an Asimov dataset with ten thousand values, built to follow the pdf shown by the red line.

An Asimov dataset is representative of an ensemble of toy datasets. If a pdf is fitted to an Asimov dataset to estimate a given parameter, the value that correspond to the median of the results from fitting many toys is directly obtained.

Asymptotic approximation

A test statistic alternative to the one given in Equation 4.2 is defined as

$$q_\mu = \begin{cases} -2\ln\left[\frac{\mathcal{L}(\text{data}|\mu,\hat{\theta}_\mu)}{\mathcal{L}(\text{data}|\hat{\mu},\hat{\theta})}\right] & \text{for } \hat{\mu} \leqslant \mu, \\ 0 & \text{for } \hat{\mu} > \mu, \end{cases} \tag{4.10}$$

without the special treatment for the cases with $\hat{\mu} < 0$.

The distributions of q_μ, apart of the Dirac peak at $q_\mu = 0$, are expected to follow a χ^2 distribution for one degree of freedom, for Wilks' theorem [102]. This allows various simplifications at the moment of computing exclusion limits. For example, for signal-plus-background datasets generated with signal strength hypothesis μ, the q_μ distribution approaches to the pdf

$$f(q_\mu|\mu) = \frac{1}{2}\delta(q_\mu) + \frac{1}{2}\frac{1}{\sqrt{2\pi}}\frac{1}{\sqrt{q_\mu}}\exp\left(-\frac{q_\mu}{2}\right) \qquad \text{with } q_\mu \geqslant 0. \tag{4.11}$$

On the other hand, the distributions of $\tilde{q}_\mu$ are more complex. In this case, the equivalent of Equation 4.11 has been shown in [101] to be

$$f(\tilde{q}_\mu|\mu) = \frac{1}{2}\delta(\tilde{q}_\mu) + \begin{cases} \frac{1}{2}\frac{1}{\sqrt{2\pi}}\frac{1}{\sqrt{\tilde{q}_\mu}}\exp\left(-\frac{\tilde{q}_\mu}{2}\right) & \text{for } 0 \leqslant \tilde{q}_\mu \leqslant \frac{\mu^2}{\sigma^2}, \\ \frac{1}{\sqrt{2\pi}(2\mu/\sigma)}\exp\left[-\frac{1}{2}\frac{(\tilde{q}_\mu+\mu^2/\sigma^2)^2}{(2\mu/\sigma)^2}\right] & \text{for } \tilde{q}_\mu > \frac{\mu^2}{\sigma^2}; \end{cases} \tag{4.12}$$

where σ is the standard deviation of $\hat{\mu}$, in this case for signal-plus-background datasets, and it is a characteristic parameter of the distribution.

Nevertheless, in the asymptotic limit, the test statistics $\tilde{q}_\mu$ and q_μ have been found to provide the same results for the exclusion upper limits [101]. For this reason, in order to take advantage of the simplifications of q_μ, it is often used.

The cumulative probability function for the pdf $f(q_\mu|\mu)$ (Equation 4.11) is [101]

$$F(q_\mu|\mu) = \Phi\left(\sqrt{q_\mu}\right) \qquad \text{with } q_\mu > 0, \tag{4.13}$$

and similarly, for background-only datasets the cumulative probability function is found to be:

$$F(q_\mu|0) = \Phi\left(\sqrt{q_\mu} - \frac{\mu}{\sigma}\right) \qquad \text{with } q_\mu > 0; \tag{4.14}$$

where Φ is the cumulative function for the normal Gaussian:

$$\Phi(x) = \frac{1}{2}\left[1 + \text{erf}\left(\frac{x}{\sqrt{2}}\right)\right] \tag{4.15}$$

As explained in [101], the standard deviation σ of $\hat{\mu}$, for background-only datasets, can be obtained computing q_μ for a background-only Asimov dataset (the resulting q_μ is denoted as $q_{\mu,A}$), using the relation

$$\sigma^2 = \frac{\mu^2}{q_{\mu,A}}; \tag{4.16}$$

Then, from Equations 4.14 and 4.16, CL_s is obtained

$$CL_s = \frac{1 - \Phi(\sqrt{q_\mu})}{\Phi(\sqrt{q_{\mu,A}} - \sqrt{q_\mu})}. \tag{4.17}$$

In order to compute the median expected limit μ_{up}^{med} for the background-only hypothesis, with $(1-\alpha)$ confidence level, one needs to consider the median expected

q_μ value for this hypothesis, which is $q_{\mu,A}$. It yields

$$\mu_{\rm up}^{\rm med} = \sigma\Phi^{-1}(1-0.5\alpha) \tag{4.18}$$

Similarly, one can find a general expression for the μ values corresponding to the $N\sigma$ error bands [99]:

$$\mu_{up}^{med+N\sigma} = \sigma\{\Phi^{-1}[1-\alpha\Phi(N)]+N\} \tag{4.19}$$

4.4 Testing the background-only hypothesis

This chapter explains how to quantify the importance of an excess, in order to make statements about its compatibility with statistical fluctuations of the background. Here, the importance of an excess is quantified based on the probability that the background fluctuates creating a signal-like excess equal or larger than what is observed. This probability (p-value) is usually denoted as p_0.

p_0 is computed using a test statistic defined as follows:

$$q_0 = \begin{cases} 0 & \text{for } \hat{\mu} < 0, \\ -2\ln\left[\frac{\mathcal{L}(\text{data}|0,\hat{\theta}_0)}{\mathcal{L}(\text{data}|\hat{\mu},\hat{\theta})}\right] & \text{for } \hat{\mu} \geqslant 0, \end{cases} \tag{4.20}$$

The more important is an excess, the larger is the difference between the two likelihoods considered in this equation and the larger is the corresponding q_0 value. (For a given dataset, $\mathcal{L}(\text{data}|\hat{\mu},\hat{\theta})$ is always larger or equal than $\mathcal{L}(\text{data}|0,\hat{\theta}_0)$.)

Again, the different treatment for the cases with $\hat{\mu} < 0$ is associated with the physical fact that the number of signal events can only be positive. In this case, it produces a Dirac peak in the distribution of q_0, at $q_0 = 0$; it represents the 50% of the times that background-only datasets have downward fluctuations. Figure 4.3 shows the q_0 distribution for background-only toys.

The background-only toys are generated following frequentist conventions, using the nuisance parameter values $\hat{\theta}_0^{obs}$ and event counts following Poisson probabilities. From this toys distribution a probability density function $f(q_0|0,\hat{\theta}_0^{obs})$ is built.

The probability p_0 corresponding to a given experimental observation q_0^{obs} is evaluated as follows:

$$p_0 = P(q_0 \geqslant q_0^{obs}|\text{background-only}) = \int_{q_0^{obs}}^{\infty} f(q_0|0,\hat{\theta}_0^{obs})dq_0 \tag{4.21}$$

Usually, the p_0 values are translated to a scale of *significance* (Z), or number of standard deviations. It is done by using the inverse of the cumulative function for the normal Gaussian Φ [101],

$$Z = \Phi^{-1}(1-p_0) \tag{4.22}$$

For example, in the background-only hypothesis, the probability to have an excess with 5σ significance ($Z = 5$) is $p_0 = 3\cdot 10^{-7}$; 5σ is conventionally the significance required for claiming the observation of a new particle.

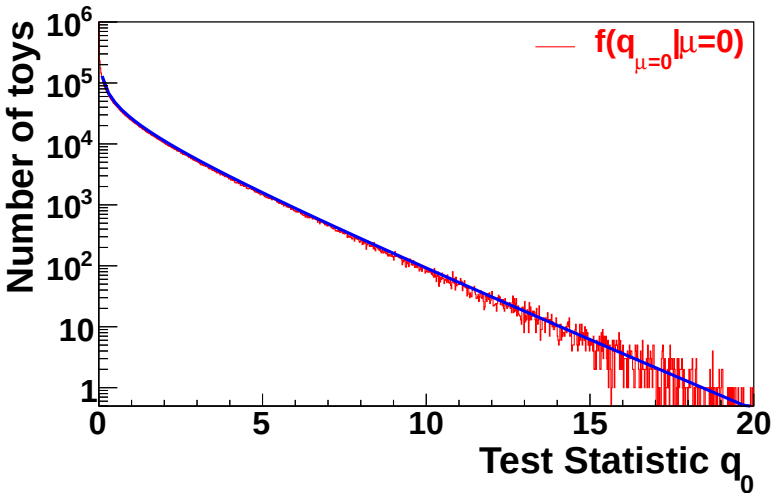

Figure 4.3: Distribution of the q_0 test statistic for background-only toys [99].

Going back to the q_0 test statistic definition, actually the definition for the cases with $\hat{\mu} < 0$ has been modified in the latest version of the statistical recommendations to be used at the LHC. Now q_0 is defined as:

$$q_0 = \begin{cases} +2\ln\left[\frac{\mathcal{L}(\text{data}|0,\hat{\theta}_0)}{\mathcal{L}(\text{data}|\hat{\mu},\hat{\theta})}\right] & \text{for } \hat{\mu} < 0, \\ -2\ln\left[\frac{\mathcal{L}(\text{data}|0,\hat{\theta}_0)}{\mathcal{L}(\text{data}|\hat{\mu},\hat{\theta})}\right] & \text{for } \hat{\mu} \geqslant 0, \end{cases} \tag{4.23}$$

The only reason for doing this is verifying the sanity of the analysis allowing also the quantification of negative fluctuations: in the background-only hypothesis positive and negative fluctuations should be equal, on the average. The p_0 values computed using the definition in Equation 4.20 are called *capped* p_0, and they are always below 0.5; while the ones computed with this last definition are called *un-capped* p_0 and they can go above 0.5.

Asymptotic approximation for quantifying an excess

In the asymptotic limit, the distribution of q_0 for background-only datasets follows a χ^2 distribution for one degree of freedom, for Wilks' theorem [102]. It is illustrated in Figure 4.3, where the solid line corresponds to the χ^2 distribution for one degree of freedom. Then, the probability p_0 can be directly calculated from q_0 as [101]

$$p_0 = 1 - \Phi(\sqrt{q_0}), \tag{4.24}$$

as well as the significance

$$Z = \sqrt{q_0}. \tag{4.25}$$

Which largely reduces the computing time and resources required.

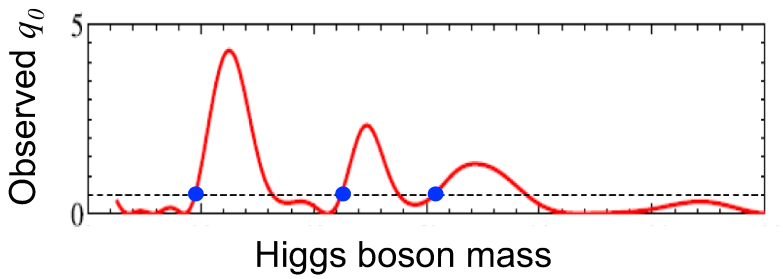

Figure 4.4: For a scan of mass region, N_u is defined as the number of times that the observed q_0 as function of m_{H} up-cross a given q_0 value threshold u. The up-crossing points are indicated by the blue dots. [99].

Look-elsewhere effect

In the Higgs boson search, various Higgs boson mass hypotheses (m_{H}) are tested, not only one, and therefore various excesses in different regions of the hypothesis discriminant distribution are quantified; for example in the $H \to \gamma\gamma$ analysis, a scan is performed over a given region of the diphoton invariant mass $m_{\gamma\gamma}$ distribution. The p_0 value is the probability of the background to fluctuate creating a signal-like excess equal or larger than what is observed, *when a single test is performed*, or for a single mass point.

When several tests at different mass points are performed, for the largest excess (i.e. the one with highest significance) observed anywhere in the scanned mass region, the probability to be equal or larger on significance than the one observed in the analyzed data-sample is higher than p_0. For this reason, p_0 is better referred as *local* p_0 and the associated significance as *local significance*.

The *global test statistic* to be associated with the search in some broad mass range can be written as follows:

$$q_0(\hat{m}_{\mathrm{H}}) = \max_{m_{\mathrm{H}}}[q_0(m_{\mathrm{H}})]. \tag{4.26}$$

Then, a *global* p_0 and a *global significance* could be extracted by building a pdf for $f(q_0(\hat{m}_{\mathrm{H}})|0, \hat{\theta}_0^{obs})$ using toys. The ratio of global and local p-values is usually referred to as *trial factor*.

Nevertheless, in the asymptotic regime and for very small p_0 values, this effect can be evaluated with a less computing demanding procedure proposed in [103]. In this reference, it is shown that the global p_0 value can be written as follows:

$$p_0^{\mathrm{global}} = P[q_0(\hat{m}_{\mathrm{H}}) > u|\text{background-only}] \leqslant \langle N_u \rangle + \frac{1}{2} P_{\chi_1^2}(u). \tag{4.27}$$

For a mass region scan, N_u is defined as the number of times that the observed q_0 as function of m_{H} up-cross a given q_0 value threshold u, as illustrated in Figure 4.4; in this figure the up-crossing points are indicated by the blue dots. Here, $P_{\chi_1^2}$ is the survival function of χ^2 for one degree of freedom.

It is also shown that the average number of up-crossings at two levels u and u_0

are related by the following formula [103]

$$\langle N_u \rangle = \langle N_{u_0} \rangle e^{-\frac{(u-u_0)}{2}}. \tag{4.28}$$

Thus, $\langle N_u \rangle$ for a large value of u, at which the p_0^{global} value need to be computed, can be obtained by estimating $\langle N_{u_0} \rangle$ for a lower threshold u_0; and $\langle N_{u_0} \rangle$ can be estimated with a relatively small number of toys.

4.5 Systematic uncertainties

In order to consider a systematic uncertainty on a parameter of a pdf used in the likelihood function, an additional nuisance parameter θ_i is introduced, constraining it by a probability density function $\rho(\theta_i)$ defined by the concerned uncertainty.

For example, lets consider the parameter corresponding to the expected number of signal events S in the likelihood function (see Equation 4.1). This parameter is fixed to its estimated value during the likelihood function maximizations (i.e. during the fits). In order to consider the relative uncertainty σ_S on the estimated value of S, a scale factor parameter θ_S is introduced for S. But, this scale factor is constrained introducing in the likelihood function for instance a gaussian pdf $\rho_S(\theta_S)$, with a width defined by the σ_S, as follow:

$$\rho_S(\theta_S) = \frac{1}{\sqrt{2\pi}\sigma_S} \exp\left[-\frac{(\theta_S - 1)^2}{2{\sigma_S}^2}\right]. \tag{4.29}$$

In this case the likelihood function would be defined as:

$$\mathcal{L}(\text{data}|\mu, \theta) = k^{-1} \prod_i \left[\mu\theta_S S f_s(x_i) + B f_b(x_i)\right] e^{-(\mu S + B)} \rho_S(\theta_S); \tag{4.30}$$

In the generation of toys, the value of a nuisance parameter associated with an uncertainty is taken randomly for each toy according to the constraint pdf $\rho(\theta_i)$.

For two observables with 100% correlated uncertainties, a single nuisance parameter is introduced to scale the corresponding observable parameter.

Actually, the Gaussian pdf is not suitable for positively defined observables like the expected number of signal events. In cases like this one, the recommendation is to use a log-normal pdf as constraint. The log-normal pdf is defined as:

$$\rho(\theta) = \frac{1}{\sqrt{2\pi}\ln(\kappa)} \exp\left[-\frac{\ln^2(\theta)}{2\ln^2(\kappa)}\right] \frac{1}{\theta}. \tag{4.31}$$

The width of the log-normal pdf is characterized by κ. $\kappa = 1.10$ implies that the observable can be larger or smaller by a factor 1.10.

Chapter 5

The $H \to \gamma\gamma$ analysis

5.1 Introduction

The $H \to \gamma\gamma$ channel is one the most promising modes to search the Standard Model (SM) Higgs boson at low mass, at the Large Hadron Collider (LHC). It is the channel with the highest sensitivity in the mass range below 125 GeV, down to the exclusion limit set by the LEP experiments at 114 GeV. In the analysis presented here, the Higgs boson search is performed from 110 GeV to 150 GeV.

The photons expected from the Higgs boson decay are very well reconstructed in ATLAS, as shown in Chapter 3. Both, the direction and energy of these particles are very well measured. Then, the distribution of invariant mass for diphotons from the $H \to \gamma\gamma$ process is expected to be a narrow peak, with about 3.8 GeV of full width at half maximum (FWHM). Nevertheless, this peak is expected to appear on top of a quite large amount of background, whose statistical fluctuations difficult the peak observation.

The processes contributing to the background in the $H \to \gamma\gamma$ search are: the QCD diphoton production ($\gamma\gamma$ background), the associated production of a photon with jets (γj background), the processes with several jets in the final state (jj background) and the Drell-Yan processes. The second and third processes in this list contribute to the background when one or two jets fragmenting into neutral mesons (mainly π^0) are misidentified as photons. The Drell-Yan background is due to the misidentification of electrons as photons, mostly as converted photons. The $\gamma\gamma$ background is usually referred as *irreducible*, while the rest of the background components together are called *reducible*. The $\gamma\gamma$ and γj components constitute most of the background.

The statistical procedure used to quantify the probability of having a signal in the analyzed data sample has been discussed in Chapter 4.

A set of event categories have been defined in order to increase the sensitivity to observe a signal. The diphoton candidate events are classified in these categories according to either kinematic or experimental criteria, making event sub-samples with different signal-to-background ratio.

This analysis started to be developed about 20 years ago [104]; it has been used as a benchmark during the design of the ATLAS electromagnetic calorimeter. Several documents reported estimations of the sensitivity to observe the Higgs boson based on Monte Carlo (MC) simulations; among these documents there are [9, 90, 105].

After the LHC started operating, several publications have been done reporting the results of analyzing the increasing collected data [13–21, 106]. As well, various students have made PhD theses on this subject; among these theses, some of them made recently in French laboratories are [107–110]. Since the time of MC based studies, different strategies of analysis have been evaluated, and since the first data results presented two years ago, the analysis has evolved improving its sensitivity. What is described here corresponds to the analysis performed between spring and summer 2012; these are the results published in [106], which are basically the same results presented at CERN on the 4th of July seminar and at the ICHEP 2012 conference [20], except for some minor modifications.

As you will see in details in the last section of this chapter, an excess of events has been observed in the diphoton invariant mass distribution at 126.5 GeV. For this reason, this mass value is used as reference point in several tables and figures quoting the signal expectations in this document.

5.2 Samples

5.2.1 Data samples

Two data samples have been used for this analysis. The first sample correspond to the data taken by ATLAS in 2011 during the proton-proton collisions at $\sqrt{s} = 7$ TeV. The second sample correspond to the data taken in the first half of 2012, until June 18th, at $\sqrt{s} = 8$ TeV collisions.

During these two data taking periods the instantaneous luminosity has varied from about 10^{32} cm^{-2}s^{-1} to 6.8×10^{33} cm^{-2}s^{-1}. Figure 5.1 shows the distribution of the mean number of interactions per bunch crossing for each period. On average, the mean number of interactions per bunch crossing is about twice larger for the 8 TeV sample than for the 7 TeV sample. The bunch-to-bunch time spacing has been kept to be 50 ns in both years.

The data are required to satisfy quality criteria based on the good functioning of the calorimeters, the inner detector and the trigger system, and the beam quality. These requirements are applied to small sets of data corresponding to short data taking periods, of about one minute. After these data-quality conditions, the integrated luminosity on the 7 TeV sample is estimated to be 4.8 fb^{-1}, with a relative uncertainty of 1.8% [112]. For the 8 TeV sample, the integrated luminosity is estimated to be 5.9 fb^{-1}, with a relative uncertainty of 3.6%. Details on how the luminosity is calculated can be found in [111,112]; the uncertainties on the estimated luminosities are different because different methods have been used.

5.2.2 Monte Carlo samples

Signal samples

For the $H \to \gamma\gamma$ signal studies, Monte Carlo (MC) samples produced with a complete simulation of the ATLAS detector are used. Two set of samples have been produced, one at $\sqrt{s} = 7$ TeV and another at $\sqrt{s} = 8$ TeV; they have been produced for several Higgs boson mass hypotheses from 100 to 150 GeV, every 5 GeV, and separately

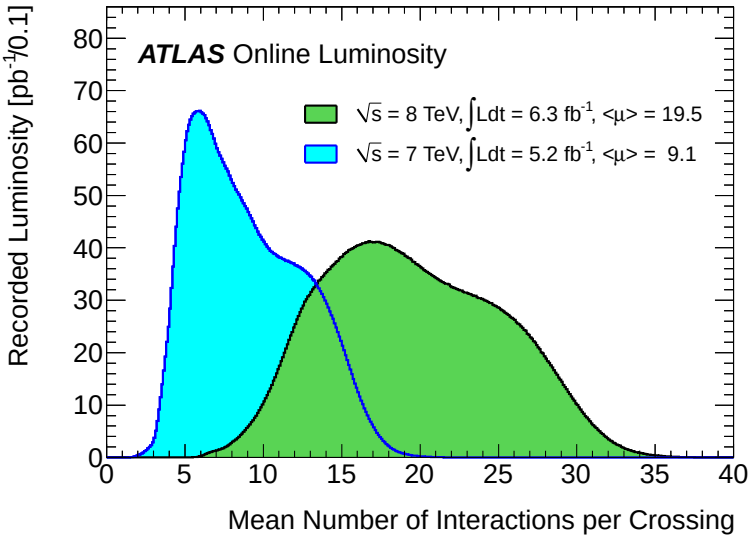

Figure 5.1: Luminosity-weighted distribution of the mean number of interactions per bunch crossing for the 2011 and 2012 data [71]. This shows the full 2011 run and 2012 data taken between April 4th and June 18th. The integrated luminosities recorded by ATLAS and the mean mu values are given in the figure. Details about how the mean number of interactions per crossing is calculated can be found in [71, 111].

for the five Higgs boson production modes at the LHC: gluon fusion, vector boson fusion, and the associated production modes with the W and Z vector bosons and with top quarks. For the leading production mode represented by the gluon fusion, about hundred thousand events have been generated per sample, and for the other modes about thirty thousand events, corresponding to integrated luminosities of more than hundred times the one in the data samples.

The MC samples corresponding to the Higgs boson production via gluon fusion and vector boson fusion have been generated at next-to-leading order (NLO) with POWHEG [113, 114], interfaced with PYTHIA [83, 84] for the showering and hadronization processes. The samples for the associated production modes have been generated with PYTHIA. Whenever PYTHIA is used, the version PYTHIA6 [83] is used for the $\sqrt{s} = 7$ TeV samples, and PYTHIA8 [84] for the $\sqrt{s} = 8$ TeV.

The samples have been normalized according to the production cross-sections from high order calculations, quoted in Chapter 1, Section 1.3.

For the gluon fusion samples at $\sqrt{s} = 7$ TeV, event weights are applied to match the Higgs boson transverse momentum distribution obtained from high order calculations [38]. While for the 8 TeV sample, it was taken into account directly during the sample generation with POWHEG.

Event weights are also assigned in the gluon fusion samples to correct for the destructive interference between the $gg \to \gamma\gamma$ and $gg \to H \to \gamma\gamma$ processes [115]. These corrections range between -2% and -5%, depending on the diphoton invariant mass.

Background samples

Some background Monte Carlo samples with complete simulation of the ATLAS detector have been used for cross-checks, but not for extracting information that affects the final results. Prompt diphoton $\gamma\gamma$ samples have been generated with

SHERPA [116], and samples of the associated production of prompt photons with jets γj have been generated with ALPGEN [117].

In order to test the parametrization used for the background diphoton mass distribution, three generator level MC samples have been used; these samples have been used only for an estimation of the systematic uncertainties assigned to the parametrization. For these samples, a very high number of events have been generated, so that the statistical fluctuations are negligible. The $\gamma\gamma$ component of the background, which is the main component, has been produced with three MC generators with high order calculations, RESBOS [118], DIPHOX [119], and SHERPA [116]; while a common sample of the reducible background has been used for the three samples. The name of the generator used for the $\gamma\gamma$ component is used to refer to each of the three MC samples below. The γj and jj components have been generated with SHERPA and PYTHIA6 [83] respectively. The Drell-Yan component has been added following the shape extracted from the data, from the reconstructed $Z \to ee$ peak. The different background components have been combined according to the data-driven estimated fractional composition of the data sample, reported in Section 5.4, and each full composite MC sample has been normalized to the number of events found in the data sample.

Since a very large number of events is required to avoid statistical fluctuations, the MC generation level output has been used without full simulation of the detector, but detector effects that may affect the mass distribution have been taken into account:

- The photon identification efficiency as a function of the photon transverse momentum has been introduced through event weights.
- In the preparation of the PYTHIA and SHERPA samples, the photon energy has been smeared to take into account the detector resolution, and for each photon a conversion status has been assigned randomly, according to the expected conversion fractions for the different detector regions.
- In the case of the γj and jj samples, event weights have been assigned to take into account the jet rejection as a function of the jet transverse momentum.

5.2.3 Diphoton event selection

An explanation of the photon reconstruction and the requirements applied in the photon selection used for this analysis have been given in Chapter 3.

The selection of diphoton events starts at the trigger level. For the 7 TeV collisions, at the first trigger level, events were required to have at least two electromagnetic clusters with transverse energy $E_{\mathrm{T}} > 12$ GeV or $E_{\mathrm{T}} > 14$ GeV, according to the data-taking period. Additionally, at the higher trigger levels, events were required to have at least two photons satisfying the *loose* identification criteria and with $E_{\mathrm{T}} > 20$ GeV.

For the 8 TeV collisions, a similar trigger selection is used, but the transverse energy thresholds were increased. It was done to reduce the event rate at the high luminosity conditions during 2012. At the first trigger level, the electromagnetic cluster leading on transverse energy is required to have at least 16 GeV, and the

sub-leading one at least 12 GeV. At the higher levels, the leading and sub-leading photon E_{T} thresholds are 35 and 25 GeV respectively.

For the offline selection, events are required to have at least two reconstructed photons, with each photon satisfying the following requirements:

- $|\eta| < 1.37$ or $1.52 < |\eta| < 2.37$. The excluded regions $1.37 < |\eta| < 1.52$ correspond to the transition between the barrel and the end-caps of the electromagnetic calorimeter.
- Object quality criteria. The photon candidates reconstructed in problematic regions of the detector are not considered.
- Calorimeter-based identification (ID) criteria. The neural-network based selection is used for the 7 TeV sample, while the cut-based *tight* criteria are used for the 8 TeV sample.
- The isolation transverse energy is required to be $E_{\mathrm{T}}^{\mathrm{isol}} < 4$ GeV.
- The photon leading on transverse energy is required to have $E_{\mathrm{T}}^{\gamma 1} > 40$ GeV, and the sub-leading one $E_{\mathrm{T}}^{\gamma 2} > 30$ GeV.

The different thresholds used in this selection, on the photon transverse energy, for the photon identification and for the isolation criterion, have been optimized to provide the best compromise between sensitivity and robustness of the analysis. Details about how the analysis sensitivity is evaluated have been given in Chapter 4.

The use of the neural-network for the photon ID requires a detailed study of the distributions used as input. The different pileup conditions in 2012 make necessary an update of previous studies with the recent 8 TeV sample. It is currently in progress, and that is why for the moment the simpler cut-based selection has been used for the 8 TeV sample.

Then, the diphoton invariant mass $m_{\gamma\gamma}$ is computed as described in Section 5.2.5, and only events with $m_{\gamma\gamma}$ between 100 and 160 GeV are considered for the analysis. After the whole event selection, 23788 diphoton candidates have been found in the 7 TeV sample in this mass range, whereas 35251 candidates were selected in the 8 TeV sample.

Figures 5.2, 5.3, 5.4 and 5.5 display four of the selected diphoton candidate events. The green region represents the electromagnetic calorimeter, and the energy deposited by the photons is represented by yellow clusters in this region. In the first event, Figure 5.2, one of the photons have been reconstructed as a converted photon. The panel on the middle right side shows a close-up view of this photon, where the electron-positron pair tracks are visible. In the event shown in Figure 5.3, the detector looks quite busy because of the multiple interaction pileup. Figures 5.4 and 5.5 show events where jets have been also reconstructed, and in the event on Figure 5.4 the diphoton-system has high transverse momentum. These are features that are used to classify the events into different categories in order to increase the sensitivity for the observation of a signal; it is discussed in details in Section 5.5.

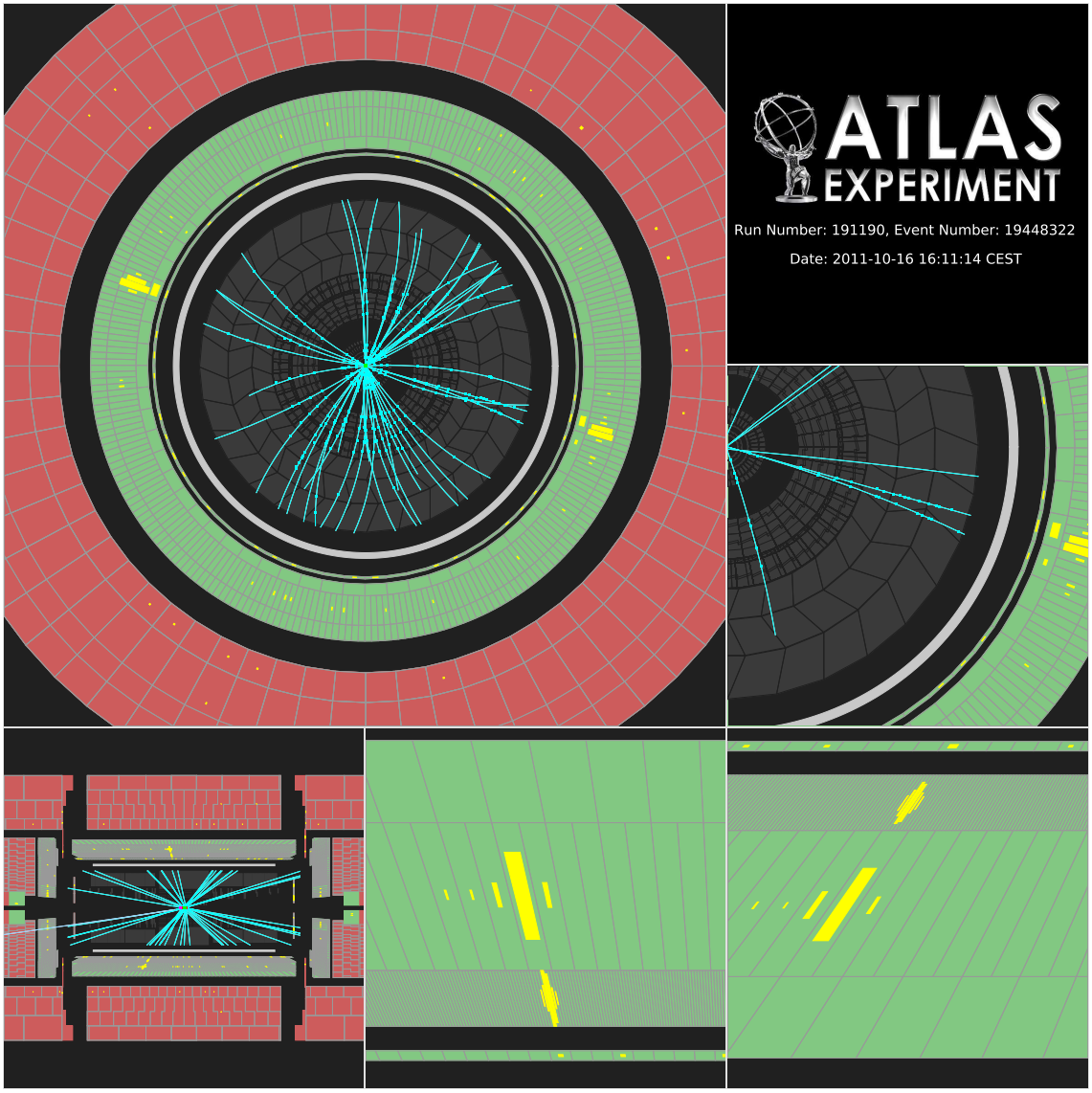

Figure 5.2: Diphoton candidate event from the $\sqrt{s} = 7$ TeV collisions. The sub-leading photon has been reconstructed as a converted photon. The green region represents the electromagnetic calorimeter, and the two yellow clusters in that region correspond to the energy deposited by the photons. The panel on the middle right side shows a close-up view of the converted photon, where the electron-positron pair tracks are visible. The conversion radius is estimated to be 8.1 cm. Here are the values for some important parameters of this photon pair: $E_{\mathrm{T}}^{\gamma 1} = 66.8$ GeV, $\eta^{\gamma 1} = -0.27$, $E_{\mathrm{T}}^{\gamma 2} = 56.9$ GeV, $\eta^{\gamma 2} = -0.67$, $m_{\gamma\gamma} = 125.8$ GeV, $p_{\mathrm{T}}^{\gamma\gamma} = 10.4$ GeV and $p_{\mathrm{Tt}} = 3.1$ GeV (p_{Tt} is defined in Section 5.5.2). Only tracks with transverse momentum above one GeV and with hits in all the tracking sub-sections, satisfying some quality requirements, are shown.

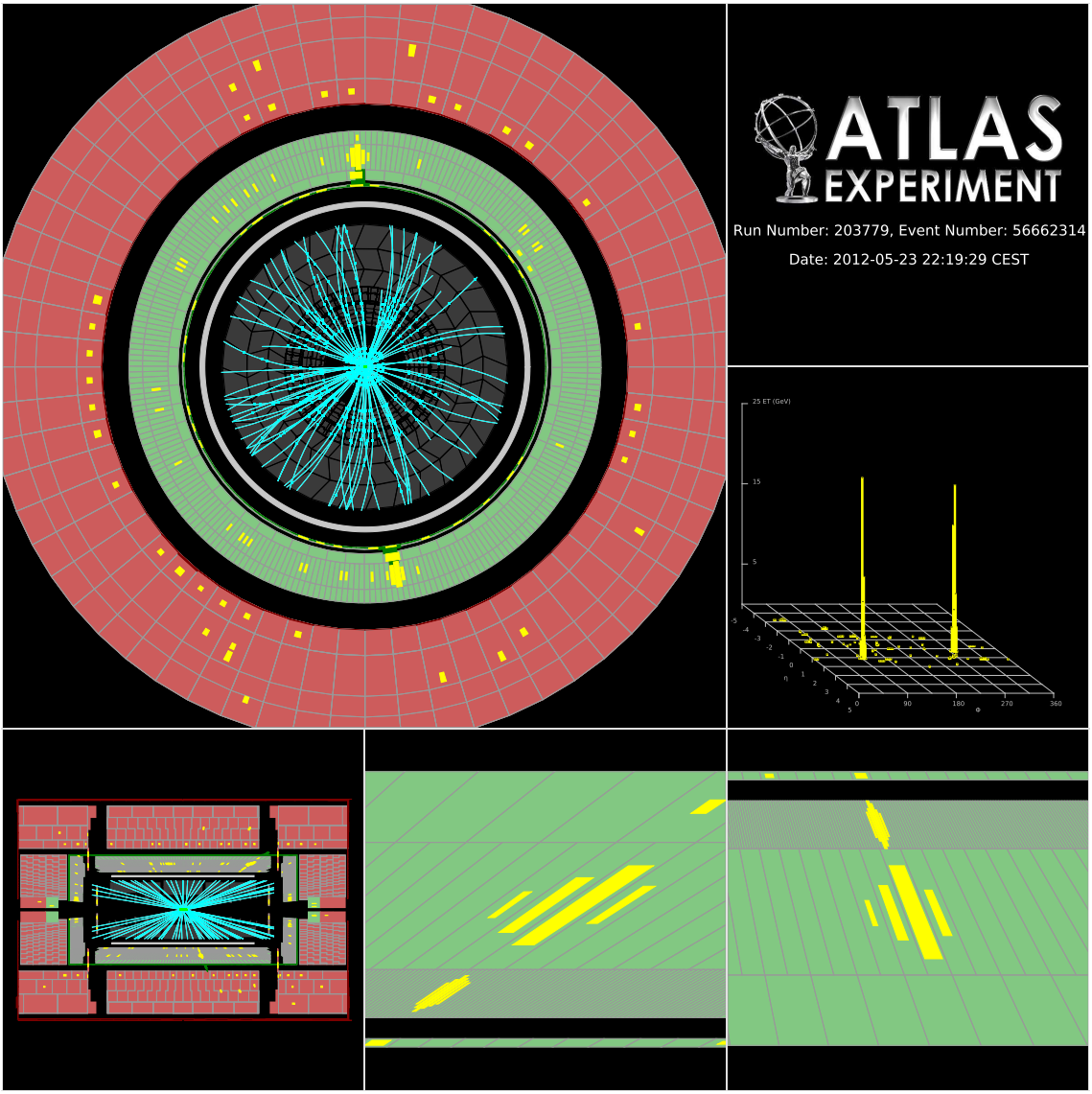

Figure 5.3: Diphoton candidate event from the $\sqrt{s} = 8$ TeV collisions. In this event, the detector looks quite busy because of the multiple interaction pileup. The green region represents the electromagnetic calorimeter, and the two yellow clusters in that region correspond to the energy deposited by the photons. Here are the values for some important parameters of this photon pair: $E_{\mathrm{T}}^{\gamma 1} = 62.2$ GeV, $\eta^{\gamma 1} = 0.39$, $E_{\mathrm{T}}^{\gamma 2} = 55.5$ GeV, $\eta^{\gamma 2} = 1.18$, $m_{\gamma\gamma} = 126.9$ GeV, $p_{\mathrm{T}}^{\gamma\gamma} = 9.3$ GeV and $p_{\mathrm{Tt}} = 6.5$ GeV (p_{Tt} is defined in Section 5.5.2). Only tracks with transverse momentum above one GeV and with hits in all the tracking sub-sections, satisfying some quality requirements, are shown.

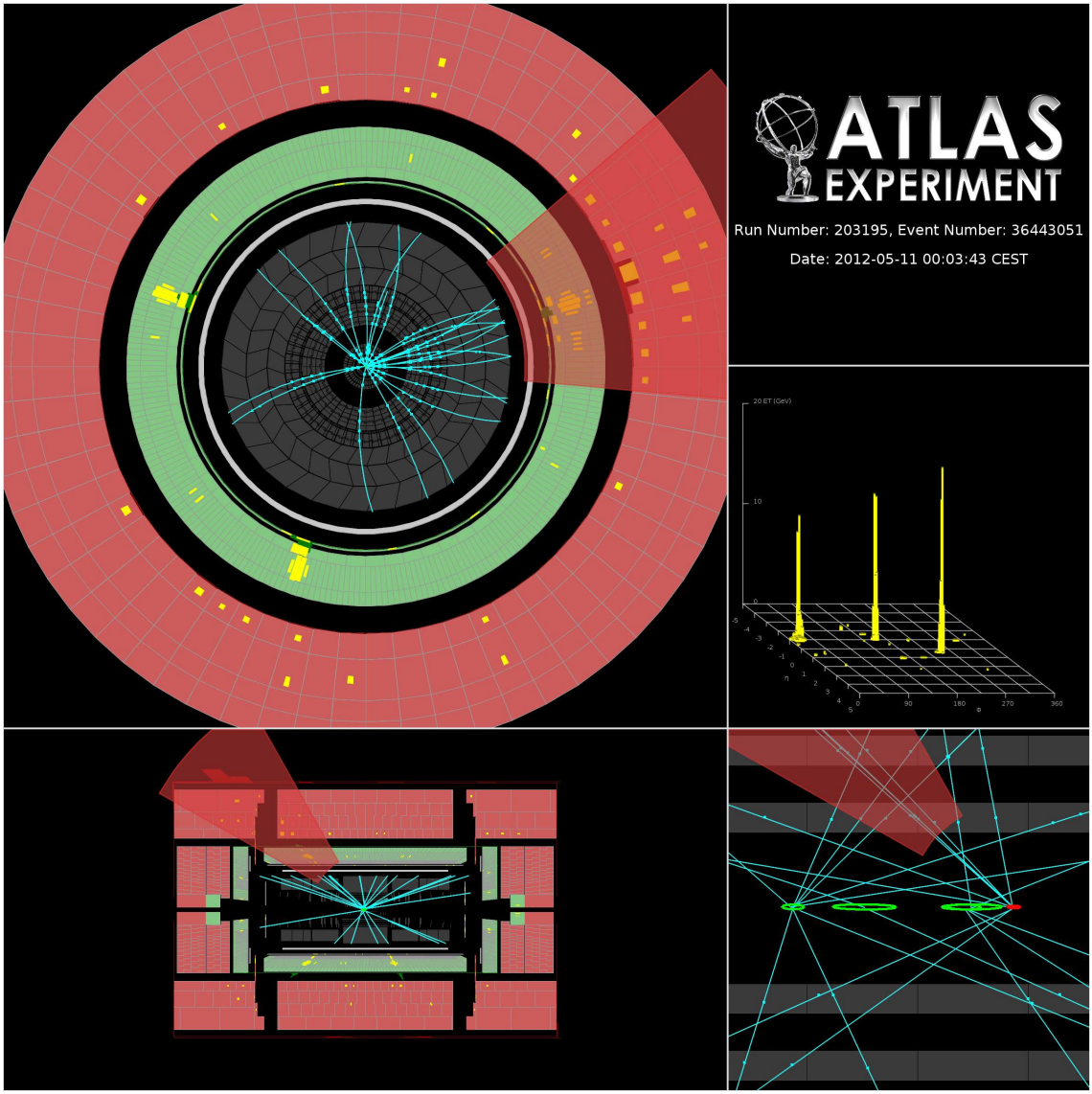

Figure 5.4: Diphoton candidate event from the $\sqrt{s} = 8$ TeV collisions. In this event, the diphoton-system have high transverse momentum, and one jet has been also reconstructed. The green region represents the electromagnetic calorimeter, and the two yellow clusters on the left side in that region correspond to the energy deposited by the photons. The jet is indicated by the red transparent semi-circle. Here are the values for some important parameters of this photon pair: $E_{\mathrm{T}}^{\gamma 1} = 63.0$ GeV, $\eta^{\gamma 1} = 0.50$, $E_{\mathrm{T}}^{\gamma 2} = 56.1$ GeV, $\eta^{\gamma 2} = -0.96$, $m_{\gamma\gamma} = 127.0$ GeV, $p_{\mathrm{T}}^{\gamma\gamma} = 83.9$ GeV and $p_{\mathrm{Tt}} = 83.3$ GeV (p_{Tt} is defined in Section 5.5.2). The jet has $E_{\mathrm{T}}^{j} = 113$ GeV and $\eta^{j} = -0.9$. Only tracks with transverse momentum above one GeV and with hits in all the tracking sub-sections, satisfying some quality requirements, are shown.

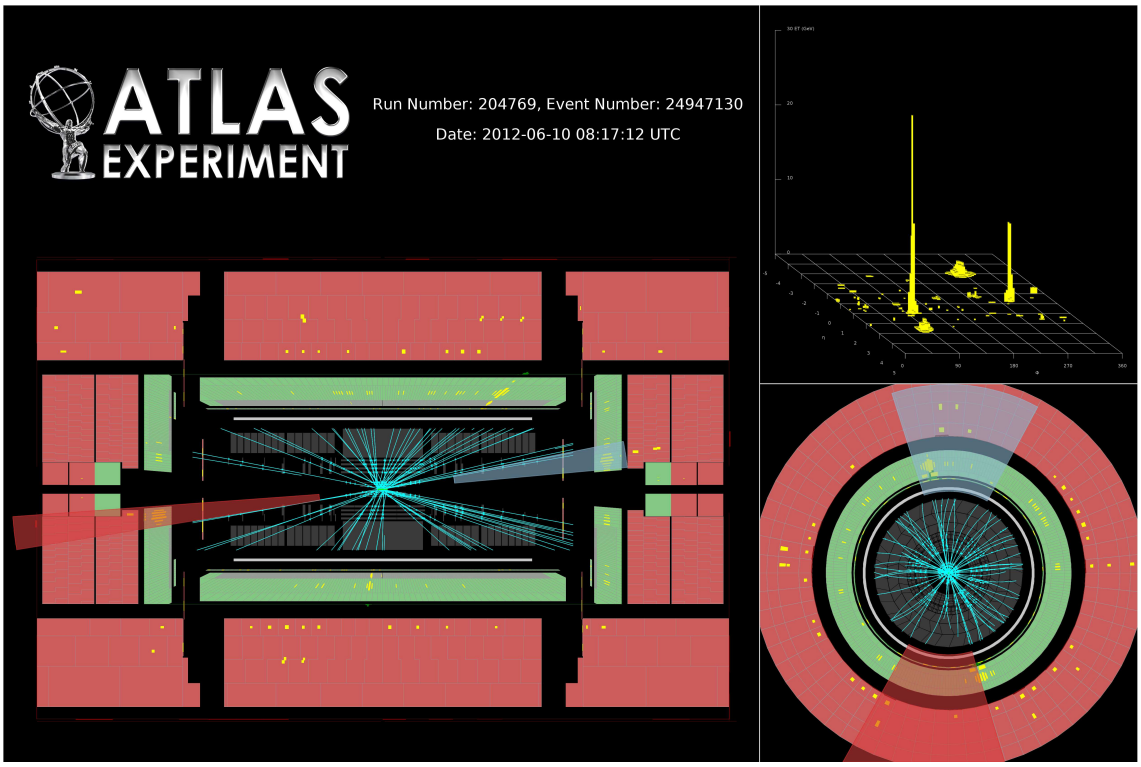

Figure 5.5: Diphoton candidate event from the $\sqrt{s} = 8$ TeV collisions. In this event, two jets have been reconstructed in the forward region, like what is expected for a typical Higgs boson event in the vector-boson fusion (VBF) production mode (the experimental signature of the Higgs boson VBF events is discussed in Section 5.5.3). The jets are indicated by the transparent semi-circles, in red and gray color. Here are the values for some important parameters of this photon pair: $E_{\mathrm{T}}^{\gamma 1} = 80.1$ GeV, $\eta^{\gamma 1} = 1.01$, $E_{\mathrm{T}}^{\gamma 2} = 36.2$ GeV, $\eta^{\gamma 2} = -0.17$, $m_{\gamma\gamma} = 126.9$ GeV, $p_{\mathrm{T}}^{\gamma\gamma} = 44.3$ GeV and $p_{\mathrm{Tt}} = 6.2$ GeV (p_{Tt} is defined in Section 5.5.2). And here are the values for some parameters corresponding to the jets: $E_{\mathrm{T}}^{j1} = 120$ GeV, $\eta^{j1} = -2.9$, $E_{\mathrm{T}}^{j2} = 81$ GeV, $\eta^{j2} = 2.7$ and $m_{jj} = 1.6$ TeV. The difference $\Delta\phi$ between the diphoton system and the two-jets system is 2.9. Only tracks with transverse momentum above one GeV and with hits in all the tracking sub-sections, satisfying some quality requirements, are shown.

5.2.4 Selection of the primary vertex

While in an event with prompt leptons the lepton tracks point explicitly to its corresponding primary vertex (PV), in a diphoton event, since there is no always track associated to the photons, it is not obvious which of the multiple reconstructed primary vertices corresponds to the photon pair. The PV identification is relevant for two aspects of the analysis: for a precise estimation of the photon pseudorapidity η which is an input for the diphoton invariant mass computation, and for a selection of jets associated to the diphoton system.

The η measurement given by the photon cluster barycenter in the calorimeter would correspond to the photon direction of flight if the photon were originated at the geometrical center of the detector. Nevertheless, the position of the proton-proton interactions in ATLAS in the longitudinal z-axis is dispersed with a RMS of about 50 mm, which imply an imprecision on the measured η direction of photons; in fact, the resolution on the photon pseudorapidity η is dominated by the determination of the PV z-position.

A selection of diphoton events with jets is done to separate signal candidates from production modes generating jets in the final state. The selection of these events is presented in Section 5.5.3. In order to avoid considering jets from pileup events, the jet selection includes a requirement based on the tracks associated to both the jet under study and the selected primary vertex. The identification of the primary vertex is also relevant if a tracking isolation criterion is used in the photon selection, to consider only tracks from the selected PV to avoid pileup effects, as is now done in the ATLAS $H \to \gamma\gamma$ analysis [21].

An estimation of the PV z-position can be extracted from each photon candidate. The electromagnetic cluster barycenter measured at the first layer of the calorimeter is combined with the cluster barycenter in the second layer by fitting an straight-line in the R-z plane; the interception of this line with the ATLAS beam axis provides an estimation of the PV z-position z_γ, with an associated uncertainty $\sigma_{z\gamma}$ [90]. In the case of early converted photons with measurements in the silicon tracker, the coordinates of the conversion vertex are also considered in the fit of the straight-line, which provides a precise measurement of the PV z-position.

Figure 5.6 shows the distribution of the difference Δz between the two z_γ measurements provided by unconverted photons in diphoton events, with both photons reconstructed in the calorimeter barrel. The figure shows a comparison of the distributions obtained with Monte Carlo simulation and with data collected in 2011, in two periods with different beam and pileup conditions [20]. A good agreement between the different distributions is observed.

The two z estimations z_{γ_1} and z_{γ_2} from the two photons in the event are combined, considering also the distribution of reconstructed primary vertices in the z direction. It is done computing a weighted average, taking into account the corresponding estimation uncertainties $\sigma_{z\gamma_1}$ and $\sigma_{z\gamma_2}$, and the RMS of the distribution of primary vertexes in the z direction, which is about 5.5 cm. It yields a common value $z_{\gamma\gamma}$ with uncertainty $\sigma_{z\gamma\gamma}$. Then, this z estimation is used together with information of the various primary vertices reconstructed in the event in order to choose one of them.

For each reconstructed primary vertex, the sum of ${p_\mathrm{T}}^2$ of all the tracks associated to it is computed. This sum tends to be higher for the hard-scattering vertices

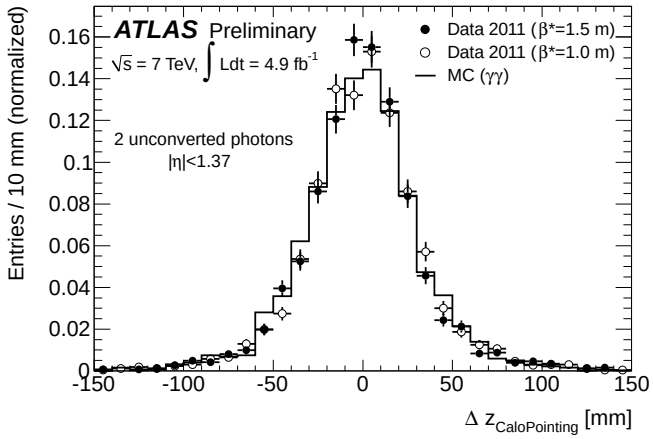

Figure 5.6: Distribution of the difference Δz between the two z_γ measurements provided by unconverted photons in diphoton events, with both photons reconstructed in the calorimeter barrel. It shows a comparison of the distributions obtained with Monte Carlo simulation and with data collected in 2011, in two periods with different beam and pileup conditions [20].

corresponding to the diphoton system than for the rest of overlapping vertices mostly from soft interactions. For this discriminant variable, a probability density function (pdf) for pileup vertices is extracted from collision events selected randomly during the data acquisition, without any trigger-level requirement; these events are usually called *minimum bias* events. A pdf for the hard-scattering vertices is also extracted from the data, considering some Monte Carlo information and using the kernel estimation technique from [120].

A likelihood function is built for the reconstructed primary vertices, as a function of the PV z-position and of the sum of associated track squared p_{T}. It is done based on the per event z estimation from the photon pair information ($z_{\gamma\gamma}$) and the corresponding uncertainty $\sigma_{z\gamma\gamma}$, and the pdf's extracted for the second variable, as follows:

$$\begin{aligned}\mathcal{L}(z, \textstyle\sum {p_{\mathrm{T}}}^2; z_{\gamma\gamma}, \sigma_{z\gamma\gamma}) &= \mathcal{L}(\textstyle\sum {p_{\mathrm{T}}}^2) \cdot \mathcal{L}(z; z_{\gamma\gamma}, \sigma_{z\gamma\gamma}) \\ &= \frac{P_{\substack{\mathrm{hard}\\ \mathrm{scat}}}(\sum {p_{\mathrm{T}}}^2)}{P_{\substack{\mathrm{min}\\ \mathrm{bias}}}(\sum {p_{\mathrm{T}}}^2)} \cdot \exp\left(-\frac{(z - z_{\gamma\gamma})^2}{2\,{\sigma_{z\gamma\gamma}}^2}\right); \end{aligned} \tag{5.1}$$

where the first term gives the probability for a given PV to correspond to a hard-scattering process, and the second term gives the probability for that PV to correspond to the reconstructed photon pair. Then, the primary vertex with the highest likelihood value in the event is selected.

The performance obtained using the alternative methods for the primary vertex selection are shown in Figure 5.7. The left side figure shows the selection efficiency as a function of the number of primary vertexes reconstructed per event, for signal events. For the efficiency evaluation, the selection is considered effective if the distance between the reconstructed PV selected and the Monte Carlo true PV is less than 0.2 mm. The blue points correspond to the efficiency obtained with the nominal selection method based on the likelihood function, and the black points correspond to the one obtained considering only the sum of track p_{T} squared.

The right side figure shows the diphoton invariant mass distributions expected for signal events. The green distribution corresponds to the ideal case, considering

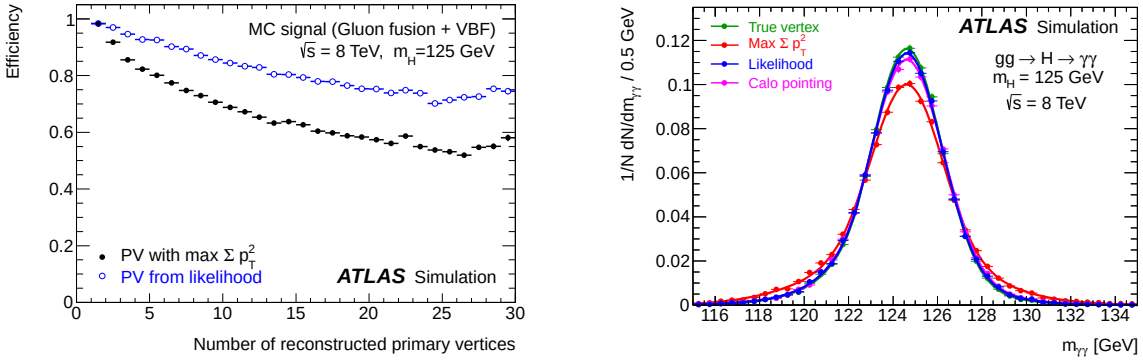

Figure 5.7: Comparisons of the performance obtained using alternative methods for the primary vertex (PV) selection described in the text. The left side figure shows the efficiency of the selection as a function of the number of primary vertexes reconstructed per event, on signal events. For this efficiency evaluation, the selection is considered right if the distance between the reconstructed PV selected and the Monte Carlo true PV is less than 0.2 mm. The figure on the right side shows the diphoton invariant mass distribution expected for signal events. The green distribution corresponds to the ideal case, considering in the mass calculation the true position of the Higgs boson primary vertex, and the red, pink and blue distributions are obtained with different estimations of the PV z-position. Both figures were obtained from $\sqrt{s} = 8$ TeV Monte Carlo samples for a 125 GeV Higgs boson; the figure on the left side only includes the events produced via gluon fusion and vector boson fusion.

in the mass calculation the true position of the Higgs boson primary vertex. The red, pink and blue distributions correspond to z estimations considering the sum of track squared p_{T} only, the two photon pointing information only, and the nominal z estimation from the likelihood function, respectively. One can see that the result obtained with the likelihood function is the very effective and is close to the ideal case, but if only the photon pointing information were used the result would be similarly good.

5.2.5 Diphoton invariant mass

The diphoton invariant mass $m_{\gamma\gamma}$ is computed from the photon parameters, energies E_i, pseudorapidities η_i and ϕ_i directions, as follows

$$m_{\gamma\gamma} = \sqrt{2E_1E_2\frac{[\cosh(\eta_1 - \eta_2) - \cos(\phi_1 - \phi_2)]}{\cosh\eta_1 \cosh\eta_2}} \tag{5.2}$$

The reconstruction of these parameters has been discussed in Chapter 3.

For this calculation, the pseudorapidity η of the photons is estimated considering the position of the photon cluster in the first layer of the EM calorimeter, and the z position of the selected primary vertex.

The mass distributions of the data samples are shown in Figure 5.8. It is shown on the top part for each data sample separately, on the left side for the 7 TeV sample and on the right side for the 8 TeV sample, and on the bottom part combining both samples. The overlaid solid red line present the background-only model fitted to the data, and the dashed line shows the expected $H \to \gamma\gamma$ signal for a Standard Model Higgs boson of mass 126.5 GeV. The bottom inset displays the data residuals after subtracting the background model. The background model presented here consists of the sum of various background models fitted to separated data categories (the data categorization is discussed in Section 5.5, and details on the data modeling are discussed in Section 5.6).

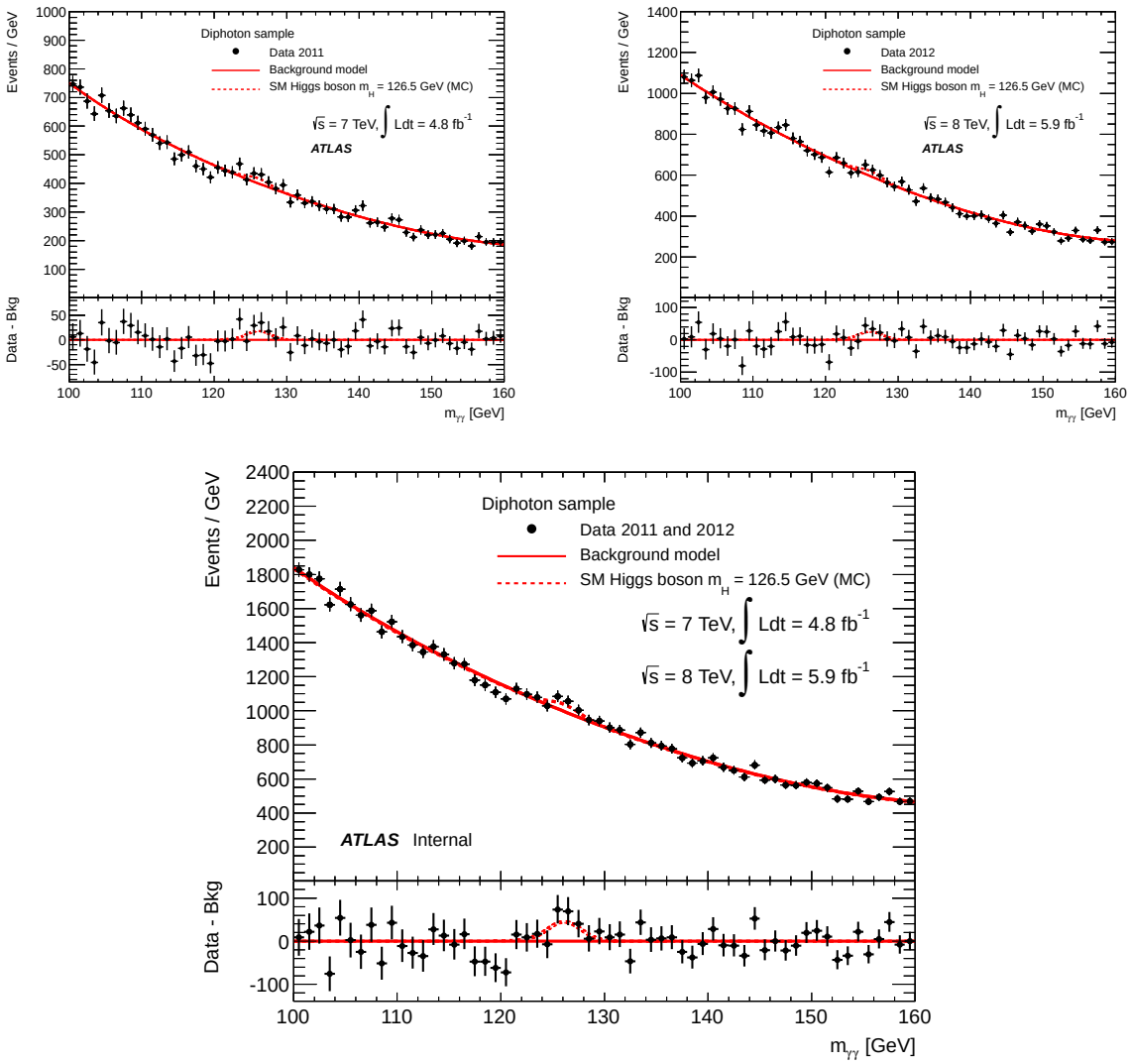

Figure 5.8: Diphoton invariant mass distribution, on the top part for each data sample separately, on the left side for the 7 TeV sample and on the right side for the 8 TeV sample, and on the bottom part combining both samples. The overlaid solid red line present the background-only model fitted to the data, and the dashed line shows the expected $H \to \gamma\gamma$ signal for a Higgs boson of mass 126.5 GeV. The bottom inset displays the data residuals after subtracting the background model. The background model presented here consist of the sum of various background models fitted to separated data categories (the data categorization is discussed in Section 5.5, and details on the data modeling are discussed in Section 5.6).

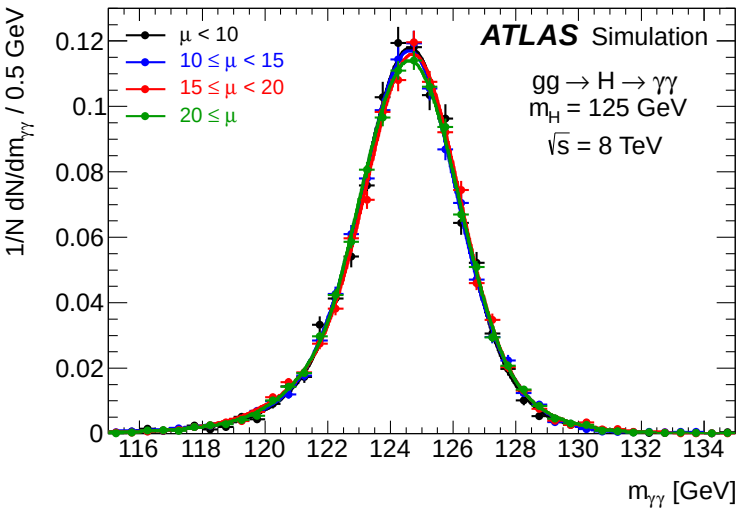

Figure 5.9: Diphoton invariant mass distribution expected for a Higgs boson of mass 125 GeV, at the $\sqrt{s}$ = 8 TeV sample conditions, under different pileup conditions, specifically for different values of the mean number of interactions per bunch crossing μ.

5.3 Expected signal

5.3.1 Signal mass distribution

The diphoton invariant mass distribution expected in this analysis for the signal of a Higgs boson of mass 125 GeV is shown in the right side of Figure 5.7, in blue color, for the $\sqrt{s} = 8$ TeV sample conditions. The expected full width at half maximum (FWHM) of the peak is about 3.9 GeV. Figure 5.9 presents the expected mass distribution under different pileup conditions, specifically for different values of the mean number of interactions per bunch crossing. It shows the robustness of the mass resolution against the pileup effects.

This mass distribution is completely driven by the detector resolution; compared with this distribution, the intrinsic $H \to \gamma\gamma$ mass distribution is almost a Dirac peak, for it has a width of a few MeV at the low mass range [24].

The parametrization of the reconstructed photon energy resolution has a Gaussian core and a non-gaussian tail toward low mass, which arises mostly from converted photons that have lost a significant fraction of energy in the inner detector material.

The following list presents the various sources of systematic uncertainties on the expected diphoton mass resolution:

- **Calorimeter energy resolution:** The energy resolution of the electromagnetic calorimeter is discussed in Chapter 2, Section 2.5.1; the main uncertainty on the energy resolution for the energy range of interest in this analysis is the uncertainty on the constant term. Varying the constant term within its uncertainties, the effect on the diphoton invariant mass resolution has been estimated to be of about 12%.

- **Electron to photon extrapolation of the calibration:** The photon energy calibration based on an extrapolation of the electron calibration with $Z \to ee$

data events is described in Chapter 3, Section 3.3. The differences in the calorimeter response to electrons and photons are assumed to be dominated by the effects of the upstream material. A study has been done performing the electron calibration procedure on $Z \to ee$ Monte Carlo samples, and applying this calibration to photons on $H \to \gamma\gamma$ samples, with both sample sets generated with additional upstream material on detector simulation. Then, an uncertainty of 6% has been assigned to the mass resolution based on this study.

- **Pileup effects:** In order to evaluate the impact of an imperfect simulation of the pileup when generating the Monte Carlo samples, the MC samples have been split in two sample sets with low and high pileup conditions, according to the mean number of interactions per bunch crossing. The pileup effects have been studied by comparing the mass resolution in both samples. An uncertainty of 3% has been assigned due to these effects.

- **Primary vertex selection:** A mis-modeling of the information used for the selection of the primary vertex would have an impact on the mass resolution. These effects have been studied considering small differences observed between the data and the MC samples. The effect on the mass resolution is found to be smaller than 0.2% and is neglected.

The combination of all these uncertainties makes a total systematic uncertainty of 14% on the width of the signal peak.

5.3.2 Uncertainty on the signal peak position

The calibration of the photon energy scale has been discussed in Chapter 3, Section 3.3.

Three factors have been found to induce significant uncertainties on the photon energy scale, and therefore on the diphoton invariant mass scale. These are the amount of material in front of the calorimeter, the calorimeter pre-sampler energy scale and the method used for the in-situ calibration. As mentioned above, a difference on the amount of material expected to be in front of the calorimeter affects the electron to photon extrapolation of the calibration. These effects have been considered separated for photons with $|\eta| < 1.8$ and $|\eta| > 1.8$, which correspond to the regions covered and not covered by the calorimeter pre-sampler. The uncertainty on the pre-sampler energy scale is of about 5% in the barrel and 10% in the end-caps.

The total uncertainty on the diphoton mass scale and therefore on the signal peak position is estimated to be 0.6%.

5.3.3 Signal efficiency and yields

The $H \to \gamma\gamma$ event selection efficiencies and the number of events expected for the data integrated luminosities are quoted in Table 5.1, as obtained from the various Monte Carlo samples at 7 and 8 TeV. These values are quoted for various Higgs boson mass hypotheses, separately for the different Higgs boson production modes. For a 125 GeV Standard Model Higgs boson, about 81 and 114 events are expected in the 7 and 8 TeV diphoton samples respectively.

Table 5.1: $H \to \gamma\gamma$ event selection efficiencies and the number of events expected for 4.8 fb^{-1} of proton collisions at $\sqrt{s} = 7$ TeV, and 5.9 fb^{-1} at $\sqrt{s} = 8$ TeV, as obtained from the various Monte Carlo samples. These values are quoted for various Higgs boson mass hypothesis, separately for the different Higgs boson production modes.

		ggF		VBF		WH		ZH		ttH		Total
$\sqrt{s}$	m_H [GeV]	ε[%]	N_{evt}	ε[%]	N_{evt}	ε[%]	N_{evt}	ε[%]	N_{evt}	ε[%]	N_{evt}	N_{evt}
7 TeV	110	37.3	71.7	37.9	5.2	33.5	2.8	33.5	1.5	33.7	0.4	81.6
	115	39.5	73.8	40.1	5.5	34.9	2.8	35.5	1.5	34.9	0.3	83.9
	120	40.9	73.5	42.1	5.8	37.0	2.6	36.9	1.4	35.9	0.3	83.6
	125	42.0	70.9	43.8	5.8	38.1	2.4	38.4	1.3	37.2	0.3	80.7
	130	43.1	66.3	44.8	5.7	39.3	2.1	39.9	1.2	37.8	0.3	75.6
	135	44.6	59.8	46.9	5.3	40.7	1.8	40.8	1.0	38.7	0.2	68.1
	140	45.2	51.7	48.7	4.8	41.8	1.5	42.3	0.9	39.5	0.2	59.1
	145	45.8	42.3	49.8	4.1	42.5	1.2	43.6	0.7	40.5	0.2	48.5
	150	45.8	31.6	49.7	3.1	44.1	0.9	44.7	0.5	40.7	0.1	36.2
8 TeV	110	33.8	100.6	34.5	7.4	29.9	3.7	29.5	2.1	27.3	0.6	114.4
	115	35.6	103.8	36.2	7.9	30.6	3.6	32.5	2.1	27.9	0.6	118.0
	120	37.2	103.6	38.1	8.2	32.7	3.4	32.9	2.0	29.4	0.6	117.8
	125	38.3	100.3	39.6	8.3	33.9	3.2	34.2	1.8	29.7	0.5	114.1
	130	39.1	94.1	41.2	8.0	35.1	2.8	35.9	1.6	31.1	0.5	107.0
	135	40.4	85.3	42.4	7.6	35.7	2.4	36.6	1.4	32.2	0.4	97.1
	140	41.1	74.0	43.0	6.8	37.0	2.0	36.8	1.2	32.4	0.3	84.3
	145	41.6	60.6	43.7	5.8	38.0	1.6	38.5	0.9	33.6	0.3	69.2
	150	41.7	45.3	44.8	4.4	38.2	1.1	39.2	0.7	34.0	0.2	51.7

The factors inducing uncertainties on the event selection efficiency are the following:

- **Uncertainty on the photon identification efficiency:** This uncertainty has been evaluated separately for the 7 and 8 TeV samples, for which the neural-network based and cut-based photon selections are used respectively. It was done based on the comparison of the photon efficiency obtained using Monte Carlo and various data-driven measurements. The data-driven estimations were done using photons from $Z \to ee\gamma$, electrons from $Z \to ee$, and a sideband technique (see Chapter 3, Section 3.4). Then, the uncertainty on the diphoton efficiency is computed treating the uncertainties on the two photons as fully correlated. It has been found to be 8% for the 7 TeV sample and 11% for the 8 TeV sample.

- **Pileup effects on the photon reconstruction and identification:** This uncertainty has been evaluated following a similar procedure to the one used to evaluate the pileup induced uncertainty on the mass resolution (Section 5.3.1). This study has been done independently for 7 and 8 TeV samples, obtaining similar results. An uncertainty of 4% is taken into account to consider these effects.

- **Trigger efficiency:** The trigger efficiency has been estimated using Monte Carlo simulations and two data-driven approaches, a bootstrap method [121] where another trigger configuration with lower threshold is used, and with photons from $Z \to ee\gamma$ events. The agreement between the data-driven methods is at the level of 1%. Thus, a systematic uncertainty of 1% has been assigned to the trigger efficiency.

- **The photon isolation energy simulation:** It implies an uncertainty on the efficiency of the isolation requirement. For the 7 TeV sample it has been estimated to be 0.4%, and 0.5% for the 8 TeV sample. These uncertainties correspond to the differences observed between Monte Carlo and data samples of $Z \to ee$ events. Specifically, a shift of $\sim$100 MeV is observed between

the isolation energy distribution from the two samples. This uncertainty is negligible compared with the previous ones.

- **Photon energy scale uncertainty:** It entails an uncertainty of 0.3% on the event selection efficiency, because of the kinematic transverse energy requirement on the photon selection. It is negligible compared with the previous uncertainties.

The theoretical uncertainties of the SM Higgs boson production cross section for the different production processes are quoted in Table 5.7 (page 118) [29, 30]. The uncertainties related to the parton distribution functions are estimated following the prescription given in [122] and by using the PDF sets of CTEQ [123], MSTW [124] and NNPDF [125]. They are assumed to be fully correlated among processes with identical initial states.

The uncertainty on the Higgs boson decay branching ratio to two photons is 5% [126].

As quoted above, the uncertainties on the integrated luminosity are 1.8% for the 7 TeV sample, and 3.6% for the 8 TeV sample.

5.4 Background composition

As mentioned above, four kind of processes contribute to the background, $\gamma\gamma$, γj, jj and Drell-Yan ee processes. Using different methods and considering mainly information from the data, the background fractions corresponding to each of these components have been extracted. The methods used in this analysis have been also used in the measurements of diphoton production cross-section done by ATLAS [12, 57], and some of these methods are extensions of methods used in the measurements of the single photon production cross-section by ATLAS [10,11]. A brief description of two of these methods is provided here, while further details can be found in the documents reporting those measurements, and a description of a third decomposition method can be found in [12].

The estimated background composition is not directly used to extract the final analysis results, nevertheless this decomposition allows monitoring the performance of the photons identification, and it is also used for background parametrization studies.

5.4.1 Decomposition methods

The methods described in this section use the photon identification and isolation variable distributions of the diphoton candidates. This information is used to distinguish three background components: $\gamma\gamma$, γj and jj; the Drell-Yan background component is included on the fraction of events assigned by these methods to the $\gamma\gamma$ component, because the variables used do not discriminate between electrons and photons. The data considered correspond to a sample larger than the nominal one, for which the isolation cut is not applied, and some of the photon identification criteria are relaxed.

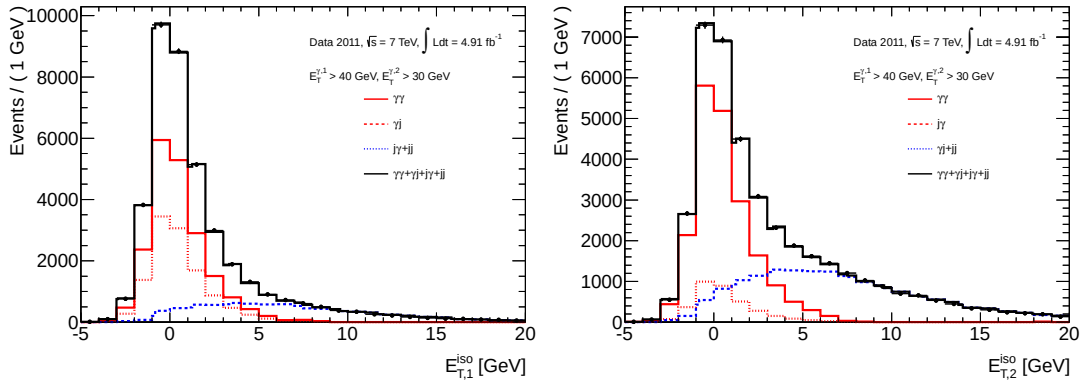

Figure 5.10: Photon isolation energy distributions for the 7 TeV sample, and projections of the two-dimensional pdf's resulting from the fit. It is shown on the left side for the leading photon candidates, and on the right side for the sub-leading candidates.

One of the methods consists in a *template fit* of the two-dimensional isolation energy distribution of the diphoton candidates. Each dimension corresponds to the isolation energy for one of the photon candidates.

The unidimensional isolation energy distributions for prompt and fake photons are extracted separately for the leading and sub-leading photons.

A control region rich in fake photons (misidentified jets) is used to extract their isolation energy distribution. This control region is defined by requiring photons to fail at least one of the *tight* cuts applied on four identification variables (w_{S3}, F_{side}, ΔE, E_{ratio}; they are defined in Chapter 3, Section 3.4). These four variables have been chosen for having very low correlation with the photon isolation energy. This control region is referred to as the *non-tight* region.

The isolation energy distribution of prompt photons is obtained from the distribution of photon candidates that satisfy the identification criteria in the following way: the fake photon distribution is normalized to match the distribution of candidates satisfying the identification criteria in the high isolation energy tail, above 7 GeV; this tail is dominated by fake photons; then the normalized fake photon distribution is subtracted from the distribution of photon candidates, and the result of the subtraction is taken as template for the prompt photons.

After extracting the probability density functions (pdf) for prompt photons and fake photons (jets), four two-dimensional pdf's are built, one for each background component, $\gamma\gamma$, γj, $j\gamma$ and jj. Where the γj background have been decomposed in two, γj and $j\gamma$, making the distinction of which photon candidate is the fake photon, the leading photon candidate or the sub-leading one. Then, the sum of the four pdf's is fitted to the diphoton sample giving as result the background composition.

Figure 5.10 shows the photon isolation energy distributions for the 7 TeV sample, and projections of the two-dimensional pdf's resulting from the fit. It is shown on the left side for the leading photon candidates, and on the right side for the sub-leading candidates. The black line correspond to the sum of the four pdf's, and the solid red line shows the estimated $\gamma\gamma$ component.

Another method uses the number of diphoton candidates observed in control sidebands to estimate the amount of γj and jj events in the signal region. The photon signal region is the one defined by the nominal photon selection, where events

Table 5.2: Estimated composition of the diphoton candidate samples, as obtained with the 2x2D sidebands method. A sum in quadrature of statistical and systematic uncertainties is quoted.

$\sqrt{s}$	$\gamma\gamma$	γj	jj	Drell-Yan
7 TeV	$(78 \pm 4)\%$	$(19 \pm 3)\%$	$(1.8 \pm 0.5)\%$	$(1.4 \pm 0.1)\%$
8 TeV	$(75 \pm 3)\%$	$(22 \pm 2)\%$	$(2.6 \pm 0.5)\%$	$(0.7 \pm 0.1)\%$

are required to be isolated ($E_{\mathrm{T}}^{\mathrm{isol}} < 4$ GeV) and to satisfy the identification criteria. Three control regions are defined for fake photons in the following ways: 1) requiring the photon candidates to be not isolated, 2) requiring the photon candidates to be in the *non-tight* sideband and isolated, 3) requiring the photon candidates to be in the *non-tight* sideband and not isolated. It makes four different regions for photons and a total of 16 different regions for diphoton events, distinguishing between the leading and sub-leading photon candidates. After some simplifying assumptions, the composition of events in the signal region is estimated using the number of events in 7 of the 16 regions and solving a system of linear equations. This method is called *2x2D sidebands* because it uses two criteria for defining sidebands, the isolation and identification criteria, and it is done twice; one set of sidebands is defined for each photon candidate.

5.4.2 Drell Yan Background

The source for this background is the Drell-Yan process $pp \to e^+e^-$. It results from the eventual mis-reconstruction of the electron tracks. The tail of the Z resonance, which is just aside the invariant mass regions of interest, requires to take attention to this background. It is estimated by computing the electron-to-photon misidentification rate, and then it is used to extrapolate the background from the number of $Z \to ee$ events reconstructed as di-electrons.

The misidentification rate is estimated using the number of $Z \to ee$ events reconstructed as electron-photon pairs, and the ones reconstructed as di-electrons, in the invariant mass range 80 - 100 GeV. The misidentification rate has been found to be about 8%.

5.4.3 Background composition results

The fraction of events obtained for each background component are listed in Table 5.2, separately for the 7 and 8 TeV samples. These results where obtained with the 2x2D sidebands method. The other methods have yielded results compatibles with these ones. The diphoton purity of the samples has been estimated to be $(78 \pm 4)\%$ for the 7 TeV sample, and $(75 \pm 3)\%$ for the 8 TeV sample.

The fraction of Drell-Yan background is lower for the 8 TeV sample than for the 7 TeV sample. It is expected because of the improvements made on the algorithm of converted photon reconstruction, used for the moment uniquely for the 8 TeV sample (see Section 3.1 on Chapter 3).

The background decomposition has been also performed in bins of $m_{\gamma\gamma}$. The results obtained are shown in Figure 5.11, on the left side for the 7 TeV sample

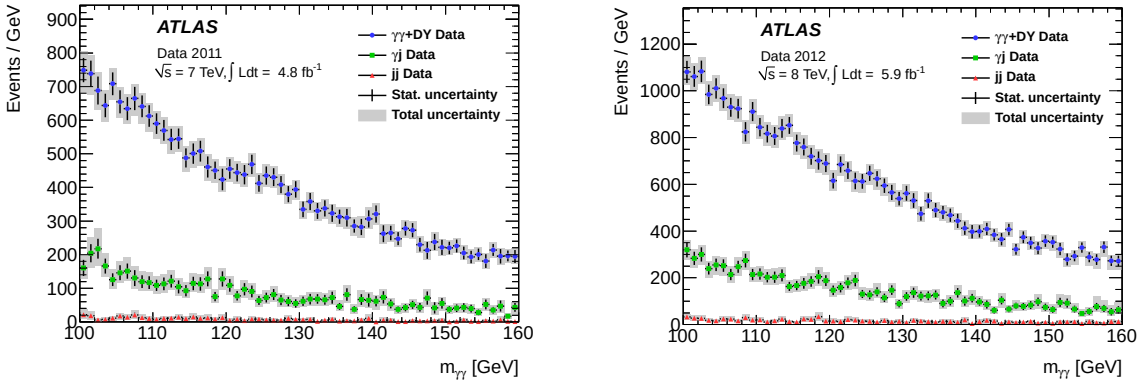

Figure 5.11: Estimated composition of the diphoton candidate samples as a function of the invariant mass, on the left side for the 7 TeV sample and on the right side for the 8 TeV sample. These results where obtained with the 2x2D sidebands method. The small contribution from the Drell-Yan background is included shown together with the $\gamma\gamma$ component.

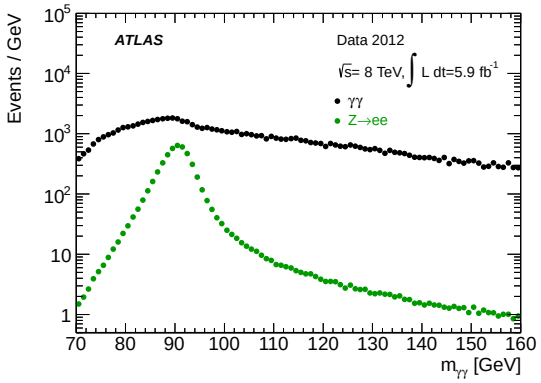

Figure 5.12: Estimated Drell-Yan background as a function of the invariant mass, for the 8 TeV sample. The black points correspond to the diphoton candidate sample, and the green points shows the Drell-Yan background.

and on the right side for the 8 TeV sample. In this figure, the small contribution from the Drell-Yan background is included in the $\gamma\gamma$ component. Then, Figure 5.12 shows the estimated Drell-Yan background as a function of the mass $m_{\gamma\gamma}$, for the 8 TeV sample. In the region from 100 to 160 GeV, this background component is mainly concentrated in the low mass part.

5.5 Event categorization

In order to increase the sensitivity to observe a SM-like Higgs boson, the events are separated according to different criteria in ten categories, resulting in event subsamples with different signal-to-background ratios. The criteria considered for this categorization are:

- the conversion status and η direction of the photons, for the resolution on the photon energy measurement depends on them;
- a discriminant variable related to the diphoton transverse momentum $p_{\mathrm{T}}^{\gamma\gamma}$, which exploits kinematic differences between the signal and the background;

- and a 2-jet based selection, optimized to collect signal events produced by vector-boson fusion.

Each of the two data samples is separated in the ten categories, making a total of twenty event sub-samples.

Then, for the statistical analysis, signal and background pdf's (probability density function) are defined for each category. They are fitted all simultaneously keeping a common signal strength parameter μ.

5.5.1 Categorization according to the photon conversion status and η direction

The photon energy resolution depends on the conversion status and η direction of the photons. In Chapter 3, Figure 3.4 shows the energy resolution separately for converted and unconverted photons, as a function of η. This figure shows also the fraction of photons with energy badly measured. The energy is better reconstructed for the unconverted photons than for the converted ones. In the central part of the EM calorimeter barrel, low η, the photon energy is better measured than in the rest of the calorimeter. And in the region near the transition between the barrel and the end-caps, the energy is not very well measured.

Therefore, separating the events according to the photon conversion status and η yields categories with different resolutions on the diphoton invariant mass. It means that some categories will have a thinner signal peak, and therefore a better signal-to-background ratio, than others.

Five event categories have been defined based on this energy resolution dependency. They are defined as follows:

- Unconverted central: For events with both photons reconstructed as unconverted, and both of them in the central part of the calorimeter barrel, specifically in the region $|\eta| < 0.75$.

- Unconverted rest: For events with both photons reconstructed as unconverted, and not satisfying the η requirements to be in the category unconverted central.

- Converted central: For events with at least one photon reconstructed as converted, and both photons in the central part of the calorimeter barrel ($|\eta| < 0.75$).

- Converted transition: For events with at least one photon reconstructed as converted, and at least one photon near to the transition between the barrel and the end-caps of the calorimeter, specifically in the region $1.3 > |\eta| > 1.75$.

- Converted rest: For events with at least one photon reconstructed as converted, and not satisfying the η requirements to be either in the category converted central or converted transition.

The category unconverted central has the best resolution, while the category converted transition has the widest peak.

The introduction of these five categories in the analysis improve the expected sensitivity by about 15%. In spite of being the mass resolution the main motivation

for this event classification, part of this gain is also due to kinematic differences between the signal and the background; they are distributed differently among the defined η bins.

5.5.2 Categorization based on the $p_{\mathrm{Tt}}^{\gamma\gamma}$ discriminant variable

For the Higgs boson production modes vector-boson fusion (VBF), and associated production with vector-bosons or top quarks (VH or $t\bar{t}H$), the Higgs boson transverse momentum is expected to be typically larger than for the production via gluon fusion (ggF). It is also expected to be typically larger than the diphoton system transverse momentum in the background processes. Therefore, the transverse momentum of the diphoton system $p_{\mathrm{T}}^{\gamma\gamma}$ can be used as a discriminant variable for these events.

There is a way to decompose $\vec{p}_{\mathrm{T}}^{\,\gamma\gamma}$ in two orthogonal components which has been found to be convenient to use [127, 128] because one of this components is almost insensitive to the experimental momentum resolution of the individual photons [128]. This decomposition is illustrated in the following figure:

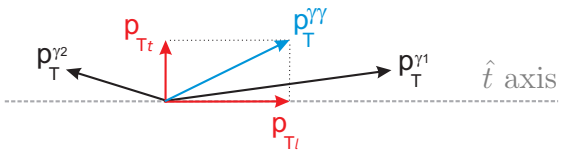

Figure 5.13: Decomposition of $\vec{p}_{\mathrm{T}}^{\,\gamma\gamma}$.

The transverse momentum of the diphoton system $\vec{p}_{\mathrm{T}}^{\,\gamma\gamma}$ is defined as usually,

$$\vec{p}_{\mathrm{T}}^{\,\gamma\gamma} = \vec{p}_{\mathrm{T}}^{\,\gamma 1} + \vec{p}_{\mathrm{T}}^{\,\gamma 2}. \tag{5.3}$$

The $\hat{t}$ axis is defined in the direction of the vectorial difference between the two photons' transverse momentum,

$$\hat{t} = \frac{\vec{p}_{\mathrm{T}}^{\,\gamma 1} - \vec{p}_{\mathrm{T}}^{\,\gamma 2}}{|\vec{p}_{\mathrm{T}}^{\,\gamma 1} - \vec{p}_{\mathrm{T}}^{\,\gamma 2}|}. \tag{5.4}$$

Then, $\vec{p}_{\mathrm{T}}^{\,\gamma\gamma}$ can be decomposed in two, the component parallel to the $\hat{t}$ axis $\vec{p}_{\mathrm{Tl}}^{\,\gamma\gamma}$, and the one perpendicular to the $\hat{t}$ axis $\vec{p}_{\mathrm{Tt}}^{\,\gamma\gamma}$,

$$\vec{p}_{\mathrm{Tl}}^{\,\gamma\gamma} = (\vec{p}_{\mathrm{T}}^{\,\gamma\gamma} \cdot \hat{t}) \cdot \hat{t}, \tag{5.5}$$

$$\vec{p}_{\mathrm{Tt}}^{\,\gamma\gamma} = \vec{p}_{\mathrm{T}}^{\,\gamma\gamma} - (\vec{p}_{\mathrm{T}}^{\,\gamma\gamma} \cdot \hat{t}) \cdot \hat{t}. \tag{5.6}$$

The transverse component $p_{\mathrm{Tt}}^{\gamma\gamma}$ is the one that is almost insensitive to the photon momentum resolution, and it continue being a discriminant variable between the different processes as $p_{\mathrm{T}}^{\gamma\gamma}$. Figure 5.14 shows the $p_{\mathrm{Tt}}^{\gamma\gamma}$ distribution for signal events produced via gluon fusion in blue and for the rest of production modes in red, and the distribution for the $\gamma\gamma$ and γj background events in green, as obtained from Monte Carlo samples.

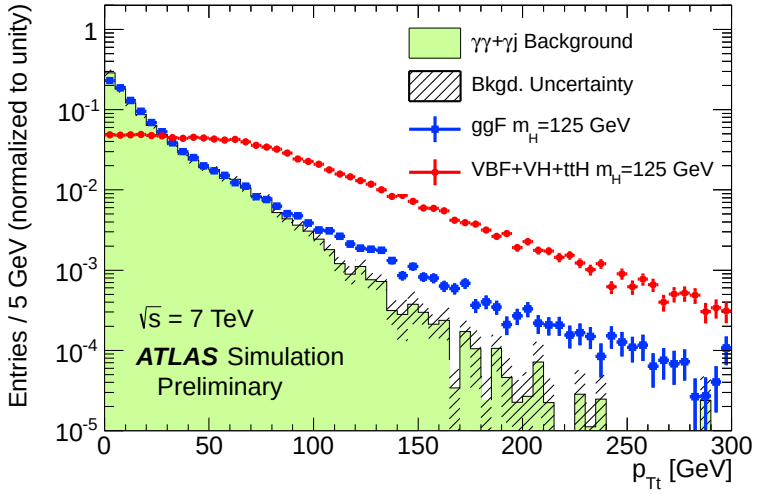

Figure 5.14: $p_{\mathrm{Tt}}^{\gamma\gamma}$ distribution (see the definition of $p_{\mathrm{Tt}}^{\gamma\gamma}$ in the text) for signal events produced via gluon fusion in blue and for the rest of production modes in red, and the for the $\gamma\gamma$ and γj background events in green, as obtained from Monte Carlo samples. The signal distributions correspond to a Higgs boson of mass 125 GeV. The three distributions are normalized to one.

In this analysis, events are separated according to the $p_{\mathrm{Tt}}^{\gamma\gamma}$ values, as low p_{Tt} events those with $p_{\mathrm{Tt}} < 60$ GeV and high p_{Tt} events those with $p_{\mathrm{Tt}} \geqslant 60$ GeV. Four out of the five categories presented in the previous section are split in two in this way, resulting in nine categories. The converted transition category which is the one with bad mass resolution is not split.

In the resulting categories, the signal-to-background ratio for the high p_{Tt} categories is larger than for the low p_{Tt} categories.

This p_{Tt} based categorization increases the sensitivity to observe a SM Higgs boson by about 6%.

5.5.3 2-jet category

In the signal events produced via vector boson fusion (VBF), the Higgs boson is accompanied by two quarks in the final state (see the diagram in Figure 1.5, Chapter 1), experimentally two jets [1]. These two jets arrive typically in the forward region of the detector, large η region, and represent a discriminant signature of these events. The VBF process is the second leading in the production of the Higgs boson at the LHC, and accounts for about 8% of the production for a 125 GeV Higgs boson at $\sqrt{s} = 8$ TeV. In this analysis, a selection is defined to collect events with this topology, and they are separated in an additional category. The introduction of this category in the analysis provides an improvement of about 3% on the sensitivity to observe a SM Higgs boson, and also allows studying the production mechanism if a signal is observed.

The jets are reconstructed from topological clusters of energy deposits in the calorimeters. The reconstruction is done using the anti-k_t algorithm [129], with

[1] Jets are the product of quark or gluon hadronization and subsequent decays of unstable hadronic particles, or the hadronic decay of tau-leptons. Jets are a bunch of particles, mainly hadrons, that arrive collimated in a given region of the detector. The jet direction and energy are associated with the direction and energy of its originating particle.

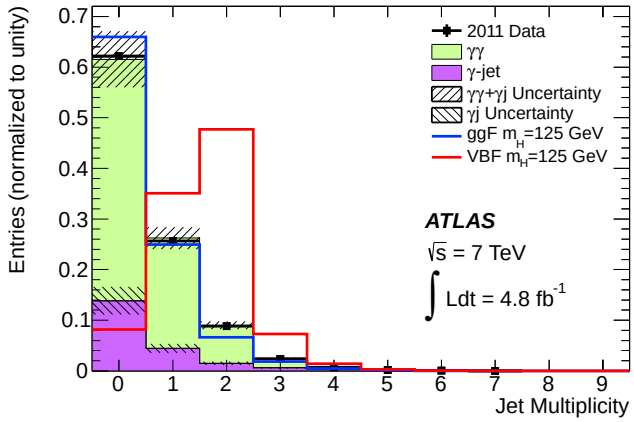

Figure 5.15: Distribution of number of jets per event that pass the jet selection described in the text, for signal gluon fusion and vector boson fusion events separately, and for the background processes, including $\gamma\gamma$ and γj, obtained from Monte Carlo samples. The signal distributions correspond to a Higgs boson of mass 125 GeV. The data sample distribution is also shown. These distributions correspond to 7 TeV samples.

a radius parameter $R = 0.4$. The jet energy and direction are calibrated and corrected based on Monte Carlo simulations and *in situ* studies, in which the transverse momentum balance between a jet and a reference object are exploited to derive correction factors. Additionally, corrections are applied based on the number of primary vertices reconstructed and the average number of interactions per bunch crossing, in order to minimize the pileup effects. The jet direction is corrected considering the reconstructed primary vertex with the highest sum of ${p_{\mathrm{T}}}^2$ of tracks associated to the jet. Details about the jet reconstruction and calibration can be found in [130–132].

For the 2-jet category, jets are selected requiring:

- $|\eta_j| < 4.5$
- $p_{\mathrm{T}}^j > 25$ GeV for the 7 TeV sample, and $p_{\mathrm{T}}^j > 30$ GeV for the 8 TeV sample for jets in the region $2.5 < |\eta_j| < 4.5$. This second increased threshold is set to reduce the contamination with jets from pileup events.
- Object quality criteria.
- For jets in the tracker acceptance region $|\eta| < 2.5$, the sum of p_{T} of the tracks associated to the jet and the selected primary vertex is computed, and it is required be more than 75% of the total sum of p_{T} of the tracks associated to the jet; this fractional value is usually called *jet-vertex fraction*. This is done to reduce the contamination with jets from pileup events.
- Jets are required not to overlap with the selected photons, requiring the distance ΔR in the η-ϕ space with respect to the photons to be higher than 0.4.

Then, the two jets with highest transverse momentum are chosen. Figure 5.15 shows the distribution of the number of jets per event that pass this selection for signal gluon fusion and VBF events separately, and for the background processes, including $\gamma\gamma$ and γj, obtained from Monte Carlo samples; the distribution is also shown for the data sample. Then, Figure 5.16-a shows the transverse momentum

a) Jet distributions

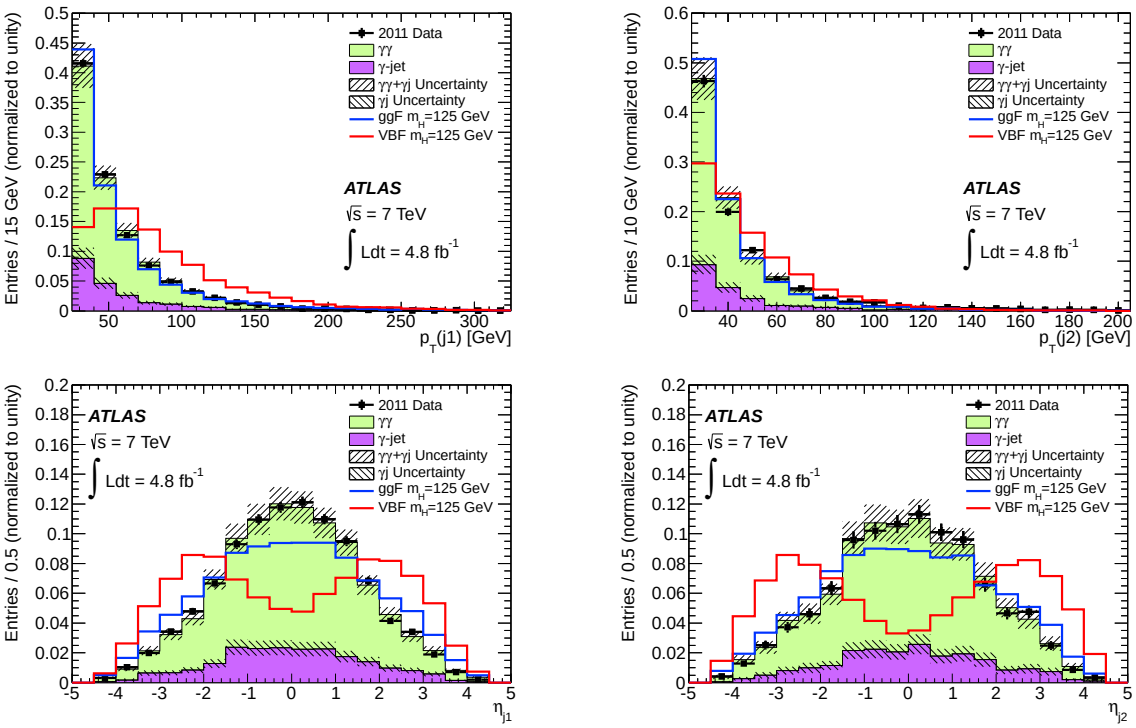

b) Event distributions

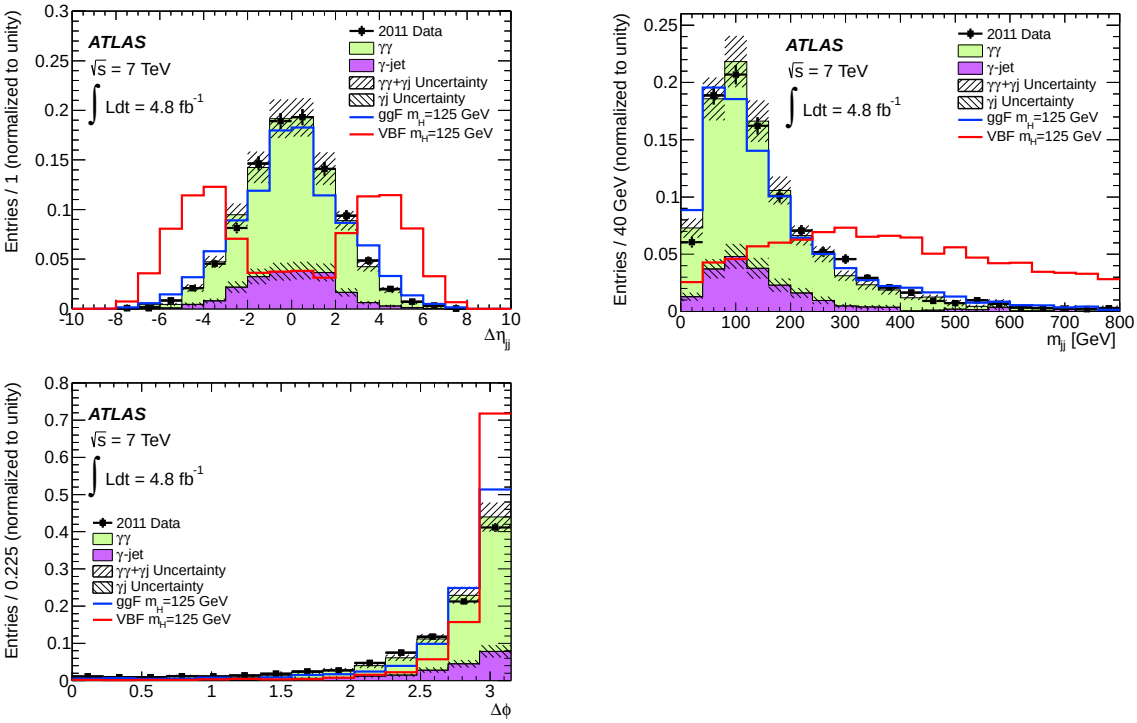

Figure 5.16: Jet and two-jet event distributions for various variables used in the selection of events with the topology of signal events produced via vector boson fusion (VBF). The different distributions are shown for signal gluon fusion and VBF events separately, and for the background processes, including $\gamma\gamma$ and γj, obtained from Monte Carlo 7 TeV samples. The signal distributions correspond to a Higgs boson of mass 125 GeV. The data sample distributions are also shown. On the part (a), the transverse momentum p_{T} and η distributions for the leading and sub-leading selected jets separately are shown. On the part (b), the distributions correspond to the following per event variables: the η different between the two jets $\Delta\eta_{jj}$, the two-jets invariant mass m_{jj}, and the azimuthal angle $\Delta\phi$ between the diphoton system and the two-jets system.

p_{T} and η distributions for the leading and sub-leading selected jets separately, for the same samples.

Once the jet selection is done, three additional requirements are applied to the events, based on three discriminant variables:

- The η difference between the two jets $\Delta\eta_{jj}$ is required to be larger than 2.8.
- The two-jets invariant mass m_{jj} is required to be larger than 400 GeV.
- The azimuthal angle $\Delta\phi$ between the diphoton system (vectorial-sum of the photons' momentum) and the two-jets system (vectorial-sum of the jets' momentum) is required to be larger than 2.6 rad.

The distributions for these event discriminant variables are shown in Figure 5.16-b, as before for signal gluon fusion and VBF events separately, for the main background processes from MC, and for the data sample.

The efficiency of this jet based selection to collect signal VBF events has been found to be 29% in the 7 TeV Monte Carlo samples, and 24% in the 8 TeV MC samples.

5.5.4 Categorization summary

The photon η-conversion based separation of the events makes five categories, four of them are split in two according to the $p_{\mathrm{Tt}}^{\gamma\gamma}$ values resulting in nine categories, and the 2-jet category makes a total of ten categories.

The number of signal events expected per category for a SM Higgs boson with mass 126.5 GeV are quoted in Table 5.3, for the data integrated luminosities. Also for each category, the fractions of events corresponding to each production mode are given. The fractional contribution from the secondary production modes is higher in the high p_{Tt} categories than in the low p_{Tt} categories, and the vector boson fusion is the main production mode for events in the 2-jet category, contributing with about 70-75% of the events.

Table 5.3: Number of signal events expected per category for a $m_H = 126.5$ GeV Standard Model Higgs boson, for the data integrated luminosities, and fractional contribution per production mode for each category.

			Contribution per prod. mode [%]				
$\sqrt{s}$	Category	N_{evt}	ggF	VBF	WH	ZH	ttH
7 TeV	Inclusive	79.4	87.8	7.3	2.9	1.6	0.4
	Unconverted central, low p_{Tt}	10.5	92.9	4.0	1.8	1.0	0.2
	Unconverted central, high p_{Tt}	1.5	66.5	15.7	9.9	5.7	2.4
	Unconverted rest, low p_{Tt}	21.6	92.8	3.9	2.0	1.1	0.2
	Unconverted rest, high p_{Tt}	2.8	65.4	16.1	10.8	6.0	1.8
	Converted central, low p_{Tt}	6.7	92.8	4.0	1.9	1.0	0.2
	Converted central, high p_{Tt}	1.0	66.6	15.3	10.0	5.7	2.5
	Converted rest, low p_{Tt}	21.1	92.8	3.8	2.0	1.1	0.2
	Converted rest, high p_{Tt}	2.7	65.3	15.9	11.0	5.9	1.8
	Converted transition	9.5	89.4	5.2	3.3	1.7	0.3
	2-jet	2.2	22.5	76.7	0.4	0.2	0.1
8 TeV	Inclusive	111.9	87.9	7.3	2.7	1.6	0.5
	Unconverted central, low p_{Tt}	14.2	94.0	4.3	1.7	1.0	0.3
	Unconverted central, high p_{Tt}	2.5	73.5	14.3	7.0	4.3	2.4
	Unconverted rest, low p_{Tt}	30.9	93.7	4.2	2.0	1.1	0.2
	Unconverted rest, high p_{Tt}	5.2	72.9	14.0	7.9	4.7	1.7
	Converted central, low p_{Tt}	8.9	94.0	4.3	1.7	1.0	0.3
	Converted central, high p_{Tt}	1.6	73.8	13.6	7.2	4.2	2.3
	Converted rest, low p_{Tt}	26.9	93.8	4.2	2.0	1.1	0.2
	Converted rest, high p_{Tt}	4.5	72.1	14.1	8.5	4.8	1.8
	Converted transition	12.8	90.1	5.9	3.1	1.8	0.4
	2-jet	3.0	30.8	69.3	0.4	0.2	0.2

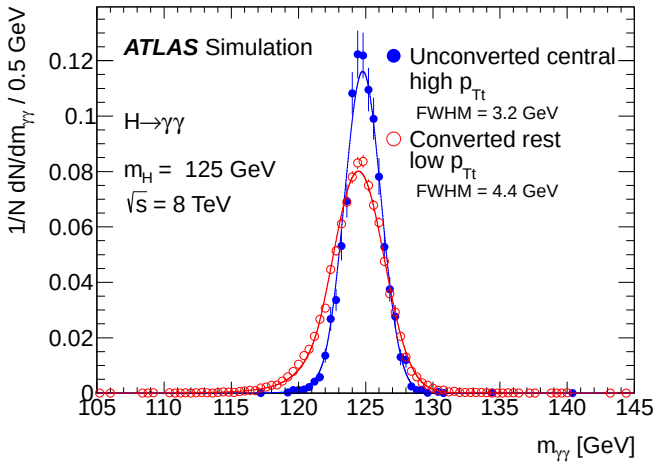

Figure 5.17: Diphoton invariant mass distributions for a SM Higgs boson with mass 125 GeV at $\sqrt{s} = 8$ TeV, for the category with best resolution, unconverted central high p_{Tt}, and for the category converted rest low p_{Tt} which has a wider peak than the first one.

Table 5.4: Number of diphoton candidates found in the data samples per category.

Category	$\sqrt{s} = 7$ TeV	$\sqrt{s} = 8$ TeV
Unconverted central, low p_{Tt}	2054	2945
Unconverted central, high p_{Tt}	97	173
Unconverted rest, low p_{Tt}	7129	12136
Unconverted rest, high p_{Tt}	444	785
Converted central, low p_{Tt}	1493	2015
Converted central, high p_{Tt}	77	113
Converted rest, low p_{Tt}	8313	11099
Converted rest, high p_{Tt}	501	706
Converted transition	3591	5140
2-jet	89	139
Total	23788	35251

A comparison of the signal diphoton invariant mass distribution for two categories is shown in Figure 5.17. It shows the distributions for the category with the best resolution, unconverted central high p_{Tt}, and for the category converted rest low p_{Tt} which has a wider peak than the first one.

The number of diphoton candidates found in the data samples per category are quoted in Table 5.4, and the invariant mass distributions are shown in figures 5.18, 5.19 and 5.20. The solid red line overlaid to each distribution present the background-only model fitted to the data, and the dashed line shows the expected $H \to \gamma\gamma$ signal for a Higgs boson of mass 126.5 GeV. (Details on the data modeling are discussed in Section 5.6.) The bottom inset displays the data residuals after subtracting the background.

Table 5.5 presents the full width at half maximum (FWHM) expected for the signal peak in each category, and the signal-to-background ratio $n_{\mathrm{S}}/n_{\mathrm{B}}$ expected for a SM Higgs boson of mass 126.5 GeV. For the signal-to-background ratio calculation, the number of background events is extracted from the background model fit to the data, integrating the number of events in the mass region containing 90% of the signal peak; then, of course only 90% of the signal events is considered.

The highest signal-to-background ratios are found in the categories: 2-jet, unconverted central high p_{Tt} and converted central high p_{Tt}. It is important to know that these are not necessarily the categories with the highest sensitivity for the signal observation, or the ones with the highest weight in the statistical analysis; this is because the number of events in the category is also a determining factor.

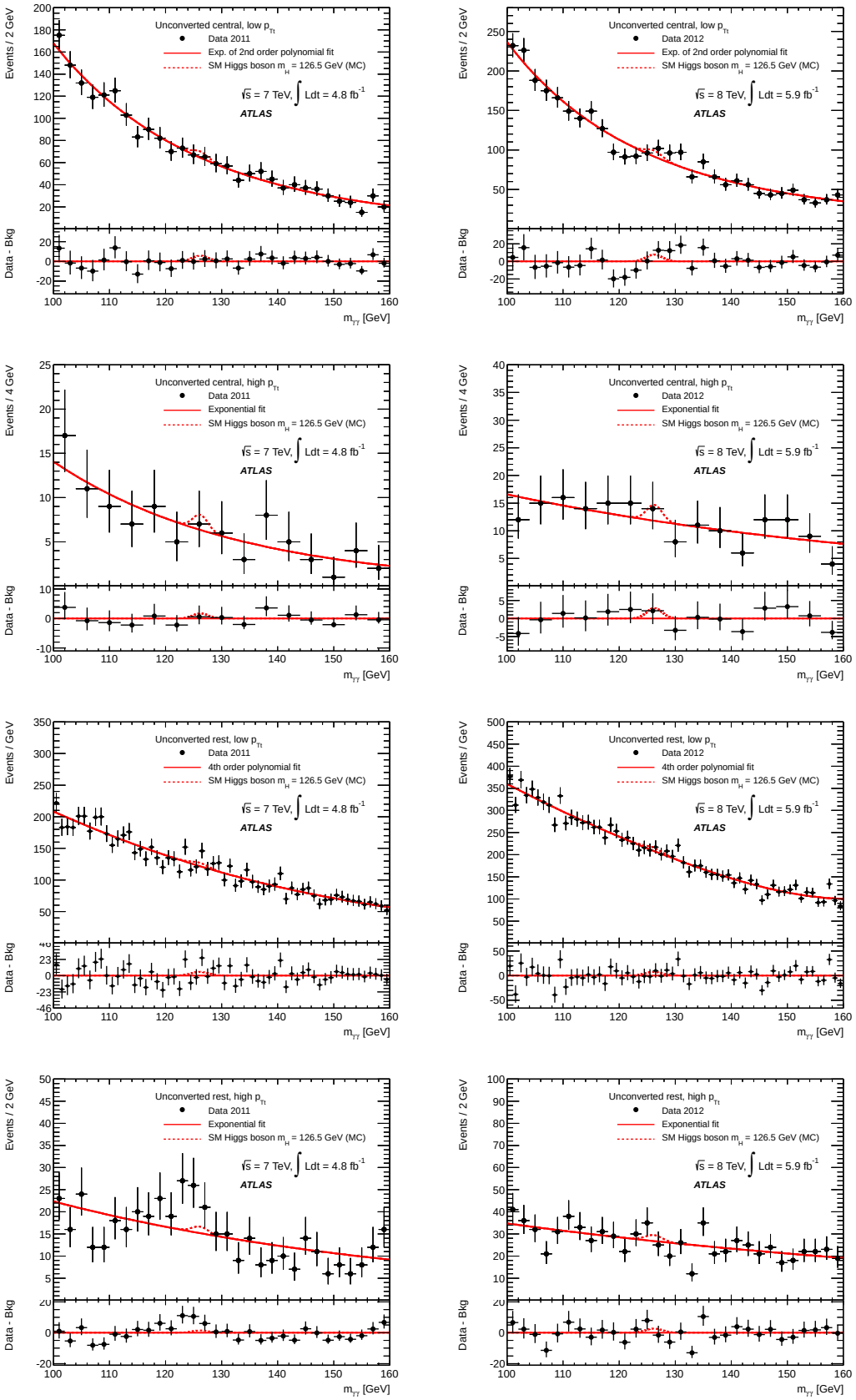

Figure 5.18: Diphoton Invariant mass distribution per category, on the left side for the 7 TeV data sample and on the right side for the 8 TeV sample. The overlaid solid red line present the background-only model fitted to the data, and the dashed line shows the expected $H \to \gamma\gamma$ signal for a Higgs boson of mass 126.5 GeV. Details on the data modeling are discussed in Section 5.6. The bottom inset displays the data residuals after subtracting the background model.

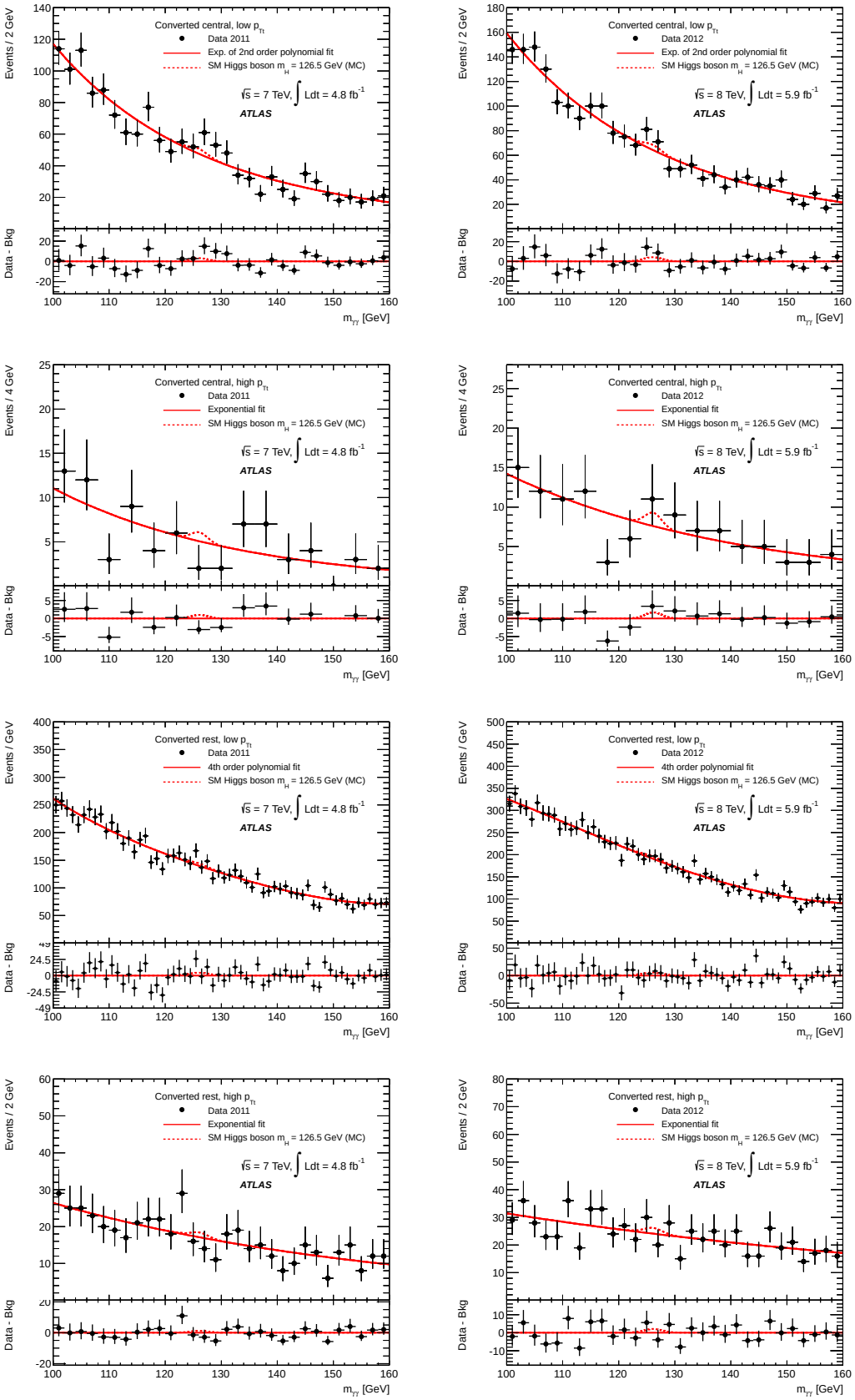

Figure 5.19: Diphoton Invariant mass distribution per category, on the left side for the 7 TeV data sample and on the right side for the 8 TeV sample. The overlaid solid red line present the background-only model fitted to the data, and the dashed line shows the expected $H \to \gamma\gamma$ signal for a Higgs boson of mass 126.5 GeV. Details on the data modeling are discussed in Section 5.6. The bottom inset displays the data residuals after subtracting the background model.

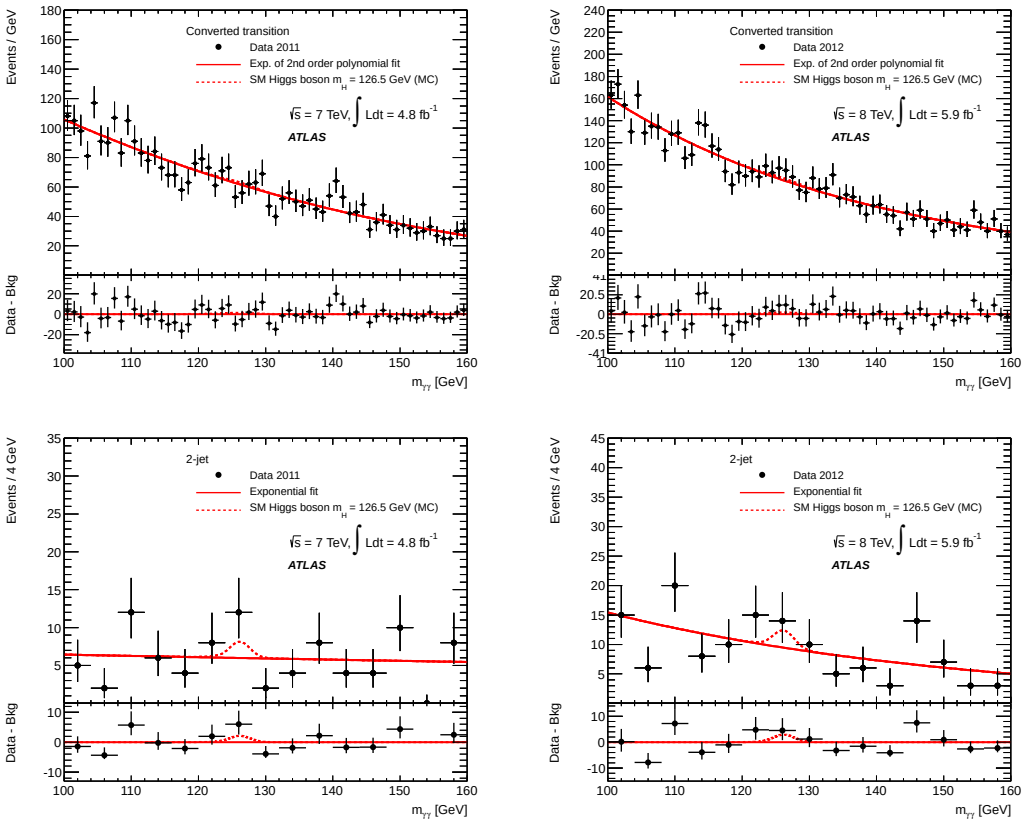

Figure 5.20: Diphoton Invariant mass distribution per category, on the left side for the 7 TeV data sample and on the right side for the 8 TeV sample. The overlaid solid red line present the background-only model fitted to the data, and the dashed line shows the expected $H \to \gamma\gamma$ signal for a Higgs boson of mass 126.5 GeV. Details on the data modeling are discussed in Section 5.6. The bottom inset displays the data residuals after subtracting the background model.

Table 5.5: Full width at half maximum (FWHM) expected for the signal peak in each category, and the signal-to-background ratio n_S/n_B expected for a $m_H = 126.5$ GeV SM Higgs boson. For the signal-to-background ratio calculation, the number of background events is extracted from a background model fit to the data, integrating the number of events in the mass region containing 90% percent of the signal peak; then, of course only 90% of the signal events is considered.

	$\sqrt{s} = 7$ TeV				$\sqrt{s} = 8$ TeV			
Category	FWHM	n_S	n_B	n_S/n_B	FWHM	n_S	n_B	n_S/n_B
Inclusive	3.8	72	2559	0.028	3.9	101	3585	0.028
Unconverted central, low p_{Tt}	3.4	9.4	155	0.061	3.4	13	225	0.057
Unconverted central, high p_{Tt}	3.2	1.3	7.2	0.181	3.2	2.3	13.6	0.169
Unconverted rest, low p_{Tt}	3.7	20	670	0.029	3.7	28	1122	0.025
Unconverted rest, high p_{Tt}	3.4	2.5	39	0.066	3.6	4.7	68	0.069
Converted central, low p_{Tt}	3.8	6.0	136	0.044	3.9	8.0	187	0.043
Converted central, high p_{Tt}	3.5	0.9	6.4	0.141	3.5	1.5	9.7	0.155
Converted rest, low p_{Tt}	4.2	19	967	0.020	4.4	24	1300	0.019
Converted rest, high p_{Tt}	3.8	2.5	51	0.049	3.9	4.0	71	0.056
Converted transition	5.5	8.5	704	0.012	6.1	12	821	0.014
2-jet	3.6	2.0	8.7	0.230	3.7	2.7	13.3	0.203

5.5.5 Systematic uncertainties on the distribution of signal events among the categories

Here is a list of factors that may change the expected distribution of the signal events among the various categories:

- **Amount of material in front of the calorimeter:** If the amount of material is higher than what is estimated, the photon conversion rate would increase, increasing the number of events in the converted categories and reducing it in the unconverted ones. This uncertainty has been evaluated comparing the nominal number of events per category with another set obtained with a different Monte Carlo sample produced with a modified description of the detector. An uncertainty of 4% has been assigned to the number of events in the unconverted categories. The number of events corresponding to this 4% of the unconverted categories represent 3.5% of the converted categories.

- **Pileup effects:** As discussed in Chapter 3, Section 3.1, an increase of the amount of pileup events may increase artificially the photon conversion rate, by increasing the fake conversion reconstruction. Also, more pileup may increase the number of signal events passing the selection for the two-jet category, because of jets from the pileup events triggering the selection. This uncertainty has been evaluated following the same procedure used to evaluate the uncertainty on the mass resolution due to pileup effects (Section 5.3.1). The uncertainties that have been assigned are quoted in Table 5.7. The uncertainty for the 2-jet category is significantly higher for the $\sqrt{s} = 8$ TeV MC samples than for the 7 TeV ones because of the different pileup conditions.

- **Theoretical uncertainty on the Higgs boson p_{T} distribution:** A variation of the Higgs boson p_{T} distribution induces variations in the distribution of the signal events between the low and high p_{Tt} categories. As the kinematics of jets associated to the Higgs boson production is correlated to the Higgs boson transverse momentum, it affects also the 2-jet category. This uncertainty has been evaluated modifying the scale and parton distribution functions used in the Monte Carlo sample generation. The uncertainties that have been assigned are quoted in Table 5.7.

- **Theoretical uncertainty on the cross-section for $gg \to H + 2\,jets$:** This uncertainty has an impact on the number of signal events from gluon fusion in the 2-jet category, while it is negligible for the rest of categories. It has been evaluated following the studies from [133,134], and has been found to be 25%.

- **Underlying event simulation:** The uncertainty due to the modeling of the underlying event is estimated by comparing Monte Carlo samples generated with different tunes of the underlying event [88]. The AUET2B tune is used for the default results, while the Perugia2011 tune is used for systematic studies. For the 2-jet category, a 30% uncertainty is assigned to the contribution from gluon fusion and the associated production processes, and a 6% uncertainty is assigned to the contribution from vector-boson fusion.

Table 5.6: Systematic uncertainties on the signal peak position due to the uncertainties on the photon energy scale, for each of the categories.

Category	Relative uncertainty on the signal peak position [%]				
		Amount of material		Presampler	
	Method	$\|\eta\| < 1.8$	$\|\eta\| > 1.8$	Barrel	End-Cap
Unconverted central, low p_{Tt}	±0.3	±0.3	-	±0.1	-
Unconverted central, high p_{Tt}	±0.3	±0.3	-	±0.1	-
Unconverted rest, low p_{Tt}	±0.3	±0.5	±0.1	±0.2	-
Unconverted rest, high p_{Tt}	±0.3	±0.5	±0.1	±0.3	-
Converted central, low p_{Tt}	±0.3	±0.1	-	-	-
Converted central, high p_{Tt}	±0.3	±0.1	-	-	-
Converted rest, low p_{Tt}	±0.3	±0.2	±0.1	±0.1	-
Converted rest, high p_{Tt}	±0.3	±0.2	±0.1	±0.1	-
Converted transition	±0.4	±0.6	-	-	±0.1
2-jet	±0.3	±0.3	-	±0.1	-

- **Jet energy scale:** The uncertainty from the jet energy scale is evaluated by varying the scale corrections within their respective uncertainties [130]. The uncertainty on the number of events per category is found to be 19% for the 2-jet category, and 4% for the other categories. On the other hand, the uncertainty on the jet energy resolution is found to have a negligible impact.

- **Tracking jet-vertex fraction:** The systematic uncertainty on the efficiency of the jet-vertex-fraction requirement is estimated from the differences of efficiencies between data and MC simulation in $Z + 2jets$ events. For the $\sqrt{s} = 8$ TeV analysis, a 13% uncertainty is assigned.

- **Primary vertex selection:** The quantity sum of track ${p_{\mathrm{T}}}^2$, evaluated for signal and background, used for the identification of the primary vertex, has been varied by an amount larger than the difference observed between data and MC. The effect on the expected yield in the different categories is smaller than 0.1% and is neglected.

The factors inducing uncertainties on the photon energy and therefore on the signal peak position have been introduced in the Section 5.3.2. These factors affect differently the various categories. Table 5.6 summaries the uncertainties for each category.

5.6 Data modeling

5.6.1 Signal parametrization

Figure 5.7 shows on the right side in blue the invariant mass distribution expected in this analysis, for a SM Higgs boson with mass 125 GeV, at $\sqrt{s} = 8$ TeV, and the continuous blue line shows the parametrization model. The model F_{s} consists of a

narrow Crystall Ball function[2] $F_{\rm CB}$ plus a gaussian $F_{\rm G}$, as follows:

$$F_{\rm S}(m_{\gamma\gamma};\mu_{\rm CB,G},\sigma_{\rm CB},\alpha_{\rm CB},n_{\rm CB},f_{\rm CB},\sigma_{\rm G}) = f_{\rm CB}F_{\rm CB}(m_{\gamma\gamma};\mu_{\rm CB,G},\sigma_{\rm CB},\alpha_{\rm CB},n_{\rm CB})+ \\ (1-f_{\rm CB})F_{\rm G}(m_{\gamma\gamma};\mu_{\rm CB,G},\sigma_{\rm G}); \tag{5.7}$$

where $F_{\rm CB}$ and $F_{\rm G}$ are normalized to one, $f_{\rm CB}$ is the fraction of the distribution corresponding to the Crystall Ball, $\sigma_{\rm CB}$, $\alpha_{\rm CB}$ are $n_{\rm CB}$ are parameters of the Crystall Ball, $\sigma_{\rm G}$ is a gaussian parameter, and $\mu_{\rm CB,G}$ is a common parameter of both functions. The Crystall Ball function is the main component of the model. The non-gaussian tail toward low mass arises mostly from events with converted photons that have lost a significant fraction of energy in the inner detector material. The second term of the model, the gaussian, corresponds only to a few percents of the distribution. This gaussian component is wider than the Crystall Ball, and it models the events with mis-calibrated photons and invariant mass laying far outside of the peak. The Crystall Ball and gaussian are constrained to have the maximum at the same position $\mu_{\rm CB,G}$.

As mentioned in Section 5.2.3, signal Monte Carlo (MC) samples have been generated for several values of $m_{\rm H}$, from 100 to 150 GeV, in steps of 5 GeV. But in the statistical analysis, the signal hypothesis is tested every 0.5 GeV, and one might need to do it with an even finer step; for example in the case of observing a signal, for the signal mass measurement. Then, in order to extrapolate the resolution function for the intermediate $m_{\rm H}$ values in a smooth way, a global fit of all the signal MC samples is performed, where the signal model parameters are function of $m_{\rm H}$. It provides a continuous smooth function for the resolution at any $m_{\rm H}$ value in the required range. Additionally, in this way one exploits at maximum the statistical power of the MC samples, unlike fitting each sample separately. The width of the peak and therefore the parameters $\sigma_{\rm CB}$ and $\sigma_{\rm G}$ increase linearly, as the mass hypothesis $m_{\rm H}$ increases.

This global fit includes also the parametrization of the number of signal events expected for every Higgs boson mass hypothesis $m_{\rm H}$. This number is found to change parabolically as function of $m_{\rm H}$, with a maximum around $m_{\rm H} = 115$ GeV. The signal related values quoted in tables 5.1, 5.3 and 5.5 are outputs of the global signal model.

The global fit is of course performed separately for every event category.

[2]The Crystall Ball function consists of a gaussian core with a power law tail on one side [98]. It is defined as follows:

$$F_{\rm CB}(m;\mu,\sigma,\alpha,n) = N \begin{cases} e^{-\frac{(m-\mu)^2}{2\sigma^2}} & \text{for } \frac{m-\mu}{\sigma} < -\alpha \\ A\left(B-\frac{m-\mu}{\sigma}\right)^{-n} & \text{for } \frac{m-\mu}{\sigma} \geqslant -\alpha \end{cases}$$

where

$$A = \left(\frac{n}{|\alpha|}\right)^n e^{-\frac{\alpha^2}{2}}, \\ B = \frac{n}{|\alpha|} - |\alpha|.$$

Where μ and σ are the usual parameters of a gaussian function; μ is the position of the peak maximum and σ control the peak width; n is the power for the tail; α corresponds to the point at which the gaussian becomes the power law tail; and N is a normalization factor.

5.6.2 Signal systematic uncertainties

The systematic uncertainties on the expected signal have been discussed separately in the previous sections, and are now compiled in Table 5.7. These uncertainties can be classified in four sets, the ones affecting the expected number of events, the uncertainties on the distribution of events among the categories (producing event migrations), the ones affecting the mass resolution and the signal peak position.

Table 5.7: Compilation of systematic uncertainties on the expected signal. The values given are relative uncertainties in percent unit.

Uncertainties source	Relative uncertainty [%]		
	$\sqrt{s} = 7$ TeV		$\sqrt{s} = 8$ TeV
Event yield			
Higgs boson cross section (perturbative)	ggF: $^{+12}_{-8}$		ggF: $^{+7}_{-8}$
Higgs boson cross section (PDF+α_S)	ggF: $^{+8}_{-7}$		ggF: $^{+8}_{-7}$
	VBF: $^{+2.5}_{-2.1}$		VBF: $^{+2.6}_{-2.8}$
Photon identification	± 8		± 11
Higgs boson branching ratio		± 5	
Pileup effects on the photon rec/ID		± 4	
Trigger		± 1	
Luminosity	± 1.8		± 3.6
Distribution of events among the categories			
Material		Unconv: ± 4	
		Conv: ∓ 3.5	
Pileup effect	Unconv: ± 3		Unconv: ± 2
	Conv: ∓ 2		Conv: ∓ 2
	2-jets: ± 2		2-jets: ± 12
Higgs boson p_{T} modeling		Low p_{Tt}: ± 1.1	
		High p_{Tt}: ∓ 13	
		2-jets: ∓ 9	
$gg \to H + 2\,jets$ cross-section (2-jet)		± 25	
Underlying Event (2-jet)		ggF: ± 30	
		VBF: ± 6	
Jet energy scale (2-jet)	ggF: ± 19		ggF: ± 18
	VBF: ± 8		VBF: ± 9
Jet-vertex-fraction (2-jet)			± 12
Mass resolution			
Calorimeter energy resolution		± 12	
Electron to photon extrapolation of the calibration		± 6	
Effect of pileup on energy resolution		± 3	
Peak position			
Photon energy scale		see Table 5.6	

These systematic uncertainties have been taken into account by introducing in the model nuisance parameters with constraints, as explained in Section 4.5, Chapter 4. The uncertainties on the event yields and on the distribution of events among the categories are implemented with terms that scale the normalization of the signal pdf per category. The terms added to consider the uncertainties on the resolution affect the two parameters σ_{CB} and σ_{G}. The uncertainties quoted in Table 5.6 affect the parameter $\mu_{\mathrm{CB,G}}$ of the signal model. For most of the introduced nuisance parameters the constraint pdf is log-normal. Only for the event migration uncertainties, gaussian constraints are used. For the asymmetric uncertainties from the Higgs boson cross-section, asymmetric log-normal pdf's are used.

Most of the signal systematic uncertainties are treated as correlated between the different categories, and between the 7 and 8 TeV models. In these cases, for each uncertainty there is a single nuisance parameter common for all the categories. Only the luminosity uncertainty is treated as uncorrelated between 7 and 8 TeV, because

the luminosity measurement methods are different. In the case of the event migration uncertainties, the uncertainty effects are anti-correlated among some categories. For instance, an increase of the material in front of the calorimeter would increase the number of events in the converted categories, and decrease it in the unconverted categories, by the same number of events. That is why in Table 5.7 the two symbols $\pm$ and $\mp$ are used for some uncertainties.

5.6.3 Background parameterization and uncertainties

In this analysis, the invariant mass distribution of the background has a smoothly decreasing shape, as one can see in Figure 5.8. This is also the case after splitting the data in categories (see figures 5.18, 5.19 and 5.20). Initially, the background was parametrized with an exponential function. Then, as the amount of data has increased, reducing the relative size of the statistical fluctuations, small differences between the background model and the true shape of the background might have a non-negligible impact on the statistical analysis. This is true in particular because the amount of background is quite large compared with the size of the expected signal. An underestimation of the background in a region increases artificially the significance of any excess observed there, and oppositely an overestimation of the background decreases the excesses significance. In a similar way, this would bias the exclusion limit results.

In order to reduce possible bias from the background parameterization, one can for instance use a flexible functional form like a high order polynomial, which would guarantee a good fit of the background shape. But using a very flexible model would also reduce the statistical sensitivity to observe a signal. Then, one needs to choose a model keeping a compromise between statistical power and goodness of the background parameterization. The following sections contain descriptions of the procedures used to estimate the size of possible background modeling biases, to take into account the possible biases as a systematic uncertainty in the analysis, and to choose among various alternative models.

Estimation of the possible bias induced by a background model

Let us consider the effect of mis-modeling the background in terms of number of signal events fitted. Let us say that we generate toy pseudo-experiments with a background-only model, and then fit them with a signal-plus-background model. On one hand, if the background model used for the fit is the same as the one used to generate the toys, the average number of signal events fitted will be zero (i.e. statistically compatible with zero). On the other hand, if the background model used for the fit is different from the one used in the generation of toys, the background might be underestimated or overestimated in the region where the signal component is placed, and the average number of signal events fitted will deviate from zero. Thus, in this analysis a background mis-modeling is quantify as a bias on the number of signal events fitted. The exercise described above could be also done performing a single fit of an asimov dataset, instead of fitting toys pseudo-experiments (the asimov dataset principle is explained in Chapter 4, Seccion 4.3).

Now, the true background shape is not known precisely, but the possible bias induced by each of the models tested has been roughly estimated using three different

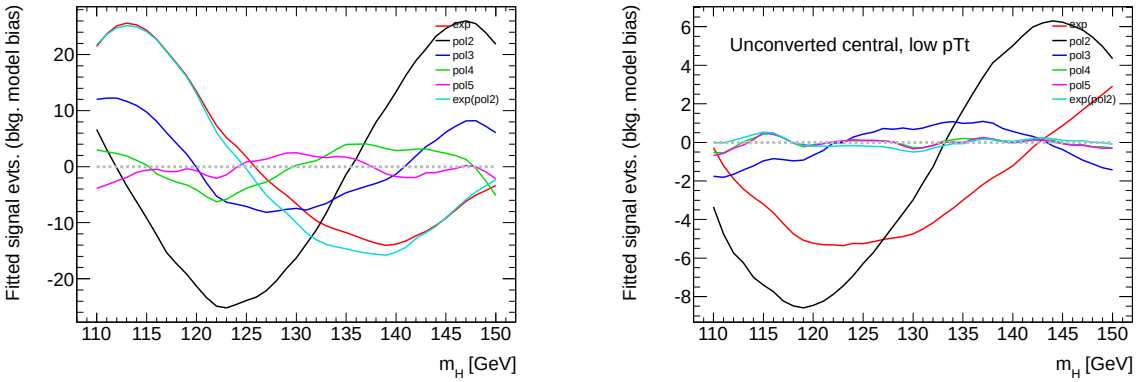

Figure 5.21: Number of signal events fitted as a function of the signal mass hypothesis m_{H}, obtained fitting a background-only Monte Carlo samples, at $\sqrt{s} = 7$ TeV. It is shown on the left side for the inclusive samples and on the right side for the category unconverted central, low p_{Tt}. The various curves were obtained with different functions as background model, an exponential function (*exp*), 2nd, 3rd, 4th and 5th order polynomials (*pol*2, *pol*3, *pol*4 and *pol*5), and the exponential of the a 2nd order polynomial(*exp*(*pol*2)).

Monte Carlo (MC) samples. The preparation of these samples has been described in Section 5.2.2. These MC samples have been prepared with very high number of events, so that the statistical fluctuations are negligible, like in an asimov dataset. The main component of the background (the $\gamma\gamma$ background) have been generated with three MC generators of high order calculations, RESBOS [118], DIPHOX [119], and SHERPA [116].

Each of these background-only MC samples has been fitted with signal-plus-background models, testing different functions for the background model, and varying the signal mass hypothesis m_{H} from 110 to 150 GeV. Figure 5.21 shows as example the number of signal events fitted as a function of m_{H} for the different background model functions, as obtained by fitting the DIPHOX MC sample for $\sqrt{s} = 7$ TeV; it is shown on the left side for the inclusive samples and on the right side for the category unconverted central, low p_{Tt}. As expected, one can see in this figure that using the exponential and 2nd order polynomial functions as background model, the bias induced by the model is larger than when using the high order polynomials, which are more flexible than the former ones. After performing these fits, the maximum absolute number of signal events fitted in the scanned range have been taken as estimator of the possible bias for the background model under test. The results on the bias estimation obtained with the three different MC samples are compatibles with each other.

Implementation of background modeling systematic uncertainties

The estimated possible bias from the background model is introduced in the statistical analysis as a systematic uncertainty. It is done by adding to the background pdf a component with the shape of the signal pdf, with the normalization floating, but with a gaussian constraint. The mean value of the gaussian constraint is set to zero, and the width (the parameter σ) is set to the value of the estimated possible bias; in this case, the possible bias estimated with the SHERPA sample is used.

As result of this implementation, the uncertainty on the signal strength parameter increases as if the background modeling uncertainty was added to it in quadra-

ture. In the presence of an excess, in most of the cases this uncertainty reduces the measured significance of the excess, and in the presence of a deficit, it reduces the confidence level on the exclusion limit set.

Procedure to choose the background model

Several alternative background models have been tested. A first filtering of the various models is done by requiring the estimated bias to be less than 20% of the statistical uncertainty on the strength parameter μ, or less than 10% of the expected number of signal events for a SM Higgs boson. If none of the two requirements are satisfied, the background model under test is rejected. In this case, the results obtained with the three Monte Carlo samples is considered, taking the maximum estimated bias to match this requirement.

Then, with the remaining models, the expected p_0 value for a SM Higgs boson is computed, including the estimated bias for each of them as systematic uncertainty with the procedure described above. The choice of the model is done based on the expected p_0 value at $m_{\mathrm{H}} = 125$ GeV obtained with each alternative. In this way, both the systematic uncertainty and the statistical power associated to each background model is considered for the selection.

Background models tested

Various functional forms have been tested as background model, an exponential function, the sum of two exponentials, polynomials of second, third, fourth and fifth order, the exponential of a second order polynomial, and the exponential of a third order polynomial.

Another alternative that has been also tested is performing the fit in a reduced mass range; the nominal fitting range covers 60 GeV (from 100 to 160 GeV), and ranges of 40 and 30 GeV have been also tested. In these cases the fitting range has been changed according to the signal mass hypothesis m_{H} under test, in such a way that m_{H} is at the center of the fitting range. For example, when fitting with a 30 GeV range, the fits for the signal hypothesis $m_{\mathrm{H}} = 115$ GeV have been performed in the range 100 - 130 GeV, while for the hypothesis $m_{\mathrm{H}} = 150$ GeV the fitting range is 135 - 165 GeV[3]. On one hand, reducing the fitting range allows a given functional form to fit the main region of interest, without requiring it to fit far away side bands. In this way, the possible background modeling bias are reduced. But on the other hand, the amount of data fitted is reduced and so the statistical power decreases.

Results of the background parameterization studies

The estimation of the possible bias and the choice of the background model have been done separately for each category. The obtained results are summarized in Table 5.8. It shows the functional form chosen for each data category, and the estimated uncertainty for each of them. The fitting range chosen is the nominal [100 - 160 GeV]. The single exponential function is used for the categories with low

[3]As the background distribution below 100 GeV change of form because of the Drell-Yan peak and the kinematic turn-on, the fitting ranges have been limited to be always above 100 GeV. Thus, following the previous example, for $m_{\mathrm{H}} = 110$ GeV the fitting range used is 100 - 130 GeV.

Table 5.8: List of the functional forms chose for each of the categories, and the estimated possible bias from the model, which are used as systematic uncertainty in the statistical analysis. The systematic uncertainty is quoted as number of events.

Category	Parametrization	Uncertainty [N_{evt}]	
		$\sqrt{s} = 7$ TeV	$\sqrt{s} = 8$ TeV
Inclusive	4th order pol.	7.3	10.6
Unconverted central, low p_{Tt}	Exp. of 2nd order polynomial	2.1	3.0
Unconverted central, high p_{Tt}	Exponential	0.2	0.3
Unconverted rest, low p_{Tt}	4th order polynomial	2.2	3.3
Unconverted rest, high p_{Tt}	Exponential	0.5	0.8
Converted central, low p_{Tt}	Exp. of 2nd order polynomial	1.6	2.3
Converted central, high p_{Tt}	Exponential	0.3	0.4
Converted rest, low p_{Tt}	4th order polynomial	4.6	6.8
Converted rest, high p_{Tt}	Exponential	0.5	0.7
Converted transition	Exp. of 2nd order polynomial	3.2	4.6
2-jets	Exponential	0.4	0.6

number of events in the sample, and a 4th order polynomial or the exponential of a 2nd order polynomial are used to fit the data samples with high number of events.

5.7 Results

The data distribution has been compared with the background-only and signal-plus-background hypotheses, following the procedure described in Chapter 4. With the amount of data considered in this analysis, we have the sensitivity necessary to observe the Standard Model (SM) Higgs boson in most of the scanned mass range. And in fact a signal-like excess of events has been observed in the region around 126 GeV. In the first section, the exclusion limit set aside this excess are presented, and then studies and quantification of the excess are discussed.

5.7.1 Exclusion limits

The obtained exclusion limits are shown in Figure 5.22, as a function of the Higgs boson mass hypothesis m_{H}. This figure shows in the top part the limits obtained independently with each sample, on the left side for the 7 TeV sample and on the right side for the 8 TeV sample, and in the bottom part the results obtained combining both samples. These are 95% confidence level upper limits on a SM-like Higgs boson production cross-section, normalized to the SM predicted cross-section.

Combining the two samples (see the bottom part of the figure), the expected median limits under the background-only hypothesis (red line) vary between 0.8 and 1.6 times the SM cross-section, with values below one in the mass range 110.0 - 140.5 GeV. On the other hand, the observed limit values (black line) are below one in the mass ranges 112.0 - 123.0 GeV and 132.0 - 143.5 GeV, and so the SM Higgs boson is excluded with 95% confidence level in these two regions.

But in the region around 126 GeV, the observed limits are significantly deviated upward from the expected values, which indicates the presence of an excess of events. On the top part of the figure, one can see that this excess appears in each of the samples. The quantification of this excess is presented in the next section.

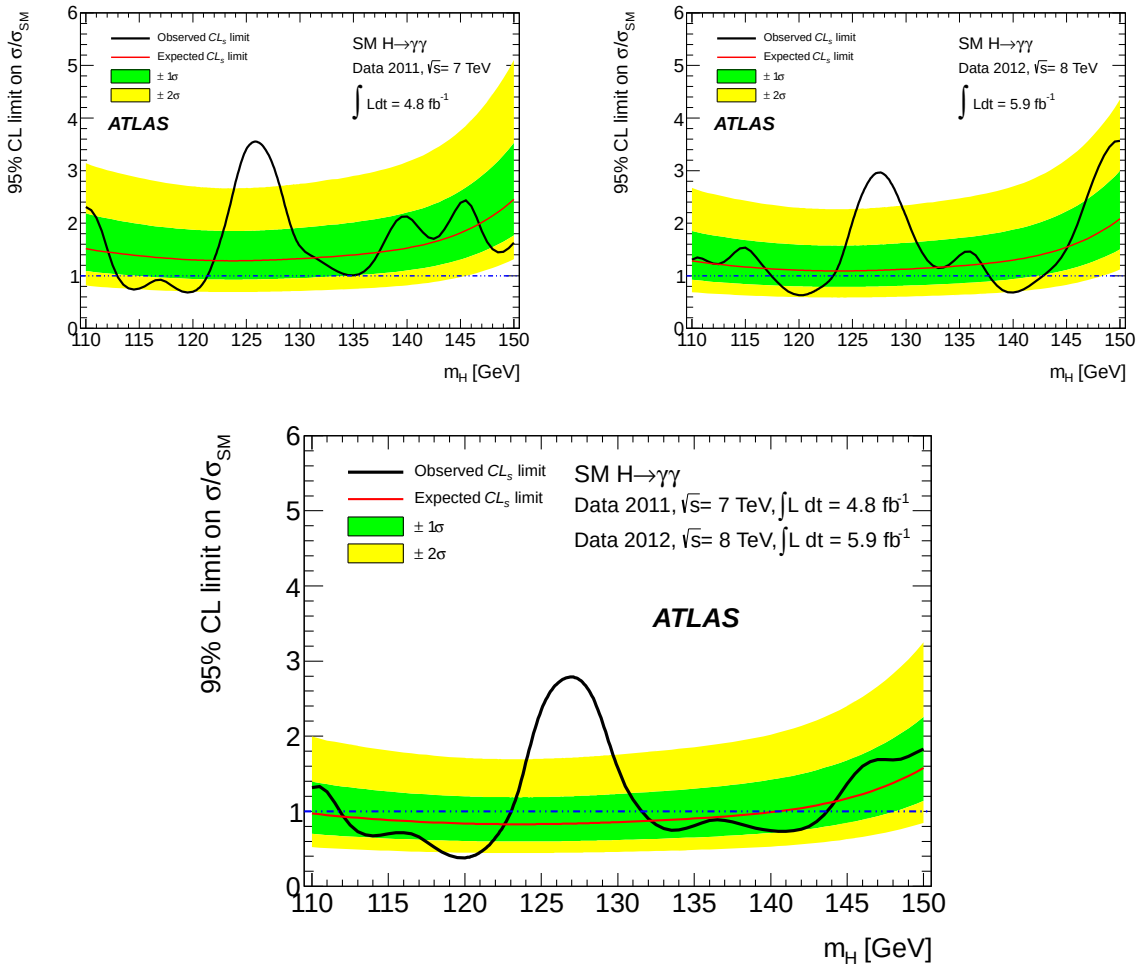

Figure 5.22: 95% confidence level upper limits on a SM-like Higgs boson production cross-section, normalized to the SM predicted cross-section, as a function of the boson mass hypothesis m_{H}. It is shown on the top part as obtained independently with each sample, on the left side for the 7 TeV sample and on the right side for the 8 TeV sample, and on the bottom part as obtained combining both samples. The black line shows the observed limits. And the red line, the green and yellow bands, show the expected median limits, the one and two standard deviations respectively, under the background-only hypothesis.

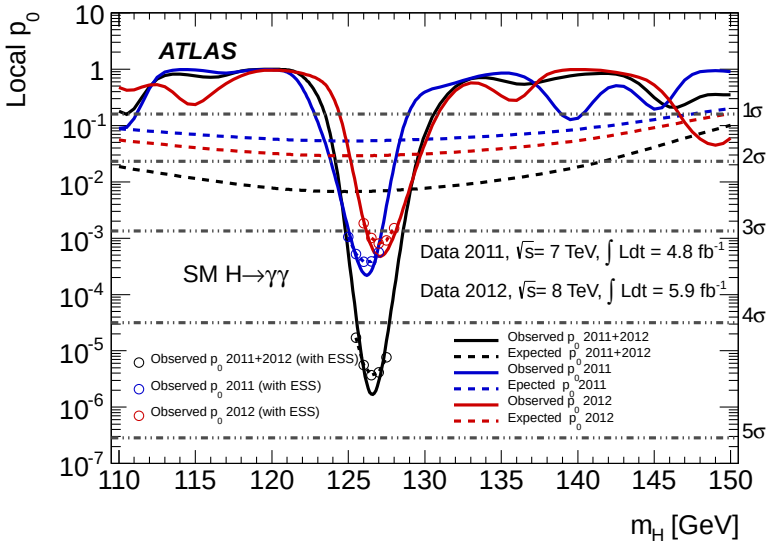

Figure 5.23: Probability p_0 of the background to fluctuate creating a signal-like excess equal or larger than what is observed, as a function of the Higgs boson mass hypothesis m_{H}. It is shown as obtained independently with each sample, and from the combination of both, the 7 and 8 TeV samples. The solid lines show the observed p_0, and the dashed lines show the expected median p_0 in the case of having a SM signal at m_{H}. The circles show the observed p_0 considering the energy scale systematic uncertainty (ESS), obtained via pseudo-experiments.

5.7.2 Excess quantification

The obtained p_0 values are shown in Figure 5.23, as a function of the Higgs boson mass hypothesis m_{H}. As explained in Chapter 4, p_0 is the probability of the background to fluctuate creating a signal-like excess equal or larger than what is observed. Thus, the lower is the p_0 value, the less compatible is the data with the background-only hypothesis, or in other words the more likely is a signal to be there. The figure shows the results obtained independently with each sample, and from the combination of both, the 7 and 8 TeV samples.

In this figure, the solid lines show the observed p_0 values. In the 7 and 8 TeV samples separately, the lowest p_0 values are found precisely at $m_{\mathrm{H}} = 126.0$ GeV and 127.0 GeV respectively (the mass scan have been done with 0.5 GeV steps). These p_0 values are of 2.4×10^{-4} and 4.8×10^{-4}, and they correspond to 3.5 and 3.3 standard deviations σ, respectively.

Combining the two samples, the lowest p_0 value is found at $m_{\mathrm{H}} = 126.5$ GeV, it is 1.7×10^{-6}, and it corresponds to 4.6σ.

In addition, at the excess region, the observed p_0 values have been computed considering the systematic uncertainty on the energy scale (ESS), via pseudo-experiments; it is shown by circles in the figure. In this case, for the combined result, the significance of the excess is 4.5σ.

Finally, considering the look-elsewhere effect, the global significance of the excess is 3.6σ. As explained in Chapter 4, this correction takes into account the fact that the test statistic is not only performed at one mass point, but it is done at different points in the range 110 - 150 GeV. Thus, this correction provides the probability of finding such an excess (or larger) anywhere in the scanned region, under the background-only hypothesis.

Figure 5.23 also shows the expected median p_0 in the case of having a Standard

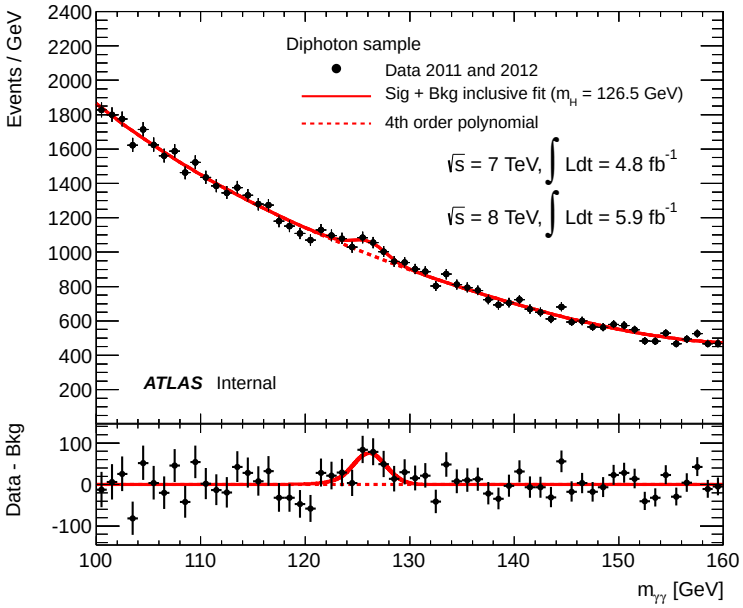

Figure 5.24: Diphoton invariant mass distribution, for the 7 and 8 TeV data samples together, overlaid with a signal-plus-background model (solid line) fitted to this inclusive data distribution. The signal model used corresponds to $m_{\mathrm{H}} = 126.5$ GeV. The dashed line shows the background component, a fourth order polynomial function. And the bottom inset displays the data residuals after subtracting the background component.

Model signal at m_{H}. It is shown by the dashed lines. One can see that the observed excess is more significant than the signal expected median. At 126.5 GeV, the expected median local significance is 2.5σ, while the corresponding observed value quoted above is 4.6σ. Nevertheless, as will be shown in the next section, the observed excess is still compatible with a SM Higgs boson.

The inclusive distribution of the diphoton invariant mass for the 7 and 8 TeV data samples together is shown in Figure 5.24, overlaid with a signal-plus-background model fit. The signal component used corresponds to the Higgs boson mass hypothesis of 126.5 GeV, and the background has been modeled with a fourth order polynomial. The bottom inset displays the data residuals after subtracting the background component of the model.

Some additional checks of the observed excess have been performed, quantifying the excess significance without splitting the data samples in categories, and also using a nine categories separation without separating the VBF like events. The results obtained are shown in Figure 5.25; on the left side it shows the obtained p_0 values, and on the right side it shows the corresponding significance (for the inclusive and ten categories analysis only). The observed significance of the excess obtained with the ten category analysis is higher than when the inclusive analysis is performed, as expected for a SM Higgs boson like signal.

The excess quantification has also been done considering the sample for each individual category separately. The obtained p_0 values are shown in the top part of Figure 5.26, on the left side for the 7 TeV sample and on the right side for the 8 TeV sample, and in the bottom part the corresponding significances are shown. One can see that the 126.5 GeV excess is consistently present in most of the individual category sub-samples.

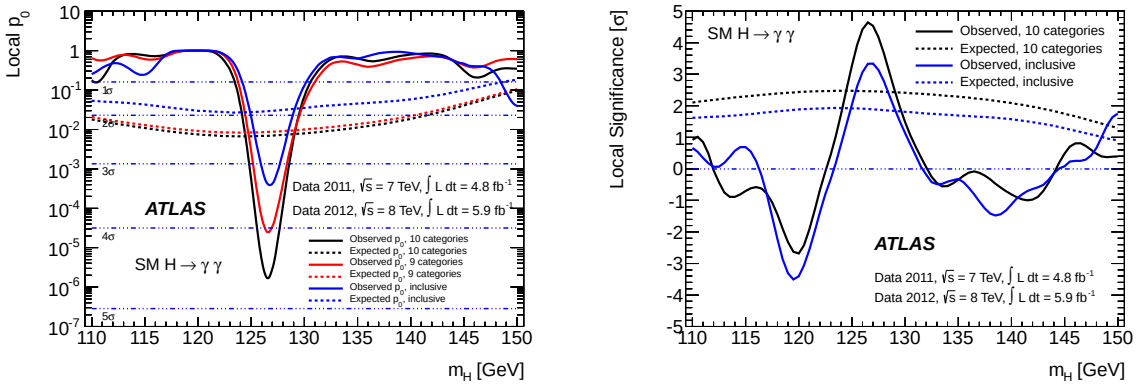

Figure 5.25: Probability p_0 of the background to fluctuate creating a signal-like excess equal or larger than what is observed (on the left side), and the corresponding significance in terms of standard deviations (on the right side). It is shown as a function of m_{H}, as obtained from the combination of the 7 and 8 TeV data samples. The solid lines show the observed values, and the dashed lines show the expected median value for a SM signal at m_{H}. The black lines show the result obtained in the nominal way, using the 10 data categories per sample; the red lines (shown on the left side plot only) present what is obtained without creating a 2-jet category, but using only 9 categories per sample; and the blue lines are obtained without any data categorization.

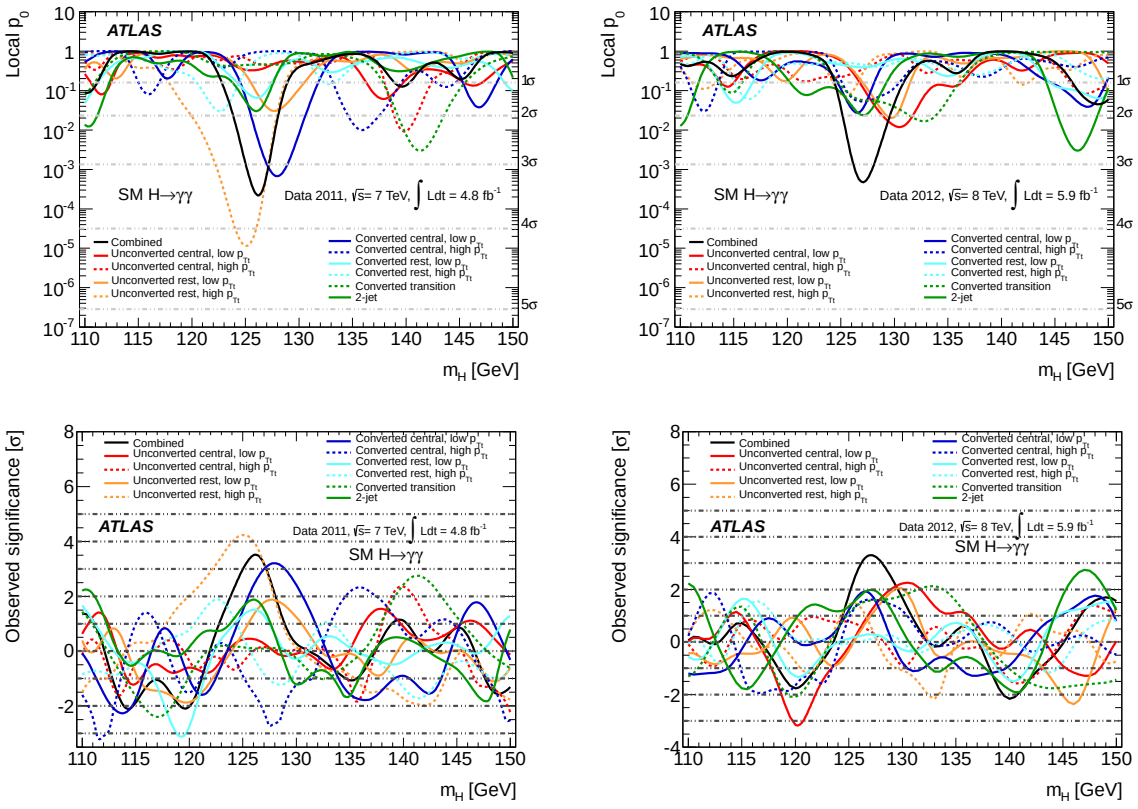

Figure 5.26: Probability p_0 of the background to fluctuate creating a signal-like excess equal or larger than what is observed (on the top part), and the corresponding significance in terms of standard deviations (on the bottom part). It is shown as a function of m_{H}, as obtained separately with the 7 TeV sample (left side) and with the 8 TeV samples (right side). The colored curves present the result obtained independently with each category, while the black curves correspond to the 10 category combine result.

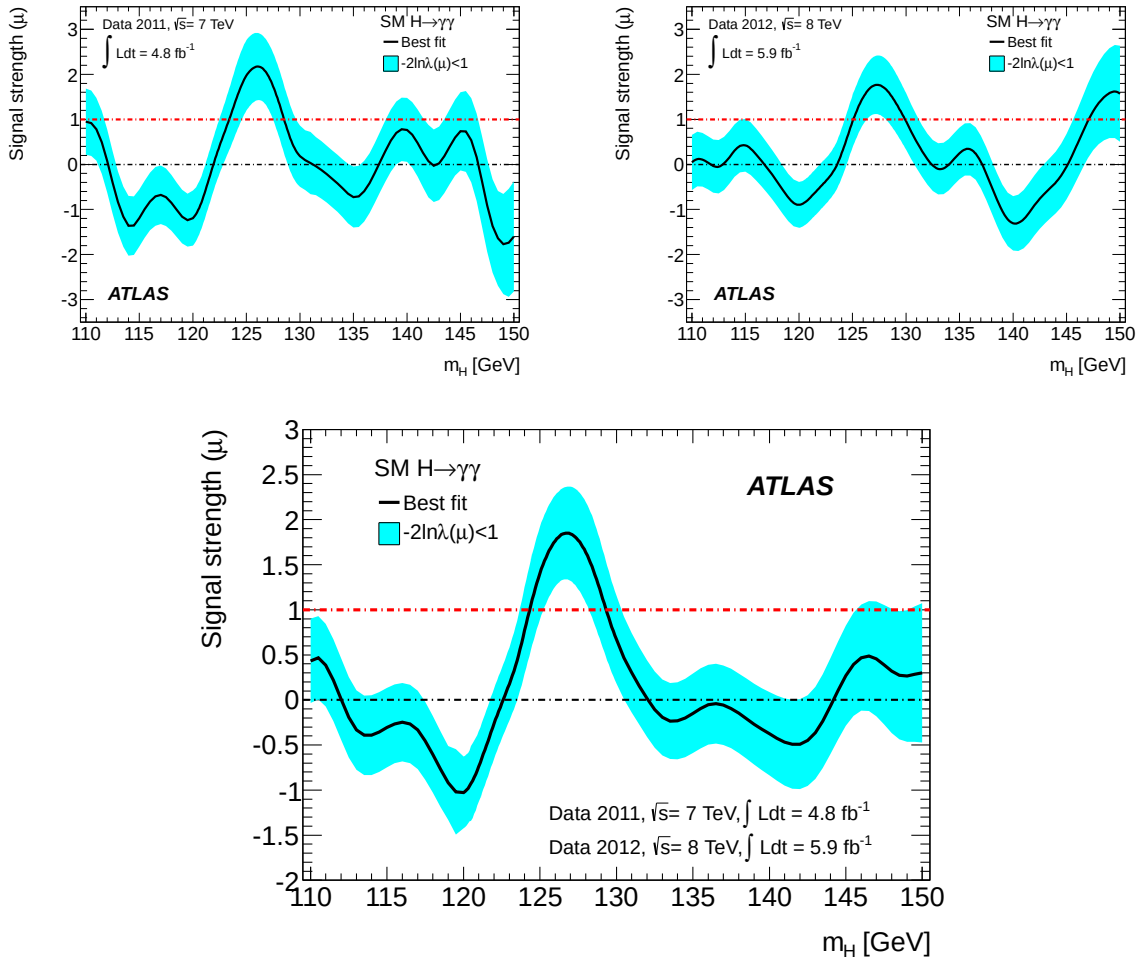

Figure 5.27: The best-fit signal strength μ as a function of the Higgs boson mass hypothesis m_{H}. It is shown on the top part as obtained independently with each sample, on the left side for the 7 TeV sample and on the right side for the 8 TeV sample, and on the bottom part as obtained combining both samples. The band indicates the approximate 68% confidence level interval around the fitted value.

5.7.3 Excess characterization

The signal strength parameter μ has been defined in Chapter 4 as a scale factor on the expected number of signal events, for the Standard Model Higgs boson. The signal strength values that best-fit the data sample for the different m_{H} hypotheses are shown in Figure 5.27, as a function of m_{H}. For the excess position, $m_{\mathrm{H}} = 126.5$ GeV, the best-fit signal strength is shown in Figure 5.28, as obtained independently for each data category. Both figures, 5.27 and 5.28, show in the top part the results obtained for each data sample, on the left side for the 7 TeV sample and on the right side for the 8 TeV sample, and in the bottom part the results obtained from the combination.

From the combined result, at $m_{\mathrm{H}} = 126.5$ GeV, the best-fit signal strength is 1.8 ± 0.5. The results from the independent fits per category are statistically consistent with this value.

Considering the uncertainty, this μ value is compatible with one, which corresponds to the SM cross-section for the Higgs boson. Additionally, since this μ value was taken at the m_{H} value giving the largest deviation from the background-only

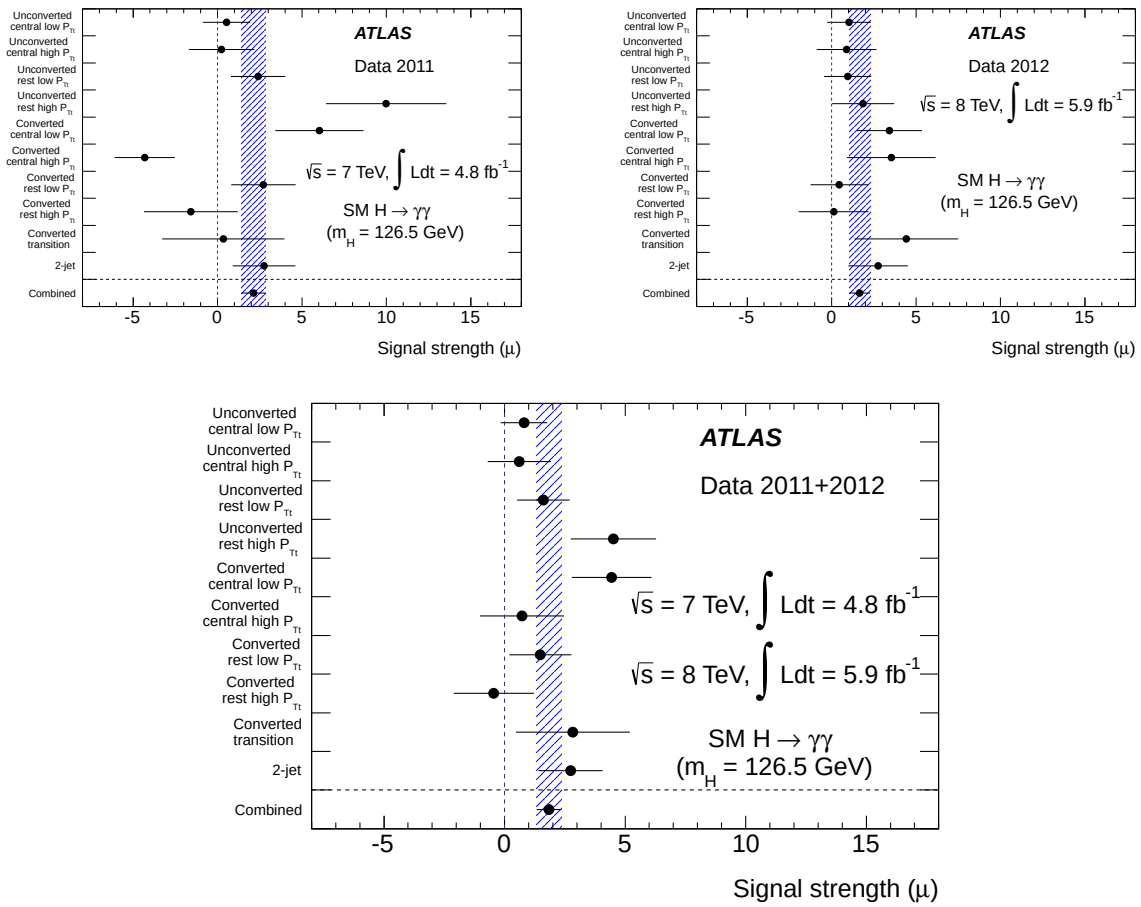

Figure 5.28: The best-fit signal strength μ at $m_{\mathrm{H}} = 126.5$ GeV obtained independently for each of the data category, and the category combined result. It is shown on the top part as obtained independently with each sample, on the left side for the 7 TeV sample and on the right side for the 8 TeV sample, and on the bottom part as obtained combining both samples. And the result from combining both samples is shown in the bottom part.

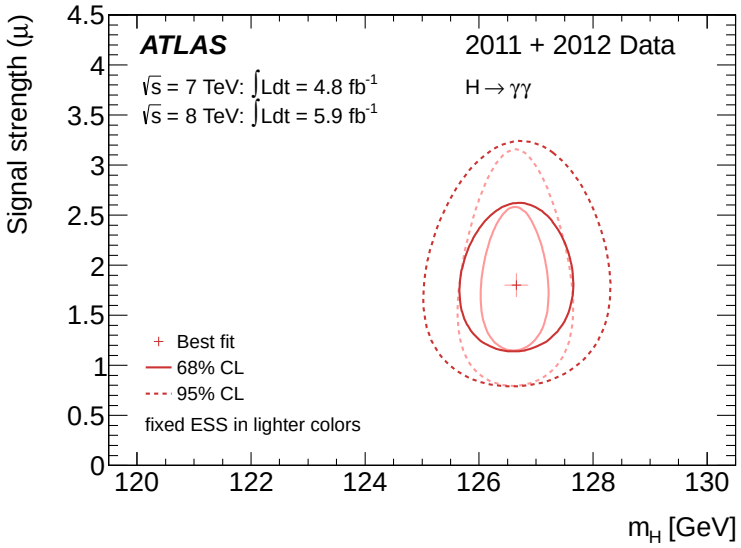

Figure 5.29: Contour plot of the test statistic $-2\ln\lambda(\mu, m_{\mathrm{H}})$ (see Equation 4.2 in Chapter 4), as a function of the signal hypothesis strength μ and mass m_{H}. The cross corresponds to the minimum of the test statistic, or best fit, and the solid and dashed contour lines enclose the 68% and 95% confidence level regions respectively. The dark lines were obtained considering the energy scale systematic uncertainty, while for the light lines this uncertainty was not considered.

hypothesis, it is expected to have a positive bias, induced by positive fluctuations of the background in the near region. This bias has been estimated with pseudo-experiments and found to be about 8%.

Given the expected number of signal events quoted in Table 5.3, Section 5.5.4, $\mu = 1.8$ corresponds to about 340 signal events.

Now, in order to estimate both the mass and strength of this potential signal that simultaneously best-fit the data, the following have been done. A two dimensional scan of the test statistic $-2\ln\lambda(\mu, m_{\mathrm{H}})$ [4] have been performed in the plane defined by the two parameters, m_{H} and μ. The result is shown in Figure 5.29. The cross corresponds to the minimum of the test statistic, or best fit, and the solid and dashed contour lines enclose the 68% and 95% confidence level regions respectively. These contour lines have been computed assuming that the test statistic follows the χ^2 distribution, for the case of two degrees of freedom. This asymptotic assumption has been validated with pseudo-experiments.

The dark lines in Figure 5.29 were obtained considering the systematic uncertainty on the energy scale, while for the light lines this uncertainty was not considered. For the signal mass measurement, one can see that this systematic uncertainty is as large as the statistical uncertainty.

The event categorization used in this analysis is sensitive to the SM Higgs boson production modes. In this categorization, events are separated according to the p_{Tt} values, which are typically lower for events produced by gluon fusion than for those from other production modes. And there is one category for VBF-like events. So, one can test also the consistency of the potentially observed particle with the SM Higgs boson on the production modes.

With this purpose, the signal probability density function (pdf) have been de-

[4] see Equation 4.2 in Chapter 4

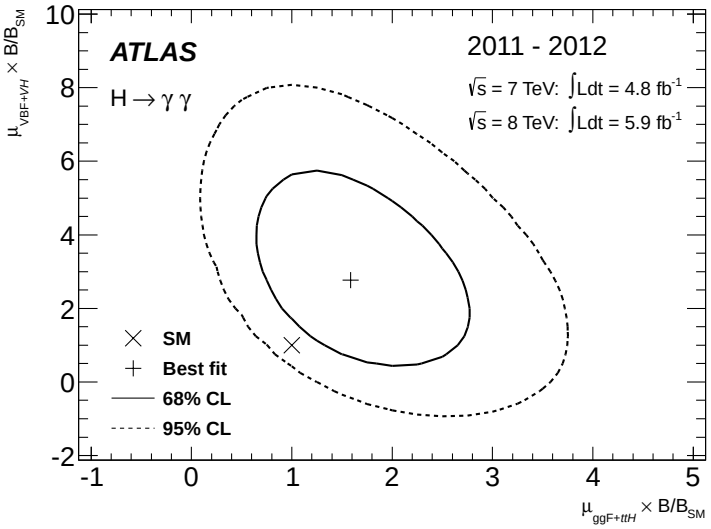

Figure 5.30: Contour plot of the test statistic, as a function of the two independent signal strength factors $\mu_{\mathrm{VBF+VH}}$ and $\mu_{\mathrm{ggF+t\bar{t}H}}$ for the different Higgs boson production modes. The mark $\times$ indicates the point one-one, which corresponds to the Standard Model expectation. The cross corresponds to the minimum of the test statistic, or best fit, and the solid and dashed contour lines enclose the 68% and 95% confidence level regions respectively.

composed in two components. One component corresponds to the production modes gluon fusion (ggF) and the associated production with top quarks ($t\bar{t}H$); both of these processes depend on the coupling tH. The other component corresponds to the production modes vector-boson fusion (VBF) and the associated production with Z or W (VH); they depend on the coupling WH/ZH. Two independent signal strength factors are defined for these two components; they are designated $\mu_{\mathrm{ggF+t\bar{t}H}}$ and $\mu_{\mathrm{VBF+VH}}$. Actually, the two signal pdf components per category have basically the same shape; it is only the distribution of signal events among the various categories that is different.

Then, the values of $\mu_{\mathrm{VBF+VH}}$ and $\mu_{\mathrm{ggF+t\bar{t}H}}$ that are simultaneously compatibles with the data sample have been estimated with the test statistic. The signal peak position is treated as a nuisance parameter. The result is shown in Figure 5.30. The mark $\times$ indicates the point one-one, which corresponds to the Standard Model expectation. The cross corresponds to the best-fit, and the solid and dashed contour lines enclose the 68% and 95% confidence level regions respectively. The excess is found to be compatible with the SM expectation for the Higgs boson.

Chapter 6

Overview of recent results of the Higgs boson search

This is an overview of recent results of the search for the Standard Model (SM) Higgs boson, by the ATLAS and CMS collaborations, and by the experiments at the Tevatron [21, 106, 135–141].

With the collisions provided by the LHC during 2011 and 2012, the ATLAS and CMS experiments achieved sensitivities beyond the one required to observe the SM Higgs boson, in the mass range from 110 GeV to around 600 GeV. Apart of the region around 125 GeV, the existence of a SM Higgs boson anywhere else in all this mass range has been excluded with at least 95% of confidence level, by either of the two experiments; Figure 6.1 presents the expected and observed upper limits on a SM-like Higgs boson production cross-section, obtained by ATLAS and CMS on the left and right plot respectively [106, 136].

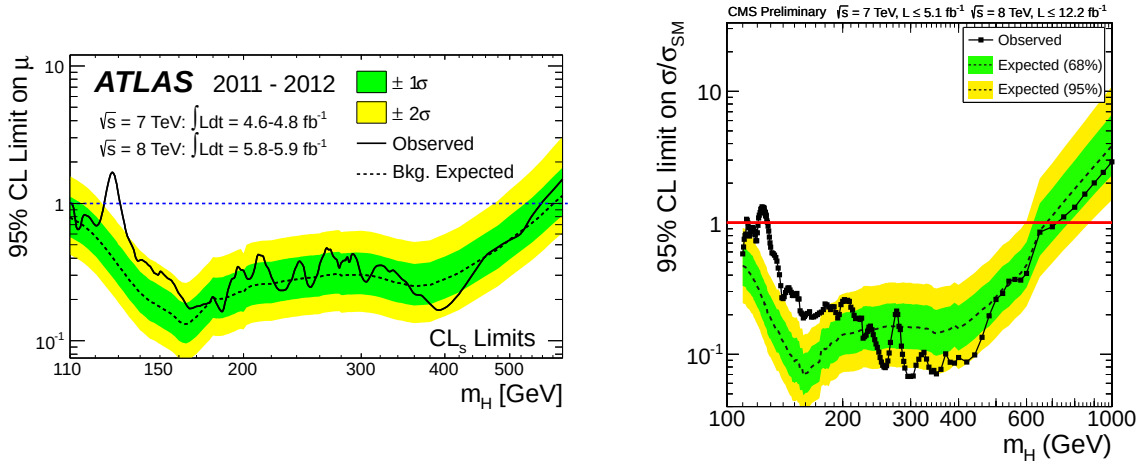

Figure 6.1: 95% confidence level upper limits on a SM-like Higgs boson production cross-section, normalized to the SM predicted cross-section, as a function of the boson mass hypothesis m_{H}, obtained by ATLAS [106] (left side) and CMS [136] (right side).

6.1 Observation of a new particle

As shown in the previous chapter, the ATLAS experiment has observed a significant excess of events in the diphoton invariant mass distribution. In addition to this excess, another narrow excess of events has been observed in the invariant mass distribution of the four lepton system for the Higgs boson search via $H \to ZZ^{(*)} \to 4l$, and a wide excess has been observed in the transverse invariant mass distribution considered in the $H \to WW^{(*)} \to e\nu\mu\nu/\mu\nu e\nu$ search. These results have been reported by the ATLAS collaboration in summer of 2012 [106, 142, 143]. All of these excesses are compatible with the SM Higgs boson and correspond to similar masses, around 125 GeV. On top of that, by the same time, the CMS experiment has also reported the observation of similar excesses in the various Higgs boson search channels, in the same mass region [135], as well as the CDF experiment at the Tevatron in the $H \to b\bar{b}$ channel [140]. These independent and compatible results indicate that the observed excesses correspond to a new particle, whose decay products indicate an integer spin.

Figure 6.2 shows on the top part updated results of the search for the Higgs boson in the diphoton decay channel, considering about 15 fb^{-1} of data in addition to the data considered for the analysis reported in this thesis. The diphoton invariant mass distribution is presented on the left side, and the excess quantification (the obtained p_0 values as a function of the Higgs boson mass hypothesis m_{H}) is presented on the right side. With the amount of data considered in this case, the 126.5 GeV excess has a local significance of 7.4 standard deviations (σ), beyond the 5σ conventionally required for stating the observation of a new particle. This updated result was released in March of 2013, and is reported in [144].

In the middle and bottom part, Figure 6.2 shows the most recent ATLAS results from the search of the Higgs boson in the decay channels $H \to ZZ^{(*)} \to 4l$ and $H \to WW^{(*)} \to e\nu\mu\nu/\mu\nu e\nu$, respectively. As in the case of the diphoton analysis plots on the top part, mass distributions are shown on the left side, and the excess quantifications are shown on the right side. The excess observed in the four leptons invariant mass distribution has a local significance of 6.6σ, and the excess observed in the transverse invariant mass distribution of $e\nu\mu\nu/\mu\nu e\nu$ has a local significance of 3.8σ. Details about these analysis and results can be found in the documents [137, 138, 142, 143, 145, 146].

The p_0 values resulting from the ATLAS combined analysis released in December of 2012, considering the previous mentioned channels plus the $H \to \tau\tau$ and $H \to b\bar{b}$ channels, are shown on the left side of Figure 6.3. This figure shows p_0 values obtained independently in the various channels with colored lines, and the black line shows the combined result. The combined local significance of the excesses is found to be 7σ. Similarly, the right side plot of Figure 6.3 shows the results reported by the CMS collaboration, with a combined local significance of 6.9σ for the observed excesses. As mentioned above, these results are compatible with the results obtained by the experiments at the Tevatron, in particular with the observation of an excess in the $H \to b\bar{b}$ channel by the CDF collaboration. Figure 6.4 shows the p_0 values as a function of the Higgs boson mass hypothesis obtained in the combined CDF and D0 analysis, considering various channels. It shows the presence of a wide excess of events, with the lowest p_0 value at 120 GeV and corresponding to 3.0σ.

a) $H \to \gamma\gamma$ channel.

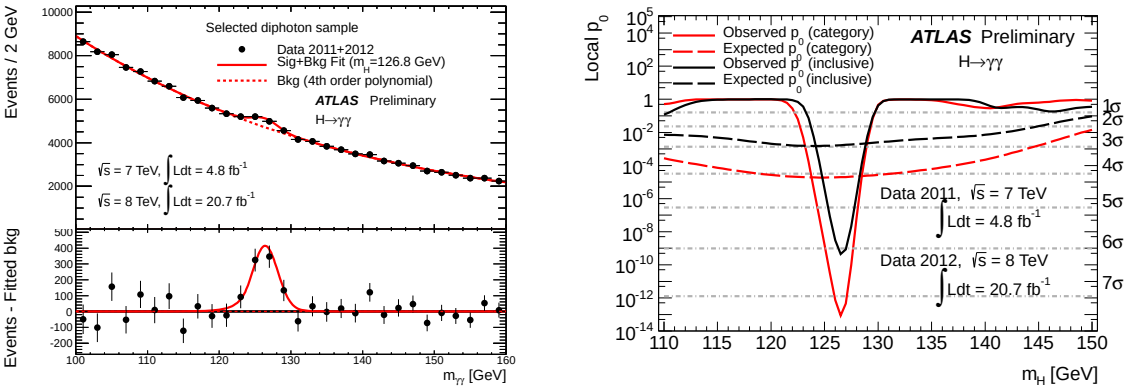

b) $H \to ZZ^{(*)} \to 4l$ channel.

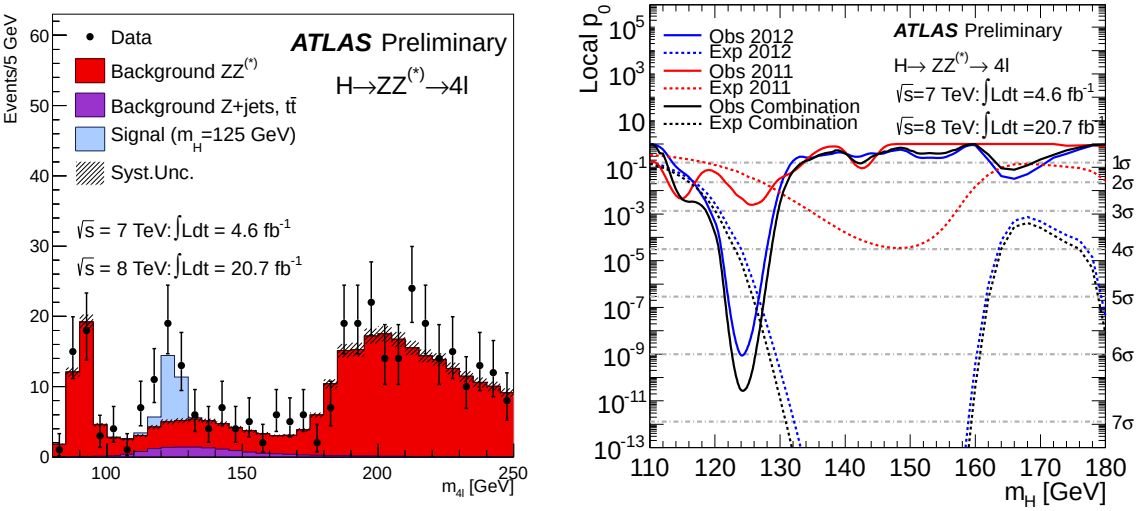

c) $H \to WW^{(*)} \to e\nu\mu\nu/\mu\nu e\nu$ channel.

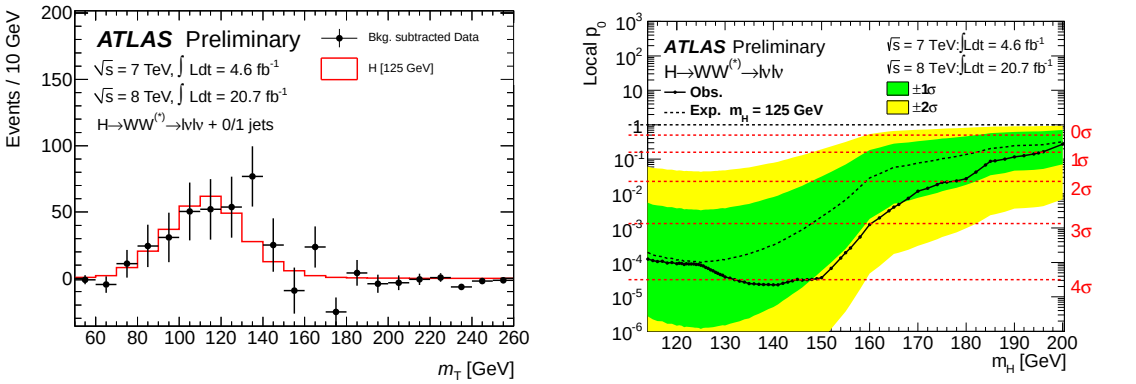

Figure 6.2: Results of the ATLAS search for the Standard Model Higgs boson, as obtained in the $H \to \gamma\gamma$ (a), $H \to ZZ^{(*)} \to 4l$ (b) and $H \to WW^{(*)} \to e\nu\mu\nu/\mu\nu e\nu$ (c) decay channel [144–146]. The plots on the left show the invariant mass and transverse invariant mass distributions observed for each channel, and the right plots show the values obtained for the probability p_0 of the background to fluctuate creating a signal-like excess equal or larger than what is observed, as a function of the Higgs boson mass hypothesis m_{H}.

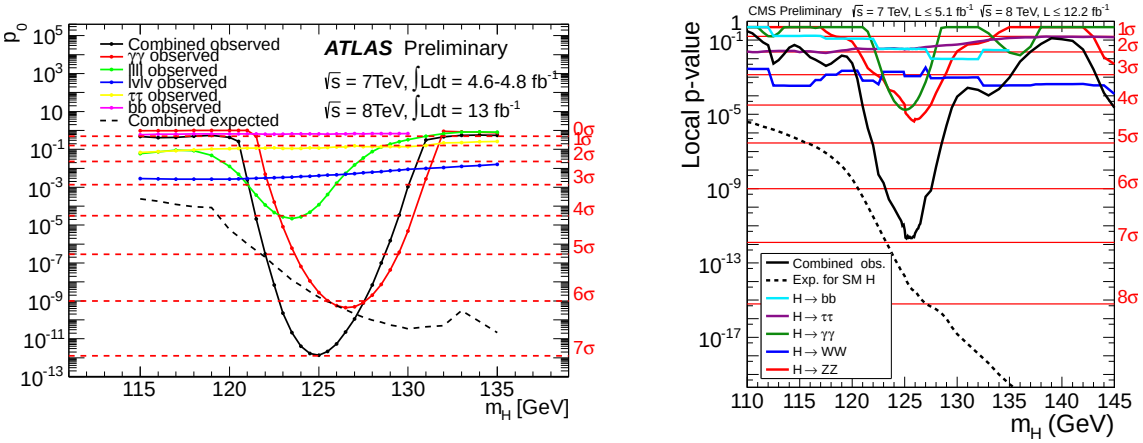

Figure 6.3: Probability p_0 of the background to fluctuate creating a signal-like excess equal or larger than what is observed, as a function of the Higgs boson mass hypothesis m_{H}, as obtained by ATLAS [139] (left side) and CMS [136] (right side), for various individual channels ($H \to \gamma\gamma$, $H \to ZZ^{(*)} \to 4l$, $H \to WW^{(*)} \to l\nu l\nu$; $H \to \tau\tau$, $H \to b\bar{b}$) and the combination all of them.

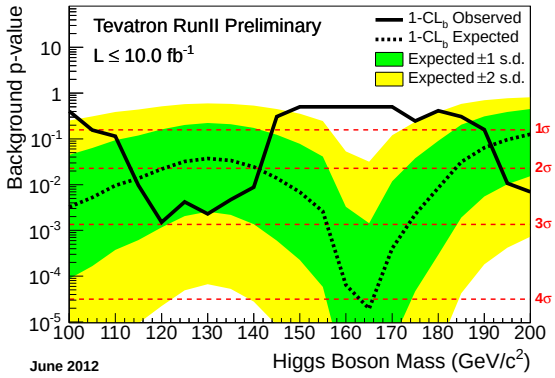

Figure 6.4: Probability of the background to fluctuate creating a signal-like excess equal or larger than what is observed, as a function of the Higgs boson mass hypothesis m_{H}, as obtained in a CDF and D0 combined analysis, considering various search channels [140].

6.2 Properties of the new boson

After the observation of this new boson, various studies have performed measuring its properties and comparing them with the expectations for the Standard Model Higgs boson.

Precise measurements of the boson mass have been performed by the ATLAS and CMS collaborations, considering the $H \to \gamma\gamma$ and $H \to ZZ^{(*)} \to 4l$ channels, which provide good mass resolution. Figure 6.5 shows two-dimensional plots presenting confidence intervals in the signal strength-mass (μ, m_{H}) plane, for each channel and for their combination. The left side plot corresponds to ATLAS and the right side plot corresponds to CMS. The ATLAS results in the $H \to \gamma\gamma$ channel shown here correspond to a recent update of the analysis reported in Chapter 5, considering about 15 fb^{-1} of additional data; it is reported in [144].

On the one hand, in the case of the ATLAS individual mass measurements, the result obtained in the $H \to \gamma\gamma$ channel is $m_{\mathrm{H}} = 126.8 \pm 0.2(\mathrm{stat.}) \pm 0.7(\mathrm{syst.})$ GeV, and for the $H \to ZZ^{(*)} \to 4l$ channel it is $m_{\mathrm{H}} = 124.3\,^{+0.6}_{-0.5}(\mathrm{stat.})\,^{+0.5}_{-0.3}(\mathrm{syst.})$ GeV. Taking

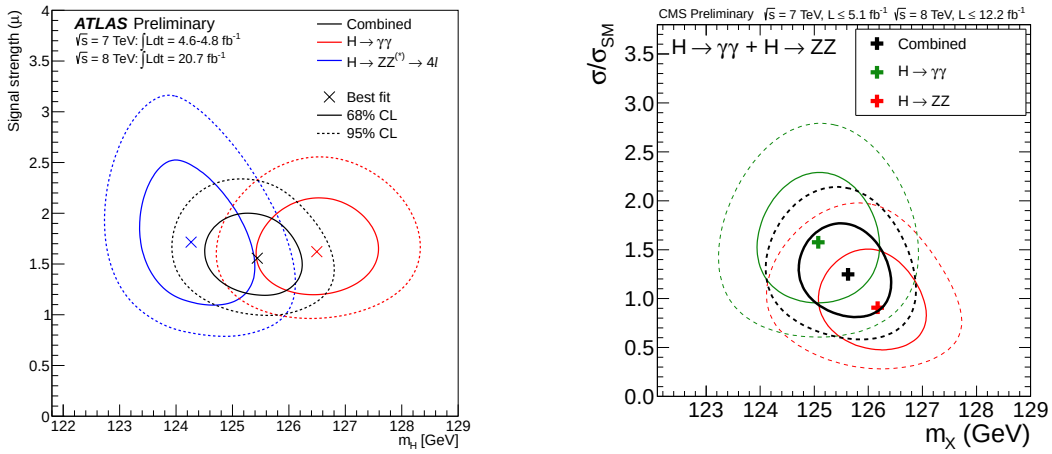

Figure 6.5: Two confidence intervals in the signal strength-mass (μ, m_{H}) plane, obtained by ATLAS [147] (left side) and CMS [136] (right side), for the $H \to \gamma\gamma$ and $H \to ZZ^{(*)} \to 4l$ individual channels, and their combination. The cross markers indicate the points with maximum likelihood estimates.

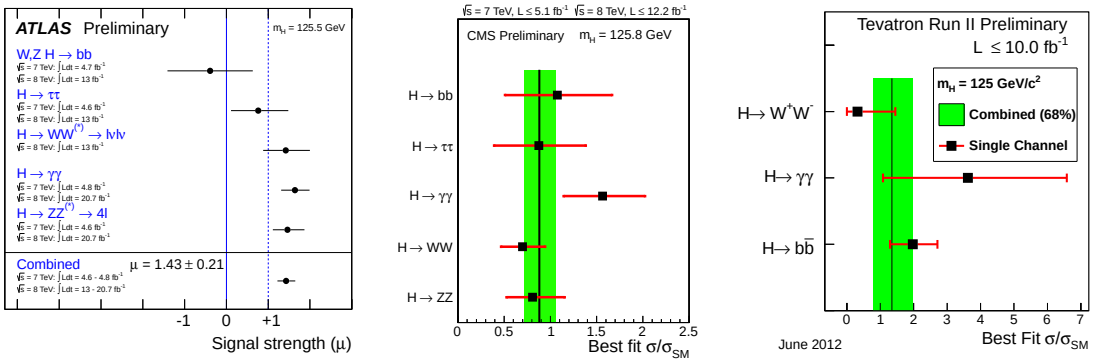

Figure 6.6: The best-fit signal strength μ obtained independently in different Higgs boson decay channels and the per experiment combined result, as obtained by ATLAS for $m_{\mathrm{H}} = 125.5$ GeV on the left side, by CMS for $m_{\mathrm{H}} = 125.8$ GeV on the middle part, and by the Tevatron for $m_{\mathrm{H}} = 125$ GeV on the right side [136, 140, 147].

into account the systematic uncertainty on the mass scale for the two channels and their correlations, the compatibility between the two measurements is estimated to be at the level of 2.4 standard deviations.

On the other hand, when the two channels are combined, the mass measurement obtained by ATLAS is $m_{\mathrm{H}} = 125.5 \pm 0.2(\mathrm{stat.})\,^{+0.5}_{-0.6}(\mathrm{syst.})$ GeV [147], and the one obtained by CMS is $m_{\mathrm{H}} = 125.8 \pm 0.4(\mathrm{stat.}) \pm 0.4(\mathrm{syst.})$ GeV [136], which are compatible with each other.

Measurements of the signal strength relative to the expected Standard Model cross-section for the Higgs boson have been performed in different channels in the various experiments. The three plots in Figure 6.6 show the measurements done by ATLAS (left side plot), CMS (middle plot), and the Tevatron (right side plot). These figures show results obtained per channel individually, as well as the combined results per experiment. The obtained results show compatibility with a SM Higgs boson. The result of the ATLAS combined measurement at $m_{\mathrm{H}} = 125.5$ GeV is $\hat{\mu} = 1.43 \pm 0.16(\mathrm{stat.}) \pm 0.14(\mathrm{syst.}) = 1.43 \pm 0.21$ [147], for CMS at $m_{\mathrm{H}} = 125.8$ GeV it is $\hat{\mu} = 0.88 \pm 0.21$ [136], and for the Tevatron at $m_{\mathrm{H}} = 125$ GeV it is $\hat{\mu} = 1.35^{+0.60}_{-0.57}$. (The signal strength value $\mu = 1$ corresponds to the SM expected cross-section.)

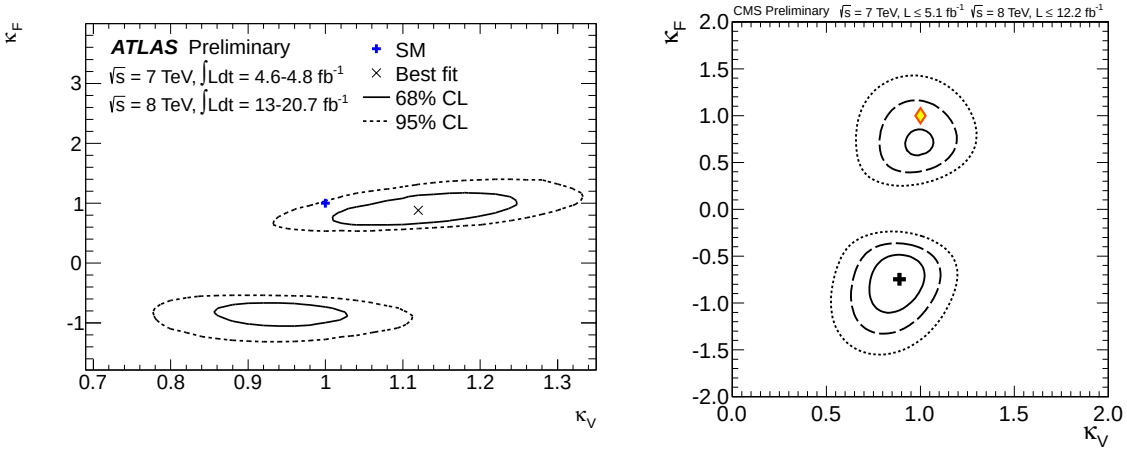

Figure 6.7: Best-fit values and confidence intervals for two scale factors for the coupling strength for fermions (κ_F) and vector bosons (κ_V), obtained by ATLAS [148] (left side) and CMS [136] (right side), in the combination of several Higgs boson decay channels.

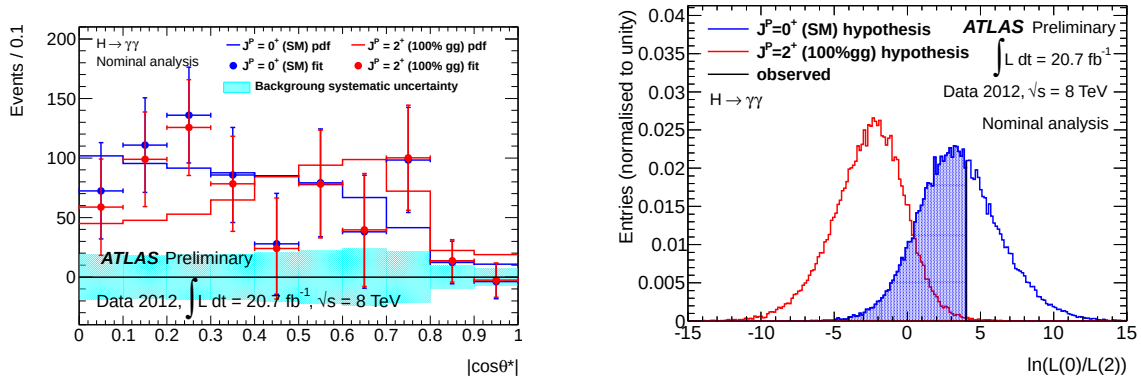

Figure 6.8: Left: Data distribution on the $|\cos\theta^*|$ variable at the signal region, after background subtraction. θ^* is the polar angle of the photons with respect to the z-axis of a particular rest frame; this angle is sensitive to the spin and parity of the new particle. The red line distribution corresponds to the SM expectation for the Higgs boson, $J^P = 0^+$, and the blue line distribution corresponds to a graviton-like spin-2 particle with minimal couplings, $J^P = 2^+_m$, produced via gluon fusion. Right: Distributions expected for the hypothesis $J^P = 0^+$ and $J^P = 2^+_m$, on a likelihood ratio variable per dataset computed from the $|\cos\theta^*|$ signal-plus-background distributions, obtained from pseudo-experiments. The black line indicate the value obtained for the analyzed dataset [149].

Considering data categories sensitive to the production modes of the Higgs boson, two parameters associated to the Higgs boson coupling strength with fermions (κ_F) and vector bosons (κ_V) have been fitted to the data, in various Higgs boson decay channels. The results are shown in Figure 6.7; the left side plot corresponds to ATLAS and the right side plot corresponds to CMS. The results from both collaborations are compatible with the Standard Model expectations for the Higgs boson.

The spin and parity of the new boson have also been investigated by studying the kinematic distributions of the boson decay products. Figure 6.8 presents results of a spin/parity measurement performed by the ATLAS collaboration in the diphoton channel [149]. The dots on the left side show the data distribution on the $|\cos\theta^*|$ variable at the signal region, after background subtraction. Here θ^* is the polar angle of the photons with respect to the z-axis of the Collins-Soper frame described in [150]; this angle is sensitive to the spin and parity of the new particle. The red line distribution corresponds to the SM expectation for the Higgs boson, $J^P = 0^+$, and

the blue line distribution corresponds to a graviton-like spin-2 particle with minimal couplings, $J^P = 2^+_m$, produced via gluon fusion. The fact that the new boson is observed in the diphoton decay channel implies that its spin is different from one, as explained in [151, 152]. The right side plot shows the distributions expected for the two hypothesis, on a likelihood ratio variable per dataset computed from the $|\cos\theta^*|$ signal-plus-background distributions, obtained from pseudo-experiments, and the black line indicate the value obtained for the analyzed dataset. From this observed value, the probability for the observed particle to be $J^P = 2^+_m$ is $p_{2^+_m} = 0.3\%$; this hypothesis is excluded with 99.3% of confidence level. The probability to be $J^P = 0^+$ is $p_{0^+} = 58.8\%$. Details can be found in [149].

The spin and parity measurements have been also performed using the channels $H \to ZZ^{(*)} \to 4l$ and $H \to WW^{(*)} \to e\nu\mu\nu/\mu\nu e\nu$, by both ATLAS and CMS [137, 141,145,153–156]. The observed boson is found to be compatible with the hypothesis $J^P = 0^+$, corresponding to the SM Higgs boson, and the hypotheses $J^P = 0^-$ and $J^P = 2^+$ are excluded with more than 95% of confidence level.

Conclusions

A search for the Standard Model Higgs boson decaying to two photons performed in the ATLAS experiment has been presented in this document. It considers proton-proton collision data collected in 2011 and the first half of 2012; the data correspond to 4.8 fb^{-1} of integrated luminosity at $\sqrt{s} = 7$ TeV, and 5.9 fb^{-1} at $\sqrt{s} = 8$ TeV.

The analysis has the sensitivity to exclude at 95% of confidence level the Standard Model (SM) Higgs boson in the mass range 110.0 - 140.5 GeV. With the analyzed data sample, the Higgs boson has been excluded in two mass ranges, from 112.0 to 123.0 GeV, and from 132.0 to 143.5 GeV, at 95% of confidence level.

In the middle mass range the SM Higgs boson is not excluded due to the presence of an excess of events in the diphoton invariant mass distribution, not compatible with the background only hypothesis. This excess has a local significance of 4.5 standard deviations, and is compatible with the signal of a SM Higgs boson of mass 126.5 GeV. Taking into account the fact that the test statistics is performed for different mass points in the range 110 - 150 GeV, the global significance of the excess is 3.6 standard deviations. It means that the probability for the background to have a positive fluctuation equal or larger than the one observed, anywhere in the tested mass range, is 1.6×10^{-4}.

This observation is compatible with other results obtained in independent searches for the SM Higgs boson, which observe signals in the same mass regions. These independent searches include searches in other decay channels by the ATLAS collaboration [106, 142, 143], in the diphoton and other decay channels by the CMS collaboration [135, 157], and by the experiments at the Tevatron [140]. All these results lead to the conclusion that definitively a new neutral particle has been observed with mass around 125 GeV.

In the analysis presented here, the signal strength has been found to be 1.8 ± 0.5 times the expected value for the SM Higgs boson, which indicates compatibility between the observed signal and the Standard Model expectations.

Additionally, these results have been confirmed after the analysis of data collected between July and December of 2012 [144], which represent 15 fb^{-1} of integrated luminosity extra.

Appendix A

Studies of non-collision background for photon production measurements

A.1 Introduction

Some measurements of the prompt photon and diphoton production cross-sections have been performed based on the first LHC collision data, collected at low luminosity in 2010, at $\sqrt{s} = 7$ TeV [10–12]; for these measurements, there was the necessity of estimating the possible contributions to the background from non-collision events. These non-collision events include events induced by the proton beams through interactions different from the desired proton-proton collisions (*beam-induced background*), and cosmic-ray showers that reach the ATLAS detector. The beam-induced background corresponds to protons lost from the beams that interact with collimator components close to the ATLAS detector, or to interactions of the proton beams with gas molecules in the beams' trajectory.

In 2010 at the LHC, the collisions started with a low luminosity of $\sim 10^{27}$ cm^{-2}s^{-1}, that was gradually increased, achieving 2.07×10^{32} cm^{-2}s^{-1} at the end of the year. Figure A.1 shows on the left side the mean number of interactions per bunch crossing, and on the right side the cumulative integrated luminosity delivered to and recorded by ATLAS, both as a function of the day in 2010. Apart from increments on the number of bunches per beam, there were gradual improvements on the beam collimation system, and on the vacuum conditions. Initially, the number of protons per bunch (bunch intensity) was about 10^{10}, and later it was increased to its nominal value of about 10^{11}.

The relative amount of non-collision background in the collision data samples is expected to change with this evolution of the proton-beam parameters and luminosity. The rate of cosmic-rays is independent of the beam parameters, and therefore the increase of the number of interactions per bunch-crossing is expected to reduce the relative fraction of cosmic-ray background in the collision samples. The number of interactions per bunch-crossing is proportional to the square of the bunch intensity (see Chapter 2, Section 2.1.5); while the beam-induced background has a linear dependence on the bunch intensity. Thus, the fraction of beam-induced background in the collision samples is expected to decrease with the increase of the

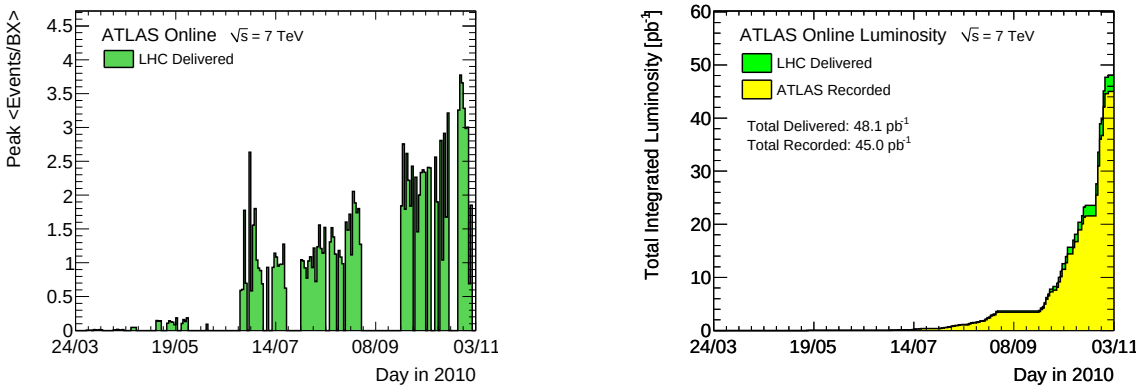

Figure A.1: The left side figure shows the mean number of interactions per bunch crossing, and the right side figure shows the cumulative integrated luminosity delivered to (green) and recorded by ATLAS (yellow), both as a function of the day in 2010 [71], for proton-proton collisions at $\sqrt{s} = 7$ TeV.

bunch intensity, as well as with the improvements in the optics and vacuum system.

The cross-section measurements mentioned above, for which the non-collision background has been estimated, are the following:

- A measurement of the inclusive isolated prompt photon production, reported in [10], based on data collected between April and beginning of August of 2010, corresponding to an integrated luminosity of 880 nb^{-1}. It is an estimation of the differential cross-section as a function of the photon transverse energy E_{T}^{γ}, in the range $15 \leqslant E_{\mathrm{T}}^{\gamma} < 100$ GeV. Three pseudorapidity ranges are considered separately, $|\eta^{\gamma}| < 0.6$, $0.6 < |\eta^{\gamma}| < 1.37$ and $1.52 < |\eta^{\gamma}| < 1.81$. In the rest of this chapter, this measurement is referred as the one for **photons at low** p_{T}.

- Another measurement of the inclusive isolated prompt photon production, reported in [11], based on data collected between August and November of 2010, with an integrated luminosity of 35 pb^{-1}. It is also an estimation of the differential cross-section as a function of the photon transverse energy E_{T}^{γ}, but in an E_{T}^{γ} range higher than the previous one, in this case the range $45 \leqslant E_{\mathrm{T}}^{\gamma} < 400$ GeV. Four pseudorapidity ranges are considered separately, $|\eta^{\gamma}| < 0.6$, $0.6 < |\eta^{\gamma}| < 1.37$, $1.52 < |\eta^{\gamma}| < 1.81$ and $1.81 < |\eta^{\gamma}| < 2.37$. In the rest of this chapter, this measurement is referred as the one for **photons at high** p_{T}.

- A measurement of the isolated diphoton production, reported in [12], also based on the data collected between August and November of 2010, with an integrated luminosity of 37 pb^{-1}. It is an estimation of the differential cross-section as a function of three variables, the diphoton invariant mass $m_{\gamma\gamma}$, the total transverse momentum of the diphoton system $p_{\mathrm{T}}^{\gamma\gamma}$, and the azimuthal photon separation $\Delta\phi_{\gamma\gamma}$. In the rest of this chapter, it is referred as the **diphoton** measurement.

The method used in this background estimation study is described in Section A.2, the event selections for the various analyses are presented in Section A.3, the obtained results are shown in Section A.4, and the conclusions are summarized in Section A.5.

A.2 Background estimation method

The non-collision background has been estimated by an extrapolation from control samples to the collision data samples. Before explaining how these control samples have been collected, some details about the proton beam structure at the LHC need to be introduced.

At the LHC, protons circulate in packets (bunches) which can be nominally 25 ns separated from each other, as explained in Chapter 2, Section 2.1.5. Under this configuration, each revolution of the beams would yield a total of 3564 possible bunch-crossings (BC) [158], which are identified with *BCID* numbers. However, not all the bunch-slots can be actually filled with bunches, for operation practical and security reasons.

The LHC fill is done by building bunch-trains, with several bunches equally spaced followed by some empty gaps. At the end of 2010, the proton bunches in a bunch-train had a separation of 150 ns, leaving five possible bunch-slots empty in-between, and the bunch-trains contained a maximum of 32 bunches, followed by a large gap. Early during that year, bunches were even injected individually, with large gaps separating them from the closest bunches.

This beam structure yields several bunch-crossing configurations: paired, unpaired and empty bunch-crossings, among other particular configurations not relevant for this study.

- In the *paired* bunch-crossings, the bunch-slots in both beams are filled; they are the ones producing the proton-proton collisions.
- In the *unpaired* bunch-crossings, the corresponding bunch slot is filled only for one beam; this means that only one proton bunch pass through the interaction region at the bunch crossing.
- In the *empty* bunch-crossings, both bunch-slots are empty, so no proton bunch pass through the ATLAS interaction region at the bunch crossing.

The trigger system of the ATLAS detector is provided with detailed information, containing the configuration for each BCID. Thus, the trigger lines aimed to collect collision events are only active for the paired bunch-crossings. But additionally, there are specific trigger channels similar to the collision ones dedicated to collect data in the unpaired and empty bunch-crossings, which are used for the study of non-collision background.

The dataset collected on empty bunch-crossings corresponds to cosmic-ray originated events, and it is used as control sample for this background. The dataset collected on unpaired bunch-crossings include both, beam-induced and cosmic-ray originated events, but it is mainly considered and referred in this analysis as a control sample for the beam-induced background.

Among the unpaired bunch-crossings, some are not considered for the control sample, because they might include interactions between filled bunches with satellite bunches from the opposite beam. The unpaired bunch-crossings actually used are only those that are at least three BCID's apart from either paired BC's or unpaired BC's with the filled bunch on the opposite beam; they are called unpaired isolated bunch-crossings.

The data collected in these unpaired isolated and empty BC configurations might not correspond purely to the background processes under study, nevertheless they serve to set upper limits to the amount of non-collision background in the collision samples. Some remnants of protons circulate in bunch slots which are in principle considered to be empty; they may lead for instance to some proton-proton collisions on "unpaired bunch-crossings", or beam-induced events on "empty bunch-crossings".

In order to estimate the amount of non-collision background on a collision data sample, the event selection used for this nominal sample is applied to the control samples; the events passing the selection on the control samples are counted, and then the results are extrapolated to the nominal collision sample. For the extrapolation, one have to take into account the number of paired, unpaired and empty bunch-crossings during the data-taking periods, N_{paired}, N_{unpaired} and N_{empty}, respectively. The extrapolation factor for the unpaired bunch-crossing samples f_{unpaired} and for the empty bunch-crossing samples f_{empty} are defined as follows:

$$f_i = \frac{N_{\text{paired}}}{N_i}, \qquad i = \text{unpaired}, \text{empty}; \tag{A.1}$$

The number of bunch-crossings in each configuration is not constant among the different data taking periods, but it changes, and for this reason these scaling factors f_i change from one period to another as well.

The beam-induced events collected on unpaired bunch-crossings correspond to the product of one proton bunch passing by the ATLAS interaction point. But in the case of the paired bunch-crossings, on which collisions are collected, two bunches pass by the ATLAS interaction point, and therefore the amount of beam-induced background is twice the one observed in the unpaired bunch-crossings.

Since the rate of cosmic-ray background is independent of the beam parameters, this background has been studied considering data collected only in a fraction of the whole data-taking period. Then, in some cases, the cosmic-ray background has been extrapolated to the full samples based on the time-length of the data-taking periods. Differently, for the study of the beam-induced background, data from all the different data-taking periods with different beam conditions have been considered.

A.3 Event selections

The event selections start as usual at the trigger, requiring the events to have at least one photon or two photons, depending on the analysis, with transverse momentum thresholds lower than the ones used in the offline selection (details can be found in the documents reporting these analyses [10–12]).

The data must satisfy quality requirements based on the good functioning of the calorimeters, the inner detector and the trigger, and the beam quality.

In order to minimize the amount of non-collision background, events are required to have at least one reconstructed primary vertex, with at least three tracks associated to it. Then, one or two reconstructed photons are required, which have to satisfy some kinematic requirements, according to the analysis:

- For the **photons at low** p_{T}, events are required to have at least one photon,

with transverse energy $E_{\mathrm{T}}^{\gamma} > 15$ GeV, in the pseudorapidity region $|\eta^{\gamma}| < 1.81$, excluding the region $1.37 < |\eta^{\gamma}| < 1.52$, which corresponds to the transitions between the barrel and the end-caps of the calorimeter.

- For the **photons at high** p_{T}, events are required to have at least one photon, with $E_{\mathrm{T}}^{\gamma} > 45$ GeV, in the region $|\eta^{\gamma}| < 2.37$, excluding the region $1.37 < |\eta^{\gamma}| < 1.52$.

- For the **diphoton** study, events are of course required to have at least two reconstructed photons, with $E_{\mathrm{T}}^{\gamma} > 16$ GeV, in the region $|\eta^{\gamma}| < 2.37$, excluding the region $1.37 < |\eta^{\gamma}| < 1.52$; additionally, each photon pair is required to have a separation in the pseudorapidity-azimuthal-angle space of $\Delta R > 0.4$ (ΔR is defined in Chapter 2, Section 2.2.4).

For either analysis, photons are first required to satisfy the *loose* identification criteria, then the *tight* identification criteria, and finally a calorimeter based isolation criterion (details about these requirements can be found in Chapter 3).

The contributions from the non-collision background to the collision data samples have been evaluated at different stages of these selections. It has been done with and without the reconstructed primary vertex requisite, with and without requiring photons to satisfy the different photon identification criteria.

For the analysis of photons at high p_{T} and diphotons, the background evaluations done specifically without applying the *loose* identification criteria are expected to over-estimate the background, for differences at the trigger level selections used for the nominal and control samples. Nevertheless, the background is studied at that stage of the photon selection, basically because only at that level the number events on the control samples is large enough for looking at the event distribution on different variables of interest. Additional evaluations of the total background are done at other stages of the selection for which no bias are expected. The reason of this over-estimation is the following; the trigger level selections used for the nominal collision samples require the photon candidates to satisfy part of the *loose* identification criteria, while the trigger level selections used in the unpaired and empty bunch-crossings for the control samples do not apply photon identification criteria.

A.4 Results

As expected, most of the non-collision events in the control samples fail the primary vertex requirement. In the case of single photons, only about one percent of the events collected in unpaired bunch-crossings satisfy this requirement, and about five percent in the diphoton case. On the cosmic-ray control samples, less than one per mil of the events has a reconstructed primary vertex.

Therefore, only if the non-collision background events occur simultaneously with proton-proton interactions, they could have some significant contribution the nominal samples. The results presented in the following tables and figures were obtained without the primary vertex requirement, so they correspond to a pessimistic estimation of the background.

Table A.1: Number of reconstructed photons N_γ on a nominal sample (collected on paired bunch-crossings), number of photons on the control sample from empty bunch-crossings N_γ^{bkg}, the corresponding value $N_\gamma^{\text{bkg-w}}$ after considering event weights equal to the scaling factor from Equation A.1, and the fraction that it represent with respect to the nominal sample $N_\gamma^{\text{bkg-w}}/N_\gamma$. These numbers are quoted before and after applying different photon identification criteria. The data considered for this table correspond to two datasets labeled in ATLAS as *run 160801* and *run 160879*, which correspond to the data-taking period E.

Photon ID	Paired BC's	Empty BC's		Ratio
	N_γ	N_γ^{bkg}	$N_\gamma^{\text{bkg-w}}$	$N_\gamma^{\text{bkg-w}}/N_\gamma$ [%]
None	438969	2418	13.88 ± 0.28	0.00316 ± 0.00006
loose	123281	870	4.99 ± 0.17	0.0040 ± 0.0001
tight	24811	5	0.029 ± 0.013	0.00012 ± 0.00005

A.4.1 Photons at low p_{T}

Cosmic rays originated background

The estimation of cosmic-ray background for the low p_{T} photons has been done based on data collected in a couple of days, at beginning of August; these data correspond to the datasets labeled internally in the ATLAS collaboration as *run 160801* and *run 160879*, and belong to the data-taking period E, which groups a large fraction of the data collected in August, in 2010.

Table A.1 shows the number of reconstructed photons collected in paired bunch-crossings N_γ, and the number of photons in the control sample from empty bunch-crossings N_γ^{bkg}. For each of the photon candidates, a weight is assigned; this weight is equal to the scaling factor defined in the Equation A.1. The values obtained after considering the event weights $N_\gamma^{\text{bkg-w}}$ are also quoted in the table, as well as the ratio of this value with respect to the nominal control samples $N_\gamma^{\text{bkg-w}}/N_\gamma$. These numbers are quoted for different stages of the selection, with and without requiring photons to satisfy the different identification criteria.

When photons are required to satisfy the *tight* criteria, the relative amount of cosmic-ray background decreases by one order of magnitude, with respect to the equivalent value for *loose* photons.

Assuming the rate of cosmic-ray background per bunch crossing per time unit to be constant in time, an estimation of the total amount of cosmic background has been obtained for all the data taking period considered in the cross-section measurement. Figure A.2 shows on the left side a comparison of the estimated background with the number of photon candidates in the nominal sample, as a function of the photon transverse momentum, and on the right side the relative amount that the background represents with respect to the nominal sample. It is shown for photons without any identification requirement, and for photons that satisfy the *loose* criteria.

The background fraction increases with the photon transverse momentum. But for the highest p_{T} bin, the amount of cosmic-ray background is still quite low, below 0.2%.

Figure A.3 shows the estimated cosmic-ray background also as a function of p_{T}, for five different data taking periods, labeled in ATLAS as A, B, C, D and E. These are periods that usually last a few weeks. As mention above, the LHC instantaneous luminosity evolved significantly in 2010; for the period A, the luminosity was the

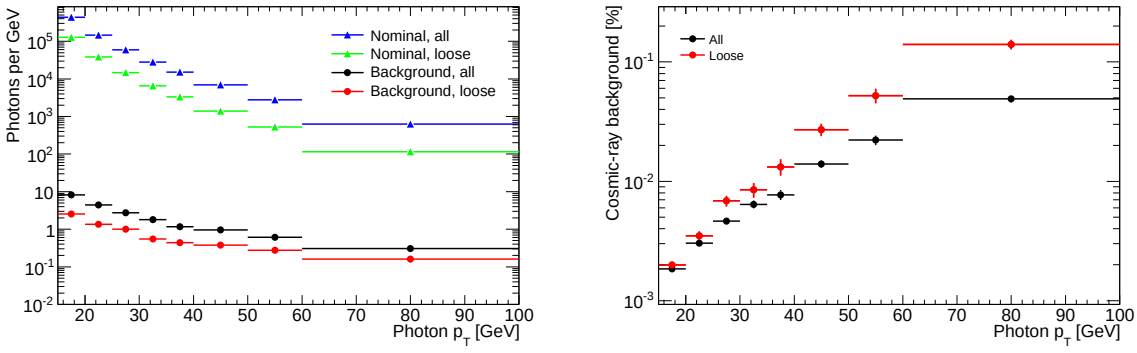

Figure A.2: Cosmic-ray originated background extrapolated from a control sample collected on empty bunch-crossings to a nominal collision sample. The left side figure shows the number of background photons together with the number of photon candidates found in the nominal sample, and the right side figure shows the relative amount of background with respect to the nominal photon sample. It is shown as a function of the photon transverse momentum p_{T}, requiring and without requiring photons to satisfy the *loose* identification criteria.

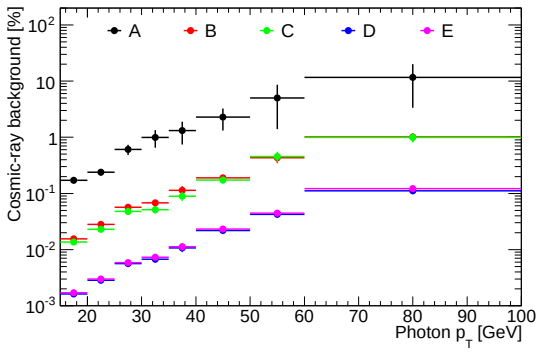

Figure A.3: Cosmic-ray originated background extrapolated from a control sample collected on empty bunch-crossings to a nominal collision sample. This is the relative amount of background with respect to the nominal photon sample as a function of the photon transverse momentum p_{T}, for photons required to satisfy the *loose* identification criteria, and it is shown separately for different data-taking periods. The number of interactions per bunch-crossing increased among these data taking periods, with the lowest values for the period A, and the highest values for the period E.

lowest one, and period E had the highest luminosity. This figure shows that the cosmic-ray background in the periods D and E is about two order of magnitude lower than at the very beginning of the data-taking (period A).

Beam-induced background

Table A.2 shows the number of reconstructed photons collected on paired bunch-crossings N_{γ}, the number of photons found in the control sample collected in unpaired bunch-crossings, the value $N_{\gamma}^{\text{bkg-w}}$ obtained applying the extrapolation weights, and the proportion that this background amount represents with respect to the nominal control sample $N_{\gamma}^{\text{bkg-w}}/N_{\gamma}$.

Figure A.4 shows on the left side the number of reconstructed photon candidates on the nominal sample and the estimated background, as a function of p_{T}. The right side figure shows the relative amount of background with respect to the nominal photon samples. This figure shows a strong dependence of the background on the photon transverse momentum, as observed also in Figure A.2 for the cosmic-ray background. For the highest p_{T} bin, the background fraction is about 0.2%, for

Table A.2: Number of reconstructed photons N_γ on a nominal sample (collected on paired bunch-crossings), number of photons on the control sample from unpaired bunch-crossings N_γ^{bkg}, the corresponding value $N_\gamma^{\text{bkg-w}}$ after considering event weights equal to the scaling factor from Equation A.1, and the fraction that it represent with respect to the nominal sample $N_\gamma^{\text{bkg-w}}/N_\gamma$. These numbers are quoted before and after applying different photon identification criteria.

Photon ID	Paired BC's	Unpaired BC's		Ratio
	N_γ	N_γ^{bkg}	$N_\gamma^{\text{bkg-w}}$	$N_\gamma^{\text{bkg-w}}/N_\gamma$ [%]
None	3035440	174	555 ± 61	0.0183 ± 0.0020
loose	836092	24	54 ± 19	0.0064 ± 0.0022
tight	164509	0	–	–

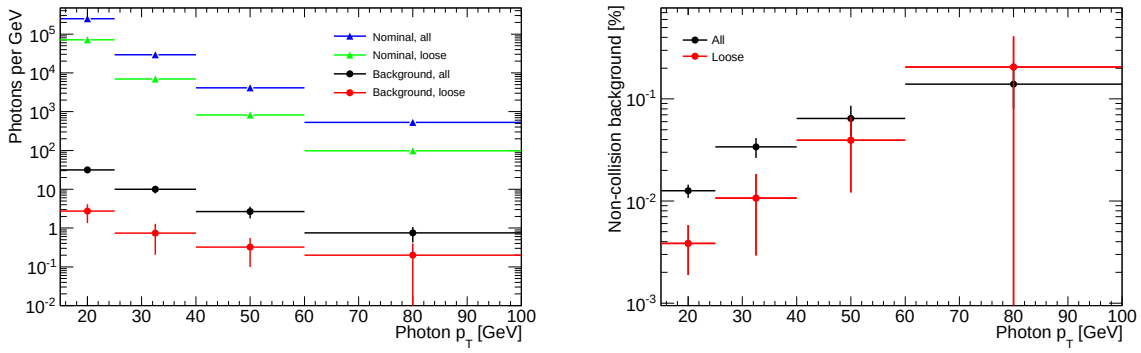

Figure A.4: Non-collision background extrapolated from a control sample collected on unpaired bunch-crossings to a collision nominal sample. The left side figure shows the number of background photons together with the number of photon candidates found in the nominal sample, and the right side figure shows the relative amount of background with respect to the nominal photon sample. It is shown as a function of the photon transverse momentum p_{T}, requiring and without requiring photons to satisfy the *loose* identification criteria.

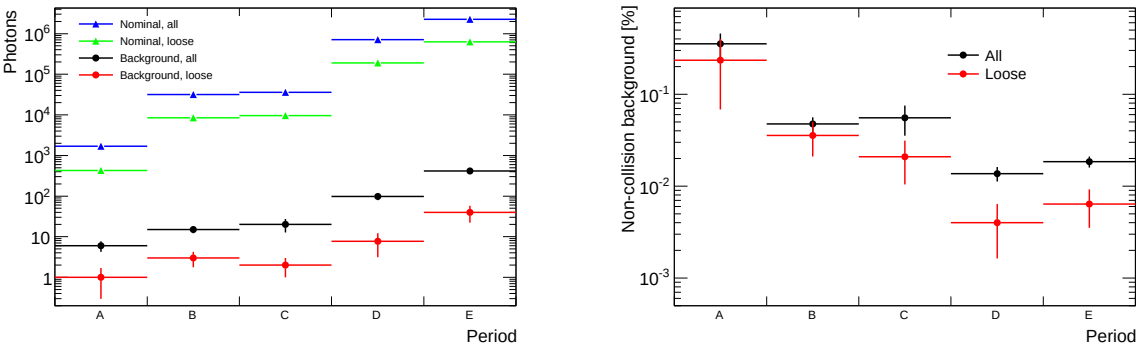

Figure A.5: Non-collision background extrapolated from a control sample collected on unpaired bunch-crossings to a collision nominal sample. The left side figure shows the number of background photons together with the number of photon candidates found in the nominal sample, and the right side figure shows the relative amount of background with respect to the nominal photon sample. It is shown for different data-taking periods, requiring and without requiring photons to satisfy the *loose* identification criteria. The number of interactions per bunch-crossing increased among these data taking periods, with the lowest values for the period A, and the highest values for the period E.

loose photons.

In Figure A.5, the absolute and relative estimated amount of non-collision background is shown as a function of the data-taking period. This figure shows a lower amount of background for the last two periods (D and E) than for the first ones, which is expected given the beam parameters and luminosity evolution. About 98% of the photon candidates used for the photon production measurement have been collected in periods D and E, where this background is estimated to be lower than 0.01%.

Comparing the amount of background estimated from the control samples collected in the unpaired and empty bunch-crossings, quoted on tables A.2 and A.1, and shown in figures A.4 and A.2 respectively, one can conclude that after requiring the photons to satisfy the *loose* identification criteria, a significant fraction of the control sample collected on unpaired bunch-crossings should correspond in fact to cosmic-ray originated background.

A.4.2 Photons at high p_{T}

Cosmic rays originated background

In the cross-section measurement for photons at high p_{T}, the data used was collected between August and November of 2010, while for the study of the cosmic-ray background, only data collected in a first part of this data-taking period was used, specifically data collected in August. The number of interactions per bunch-crossing for this first part of the data-taking was lower than for the rest. Therefore, the relative amount of cosmic-ray background in a nominal photon sample obtained in this study is expected to be higher than for the whole dataset considered in the measurement.

The estimated amount of cosmic-ray background is quoted in Table A.3, for different stages of the photon selection. Even without requiring photons to satisfy identification criteria, this background is below 0.1% of the nominal photon sample. Additionally, when photons are required to satisfy the *tight* identification criteria, this background fraction decreases by two orders of magnitude.

The estimated cosmic-ray background is shown as a function of the photon pseudorapidity η and transverse momentum p_{T} in Figure A.6. This is the relative amount of background with respect to the nominal photon sample. On the left side, it is shown as a function of η, with and without requiring photons to satisfy the *loose* criteria. On the right side, it is shown as a function of p_{T} for photons satisfying the *loose* criteria, for different pseudorapidity regions. One can see that this relative amount of background is higher for the η region corresponding to the barrel than for the one corresponding to the end-caps, which is expected for cosmic-ray originated background. As observed previously in Section A.4.1, the cosmic-ray background fraction increases with the photon p_{T}. This background represents 1% of the *loose* photon sample in the highest p_{T} bin [200, 400), and it is expected to significantly decrease with the *tight* requirements.

Table A.3: Number of reconstructed photons N_γ on a nominal sample (collected on paired bunch-crossings), number of photons on the control sample from empty bunch-crossings N_γ^{bkg}, the corresponding value $N_\gamma^{\text{bkg-w}}$ after considering event weights equal to the scaling factor from Equation A.1, and the fraction that it represent with respect to the nominal sample $N_\gamma^{\text{bkg-w}}/N_\gamma$. These numbers are quoted before and after applying different photon identification criteria. The data considered for this table correspond to data collected between August and November of 2010.

Photon ID	Paired BC's	Empty BC's		Ratio
	N_γ	N_γ^{bkg}	$N_\gamma^{\text{bkg-w}}$	$N_\gamma^{\text{bkg-w}}/N_\gamma$ [%]
None	10225	1721	9.64 ± 0.23	0.0942 ± 0.0025
loose	9342	591	3.32 ± 0.14	0.0356 ± 0.0015
tight	4186	2	0.011 ± 0.008	0.00027 ± 0.00019
tight isolated	2551	2	0.011 ± 0.008	0.00045 ± 0.00032

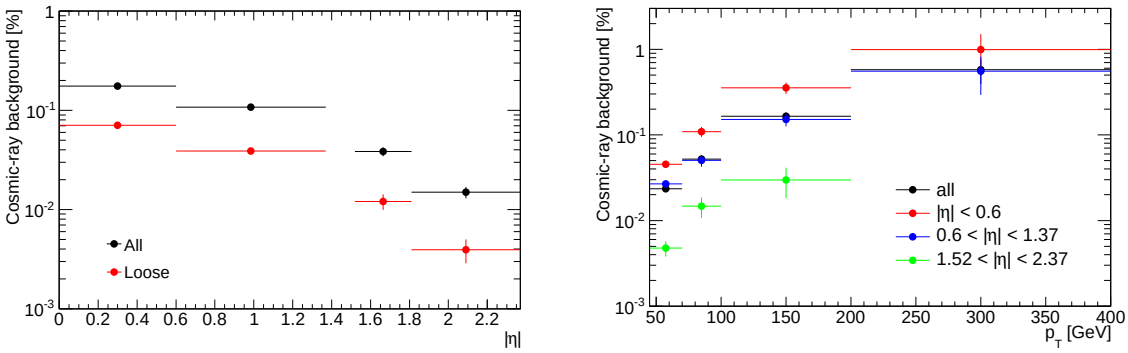

Figure A.6: Cosmic-ray originated background extrapolated from a control sample collected on empty bunch-crossings to a collision nominal sample. This is the relative amount of background with respect to the nominal photon sample. It is shown on the left side as a function of the photon pseudorapidity η, requiring and without requiring photons to satisfy the *loose* criteria, and on the right side for photons satisfying the *loose* criteria as a function of the photon transverse momentum p_{T}, for the different pseudorapidity regions.

Table A.4: Number of reconstructed photons N_γ on a nominal sample (collected on paired bunch-crossings), number of photons on the control sample from unpaired bunch-crossings N_γ^{bkg}, the corresponding value $N_\gamma^{\text{bkg-w}}$ after considering event weights equal to the scaling factor from Equation A.1, and the fraction that it represent with respect to the nominal sample $N_\gamma^{\text{bkg-w}}/N_\gamma$. These numbers are quoted before and after applying different photon identification criteria.

Photon ID	Paired BC's	Unpaired BC's		Ratio
	N_γ	N_γ^{bkg}	$N_\gamma^{\text{bkg-w}}$	$N_\gamma^{\text{bkg-w}}/N_\gamma$ [%]
None	746898	650	10300 ± 439	1.38 ± 0.06
loose	633342	30	452 ± 93	0.071 ± 0.015
tight	249297	1	17 ± 17	0.007 ± 0.007
tight isolated	148862	1	17 ± 17	0.011 ± 0.011

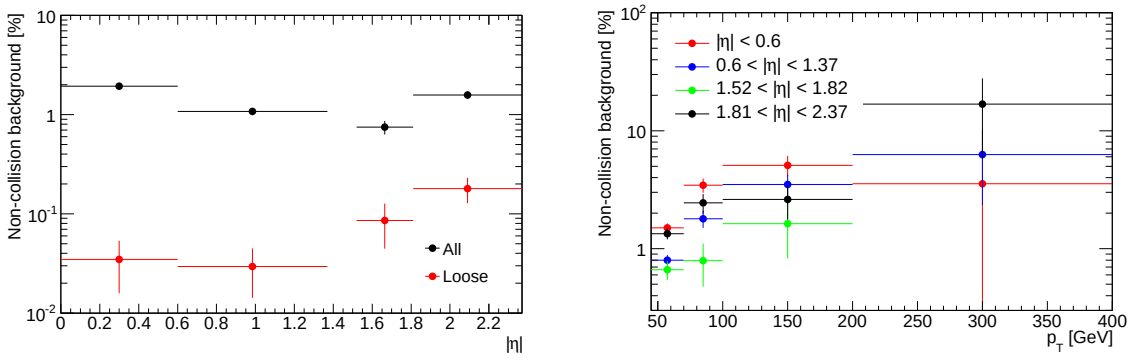

Figure A.7: Non-collision background extrapolated from a control sample collected on unpaired bunch-crossings to a collision nominal sample. This is the relative amount of background with respect to the nominal photon sample. It is shown on the left side as a function of the photon pseudorapidity η, requiring and without requiring photons to satisfy the *loose* criteria, and on the right side for photons without identification requirements as a function of the photon transverse momentum p_{T}, for the different pseudorapidity regions.

Beam-induced background

Table A.4 contains the estimated amount of non-collision background, for different stages of the photon selection. When photons are required to satisfy the *loose* identification criteria the background fraction decreases by one order of magnitude, and it further decreases by another order of magnitude when the *tight* criteria are required.

Figure A.6 shows on the left side the estimated non-collision background as a function of η, for photons required and not required to satisfy the *loose* criteria, and on the right side as a function of p_{T}, for photons without identification requirements, for different pseudorapidity regions. This is the relative amount of background with respect to the nominal photon sample. When the *loose* criteria are required, the highest relative amount of background is found for large absolute values of η (these are the forward regions closest to beam direction); this trend is expected for beam-induced background. Figure A.7 shows on the right side that the largest amount of non-collision background is found in the highest p_{T} bin for the region $1.81 < |\eta| < 2.37$; it is 20%, but it is expected to decrease by two orders of magnitude when the *tight* photon identification criteria are required.

A.4.3 Diphotons

For the estimation of non-collision background in the diphoton candidate sample, two types of background events have been considered: events in which both reconstructed photons correspond to the product of a non-collision process, and events in which a non-collision background photon overlaps with the production of a prompt photon in a proton-proton interaction.

For the second case, one can estimate the relative amount of non-collision single photons in a collision nominal sample, with respect to the number of diphoton events selected, and then one has to consider the rate of prompt photon production per bunch-crossing. This prompt photon rate per bunch-crossing can be obtained dividing the rate of prompt photons per time unit R_γ by the rate of paired bunch-

crossings per time unit $R_{\text{paired-BC}}$:

$$\begin{aligned}\frac{R_\gamma}{R_{\text{paired-BC}}} &= \frac{L\sigma_\gamma}{n_{\text{paired-BC}} f_{\text{rev}}} \\ &\sim \frac{2{\cdot}10^{32}\text{cm}^{-2}\text{s}^{-1} \cdot 2{\cdot}10^{-7}\text{b} \cdot 10^{-24}\text{cm}^2/\text{b}}{368 \cdot 10^4\text{s}^{-1}} \\ &\sim 10^{-5};\end{aligned} \tag{A.2}$$

where L is the LHC instantaneous luminosity, σ_γ is the total cross-section for the production of isolated prompt photons with $E_{\text{T}} > 16$ GeV in the η acceptance region, $n_{\text{paired-BC}}$ is the number of colliding bunch-crossings per revolution, and f_{rev} is the beam revolution frequency. For the rough estimation of this ratio, the luminosity and beam parameters corresponding to the last period of the 2010 data-taking have been considered (these are quoted in Chapter 2, Section 2.1), and a rough estimation of the photon production cross-section has been computed from the measurement reported in [10, 11].

Cosmic rays originated background

Like for the high p_{T} single photons, the diphoton cosmic-ray background has been studied with data collected in August of 2010, while the data considered for the diphoton cross-section measurement correspond to the period from August to November of the same year. The relative amount of this background for the complete dataset is expected to be lower than the values obtained in this study for a fraction of the dataset.

Table A.5 summarizes the results obtained in the estimation of the cosmic-ray background. Even before applying any photon identification criteria, the amount of cosmic-ray originated diphotons is found to be quite small, less than 0.01%. Also the number of cosmic single photons found after the whole selection is very small compared with the number of collision diphoton events.

Figure A.8 shows on the left side the estimated cosmic-ray background for photons without identification requirement, as a function of the diphoton invariant mass $M_{\gamma\gamma}$ (top), the transverse momentum $p_{T,\gamma\gamma}$ (middle), and the azimuthal difference $\Delta\phi_{\gamma\gamma}$ (bottom). The background is below 0.1% for most of the bins, except for the high $p_{T,\gamma\gamma}$ bins where it represents a few percents of the diphoton sample. Neverthe-

Table A.5: Number of reconstructed diphotons $N_{\gamma\gamma}$ on a nominal sample (collected on paired bunch-crossings), number of diphotons $N_{\gamma\gamma}^{\text{bkg}}$ and single photons N_γ^{bkg} on the control sample from empty bunch-crossings, the corresponding values $N_{\gamma\gamma}^{\text{bkg-w}}$ and $N_\gamma^{\text{bkg-w}}$ after considering event weights equal to the scaling factor from Equation A.1, and the fraction that they represent with respect to the nominal sample $N_{\gamma\gamma}^{\text{bkg-w}}/N_{\gamma\gamma}$ and $N_\gamma^{\text{bkg-w}}/N_\gamma$. These numbers are quoted before and after applying different photon identification criteria. The data considered for this table correspond to data collected between August and November of 2010.

Photon ID	Paired BC's	Empty BC's				Ratios	
	$N_{\gamma\gamma}$	$N_{\gamma\gamma}^{\text{bkg}}$	$N_{\gamma\gamma}^{\text{bkg-w}}$	N_γ^{bkg}	$N_\gamma^{\text{bkg-w}}$	$N_{\gamma\gamma}^{\text{bkg-w}}/N_{\gamma\gamma}$ [%]	$N_\gamma^{\text{bkg-w}}/N_{\gamma\gamma}$ [%]
None	1819	26	0.148 ± 0.029	8828	49.4 ± 0.5	0.0082 ± 0.0016	2.72 ± 0.07
loose	834	2	0.011 ± 0.008	2740	15.34 ± 0.29	0.0014 ± 0.0010	1.84 ± 0.07
tight	82	0	–	19	0.104 ± 0.024	–	0.13 ± 0.03
tight isolated	29	0	–	8	0.044 ± 0.016	–	0.15 ± 0.06

less, according to Table A.5, this background fraction is expected to decrease about one order of magnitude after applying the *loose* selection and even more with the additional selection requirements.

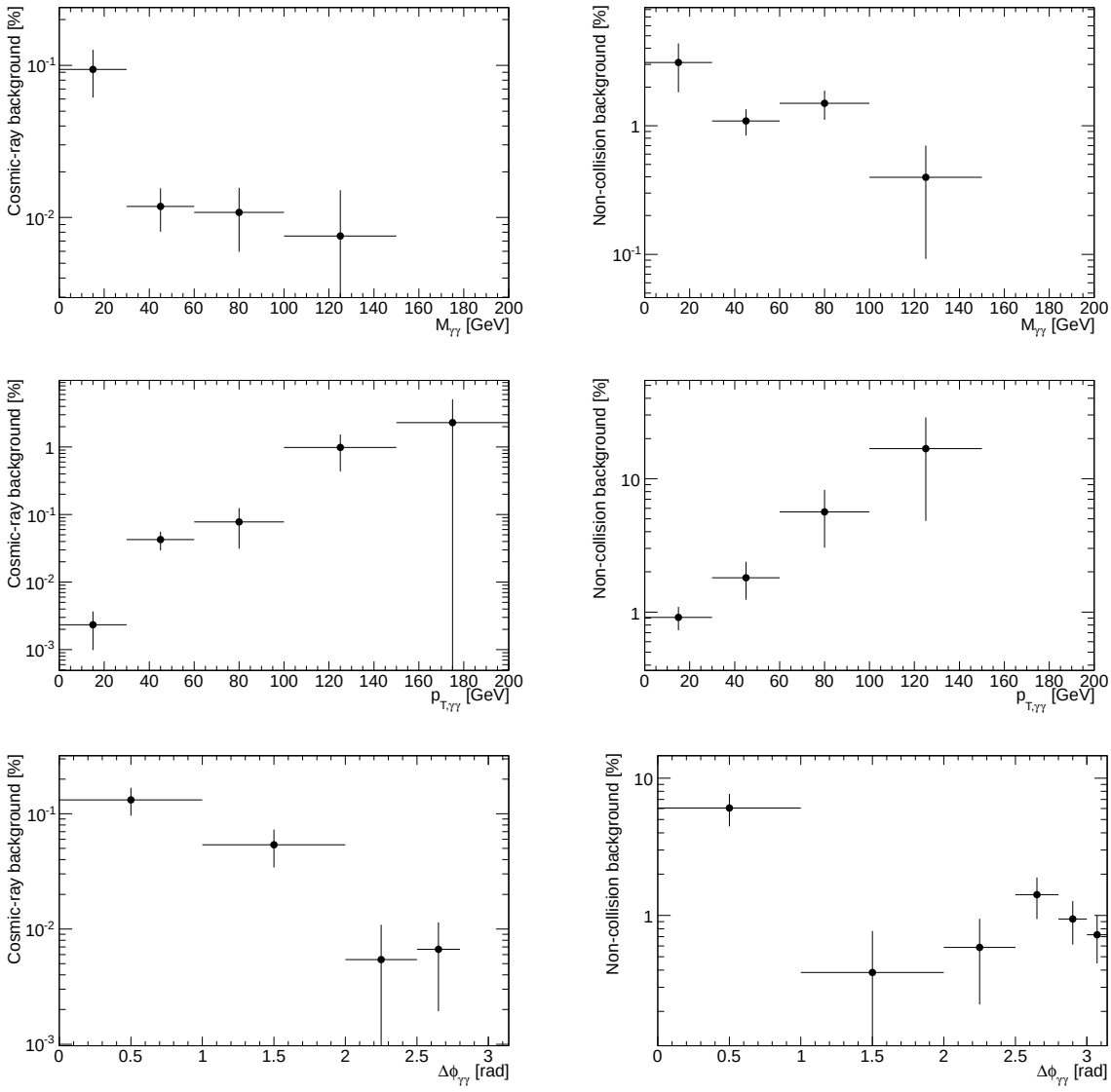

Figure A.8: Non-collision background extrapolated from control samples to collision nominal samples, for photons without identification requirements. This is the relative amount of background with respect to the nominal diphoton samples. The figures on the left side correspond to cosmic-ray background, extrapolated from a sample collected on empty bunch-crossings. For the right side figures, the background was extrapolated from samples collected on unpaired bunch-crossings, and correspond principally to beam-induced background. It is shown as a function of the diphoton invariant mass $m_{\gamma\gamma}$ (top), the total transverse momentum of the diphoton system $p_{\mathrm{T}}^{\gamma\gamma}$ (middle), and the azimuthal photon separation $\Delta\phi_{\gamma\gamma}$ (bottom).

Beam-induced background

The results of the background extrapolation from the unpaired bunch-crossing sample are quoted in Table A.6. After requiring photons to satisfy the *loose* criteria, the non-collision diphoton events are below 0.1% of the nominal sample.

In this case, the ratio $N_{\gamma}^{\text{bkg-w}}/N_{\gamma\gamma}$ achieves large values, nevertheless considering the prompt photon rate per bunch-crossing of about 10^{-5}, the probability of having

Table A.6: Number of reconstructed diphotons $N_{\gamma\gamma}$ on a nominal sample (collected on paired bunch-crossings), number of diphotons $N_{\gamma\gamma}^{\text{bkg}}$ and single photons N_{γ}^{bkg} on the control sample from unpaired bunch-crossings, the corresponding values $N_{\gamma\gamma}^{\text{bkg-w}}$ and $N_{\gamma}^{\text{bkg-w}}$ after considering event weights equal to the scaling factor from Equation A.1, and the fraction that they represent with respect to the nominal sample $N_{\gamma\gamma}^{\text{bkg-w}}/N_{\gamma\gamma}$ and $N_{\gamma}^{\text{bkg-w}}/N_{\gamma}$. These numbers are quoted before and after applying different photon identification criteria.

Photon ID	Paired BC's	Unpaired BC's				Ratios	
	$N_{\gamma\gamma}$	$N_{\gamma\gamma}^{\text{bkg}}$	$N_{\gamma\gamma}^{\text{bkg-w}}$	N_{γ}^{bkg}	$N_{\gamma}^{\text{bkg-w}}$	$N_{\gamma\gamma}^{\text{bkg-w}}/N_{\gamma\gamma}$ [%]	$N_{\gamma}^{\text{bkg-w}}/N_{\gamma\gamma}$ [%]
None	132924	46	1628 ± 251	5909	175083 ± 2544	1.22 ± 0.19	132 ± 2
loose	48934	1	44 ± 44	384	11099 ± 640	0.09 ± 0.09	23 ± 1
tight	4227	0	–	35	1132 ± 207	–	27 ± 5
tight isolated	1665	0	–	22	662 ± 153	–	40 ± 9

in the diphoton sample a non-collision background photon overlapping with the production of a prompt photon in a collision turns out to be quite small.

Figure A.8 shows on the right side the relative amount of non-collision background as a function of three variables: the diphoton invariant mass $M_{\gamma\gamma}$ (top), the transverse momentum $p_{T,\gamma\gamma}$ (middle) and the azimuthal difference $\Delta\phi_{\gamma\gamma}$ (bottom). Again the highest relative amount of background is found in the high $p_{T,\gamma\gamma}$ bins. The values observed in these figures are of course expected to decrease after requiring photons to satisfy the identification criteria.

A.5 Conclusions

The amount of non-collision background in the single photon and diphoton samples has been estimated. This background estimation has been done based on control samples collected in time slots in which only one or no proton bunch pass by the ATLAS interaction point. These samples are expected to be dominated by beam-induced and cosmic-ray originated events.

From the obtained results, the relative amount of non-collision background for the three photon analysis considered [10–12] is expected to be below 0.1%, after applying the nominal photons selections. This is the case for the different bins in the different kinematic variables considered in those photon analyses. This amount of background is negligible compared with the size of the uncertainties on the concerned cross-section measurements, which are at least of 10%.

Bibliography

[1] S. Glashow, *Partial Symmetries of Weak Interactions*, Nucl.Phys. **22** (1961) 579–588.

[2] S. Weinberg, *A Model of Leptons*, Phys.Rev.Lett. **19** (1967) 1264–1266.

[3] A. Salam, *Weak and Electromagnetic Interactions*, Conf.Proc. **C680519** (1968) 367–377.

[4] P. W. Higgs, *Broken symmetries, massless particles and gauge fields*, Phys.Lett. **12** (1964) 132–133.

[5] F. Englert and R. Brout, *Broken Symmetry and the Mass of Gauge Vector Mesons*, Phys.Rev.Lett. **13** (1964) 321–323.

[6] G. Guralnik, C. Hagen, and T. Kibble, *Global Conservation Laws and Massless Particles*, Phys.Rev.Lett. **13** (1964) 585–587.

[7] LEP Working Group for Higgs boson searches, ALEPH Collaboration, DELPHI Collaboration, L3 Collaboration, OPAL Collaboration Collaboration, R. Barate et al., *Search for the standard model Higgs boson at LEP*, Phys.Lett. **B565** (2003) 61–75, `arXiv:hep-ex/0306033 [hep-ex]`.

[8] TEVNPH (Tevatron New Phenomina and Higgs Working Group), CDF Collaboration, D0 Collaboration Collaboration, *Combined CDF and D0 Upper Limits on Standard Model Higgs Boson Production with up to 8.6 fb^{-1} of Data*, `arXiv:1107.5518 [hep-ex]`.

[9] ATLAS Collaboration, *ATLAS Sensitivity Prospects for Higgs Boson Production at the LHC Running at 7 TeV*, Tech. Rep. ATL-PHYS-PUB-2010-009, CERN, Geneva, Jul, 2010.

[10] ATLAS Collaboration, G. Aad et al., *Measurement of the inclusive isolated prompt photon cross section in pp collisions at sqrt(s) = 7 TeV with the ATLAS detector*, Phys.Rev. **D83** (2011) 052005, `arXiv:1012.4389 [hep-ex]`.

[11] ATLAS Collaboration, G. Aad et al., *Measurement of the inclusive isolated prompt photon cross-section in pp collisions at sqrt(s)= 7 TeV using 35 pb-1 of ATLAS data*, Phys.Lett. **B706** (2011) 150–167, `arXiv:1108.0253 [hep-ex]`.

[12] ATLAS Collaboration, G. Aad et al., *Measurement of the isolated di-photon cross-section in pp collisions at sqrt(s) = 7 TeV with the ATLAS detector*, Phys.Rev. **D85** (2012) 012003, arXiv:1107.0581 [hep-ex].

[13] ATLAS Collaboration, *Measurement of the backgrounds to the $H \to \gamma\gamma$ search and reappraisal of its sensitivity with 37 pb^{-1} of data recorded by the ATLAS detector*, Tech. Rep. ATLAS-CONF-2011-004, CERN, Geneva, Feb, 2011.

[14] ATLAS Collaboration, *Search for the Higgs boson in the diphoton final state with 38 pb^{-1} of data recorded by the ATLAS detector in proton-proton collisions at $\sqrt{s}$=7 TeV*, Tech. Rep. ATLAS-CONF-2011-025, CERN, Geneva, Mar, 2011.

[15] ATLAS Collaboration, *Update of the Background Studies in the Search for the Higgs Boson in the Two Photons Channel in pp Collisions at $\sqrt{s} = 7$ TeV*, Tech. Rep. ATLAS-CONF-2011-071, CERN, Geneva, May, 2011.

[16] ATLAS Collaboration, *Search for the Higgs Boson in the Diphoton Channel with the ATLAS Detector using 209 pb-1 of 7 TeV Data taken in 2011*, Tech. Rep. ATLAS-CONF-2011-085, CERN, Geneva, Jun, 2011.

[17] ATLAS Collaboration, G. Aad et al., *Search for the Standard Model Higgs boson in the two photon decay channel with the ATLAS detector at the LHC*, Phys.Lett. **B705** (2011) 452–470, arXiv:1108.5895 [hep-ex].

[18] ATLAS Collaboration, *Search for the Standard Model Higgs boson in the diphoton decay channel with 4.9 fb-1 of ATLAS data at $\sqrt{s} = 7TeV$*, Tech. Rep. ATLAS-CONF-2011-161, CERN, Geneva, Dec, 2011.

[19] ATLAS Collaboration, G. Aad et al., *Search for the Standard Model Higgs boson in the diphoton decay channel with 4.9 fb-1 of pp collisions at sqrt(s)=7 TeV with ATLAS*, Phys.Rev.Lett. **108** (2012) 111803, arXiv:1202.1414 [hep-ex].

[20] ATLAS Collaboration, *Observation of an excess of events in the search for the Standard Model Higgs boson in the gamma-gamma channel with the ATLAS detector*, Tech. Rep. ATLAS-CONF-2012-091, CERN, Geneva, Jul, 2012.

[21] ATLAS Collaboration, *Observation and study of the Higgs boson candidate in the two photon decay channel with the ATLAS detector at the LHC*, Tech. Rep. ATLAS-CONF-2012-168, CERN, Geneva, Dec, 2012.

[22] D. Griffiths, *Introduction to elementary particles*, .

[23] F. Halzen and A. D. Martin, *QUARKS AND LEPTONS: AN INTRODUCTORY COURSE IN MODERN PARTICLE PHYSICS*, .

[24] A. Djouadi, *The Anatomy of electro-weak symmetry breaking. I: The Higgs boson in the standard model*, Phys.Rept. **457** (2008) 1–216, arXiv:hep-ph/0503172 [hep-ph].

[25] Website of the LEP Electroweak Working Group, http://lepewwg.web.cern.ch/LEPEWWG/.

[26] Gfitter's website, http://gfitter.desy.de/.

[27] M. Baak, M. Goebel, J. Haller, A. Hoecker, D. Ludwig, et al., *Updated Status of the Global Electroweak Fit and Constraints on New Physics*, Eur.Phys.J. **C72** (2012) 2003, arXiv:1107.0975 [hep-ph].

[28] Website of the LHC Higgs Cross Section Working Group, https://twiki.cern.ch/twiki/bin/view/LHCPhysics/CrossSections.

[29] LHC Higgs Cross Section Working Group Collaboration, S. Dittmaier et al., *Handbook of LHC Higgs Cross Sections: 1. Inclusive Observables*, arXiv:1101.0593 [hep-ph].

[30] S. Dittmaier, S. Dittmaier, C. Mariotti, G. Passarino, R. Tanaka, et al., *Handbook of LHC Higgs Cross Sections: 2. Differential Distributions*, arXiv:1201.3084 [hep-ph].

[31] A. Djouadi, M. Spira, and P. Zerwas, *Production of Higgs bosons in proton colliders: QCD corrections*, Phys.Lett. **B264** (1991) 440–446.

[32] S. Dawson, *Radiative corrections to Higgs boson production*, Nucl.Phys. **B359** (1991) 283–300.

[33] M. Spira, A. Djouadi, D. Graudenz, and P. Zerwas, *Higgs boson production at the LHC*, Nucl.Phys. **B453** (1995) 17–82, arXiv:hep-ph/9504378 [hep-ph].

[34] R. V. Harlander and W. B. Kilgore, *Next-to-next-to-leading order Higgs production at hadron colliders*, Phys.Rev.Lett. **88** (2002) 201801, arXiv:hep-ph/0201206 [hep-ph].

[35] C. Anastasiou and K. Melnikov, *Higgs boson production at hadron colliders in NNLO QCD*, Nucl.Phys. **B646** (2002) 220–256, arXiv:hep-ph/0207004 [hep-ph].

[36] V. Ravindran, J. Smith, and W. L. van Neerven, *NNLO corrections to the total cross-section for Higgs boson production in hadron hadron collisions*, Nucl.Phys. **B665** (2003) 325–366, arXiv:hep-ph/0302135 [hep-ph].

[37] S. Catani, D. de Florian, M. Grazzini, and P. Nason, *Soft gluon resummation for Higgs boson production at hadron colliders*, JHEP **0307** (2003) 028, arXiv:hep-ph/0306211 [hep-ph].

[38] D. de Florian, G. Ferrera, M. Grazzini, and D. Tommasini, *Transverse-momentum resummation: Higgs boson production at the Tevatron and the LHC*, JHEP **1111** (2011) 064, arXiv:1109.2109 [hep-ph].

[39] U. Aglietti, R. Bonciani, G. Degrassi, and A. Vicini, *Two loop light fermion contribution to Higgs production and decays*, Phys.Lett. **B595** (2004) 432–441, arXiv:hep-ph/0404071 [hep-ph].

[40] S. Actis, G. Passarino, C. Sturm, and S. Uccirati, *NLO Electroweak Corrections to Higgs Boson Production at Hadron Colliders*, Phys.Lett. **B670** (2008) 12–17, arXiv:0809.1301 [hep-ph].

[41] D. de Florian, M. Grazzini, and M. Grazzini, *Higgs production at the LHC: updated cross sections at* $\sqrt{s} = 8\ TeV$, arXiv:1206.4133 [hep-ph].

[42] C. Anastasiou, S. Buehler, F. Herzog, and A. Lazopoulos, *Inclusive Higgs boson cross-section for the LHC at 8 TeV*, JHEP **1204** (2012) 004, arXiv:1202.3638 [hep-ph].

[43] J. Baglio and A. Djouadi, *Higgs production at the lHC*, JHEP **1103** (2011) 055, arXiv:1012.0530 [hep-ph].

[44] M. Ciccolini, A. Denner, and S. Dittmaier, *Strong and electroweak corrections to the production of Higgs + 2jets via weak interactions at the LHC*, Phys.Rev.Lett. **99** (2007) 161803, arXiv:0707.0381 [hep-ph].

[45] M. Ciccolini, A. Denner, and S. Dittmaier, *Electroweak and QCD corrections to Higgs production via vector-boson fusion at the LHC*, Phys.Rev. **D77** (2008) 013002, arXiv:0710.4749 [hep-ph].

[46] K. Arnold, M. Bahr, G. Bozzi, F. Campanario, C. Englert, et al., *VBFNLO: A Parton level Monte Carlo for processes with electroweak bosons*, Comput.Phys.Commun. **180** (2009) 1661–1670, arXiv:0811.4559 [hep-ph].

[47] P. Bolzoni, F. Maltoni, S.-O. Moch, and M. Zaro, *Higgs production via vector-boson fusion at NNLO in QCD*, Phys.Rev.Lett. **105** (2010) 011801, arXiv:1003.4451 [hep-ph].

[48] T. Han and S. Willenbrock, *QCD correction to the* $pp \to WH$ *and* ZH *total cross-sections*, Phys.Lett. **B273** (1991) 167–172.

[49] O. Brein, A. Djouadi, and R. Harlander, *NNLO QCD corrections to the Higgs-strahlung processes at hadron colliders*, Phys.Lett. **B579** (2004) 149–156, arXiv:hep-ph/0307206 [hep-ph].

[50] M. Ciccolini, S. Dittmaier, and M. Kramer, *Electroweak radiative corrections to associated WH and ZH production at hadron colliders*, Phys.Rev. **D68** (2003) 073003, arXiv:hep-ph/0306234 [hep-ph].

[51] W. Beenakker, S. Dittmaier, M. Kramer, B. Plumper, M. Spira, et al., *Higgs radiation off top quarks at the Tevatron and the LHC*, Phys.Rev.Lett. **87** (2001) 201805, arXiv:hep-ph/0107081 [hep-ph].

[52] W. Beenakker, S. Dittmaier, M. Kramer, B. Plumper, M. Spira, et al., *NLO QCD corrections to t anti-t H production in hadron collisions*, Nucl.Phys. **B653** (2003) 151–203, arXiv:hep-ph/0211352 [hep-ph].

[53] S. Dawson, L. Orr, L. Reina, and D. Wackeroth, *Associated top quark Higgs boson production at the LHC*, Phys.Rev. **D67** (2003) 071503, arXiv:hep-ph/0211438 [hep-ph].

[54] S. Dawson, C. Jackson, L. Orr, L. Reina, and D. Wackeroth, *Associated Higgs production with top quarks at the large hadron collider: NLO QCD corrections*, Phys.Rev. **D68** (2003) 034022, arXiv:hep-ph/0305087 [hep-ph].

[55] A. Djouadi, J. Kalinowski, and M. Spira, *HDECAY: A Program for Higgs boson decays in the standard model and its supersymmetric extension*, Comput.Phys.Commun. **108** (1998) 56–74, arXiv:hep-ph/9704448 [hep-ph].

[56] S. Actis, G. Passarino, C. Sturm, and S. Uccirati, *NNLO Computational Techniques: The Cases $H \to \gamma\gamma$ and $H \to gg$*, Nucl.Phys. **B811** (2009) 182–273, arXiv:0809.3667 [hep-ph].

[57] ATLAS Collaboration, G. Aad et al., *Measurement of isolated-photon pair production in pp collisions at sqrt(s) = 7 TeV with the ATLAS detector*, arXiv:1211.1913 [hep-ex].

[58] ATLAS Collaboration, G. Aad et al., *Measurement of the production cross section of an isolated photon associated with jets in proton-proton collisions at $\sqrt{s} = 7$ TeV with the ATLAS detector*, Phys.Rev. **D85** (2012) 092014, arXiv:1203.3161 [hep-ex].

[59] CERN's website, http://www.cern.ch.

[60] e. Evans, Lyndon and e. Bryant, Philip, *LHC Machine*, JINST **3** (2008) S08001.

[61] *ATLAS detector and physics performance: Technical Design Report, 1.* Technical Design Report ATLAS. CERN, Geneva, 1999. CERN-LHCC-99-14, ATLAS-TDR-14.

[62] ATLAS Collaboration, G. Aad et al., *The ATLAS Experiment at the CERN Large Hadron Collider*, JINST **3** (2008) S08003.

[63] D0 Experiment's website, http://www-d0.fnal.gov.

[64] C. Lefèvre, The CERN accelerator complex, https://cdsweb.cern.ch/record/1260465, Dec, 2008.

[65] LHCb Collaboration, J. Alves, A. Augusto et al., *The LHCb Detector at the LHC*, JINST **3** (2008) S08005.

[66] ALICE Collaboration, K. Aamodt et al., *The ALICE experiment at the CERN LHC*, JINST **3** (2008) S08002.

[67] TOTEM Collaboration, G. Anelli et al., *The TOTEM experiment at the CERN Large Hadron Collider*, JINST **3** (2008) S08007.

[68] LHCf Collaboration, O. Adriani et al., *The LHCf detector at the CERN Large Hadron Collider*, JINST **3** (2008) S08006.

[69] ATLAS Collaboration, *ATLAS high-level trigger, data acquisition and controls: Technical design report*, .

[70] Website: LHC Commissioning with Beam, `http://lhc-commissioning.web.cern.ch/lhc-commissioning/`.

[71] ATLAS's website with luminosity related public results, `https://twiki.cern.ch/twiki/bin/view/AtlasPublic/-LuminosityPublicResults`.

[72] ATLAS experiment's website, `http://www.atlas.ch/`.

[73] Particle Data Group Collaboration, J. Beringer et al., *Review of Particle Physics (RPP)*, Phys.Rev. **D86** (2012) 010001.

[74] E. Segre, *Nuclei and Particles*. New York, Benjamin, 1964.

[75] W. R. Nelson, T. M. Jenkins, R. C. McCall, and J. K. Cobb, *ELECTRON INDUCED CASCADE SHOWERS IN COPPER AND LEAD AT 1-GeV*, Phys.Rev. **149** (1966) 201–208.

[76] G. Bathow, E. Freytag, M. Koebberling, K. Tesch, and R. Kajikawa, *Measurements of the longitudinal and lateral development of electromagnetic cascades in lead, copper and aluminum at 6 gev*, Nucl.Phys. **B20** (1970) 592–602.

[77] ATLAS Collaboration, G. Aad et al., *Electron performance measurements with the ATLAS detector using the 2010 LHC proton-proton collision data*, Eur.Phys.J. **C72** (2012) 1909, `arXiv:1110.3174 [hep-ex]`.

[78] Worldwide LHC Computing Grid's website, `http://lcg-archive.web.cern.ch/lcg-archive/public/`.

[79] Athena Core software's website, `http://atlas-computing.web.cern.ch/atlas-computing/packages/-athenaCore/athenaCore.php`.

[80] The Gaudi Project's website, `http://proj-gaudi.web.cern.ch/proj-gaudi/`.

[81] ROOT's website, `http://root.cern.ch/drupal/`.

[82] ATLAS Collaboration, E. Duckeck, G. et al., *ATLAS computing: Technical design report*, .

[83] T. Sjostrand, S. Mrenna, and P. Z. Skands, *PYTHIA 6.4 Physics and Manual*, **??**JHEP **0605** (2006) 026, `arXiv:hep-ph/0603175 [hep-ph]`.

[84] T. Sjostrand, S. Mrenna, and P. Z. Skands, *A Brief Introduction to PYTHIA 8.1*, Comput.Phys.Commun. **178** (2008) 852–867, arXiv:0710.3820 [hep-ph].

[85] Herwig generator's website, https://herwig.hepforge.org/.

[86] GEANT4 Collaboration, S. Agostinelli et al., *GEANT4: A Simulation toolkit*, Nucl.Instrum.Meth. **A506** (2003) 250–303.

[87] ATLAS Collaboration, G. Aad et al., *The ATLAS Simulation Infrastructure*, Eur.Phys.J. **C70** (2010) 823–874, arXiv:1005.4568 [physics.ins-det].

[88] *ATLAS tunes of PYTHIA 6 and Pythia 8 for MC11*, Tech. Rep. ATL-PHYS-PUB-2011-009, CERN, Geneva, Jul, 2011.

[89] W. Lampl, S. Laplace, D. Lelas, P. Loch, H. Ma, S. Menke, S. Rajagopalan, D. Rousseau, S. Snyder, and G. Unal, *Calorimeter Clustering Algorithms: Description and Performance*, Tech. Rep. ATL-LARG-PUB-2008-002. ATL-COM-LARG-2008-003, CERN, Geneva, Apr, 2008.

[90] ATLAS Collaboration, G. Aad et al., *Expected Performance of the ATLAS Experiment - Detector, Trigger and Physics*, arXiv:0901.0512 [hep-ex].

[91] *Expected photon performance in the ATLAS experiment*, Tech. Rep. ATL-PHYS-PUB-2011-007, CERN, Geneva, Apr, 2011.

[92] Website of the ATLAS Electron Gamma Public Results, https://twiki.cern.ch/twiki/bin/view/AtlasPublic/-ElectronGammaPublicCollisionResults.

[93] *Electron and photon reconstruction and identification in ATLAS: expected performance at high energy and results at 900 GeV*, Tech. Rep. ATLAS-CONF-2010-005, CERN, Geneva, Jun, 2010.

[94] A. Hocker, J. Stelzer, F. Tegenfeldt, H. Voss, K. Voss, et al., *TMVA - Toolkit for Multivariate Data Analysis*, PoS **ACAT** (2007) 040, arXiv:physics/0703039 [PHYSICS].

[95] *Measurements of the photon identification efficiency with the ATLAS detector using 4.9 fb ,àí1 of pp collision data collected in 2011*, Tech. Rep. ATLAS-CONF-2012-123, CERN, Geneva, Aug, 2012.

[96] M. Cacciari, G. P. Salam, and S. Sapeta, *On the characterisation of the underlying event*, JHEP **1004** (2010) 065, arXiv:0912.4926 [hep-ph].

[97] M. Hance and H. H. Williams, *Measurement of Inclusive Isolated Prompt Photon Production in Proton-Proton Collisions at $\sqrt{s} = 7$ TeV with the ATLAS Detector*. PhD thesis, Pennsylvania U., Philadelphia, 2011. Presented 11 Jul 2011, CERN-THESIS-2011-044.

[98] J. Gaiser, *Charmonium spectroscopy from radiative decays of the J /psi and psi-prime*, .

[99] LHC Higgs Combination Group, ATLAS Collaboration, CMS Collaboration, *Procedure for the LHC Higgs boson search combination in summer 2011*, Tech. Rep. ATL-PHYS-PUB-2011-011, CERN, Geneva, Aug, 2011.

[100] A. L. Read, *Presentation of search results: The CL(s) technique*, J.Phys. **G28** (2002) 2693–2704.

[101] G. Cowan, K. Cranmer, E. Gross, and O. Vitells, *Asymptotic formulae for likelihood-based tests of new physics*, Eur.Phys.J. **C71** (2011) 1554, `arXiv:1007.1727 [physics.data-an]`.

[102] S. Wilks, *The large-sample distribution of the likelihood ratio for testing composite hypotheses*, Ann. Math. Statist. **9:pp** (1938) 60–62.

[103] E. Gross and O. Vitells, *Trial factors or the look elsewhere effect in high energy physics*, Eur.Phys.J. **C70** (2010) 525–530, `arXiv:1005.1891 [physics.data-an]`.

[104] L. Fayard and G. Unal, *Search for Higgs decay into photons with EAGLE. Add. 1 Addendum on the Higgs search with photons. Add. 2 (final?) update on Higgs decay to photons*, .

[105] *ATLAS detector and physics performance: Technical Design Report, 2.* Technical Design Report ATLAS. CERN, Geneva, 1999. CERN-LHCC-99-15, ATLAS-TDR-15.

[106] ATLAS Collaboration, G. Aad et al., *Observation of a new particle in the search for the Standard Model Higgs boson with the ATLAS detector at the LHC*, Phys.Lett. **B716** (2012) 1–29, `arXiv:1207.7214 [hep-ex]`.

[107] P. Bernat and M. Kado, *Recherche du boson de Higgs dans le canal de désintégration en deux photons avec le détecteur ATLAS au LHC. oai:cds.cern.ch:1283470. Search for the Standard Model Higgs boson in the diphoton decay channel with ATLAS detector at LHC.* PhD thesis, Orsay, Université Paris Sud, Orsay, 2010. Presented on 24 Jun 2010, CERN-THESIS-2010-098.

[108] L. Yuan and L. Roos, *Di-photon cross section measurement and Higgs sensitivity study in the two-photon final state with the ATLAS detector. oai:cds.cern.ch:1363319.* PhD thesis, Paris U., VI-VII, Paris & Beijing, 2011. Presented 22 Jun 2011, CERN-THESIS-2011-038.

[109] H. Abreu and L. Fayard, *Measurement of the inclusive prompt photon cross section and preparation of the search of the Higgs boson decaying into two photons with the ATLAS detector at the LHC. oai:cds.cern.ch:1398295.* PhD thesis, Orsay, 2011. Presented 05 Jul 2011, CERN-THESIS-2011-157.

[110] N. Andari and L. Fayard, *Observation of a BEH-like boson decaying into two photons with the ATLAS detector at the LHC. oai:cds.cern.ch:1485052.* PhD thesis, Orsay, LAL, Sep, 2012. Presented 26 Sep 2012, CERN-THESIS-2012-144.

[111] ATLAS Collaboration, G. Aad et al., *Luminosity Determination in pp Collisions at sqrt(s)=7 TeV Using the ATLAS Detector at the LHC*, hrefhttp://www.springerlink.com/content/37871nw70047xw34/Eur.Phys.J. **C71** (2011) 1630, arXiv:1101.2185 [hep-ex].

[112] *Improved Luminosity Determination in* **pp** *Collisions at* $\sqrt{\mathbf{s}} = \mathbf{7}$ *TeV using the ATLAS Detector at the LHC*, Tech. Rep. ATLAS-CONF-2012-080, CERN, Geneva, Jul, 2012.

[113] S. Alioli, P. Nason, C. Oleari, and E. Re, *NLO Higgs boson production via gluon fusion matched with shower in POWHEG*, JHEP **0904** (2009) 002, arXiv:0812.0578 [hep-ph].

[114] P. Nason and C. Oleari, *NLO Higgs boson production via vector-boson fusion matched with shower in POWHEG*, JHEP **1002** (2010) 037, arXiv:0911.5299 [hep-ph].

[115] L. J. Dixon and M. S. Siu, *Resonance continuum interference in the diphoton Higgs signal at the LHC*, Phys.Rev.Lett. **90** (2003) 252001, arXiv:hep-ph/0302233 [hep-ph].

[116] T. Gleisberg, S. Hoeche, F. Krauss, M. Schonherr, S. Schumann, et al., *Event generation with SHERPA 1.1*, JHEP **0902** (2009) 007, arXiv:0811.4622 [hep-ph].

[117] M. L. Mangano, M. Moretti, F. Piccinini, R. Pittau, and A. D. Polosa, *ALPGEN, a generator for hard multiparton processes in hadronic collisions*, JHEP **0307** (2003) 001, arXiv:hep-ph/0206293 [hep-ph].

[118] C. Balazs, E. L. Berger, P. M. Nadolsky, and C.-P. Yuan, *Calculation of prompt diphoton production cross-sections at Tevatron and LHC energies*, Phys.Rev. **D76** (2007) 013009, arXiv:0704.0001 [hep-ph].

[119] T. Binoth, J. Guillet, E. Pilon, and M. Werlen, *A Full next-to-leading order study of direct photon pair production in hadronic collisions*, Eur.Phys.J. **C16** (2000) 311–330, arXiv:hep-ph/9911340 [hep-ph].

[120] K. S. Cranmer, *Kernel estimation in high-energy physics*, Comput.Phys.Commun. **136** (2001) 198–207, arXiv:hep-ex/0011057 [hep-ex].

[121] Atlas Collaboration Collaboration, G. Aad et al., *Performance of the ATLAS Trigger System in 2010*, Eur.Phys.J. **C72** (2012) 1849, arXiv:1110.1530 [hep-ex].

[122] M. Botje, J. Butterworth, A. Cooper-Sarkar, A. de Roeck, J. Feltesse, et al., *The PDF4LHC Working Group Interim Recommendations*, arXiv:1101.0538 [hep-ph].

[123] H.-L. Lai, M. Guzzi, J. Huston, Z. Li, P. M. Nadolsky, et al., *New parton distributions for collider physics*, Phys.Rev. **D82** (2010) 074024, arXiv:1007.2241 [hep-ph].

[124] A. Martin, W. Stirling, R. Thorne, and G. Watt, *Parton distributions for the LHC*, Eur.Phys.J. **C63** (2009) 189–285, arXiv:0901.0002 [hep-ph].

[125] R. D. Ball, V. Bertone, F. Cerutti, L. Del Debbio, S. Forte, et al., *Impact of Heavy Quark Masses on Parton Distributions and LHC Phenomenology*, Nucl.Phys. **B849** (2011) 296–363, arXiv:1101.1300 [hep-ph].

[126] A. Denner, S. Heinemeyer, I. Puljak, D. Rebuzzi, and M. Spira, *Standard Model Higgs-Boson Branching Ratios with Uncertainties*, Eur.Phys.J. **C71** (2011) 1753, arXiv:1107.5909 [hep-ph].

[127] OPAL Collaboration, K. Ackerstaff et al., *Search for anomalous production of dilepton events with missing transverse momentum in e+ e- collisions at s**(1/2) = 161-GeV and 172-GeV*, Eur.Phys.J. **C4** (1998) 47–74, arXiv:hep-ex/9710010 [hep-ex].

[128] M. Vesterinen and T. Wyatt, *A Novel Technique for Studying the Z Boson Transverse Momentum Distribution at Hadron Colliders*, Nucl.Instrum.Meth. **A602** (2009) 432–437, arXiv:0807.4956 [hep-ex].

[129] M. Cacciari, G. P. Salam, and G. Soyez, *The Anti-k(t) jet clustering algorithm*, JHEP **0804** (2008) 063, arXiv:0802.1189 [hep-ph].

[130] ATLAS Collaboration, G. Aad et al., *Jet energy measurement with the ATLAS detector in proton-proton collisions at* $\sqrt{s} = 7$ *TeV*, arXiv:1112.6426 [hep-ex].

[131] *Pile-up corrections for jets from proton-proton collisions at* $\sqrt{s} = 7$ *TeV in ATLAS in 2011*, Tech. Rep. ATLAS-CONF-2012-064, CERN, Geneva, Jul, 2012.

[132] *In situ jet pseudorapidity intercalibration of the ATLAS detector using dijet events in sqrts=7 TeV proton-proton 2011 data*, Tech. Rep. ATLAS-CONF-2012-124, CERN, Geneva, Aug, 2012.

[133] I. W. Stewart and F. J. Tackmann, *Theory Uncertainties for Higgs and Other Searches Using Jet Bins*, Phys.Rev. **D85** (2012) 034011, arXiv:1107.2117 [hep-ph].

[134] J. M. Campbell, R. K. Ellis, and C. Williams, *Hadronic production of a Higgs boson and two jets at next-to-leading order*, Phys.Rev. **D81** (2010) 074023, arXiv:1001.4495 [hep-ph].

[135] CMS Collaboration, S. Chatrchyan et al., *Observation of a new boson at a mass of 125 GeV with the CMS experiment at the LHC*, Phys.Lett. **B716** (2012) 30–61, arXiv:1207.7235 [hep-ex].

[136] CMS Collaboration, *Combination of standard model Higgs boson searches and measurements of the properties of the new boson with a mass near 125 GeV*, Tech. Rep. CMS-PAS-HIG-12-045, CERN, Geneva, 2012.

[137] ATLAS Collaboration, *Observation of an excess of events in the search for the Standard Model Higgs boson in the $H \to ZZ^{(*)} \to 4\ell$ channel with the ATLAS detector*, Tech. Rep. ATLAS-CONF-2012-169, CERN, Geneva, Dec, 2012.

[138] ATLAS Collaboration, *Update of the $H \to WW^{(*)} \to e\nu\mu\nu$ Analysis with 13 fb^{-1} of $\sqrt{s} = 8$ TeV Data Collected with the ATLAS Detector*, Tech. Rep. ATLAS-CONF-2012-158, CERN, Geneva, Nov, 2012.

[139] ATLAS Collaboration, *An update of combined measurements of the new Higgs-like boson with high mass resolution channels*, Tech. Rep. ATLAS-CONF-2012-170, CERN, Geneva, Dec, 2012.

[140] Tevatron New Physics Higgs Working Group, CDF Collaboration, D0 Collaboration, C. Group, D. Collaborations, the Tevatron New Physics, and H. Working, *Updated Combination of CDF and D0 Searches for Standard Model Higgs Boson Production with up to 10.0 fb^{-1} of Data*, `arXiv:1207.0449 [hep-ex]`.

[141] CMS Collaboration, *Updated results on the new boson discovered in the search for the standard model Higgs boson in the ZZ to 4 leptons channel in pp collisions at sqrt(s) = 7 and 8 TeV*, Tech. Rep. CMS-PAS-HIG-12-041, CERN, Geneva, 2012.

[142] ATLAS Collaboration, *Observation of an excess of events in the search for the Standard Model Higgs boson in the $H \to ZZ^{(*)} \to 4\ell$ channel with the ATLAS detector.*, Tech. Rep. ATLAS-CONF-2012-092, CERN, Geneva, Jul, 2012.

[143] ATLAS Collaboration, *Observation of an Excess of Events in the Search for the Standard Model Higgs Boson in the $H \to WW^{(*)} \to \ell\nu\ell\nu$ Channel with the ATLAS Detector*, Tech. Rep. ATLAS-CONF-2012-098, CERN, Geneva, Jul, 2012.

[144] ATLAS Collaboration, *Measurements of the properties of the Higgs-like boson in the two photon decay channel with the ATLAS detector using 25* fb^{-1} *of proton-proton collision data*, Tech. Rep. ATLAS-CONF-2013-012, CERN, Geneva, Mar, 2013.

[145] ATLAS Collaboration, *Measurements of the properties of the Higgs-like boson in the four lepton decay channel with the ATLAS detector using 25 fb ,àí1 of proton-proton collision data*, Tech. Rep. ATLAS-CONF-2013-013, CERN, Geneva, Mar, 2013.

[146] ATLAS Collaboration, *Measurements of the properties of the Higgs-like boson in the $WW^{(*)} \to \ell\nu\ell\nu$ decay channel with the ATLAS detector using 25 fb^{-1} of proton-proton collision data*, Tech. Rep. ATLAS-CONF-2013-030, CERN, Geneva, Mar, 2013.

[147] ATLAS Collaboration, *Combined measurements of the mass and signal strength of the Higgs-like boson with the ATLAS detector using up to 25 fb^{-1} of proton-proton collision data*, Tech. Rep. ATLAS-CONF-2013-014, CERN, Geneva, Mar, 2013.

[148] ATLAS Collaboration, *Combined coupling measurements of the Higgs-like boson with the ATLAS detector using up to 25 fb^{-1} of proton-proton collision data*, Tech. Rep. ATLAS-CONF-2013-034, CERN, Geneva, Mar, 2013.

[149] ATLAS Collaboration, *Study of the spin of the Higgs-like boson in the two photon decay channel using 20.7 fb-1 of pp collisions collected at $\sqrt{s}$ = 8 TeV with the ATLAS detector*, Tech. Rep. ATLAS-CONF-2013-029, CERN, Geneva, Mar, 2013.

[150] J. C. Collins and D. E. Soper, *Angular Distribution of Dileptons in High-Energy Hadron Collisions*, Phys.Rev. **D16** (1977) 2219.

[151] L. Landau, *On the angular momentum of a two-photon system*, Dokl.Akad.Nauk Ser.Fiz. **60** (1948) 207–209.

[152] C.-N. Yang, *Selection Rules for the Dematerialization of a Particle Into Two Photons*, Phys.Rev. **77** (1950) 242–245.

[153] ATLAS Collaboration, *Study of the spin properties of the Higgs-like particle in the $\boldsymbol{H \to WW^{(*)} \to e\nu\mu\nu}$ channel with 21 fb^{-1} of $\sqrt{s} = 8$ TeV data collected with the ATLAS detector.*, Tech. Rep. ATLAS-CONF-2013-031, CERN, Geneva, Mar, 2013.

[154] CMS Collaboration Collaboration, S. Chatrchyan et al., *On the mass and spin-parity of the Higgs boson candidate via its decays to Z boson pairs*, Phys. Rev. Lett. **110** (2013) 081803, `arXiv:1212.6639 [hep-ex]`.

[155] CMS Collaboration, *Properties of the Higgs-like boson in the decay H to ZZ to 4l in pp collisions at sqrt s =7 and 8 TeV*, Tech. Rep. CMS-PAS-HIG-13-002, CERN, Geneva, 2013.

[156] CMS Collaboration, *Evidence for a particle decaying to W+W- in the fully leptonic final state in a standard model Higgs boson search in pp collisions at the LHC*, Tech. Rep. CMS-PAS-HIG-13-003, CERN, Geneva, 2013.

[157] CMS Collaboration, *Evidence for a new state decaying into two photons in the search for the standard model Higgs boson in pp collisions*, Tech. Rep. CMS-PAS-HIG-12-015, CERN, Geneva, 2012.

[158] ATLAS Collaboration, *Non-collision backgrounds as measured by the ATLAS detector during the 2010 proton-proton run*, Tech. Rep. ATLAS-CONF-2011-137, CERN, Geneva, Sep, 2011.

Observation d'une NOUVELLE PARTICULE
dans la recherche du BOSON de HIGGS se désintégrant en DEUX PHOTONS
dans l'expérience ATLAS au LHC

Heberth TORRES DÁVILA

Cette thèse présente une recherche du boson de Higgs du Modèle standard dans le canal de désintégration en deux photons. L'étude est basée sur les collisions proton-proton enregistrées par le détecteur ATLAS auprès du grand collisionneur de hadrons du CERN (LHC), en 2011 et 2012. Les données analysées correspondent à 4,8 fb^{-1} de luminosité intégrée à une énergie dans le centre de masse de la collision $\sqrt{s} = 7$ TeV, et 5,9 fb^{-1} à $\sqrt{s} = 8$ TeV.

Dans la distribution de masse invariante des paires de photons, un excès d'événements est observé aux alentours de 125 GeV. La probabilité d'avoir une fluctuation statistique positive dans cette distribution égale ou supérieure à l'excès observé, dans la fenêtre de masse étudiée [110 − 150 GeV], est de $1,6 \times 10^{-4}$. Cette probabilité correspond à 3,6 déviations standard. Des résultats similaire ont été obtenus dans les recherches du boson de Higgs dans d'autres canaux de désintégration par la collaboration ATLAS, ainsi que par CMS. Ces résultats démontrent l'existence d'une nouvelle particule, dont les propriétés sont compatibles avec celles du boson de Higgs du Modèle standard.

Observation of a NEW PARTICLE
in the search for the HIGGS BOSON in the TWO PHOTON decay channel
in the ATLAS experiment at the LHC

Heberth TORRES DÁVILA

This thesis presents a search for the Standard Model Higgs boson in the diphoton decay channel. It is based on the analysis of proton-proton collisions collected with the ATLAS detector at the Large Hadron Collider at CERN, in 2011 and 2012. The analyzed data correspond to 4.8 fb^{-1} of integrated luminosity at a center-of-mass energy $\sqrt{s} = 7$ TeV, and 5.9 fb^{-1} at $\sqrt{s} = 8$ TeV.

In the diphoton invariant mass distribution, an excess of events is observed around 125 GeV. The probability to have a positive statistical fluctuation in that distribution equal or larger than the observed excess, anywhere in the explored mass range [110 − 150 GeV], is 1.6×10^{-4}. This probability corresponds to 3.6 standard deviations. Similar results have been obtained in the searches of the Higgs boson in other decay channels by the ATLAS collaboration, as well as by CMS. These results indicate the existence of a new particle, whose properties are compatible with those of the Standard Model Higgs boson.